MODELLING AND ANALYSIS OF VORTEX-INDUCED VIBRATIONS OF RIGID AND FLEXIBLE CYLINDERS

HOSSEIN ZANGANEH

A thesis submitted in partial fulfilment of the requirements for the degree of Doctor of Philosophy

Department of Naval Architecture, Ocean and Marine Engineering

University of Strathclyde

©Hossein Zanganeh, 2015

This thesis is the result of the author's original research. It has been composed by the author and has not been previously submitted for examination which has led to the award of a degree.

The author wishes to declare that the reproduction and adaptation of published results of other's research campaigns have been performed via proper and highly accurate digitizer software or well-known post-processing approaches and have been provided with adequate and proper references to the original campaign. However, any imprecision involved in this process which has been remained out of sight and reach of the author must not be associated with the integrity of the original research.

The copyright of this thesis belongs to the author under the terms of the United Kingdom Copyright Acts as qualified by University of Strathclyde Regulation 3.50. Due acknowledgement must always be made of the use of any material contained in, or derived from, this thesis.

Acknowledgments

Living and studying in Glasgow is one of the happiest and most memorable periods of my life and it is all because of those who kindly and generously helped me and supported me in these years.

First of all I am very grateful to my PhD supervisor Dr Narakorn Srinil who provided this research opportunity for me. Without his continuing support, advice and supervision, this project would have never been accomplished. I am deeply indebted to him since he always trusted me, let me freely explore new challenges and develop new ideas, and generously spent a lot of his time to listen, share and discuss upon our new ideas.

I wish to thank Prof. Sandy Day for his invaluable support and help during my experiments at Kelvin Hydrodynamics Laboratory. I also wish to acknowledge all the technicians at the lab for their assistance, the experimental setup and measurement support.

I would like to thank all the faculty and staff members of the Department of Naval Architecture, Ocean and Marine Engineering particularly Dr Mahdi Khorasanchi for being such a good friend and Thelma Will for being so helpful and caring.

I would like to express my gratitude to the financial supports provided by the SORSAS and Early Career Researcher International Exchange Awards supported by the University of Strathclyde and Scottish Funding Council (via GRPe-SFC).

I wish to thank my parents and family who have been kindly and bigheartedly supportive and helpful in all stages of my life. I am also truly grateful to my beloved wife for her patience, constant encouragement and supports.

Finally, I thank God for giving me such good family, friends, colleagues, supervisors and all other blessings that remained untold and are beyond measure.

Abstract

Vortex-induced vibration (VIV) is a fundamental phenomenon commonly encountered in various practical engineering. Owing to the complexities associated with this phenomenon, modelling and prediction of VIV is a challenging task. In this research, a new predictive phenomenological model is developed for VIV of an elastically mounted rigid cylinder subjected to a fluid flow and free to vibrate in both cross-flow (CF) and in-line (IL) directions. The ensuing dynamical system is based on double Duffing-van der Pol (structural-wake) oscillators with the two structural equations containing both cubic and quadratic nonlinear terms. The cubic nonlinearities capture the geometrical coupling of CF/IL displacements excited by hydrodynamic lift/drag forces whereas the quadratic nonlinearities allow the fluid-structure interactions. The model predictions are extensively compared with published and in-house experimental results. Experiments are carried out at the Department's towing tank to calibrate and validate numerical prediction results. Comparisons illustrate the qualitative resemblance between experimental and prediction results, highlighting how the new model can capture several important VIV characteristics including a two-dimensional lock-in, jump and hysteresis phenomenon, and figure-of-eight trajectory tracing the periodically coupled CF/IL oscillations. Moreover, the parametric studies reveal the important effect of geometrical nonlinearities, mass ratio, damping ratio and natural frequency ratio. Insights into hydrodynamic properties such as VIV-induced mean drag, added mass and damping are drawn based on the newly proposed model via analytical-numerical approaches and comparisons with published literature.

Consequently, the new prediction model is applied to the VIV analysis of flexible circular cylinders subjected to uniform and linearly sheared currents. To capture a three-dimensional aspect of the flexible cylinder experiencing VIV, nonlinear equations of CF, IL and axial structural oscillations are considered to be coupled with the distributed van der Pol wake-oscillators. Governing equations are numerically solved via a space-time finite difference scheme, and the obtained numerical results highlight several aspects of VIV of elastic cylinders along with the axial motion effects. Apart from the validation of the numerical model with published experimental results, this study reveals how the effect of axial motion and its nonlinear coupling with the two transverse CF/IL motions can be very important. These depend on the reduced velocity, the fluid-structure parameters, the single or multi-mode lock-in condition, and the standing-wave versus travelling-wave features.

Publications

Journal Papers

H. Zanganeh, N. Srinil, Characterization of Variable Hydrodynamic Coefficients and Maximum Responses in Two-Dimensional Vortex-Induced Vibrations With Dual Resonances, Journal of Vibration and Acoustics, 136 (2014) Paper Number: 051010.

N. Srinil, **H. Zanganeh,** A. Day, Two-degree-of-freedom VIV of circular cylinder with variable natural frequency ratio: Experimental and numerical investigations, Ocean Engineering, 73 (2013) 179-194.

N. Srinil, **H. Zanganeh,** Modelling of coupled cross-flow/in-line vortex-induced vibrations using double Duffing and van der Pol oscillators, Ocean Engineering, 53 (2012) 83-97.

Conference Papers

H. Zanganeh, N. Srinil, Coupled Axial/Transverse VIV of Marine Risers in Sheared Currents, in: The 34th International Conference on Ocean, Offshore & Arctic Engineering, St. John's, Newfoundland, Canada, 2015.

H. Zanganeh, N. Srinil, Two-Dimensional Coupled Vortex-Induced Vibration of Circular Cylinder: Prediction and Extraction of Hydrodynamics Properties**,** in: The 32nd International Conference on Ocean, Offshore & Arctic Engineering, Nantes, France, 2013.

H. Zanganeh, N. Srinil, Interaction of Wake and Structure in Two-Dimensional Vortex-Induced Vibrations**,** in**:** The International Conference on Advances and Challenges in Marine Noise and Vibration (MARNAV2012), Glasgow, Scotland, UK, 2012.

N. Srinil, **H. Zanganeh,** A. Day, Experimental investigation of two-degree-of-freedom VIV of circular cylinder with low equivalent mass and variable natural frequency ratio, in: The 32nd International Conference on Ocean, Offshore & Arctic Engineering, Nantes, France, 2013.

E. Wang, Q. Xiao, N. Srinil, **H. Zanganeh**, Vortex-Induced Vibration of Circular Cylinder with Two Degrees of Freedom: Computational Fluid Dynamics vs. Reduced-Order Models**,** in: The 32nd International Conference on Ocean Offshore & Arctic Engineering, Nantes, France, 2013.

Table of Contents

Nomenclature

Abbreviation

1D	One-dimensional
2D	Two-dimensional
CF	Cross-flow
CFD	Computational fluid dynamics
DNS	Direct numerical simulation
DOF	Degree of freedom
Fo8	Figure-of-eight
FSI	Fluid-structure interaction
IL	In-line
RMS	Root mean square
VIV	Vortex-induced vibration

Roman symbols

A_r	Cross-sectional area
A_{wRMS}/D, A_{wRMS}/D	RMS value of the amplitude of IL and CF oscillations
A_x/D, A_y/D	Dimensionless in-line and cross-flow amplitudes
A_{xm}/D, A_{ym}/D, A_{uM}/D, A_{wM}/D	Corresponding maximum attainable amplitudes
b	Buoyancy force
C_a	Added mass coefficient
C_{ax} , C_{ay}	Hydrodynamic coefficients of forces in phase with cylinder acceleration
C_{Ax} , C_{Ay}	Added mass coefficients scaled based on cylinder acceleration
C_D	Mean drag coefficient
$\bar{C}_d$	Mean drag coefficient of stationary cylinder
C_d, C_l	Unsteady drag and lift coefficients
C_{d0}, C_{l0}	Drag and lift coefficients of a stationary cylinder
C_{DT}	Total mean drag coefficient
C_{dv}	Mean drag coefficient as a result of VIV of oscillating cylinder
$\boldsymbol{c}_{fx}$, $\boldsymbol{c}_{fy}$	Hydrodynamic damping coefficients
C_{Mx} , C_{My}	Effective added mass coefficients
$\boldsymbol{c}_{sx}$, $\boldsymbol{c}_{sy}$	Structural viscous damping coefficients
C_{vx} , C_{vy}	Hydrodynamic coefficients of forces in phase with cylinder velocity
C_x , C_y, C_z	Unsteady in-line and cross-flow force coefficients of oscillating cylinder
D	Diameter of a circular cylinder
E	Modulus of elasticity
EA_r	Axial stiffness
EI	Bending stiffness
f^*	Ratio of cylinder in-line to cross-flow natural frequencies

F_D, F_L	Fluctuating drag and lift forces
f_i	Natural frequency of the dominant mode of CF oscillations
f_{nx}, f_{ny}	Natural frequency in still water of cylinder
f_{ox}, f_{oy}	Dominant frequency of the oscillating cylinder
F_x, F_y, F_z	Hydrodynamic forces in streamwise and transverse directions
g	Gravitational acceleration
H_x, H_y	Distance between vertical pendulum and vicinity frame where the springs are attached
I	Area moment of inertia
k,k_x, k_y	Spring stiffness
L_c (L_p)	Cylinder submerged (pendulum) length
L_c/D	Aspect ratio
L_s	Distance from the universal joint to the springs
L_x, L_y	Free length of springs in the IL and CF directions
M_D, M_L	System mass parameters
m_{fx}, m_{fy}	Fluid added masses
m_{sx}, m_{sy}	Cylinder masses
n	Mode number
p, q	Reduced vortex drag and lift coefficients
Re	Reynolds number
S_G, S_{GX}, S_{GY}	Skop-Griffin parameter
St	Strouhal number
S_x, S_y	Excitation terms simulating the effect of cylinder on the near wake
T	Space-related tension
t	Dimensional time
t'	Dimensionless time
T_0	Pretension
T_d	Dynamic tensions
T_t	Total tension
$\bar{T}_t$	Mean total tension
T_{top}	Top tension
u, v, w	Dynamic displacement in IL, axial and CF directions
V	Uniform flow velocity
V_r	Reduced flow velocity
V_{rel}	Relative flow velocity
V_{rxm}, V_{rym}	Reduced velocities at maximum attainable amplitudes
W	Modal weight
X, Y	Dimensional in-line and cross-flow displacements
x, y	Dimensionless in-line and cross-flow displacements

Greek symbols

$\delta(\varphi)$	Relative phase between in-line (transverse) force and displacement
σ, a_1-a_6, k_{pq}, k_q	Coefficients resulting from analytical closed-form solution
α^*_x, α^*_y, β^*_x, β^*_y	Dimensional geometrically nonlinear coefficients

α'	Combined mass-damping parameter
α_x, α_y, β_x, β_y	Dimensionless geometrically nonlinear coefficients
γ	Stall parameter
ε_x, ε_y, ε_u, ε_w	Wake coefficients
θ	Angle of attack of the flow relative to the cylinder
θ_x, θ_y, θ_p, θ_q	Phase angles
θ_{xy}	Relative phase between x and y cylinder oscillations
λ_x, λ_y	Combined fluid-structural damping terms
Λ_x, Λ_y, Λ_u, Λ_w	Wake-cylinder coupling coefficients
μ_x, μ_y, m^*_x, m^*_y, m^*	Mass ratios
ν	Kinematic viscosity
ξ_x, ξ_y, ξ	Structural reduced damping coefficients
ρ	Fluid density
σ_w, σ_u, σ_v	Stresses induced by CF, IL and axial oscillations
Ω	Ratio of vortex-shedding to cylinder cross-flow natural frequencies
ω_f	Vortex-shedding angular frequency
ω_{nx}, ω_{ny}	Structural natural frequencies in still water
φ_n	Mode shape

List of Figures

List of Tables

Chapter 1

Introduction

Many engineering mechanical, civil and offshore structures such as thermo wells, heat exchangers, suspended bridges, skyscrapers, pipelines, risers and mooring cables are subjected to fluid flows (which is usually water or air) and may experience phenomena pertaining to the interaction between the structure and the fluid. One of the most important and most probable side effects of these fluid-structure interaction (FSI) phenomena is the structural vibrations induced by fluid flow which can be either useful or damaging. Either way, flow-induced oscillations have two main components, (i) the fluid flow and (ii) the structure. These components are coupled through the forces which are exerted from fluid to the structure and from the structure to the fluid. A schematic representation of this mechanism is depicted in Figure 1.1. Moreover, the two main components of this mechanism (the fluid and the structure) can have different variables which result in different fluid/structural dynamics. For instance, the fluid flow can be steady, unsteady, uniform, laminar, turbulent or etc. and the structure can be rigid or elastic, or have different cross-sections. Hence, based on the type of fluid flow or structure, different categorisation of flow-induced vibrations is achievable. Pertaining to steady fluid flow, a classification of these is illustrated in Figure 1.2.

As it is shown in Figure 1.2, when a structure is subjected to an external steady fluid flow, it may undertake vibrations which are caused by the vortices shedding from the structure or so-called vortex-induced vibrations (VIV). VIV is the common type of flow-induced vibration of cylindrical bluff structures which is the case for many offshore structures. Generally speaking, pertaining to the type of the structure undergoing these vibrations, VIV can be categorised into two main groups of (i) VIV of rigid structures and (ii) VIV of flexible structures. Moreover, these structures can experience VIV in direction transverse to the fluid flow [1], in the streamwise

direction [2] and (when the structure is flexible) in the longitudinal direction [3]. Each of these categories has been studied over the past decades. However, prediction of VIV, due to intrinsic complications of this fluid-structure interaction phenomenon, is still a challenging theme. Since the basic mechanism governing these cases are very similar, and for sake of simplicity, the majority of experimental VIV studies, over the past decades, were performed on an elastically mounted rigid cylinders constrained to oscillate only transverse to the fluid flow direction. Following this trend, the efforts for developing predictive VIV models as well, were focused on cross-flow-only VIV in which it was supposed that the structure undergoes simple harmonic oscillations. The inclusive summary of these VIV studies can be found in the comprehensive critical reviews by [4-6].

Figure 1.1: Schematic representation of the mechanism of fluid-structure interaction phenomena.

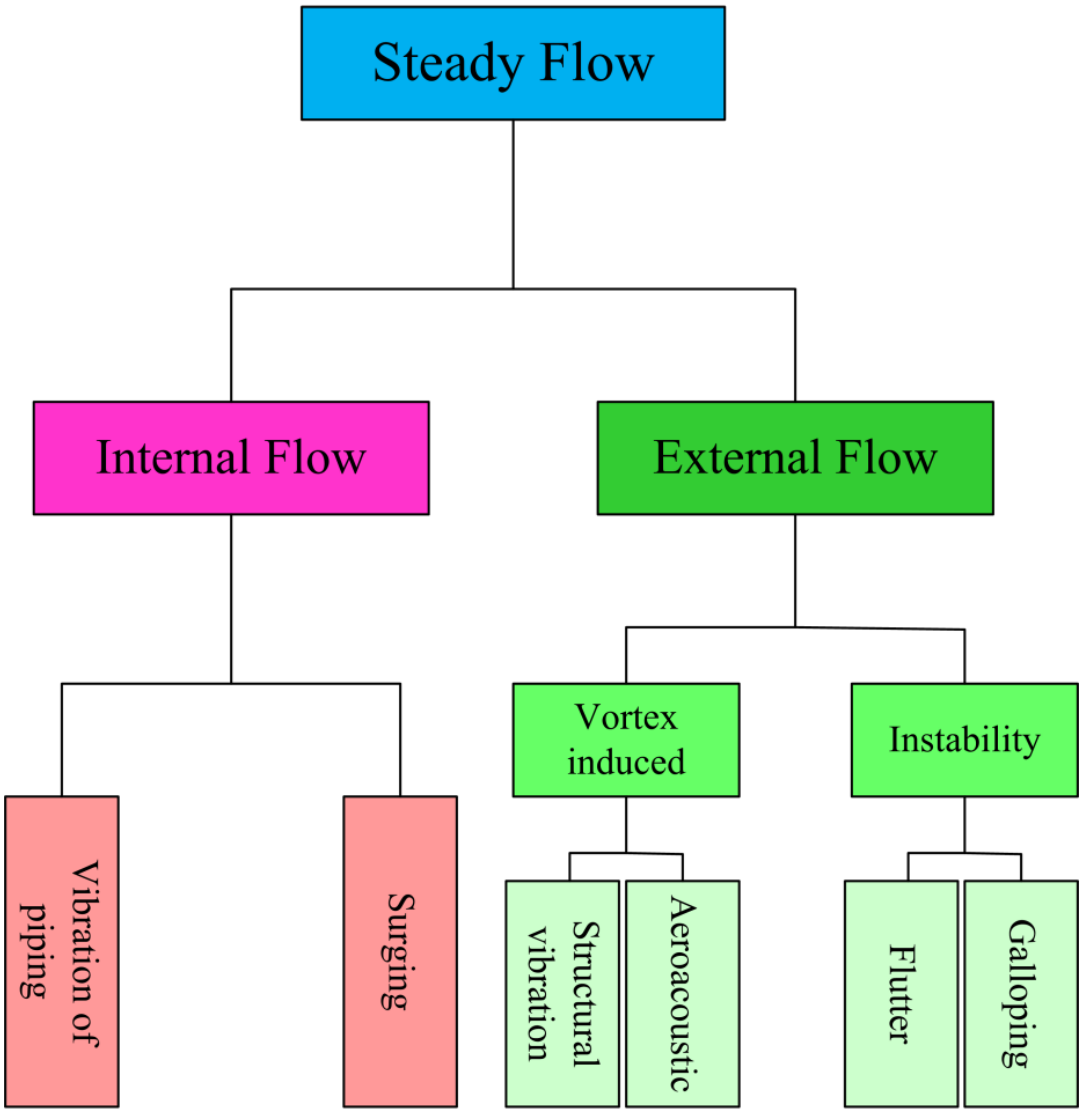

Figure 1.2: A classification of flow-induced oscillations caused by steady fluid flows, adopted from [7, 8].

Due to combined lift/drag forces associated with the shedding vortices and the fact that actual underwater structures possess multiple natural frequencies in different directions, a condition of coupled cross-flow/in-line VIV is certainly achievable in most practical situations. Recent experimental studies on both rigid and elastic cylinders revealed that under some circumstances such as those in VIV of offshore structures, the knowledge obtained from transverse-only VIV studies cannot explain vibrations of a cylinder free to oscillate in both CF and in-line (IL) directions [9-13]. These studies show that adding a degree-of-freedom (DOF) to the system results in

higher oscillation amplitudes accompanied with jump and hysteresis phenomenon, new vortex-shedding modes and more significant higher harmonic components of fluid forces and structural responses. Furthermore, these studies illustrated that IL oscillations might cause fatigue damages similar to CF oscillation and should be considered in the design process. Moreover, when it comes to elastic cylinders, in addition to CF and IL VIV, they can undertake longitudinal oscillations as well. The recent studies showed that, as the aspect ratio increases (the ratio of cylinder length to its diameter), the axial oscillations which are excited by lateral vibrations (CF and IL vibrations) of the cylinder become more significant [14].

Although the aforementioned experimental observations illustrate the importance of considering IL/axial VIV in offshore applications and significant contribution of these oscillations on the whole behavior of an offshore structure undergoing VIV, almost no predictive model which can efficiently and accurately predict and explain coupled CF/IL/axial VIV has been developed. The very few computational fluid dynamics (CFD) studies performed are time-consuming and limited to VIV of rigid cylinders at low Reynolds numbers. Also, the semi-empirical models, which usually are appropriate alternatives for uneconomic CFD numerical simulations, are focused and stagnated on CF-only VIV of rigid and elastic cylinders. Furthermore, in majority of these predictive models the nonlinearities which are inherently involved in VIV phenomenon are neglected.

This thesis will mainly focus on developing an advanced fully-nonlinear phenomenological VIV model accounting for coupled structural motions, i.e. CF/IL/axial motions, structural and geometric nonlinearities and nonlinearities associated with the hydrodynamic forces caused by uniform and linearly sheared flows. The model will be utilised to replicate, predict and explain experimental results and observations. To this end, the model will be solved, numerically (via standard finite difference and Runge-Kutta methods) and analytically (via harmonic balance method), validated and calibrated with published experimental results. The phenomenological models usually contain empirical coefficients which are considered constant, have no physical meaning and are evaluated via calibrations with experimental results. Herein, an attempt will be made to identify and define

empirical coefficients of the model as functions of physical parameters. It has been just in recent years that the importance of IL VIV has been notified, some aspects of combined CF-IL VIV (e.g. the effect of structural natural frequency ratio on system behavior) require further experimental investigations. Under these circumstances, the predictions of the model will be calibrated and validated via in-house experiments. Furthermore, significance of structural and hydrodynamic nonlinearities will be examined numerically and analytically and the results of these analyses will be applied for extracting two-dimensional hydrodynamic force coefficients.

To fulfil these aims, this dissertation is structured as follows:

- First in Chapter 2 the basic mechanism of VIV is explained and the research studies performed on VIV over past years (particularly over past decade) are reviewed.
- In Chapter 3, a low-order predictive model for a circular cylinder undergoing 2DOF VIV is proposed based on two sets of nonlinear structure-wake equations, new generic analytical functions of empirical wake coefficients are identified, fundamental 2DOF VIV behaviors and good comparisons with literature experimental results is systematically performed.
- Chapter 4 presents the details of the new experimental arrangement used for the 2DOF VIV study of a flexibly mounted circular cylinder, comparisons of experimental and numerical prediction results of six measurement datasets and comparisons of various new and published experimental results.
- In Chapter 5, analytical closed-form expressions are derived for the extraction of hydrodynamic coefficients and maximum responses from the 2DOF VIV, the system phase relationships of wake and cylinder motions and various maps of hydrodynamic coefficients are presented, the analytically-obtained contour plots of maximum cross-flow/in-line responses are highlighted and a shortcoming of using a linear structural oscillator and applying a constant empirical coefficient to the wake oscillator is underlined.
- In Chapter 6, based on the results obtained in previous chapters, a mathematical model of three-dimensional VIV of an elastic cylinder subjected to uniform current is presented and solved numerically, the

capabilities of the model in replicating experimentally-observed phenomena are demonstrated, the importance of the axial oscillations and the geometric nonlinearities are examined and discussed and the model is validated with available experimental results.

- In Chapter 7, VIV of a flexible cylinder caused by a linearly sheared flow is investigated through numerical predictions of the new model, time and frequency domain, modal and stress analyses are performed and model is validated with available experimental results.
- Finally the concluding remarks of the present study are summarised in Chapter 8 and suggestions for future research are given.

The model developed during this thesis, can provide accurate, reliable and economic VIV predictions which, in particular, will be beneficial for offshore engineers during early stages of design process. It can also be utilised for extensive parametric studies to investigate and elucidate the effects of influential physical parameters on VIV of circular cylinders. The numerical and analytical analyses performed in this thesis will illustrate the importance of structural and hydrodynamic nonlinearities for accurate VIV predictions and will open a new chapter in the field of phenomenological VIV models.

Chapter 2

VIV: An Introductory Review

This chapter provides an introduction to the vortex-induced vibrations (VIV) and reviews the research which studied this phenomenon. To manage the numerous and divers VIV studies and to fill within the scope of this thesis, these studies are reviewed through a systematic approach. The chapter is divided into four main sections. The first section explains the process of vortex-shedding from a circular cylinder. The next three sections are devoted to transverse-only VIV, combined transverse and streamwise VIV and VIV of flexible cylinders. In each of these sections, first the important physical parameters involved in the phenomenon and the characteristics of the phenomenon are explained through the experimental results. Then the phenomenological models, developed to predict and explain the experimental observations, are reviewed.

2.1. Vortex-Shedding from a Fixed 2D Circular Cylinder

2.1.1 Flow separation and vortex-shedding mechanism

When a particle of the fluid, through its path, encounters a bluff body like a cylinder, owing to the high stagnation pressure at the leading edge of the cylinder, it is forced to go around the cylinder. As the particle travels over either side of the cylinder, due to the adverse pressure gradient imposed by the geometry of the cylinder, it loses its momentum till all its kinetic energy dissipates and the particle stalls. At this moment, the boundary layer that has been developed over the cylinder surface separates and forms a shear layer in the wake region. In Figure 2.1 (a) the separation point, the boundary layer, the shear layer and the wake region are illustrated. It also shows the velocity gradient in the boundary layer which results in a significant vorticity. After separation, this vorticity is fed to the shear layers making them fold on each other and create a bigger vortex. The same course of events occurs on the other side of the cylinder as well. For a smooth cylinder, these events are controlled and described by a dimensionless quantity, so-called Reynolds number Re, which is defined as [7]:

$$\mathrm{Re} = \frac{VD}{\nu} \tag{2.1}$$

where D is the diameter of the cylinder, V the velocity of the free stream and ν the kinematic viscosity of the fluid. When the Re<5 the flow attaches to the cylinder and there is no separation of the boundary layer. It is worth mentioning that, in order to have figures with higher resolution and better quality, the results presented in Figure 2.1 and also the following figures of this chapter are mostly reproductions and adaptations of published results which are available on public domain. To this end, the Demo version of a graph digitizer named “GetData” along with Matlab software have been utilised. It is worth mentioning that GetData software is highly accurate (with less than 0.1% error) and double and triple checks have been done to avoid any discrepancies compared to the original results. In circumstances where comparison with published results are required, e.g. for validations and calibration of mathematical models, such process will be applied in future chapters as well.

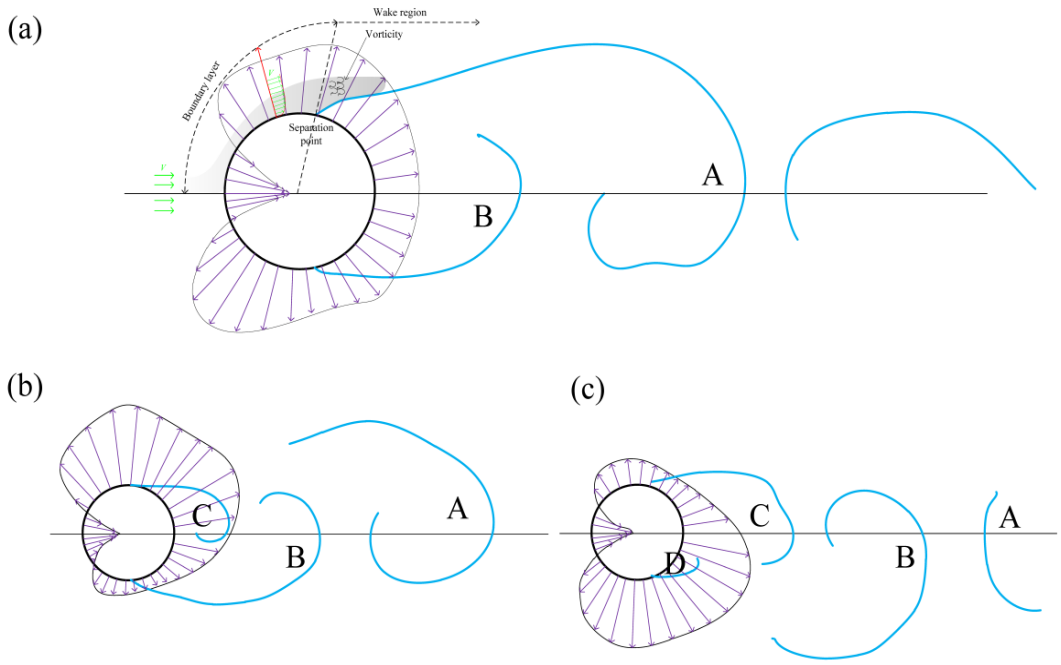

Figure 2.1: An illustration of the boundary layer, wake region (grey shadow) and pressure field distribution over the surface of a cylinder (purple vectors) along with the sequences of vortex-shedding process, the vortex-streets and pressure fields are adopted from [15] and the boundary layer representation is adopted from [16].

For higher Re (5<Re<45) separation occurs and forms a pair of symmetric vortices in the near wake and attached to the cylinder. As the Re is further increased, the wake becomes unstable and with small disturbances and perturbations the flow loses its symmetry and one vortex grows before another, e.g. consider vortices A (larger) and B (smaller) in Figure 2.1 (a). The greater vortex A, which is supposedly stronger, pulls the countra-rotating smaller vortex B downstream. As the vortex B is pulled, it grows and gains more vorticity till it gets strong enough to detach the vortex A from its boundary layer and cut off its supply of vorticity, Figure 2.1 (b). At this moment, the vortex A is shed and the flow take this discrete vortex downstream. When the vortex A is shed, a new vortex with similar sign of vorticity emerges at the same side of the cylinder, shown as vortex C in Figure 2.1 (b). The interaction of this new vortex with the vortex B, through similar steps as vortices A and B, results in detachment of vortex B and development of a new vortex D on that side of the cylinder, Figure 2.1 (c). Via continuation of this process, the vortices shed

alternatively from both sides of the cylinder and form an ordered pattern in the wake called the vortex street [16]. The frequency of this alternation and shedding of vortices, f_s, is expressed in dimensionless form, the so-called Strouhal number, as

$$\mathrm{St} = \frac{f_s D}{V} \tag{2.2}$$

2.1.2. Vortex-shedding frequency and Strouhal number

Since the flow around a smooth cylinder is controlled by Re, it is deduced that St of such a cylinder would be a function of Re, as well. The variation of St with respect to Re is depicted in Figure 2.2 [17]. Furthermore, the flow pattern and the vortex street in the wake of the cylinder at different ranges of Re are illustrated in this figure and the laminar and turbulent vortex streets are distinguished through colour codes of blue and purple vortices, respectively. As it is illustrated in this figure, for low Reynolds numbers, Re<40, where the vortices are attached to the cylinder and no vortex is shed, no St is reported. When 40<Re<150 a laminar vortex street is formed in the wake of the cylinder and St linearly increases with the increase of Re.The transition of the vortex street from laminar to fully turbulent occurs when 150<Re<300. At this range, increasing Re first decreases St and then increases it. The Reynolds number range 300<Re<1.5×10^5 is called *subcritical* in which the vortex street is fully turbulent while the boundary layers are laminar. In the subcritical range, the vortex street is well-organised and the vortices are shed orderly and periodically at an approximately constant Strouhal number of St≈0.2. With further increase of Re, the flow enters the *transitional* range (1.5×10^5<Re<3.5×10^6) in which St increases with the increase of Re. However, since in the transitional range the boundary layers become turbulent, the vortex shedding process is disrupted which leads to less structured, strong and periodic vortex shedding. In the transitional range, as Re increases, the Strouhal number can increase as high as 0.5 [7, 16].

2.1.3. Fluctuating and mean hydrodynamic coefficients

The process of flow separation from the surface of a cylinder and its consequent vortex-shedding and formation of vortex street were explained through Figure 2.1. In this figure, also, the pressure distribution around the cylinder is

illustrated by the purple arrows perpendicular to the surface of the cylinder [15]. The uneven and asymmetric (considering the front and the back side of the cylinder) pressure distribution, along with the friction effects of viscosity, results in a mean drag force which is constantly exerted to the cylinder. Moreover, due to the periodic and alternative vortex-shedding, the pressure field around the cylinder alternatively changes and causes fluctuating and oscillating drag and lift forces exerted to the cylinder.

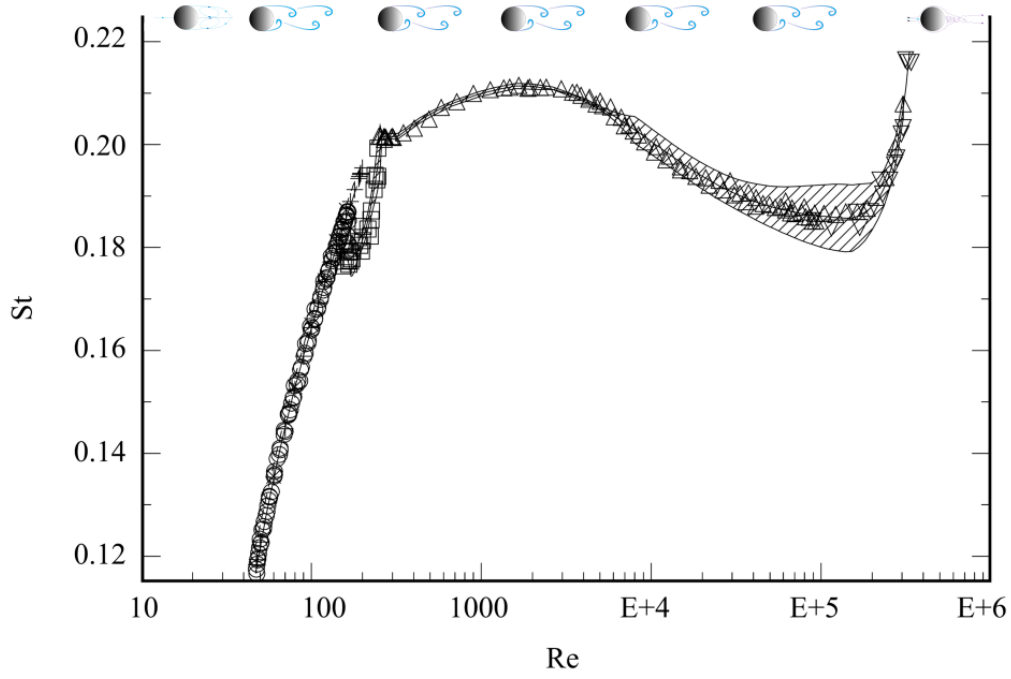

Figure 2.2: Variations of Strouhal number with Re adopted from [17]. Status of the wake of a circular cylinder at different ranges of Re is illustrated. The colours represent turbulence of boundary layer blue standing for laminar and purple standing for turbulent.

Figure 2.3 shows the mean drag coefficient, $\bar{C}_d$, and the root mean square values of fluctuating drag and lift coefficients, C_{d0} and C_{l0}, of a smooth cylinder at different Re [18, 19]. Furthermore, to draw a clearer picture of the flow behaviour, the regimes of the fluid flow in different ranges of Reynolds number are presented in this figure as well. When the flow is laminar, Re<50, $\bar{C}_d$ linearly decreases with the increase of Reynolds number. Increasing Re decreases the mean drag coefficient, until the flow enters the subcritical range where the wake becomes fully turbulent (Re>5000) and $\bar{C}_d$ reaches a constant value of approximately 1.2. In the transitional

region, all the coefficients dramatically drop (for $\bar{C}_d$ this sharp drop is called the drag crisis) which is caused due to a narrow and disorganized wake and its consequent reduction of pressure gradient. In the supercritical range where the vortex street is re-established, the mean drag coefficient gradually increases till at very high Re ($Re>3\times10^6$) where less dramatic changes occur in the boundary layer, $\bar{C}_d$ becomes steady again. Moreover, in the supercritical range, the fluctuating drag and lift coefficients are very low, which is mainly due to flow separation at large angular positions that results in weaker vortices [7].

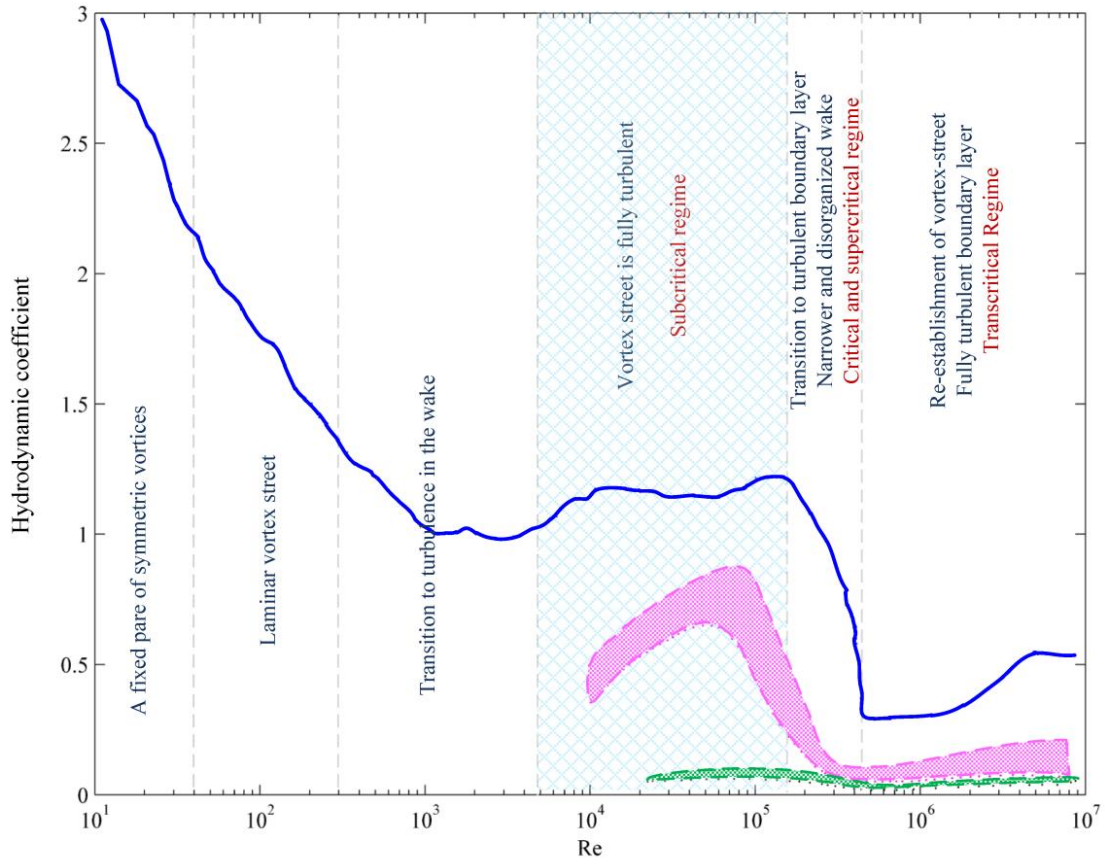

Figure 2.3: Mean drag coefficient (blue line), oscillatory drag coefficient (green dash line) and RMS of fluctuating lift coefficient (purple dash line) of a circular cylinder as a function of Re along with the status of its boundary layer and wake region at corresponding Re. The coefficients are extracted from [16] and the status of boundary layer is adopted from [18].

Highlighting the subcritical region of Figure 2.3 emphasizes the fact that strong and periodic vortex-shedding occurs in this range. The interaction of the shed vortices with the free-to-vibrate bluff body results in a phenomenon known as

vortex-induced vibrations or briefly VIV. In the following sections, the research that over the past decades was performed for better understanding of this complicated fluid-structure interaction (FIV) phenomenon is briefly reviewed.

2.2. One-DOF VIV of an Elastically-Mounted Cylinder

2.2.1 Key aspects and governing parameters

2.2.1.1 Reduced velocity and lock-in phenomenon

Figures 2.4 (a) and (b) show the circular cylinders which are subjected to a fluid flow, elastically mounted and free to vibrate in the streamwise and cross-flow (CF) directions, respectively. It was explained that the flow separation in such bluff bodies results in vortices which shed alternatively from two sides of the cylinders and create variable pressure fields around these cylinders.

The variable pressure distribution leads to fluctuating lift and drag forces. Due to the geometry of the vortex shedding, the frequency of the lift force fluctuations is f_s and the drag force oscillates with a frequency of $2f_s$ [7]. When these periodic drag and lift forces are exerted to the cylinders of Figures 2.4 (a) and (b), they will lead to in-line (IL) and CF structural oscillations or so-called IL and CF VIV, respectively. Inspired by the normalisation of the vortex-shedding frequency and its ensuing Strouhal number, the natural frequencies of the VIV systems of Figures 2.4 (a) and (b), f_n, can be nondimensionalized to develop a new parameter for expressing VIV. This parameter is known as the reduced velocity and is defined as:

$$V_r = \frac{V}{f_n D} \tag{2.3}$$

The frequency used in Eq. (2.3) can be the natural frequency either in vacuum (or air, when the medium is water) or in the fluid medium [4, 20]. The difference between these two f_ns is mainly due to the fact that when a structure oscillates in a fluid medium it must move the fluid particles as well and hence feels some extra inertia which can virtually be added to the mass of the system. This virtual mass is known as the "*added mass*" and defined as:

$$m_f = \frac{\pi}{4} C_a \rho D^2 \tag{2.4}$$

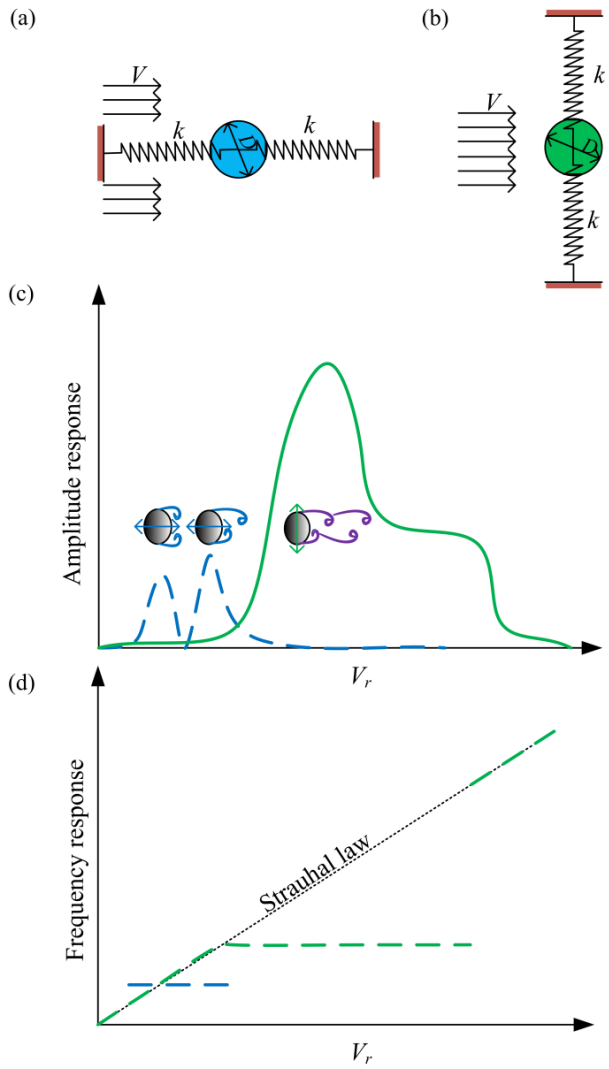

Figure 2.4: (a) and (b), schematic representation of an elastically mounted circular cylinder subjected to a uniform flow of velocity V which is free to vibrate in streamwise and transverse directions, respectively. (c), typical amplitude of streamwise (blue dash line) and transverse (green line) oscillations vs. reduced velocity. The wake condition during IL and CF lock-in is illustrated. (d) Variations if vortex-shedding frequency (normalised with the natural frequency of structure) with V_r during IL (blue dash line) and CF (green line) VIV.

where ρ is the fluid density, C_a is the added mass coefficient which can be obtained through experimental studies or potential flow calculations, namely for a circular cylinder gives C_a=1 [7]. In the present work and throughout this dissertation, the

natural frequency of the structure in a fluid medium (which is water) is used for obtaining and calculating V_r [21].

Figure 2.4 (c) shows typical amplitude responses of the IL and CF oscillations of the cylinders shown in Figures 2.4 (a) and (b) along with the schematic illustrations of their corresponding vortex streets which are plotted with respect to V_r. As it can be seen in Figure 2.4 (c), at low V_r the wake behind the cylinder is symmetric and the vortices shed simultaneously from the top and bottom sides of the cylinder. This symmetric vortex-shedding causes oscillatory drag forces exerted to the cylinder while the lift force is approximately zero. Thus, at low reduced velocities ($1.5<V_r<2.5$) the cylinder undergoes IL oscillations [22] while there will be almost no CF oscillations. As the reduced velocity increases, the wake becomes unstable and the vortices start to shed alternatively and produce fluctuating lift and drag forces. Normalising the vortex-shedding frequency by the natural frequency of the cylinders, the corresponding frequency response of the amplitude responses of Figure 2.4 (c) is depicted in Figure 2.4 (d). The frequency response illustrates that, following the Strouhal law, the vortex shedding frequency linearly increases with the increase of V_r till it reaches the natural frequency of the structure. At this point, f_s deviates from the Strouhal law and locks onto the natural frequency of the cylinder which results in the insensibility of f_s to the variations of V_r. This phenomenon, known as the "lock-in" or "synchronization" phenomenon, can cause high amplitude oscillations [23]. At the end of the lock-in range, with further increase of V_r, the vortex-shedding frequency goes back to the Strouhal law and the amplitude of oscillations drops.

Since the excitation frequency in the IL direction is twice of that in the CF direction, the lock-in for the cylinder of Figure 2.4 (a) is prior to that of Figure 2.4 (b). The typical lock-in ranges of the IL and CF oscillations are shown in Figure 2.4 (c). For the IL oscillations the lock-in range is $2.7<V_r<3.8$ [22] and the lock-in range of the CF oscillations is $4.5<V_r<8$ [24]. However, for system such as those depicted in Figures 2.4 (a) and (b) which have one degree-of-freedom (1DOF) and undergo 1DOF VIV, the lock-in ranges are not always like these and there are other physical parameters which can widen or narrow down these ranges. Mass ratio is one of these

parameters which plays a crucial role not only in the determination of the lock-in range, but in whole behaviour of the VIV system. The definition and effects of this parameter are discussed in the next section.

2.2.1.2 Mass ratio and extension of lock-in range

Mass ratio is usually defined as the ratio of the structural dry mass per unit length of the cylinder, m_s, to the mass of the displaced water per unit length of the cylinder [1], that is

$$m^* = \frac{m_s}{\frac{\pi}{4}\rho D^2} \tag{2.5}$$

However, in some literatures (mostly does dealing with mathematical modelling of VIV), mass ratio is defined based on the wet mass of the structure (i.e. m_s+m_f) as [25]

$$\mu = \frac{m_s + m_f}{\rho D^2} \tag{2.6}$$

These two definitions of mass ratio are related to each other as:

$$m^* = \frac{4}{\pi}\mu - C_M \tag{2.7}$$

Mass ratio is one of the most influential parameters of a VIV system and its variations affect different aspects of VIV phenomenon. For a 1DOF VIV system with low m^*, compared to a high mass ratio case [23]:

- Lock-in phenomenon occurs at frequency ratios different from unity. Hence, for low mass ratio system, lock-in phenomenon can be defined as matching of vortex-shedding frequency with the frequency of structural oscillations.
- The characteristic amplitude response has a distinct new branch so-called upper branch. Figure 2.5 (a) shows the comparison between the CF amplitude responses of two 1DOF VIV systems with high and low mass ratios. The figure shows the branches of these amplitude responses and illustrates that decreasing mass ratio results in the new high amplitude upper branch.

- The tendency for VIV is higher. In other word, as the mass ratio decreases it becomes more prone to VIV. This can be seen in Figure 2.5 (b) where the system with low mass ratio has a wider range of lock-in.

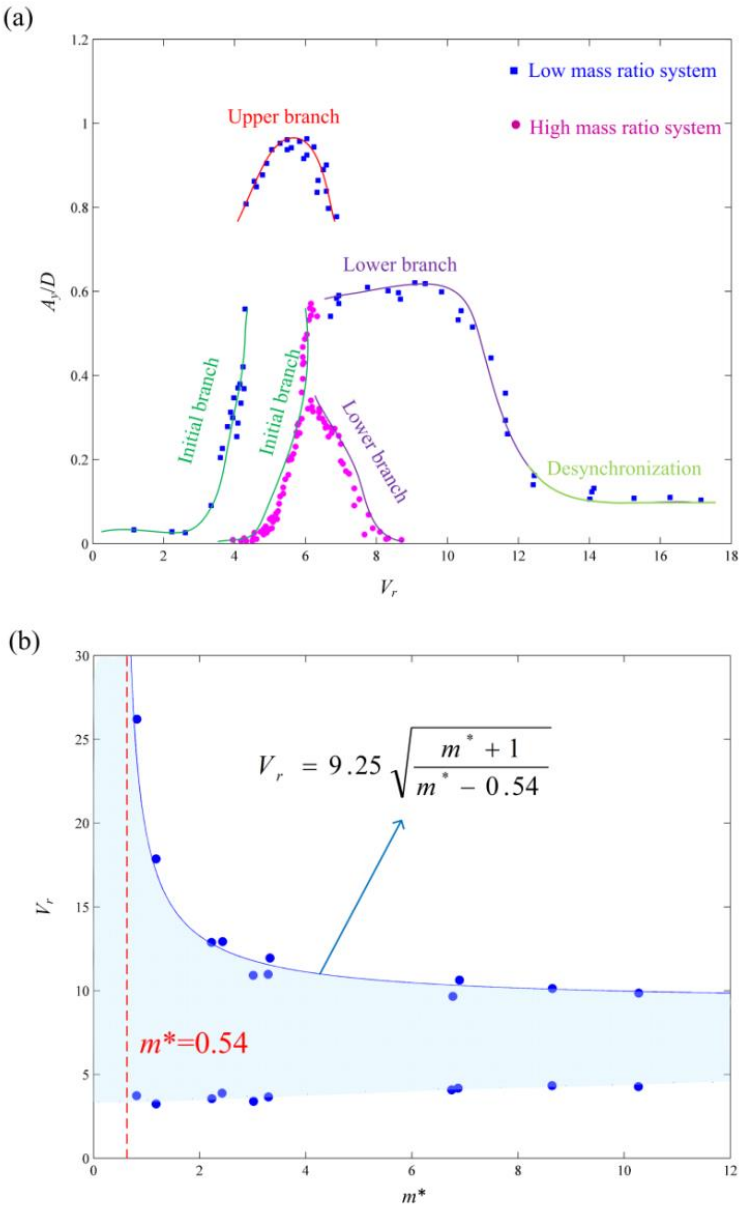

Figure 2.5: (a) Amplitude responses of CF VIV for high (m*=248) and low (m*=10.1) ratios and the response branches. (b) lock-in range as a function of m* and existence of a critical mass ratio. In (a) the experimental results are taken from [26] and in (b) the experimental curve and the data are adopted from [27].

The last aforementioned point on the effect of mass ratio on the extent of lock-in infers that decreasing m^* down to zero results in an infinitely wide lock-in range or, as it is called in literature, lock-in forever [28]. However, the experimental results show that each VIV system has a generic "critical mass ratio" different from zero which below that the lock-in condition lasts forever [27]. Figure 2.5 (b) shows the effect of m^* on the lock-in range of CF VIV of an elastically mounted rigid cylinder. In this figure, Govardhan and Williamson [27] showed that, the upper bound of the lock-in range for such a VIV system can accurately fit into a single and simple curve of

$$V_{r_{\text{end of lock-in}}} = 9.25\sqrt{\frac{m^* + 1}{m^* - 0.54}} \tag{2.8}$$

The simple formula of Eq. (2.8) indicates the existence of a critical mass ratio of 0.54 which is in the range of the mass ratio of many engineering structures and illustrates the significant importance of m^* parameter on the behaviour of the system. However, the validity of this suggested value depends on some circumstances which are determined by another influential physical parameter; the damping ratio. In the next section, the definition, types and significance of this parameter will be discussed.

2.2.1.3 Damping parameter, VIV amplitude and mean drag amplification

The energy dissipation from a vibrating structure is interpreted as damping which in classic vibration analysis is considered to be a force proportional to velocity that opposes structural motion. Generally speaking, in VIV systems such as those shown in Figures 2.4 (a) and (b), the oscillations are damped through two main mechanisms: (i) structural viscous dissipations and (ii) fluid-added damping [7]. The structural viscous damping is usually denoted by c and compared with the system value $2\sqrt{km}$ (where k is the spring stiffness or equivalent stiffness of the system) known as the critical damping c_r, to specify the system type of being under/critically/over-damped ($c<c_r$, $c=c_r$ and $c>c_r$, respectively). Normalization of damping coefficient with $2\sqrt{km}$, results in a new parameter, ξ, called damping ratio or reduced damping, that is:

$$\xi = \frac{c}{c_r} = \frac{c}{2\sqrt{km}} \tag{2.9}$$

This parameter, in VIV studies, is usually reported as the damping of the system. However, as it was mentioned before, when a cylinder oscillates in CF or IL directions, a hydrodynamic damping is added to the system. This fluid-added damping is caused by the mean drag force and, as it is derived by Blevins [7], is expressed as:

$$\xi_f = \frac{1}{K}\frac{V_r}{\mu}C_D \tag{2.10}$$

In which *K* is a constant value and, depending on the direction of the vortex-induced oscillations, can be equal to 4π or 8π for CF and IL oscillations, respectively.

Since the damping parameter is one of the basic parameters of any vibrating system, the effects of this parameter on flow-induced vibrations have been extensively investigated over the past decades, a of these studies can be found in [23, 29]. In one of the most recent studies on an elastically mounted cylinder which was free to vibrate in CF direction, Blevins [30] checked the effect of damping ratio on amplitude response, frequency responses (oscillation frequency, f_o, normalised by natural frequency vs. V_r) and the mean drag coefficient, Figures 2.6 (a-c) respectively. This study, while being consistent with previous studies, had the advantage of (i) covering a large range of damping ratios $0.2\%<\xi<40\%$, and (ii) reporting drag coefficient. The figures show that increasing damping ratio, as it can be expected, results in lower oscillation amplitudes. However, this is not the only effect of increasing ξ. As it is illustrated in Figure 2.6 (a), ξ variations result in alternation from three-branched amplitude responses to two-branched responses. Moreover, the figure shows that the mean drag coefficient follows the same trend as the amplitude response. In other words, as the amplitude of VIV oscillations increases the mean drag coefficient amplifies. The mean drag amplification is one of the VIV side effects which is generally accepted to be a linear function of the amplitude of CF oscillations and is defined as [31]:

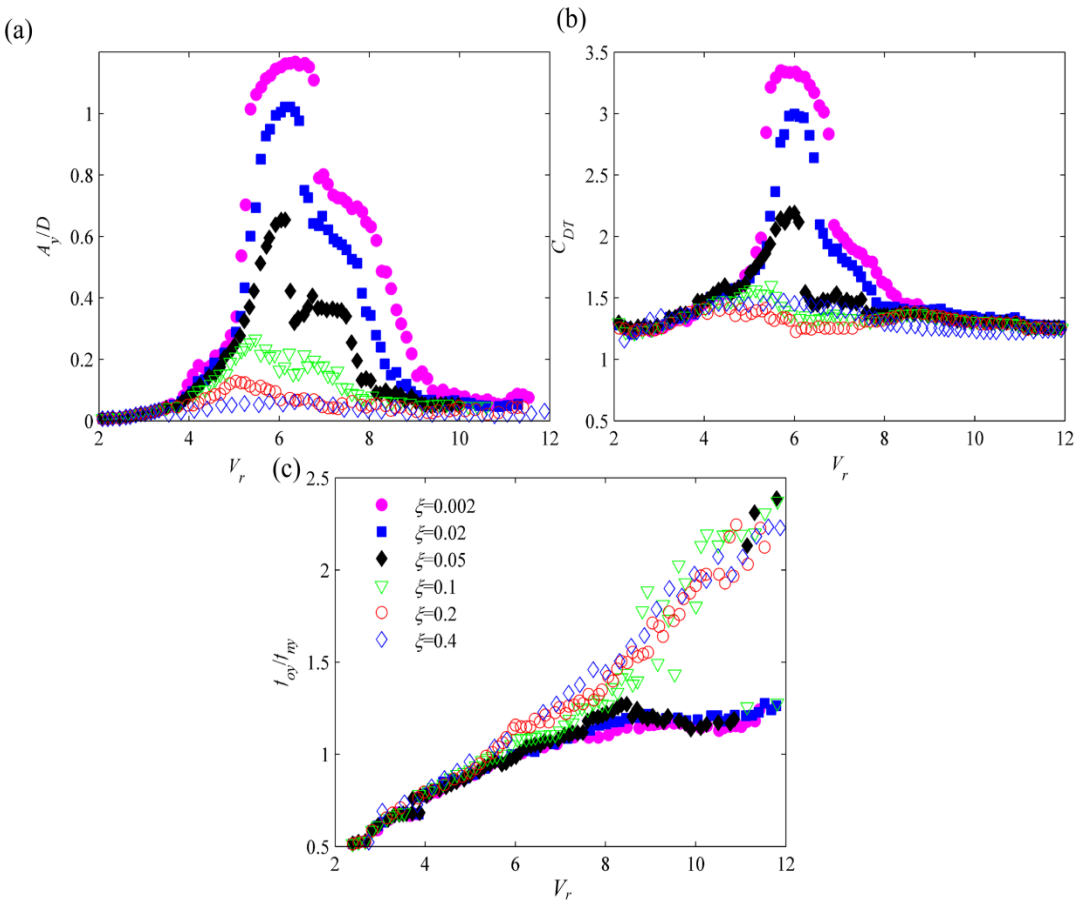

Figure 2.6: (a), amplitude response; (b), frequency response; (c), mean drag coefficient of a rigid cylinder (with m^*=5.4), undergoing CF-only VIV at six different damping ratios. This figure is a reproduction of the experimental results of [30].

$$C_{DT} = C_{D0} + 2\frac{A_y}{D} \tag{2.11}$$

The results depicted in Figure 2.6 (a) are consistent with Eq. (2.11), for instance, at ξ=2%, the maximum amplitude is A_y/D=1 which its corresponding mean drag coefficient is 3.

2.2.1.4. Combined mass-damping parameter and maximum VIV amplitude

The observations made here on the effect of damping ratio variations on the alternation between characteristic branches of amplitude responses were also made in the previous section when explaining the effect of m^*. Therefore, it can be inferred that this alteration is a function of both of these parameters whether separately or as a combined mass-damping parameter. Since 1964 when [32] for the first time used a

combined mass-damping parameter for plotting the maximum amplitude of their study, it has been a long-run debate that if the mass and damping parameters affect the VIV amplitude response individually or collectively. A comprehensive summary of these debates can be found in [6, 33]. Over these years, different research groups have developed different mass-damping parameters [23]. In one of the most recognised works of its kind, Skop and Griffin [34] compiled several experimental results and claimed that a mass-damping "response parameter" can reasonably collapse the peak amplitude of CF VIV, A_{yM}/D. This parameter which afterwards was called as Skop-Griffin parameter S_G, is defined as

$$S_G = 2\pi^3 St^2 m^* \xi \tag{2.12}$$

In recent years the works of Klamo [29, 35] showed that

- The maximum amplitude of CF VIV is not solely a function of SG and the Reynolds number also has significant effect. In other words, they showed that developing a "universal curve" which collapses all the peak amplitude data is not possible and rather it should be done through "constant-Reynolds number curves".
- They also showed that to determine the characteristic amplitude response of a VIV system of being "two-branched" or "three-branched" both mass-damping and Reynolds number should be taken into account. In other words, the upper branch appears in the amplitude response when the system has low mass-damping and high Reynolds number.

In agreement with these results, Blevins [30] showed that at similar Re, VIV systems undergoing CF oscillations experience similar peak amplitudes, these results are depicted in Figure 2.7 (a). As this figure illustrates, although the experiments has been conducted with different mass ratio, since the S_G and Re are constant, their maximum amplitude are the same. However, as m^* decreases, he effect of m^* on the lock-in range and tendency towards a critical mass ratio and lock-in forever condition can be recognised. Govardhan and Williamson [36],also, in a precise and more extensive experiment, studied the effect of m^* and mass-damping parameter and showed that at fixed Re and mass-dampings and in a wide range of mass ratios,

1<m^*<20, the maximum amplitude of the CF VIV is independent of m^*. They also introduced a modified mass-damping parameter in which the effect of added mass is taken into account and is defined as

$$\alpha' = (m^* + C_M)\xi \tag{2.13}$$

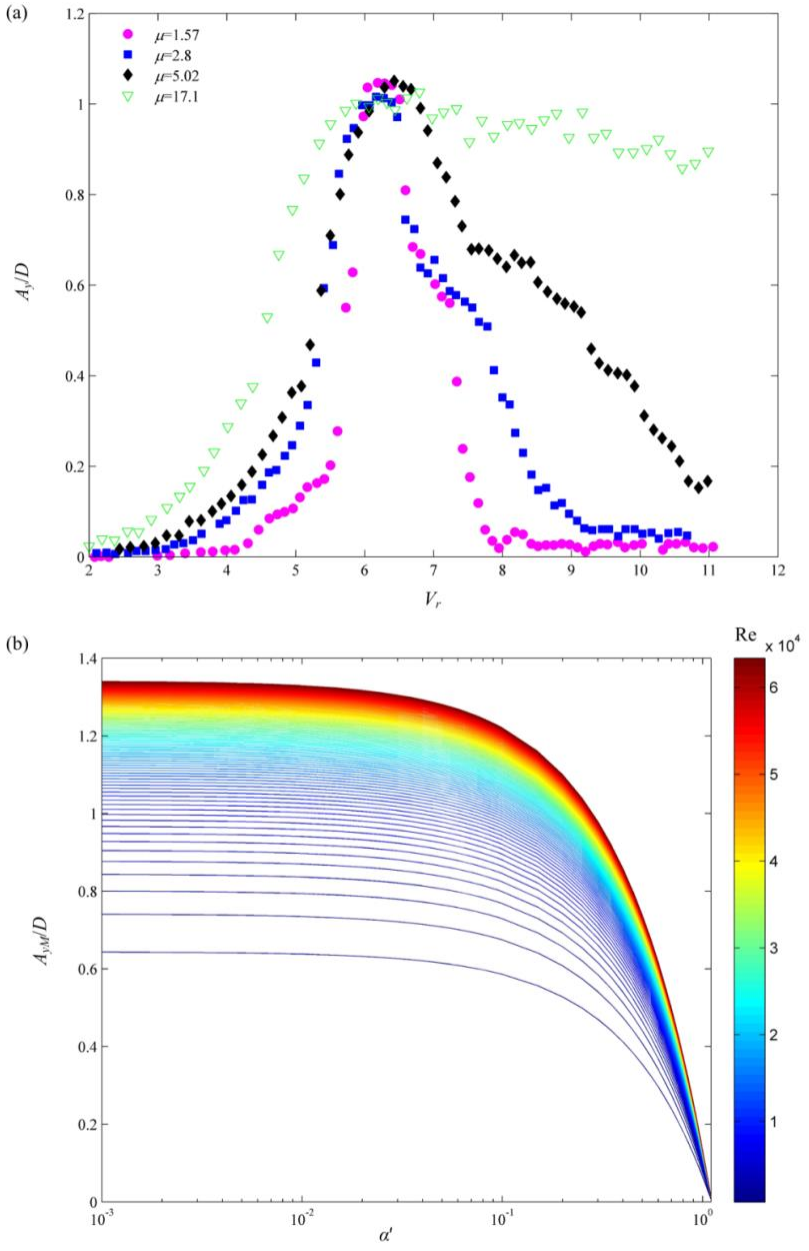

Figure 2.7: (a) Amplitude responses of CF oscillations of rigid cylinders with different mass ratios and similar α=0.126. (b) maximum attainable amplitude of CF VIV as a function of α and Re. In (a) the results are extracted from adopted from [30] and in (b) the curves are produced via empirical relation developed by [36].

Using this new parameter and considering the effect of Re, they developed an empirical relation to evaluate the peak amplitude of CF vortex-induced oscillation, that is

$$\frac{A_{yM}}{D} = (1 - 1.12\alpha' + 0.30\alpha'^2)\log(0.41\mathrm{Re}^{0.36}) \tag{2.14}$$

Using this relation, the effect of α' and Re on A_{yM}/D is illustrated in Figure 2.7 (b).

2.2.2. Free and forced 1DOF VIV experiments

The parameters introduced and the discussions made in the previous sections reflect just part of the outcomes of some of the fundamental VIV studies. Over the past decades, several research studies have been conducted to provide better understanding and knowledge of VIV mechanism and physics. Some of these investigations are summarised in Table 2.1 which includes both free and forced vibration studies. In the framework of forced oscillations where the cylinder amplitudes and frequencies are prescribed *a priori*, attempts have been made by several authors– mostly in the CF-only VIV case – to evaluate the fluid lift force and its phase relative to the CF motion. The phase difference between lift force and CF motion is a key parameter to determine whether the fluid adds energy to or removes it from the dynamic system and, therefore, whether the free vibration prediction is feasible. This phase difference, through evaluation of the lift force which is in phase with the structural acceleration, also helps to obtain the effective added mass. In addition, when a jump in the fluid force and phase associated with the upper-to-lower branch response occurs, the vortex wake formation pattern may change from being the 2P (two pairs of vortices) to 2S (two single vortices) mode. This is in accordance with the free vibration result of, e.g., [37], highlighting the possible association between forced and free vibration results. Hence, as it is indicated in Table 2.1, numbers of research campaigns have been conducted to compare forced and free-vibration tests and determine the circumstances where controlled vibrations are applicable for free vibration predictions.

Table 2.1: A summary of the main findings of the free and forced CF and IL-only VIV experiments on rigid circular cylinders.

The experiment type	Relevant research studies	Main findings
Free CF VIV	[26, 27, 36, 38-41]	• Lock-in phenomenon. Jump and hysteresis in amplitude and is due to a jump in vortex-shedding timing and jump in the phase angle during lock-in • High Re causes very high oscillation amplitudes
Forced CF VIV	[31, 42-50]	• Big difference between the lift force phase angle of large and small amplitude oscillations. • The added mass obtained via classic methods, is applicable in VIV • Forced vibration tests can be applied for prediction of VIV • Fluid forces can be decomposed into two potential and vortex force components and this decomposition is valid for general viscous flows • Energy transfer is very sensitive to the cylinder motion
Free IL VIV	[22, 51, 52]	• IL lock-in ranges due to symmetric and asymmetric vortex-shedding
Forced IL VIV	[2, 53-55]	• Observation of P+S vortex-shedding modes • Inertia coefficient at high reduced velocities could be determined from the Morison's equation • Two IL excitation regions correspond with two ranges of V_r with negative added fluid damping.

Table 2.1 clearly shows that the majority of these studies were focused on the problem of CF-only VIV while IL VIV is less studied. This is mainly due to the fact that the amplitude of vortex-induced oscillations in IL direction is much lower than CF oscillations which made it less important and interesting. Moreover, it was supposed that the knowledge obtained from studying VIV systems with 1DOF would be beneficial and enough for prediction of IL oscillations of such systems.

2.2.3. Semi-empirical modelling of CF-only VIV

Owing to the complexity of the vortex hydrodynamics, the intrinsic mechanism of the structure, the overall elasto-hydro nonlinearities, the influence of several mechanical/physical parameters, and the necessity to calibrate and validate the simulation model with substantial experimental data, modelling of VIV remains a challenging theme [56]. The information provided by the experimental studies summarised in Table 2.1 (and those not listed in that table), also, have been utilised for development of semi-empirical or phenomenological VIV models. These models can replicate the experimentally observed behaviours of a VIV system and are used for VIV predictions in engineering applications.

2.2.3.1 Wake-oscillator models: general features

A classification of these models is provided by [4] which is associated with a comprehensive review of each type of these models. Among the models explained by them, wake oscillator is more popular than the other models, e.g. force decomposition models and SDOF models. The background of wake oscillator models stems back to the idea that the self-limiting and self-exciting nature of time-varying fluid forces induced by vortex shedding can be represented by van der Pol/Rayleigh-type equations [57, 58]. This wake oscillator model then is coupled to a simple harmonic equation which represents the structural oscillations. A timeline of the activities performed for development and improvement of these semi-empirical models is shown in Figure 2.8. Similar to the experimental studies summarised in Table 2.1 and for the same reasons, most of the wake oscillator models were primarily developed for prediction of CF-only flow-induced oscillations. The distinction between the models developed over these years mostly is due to:

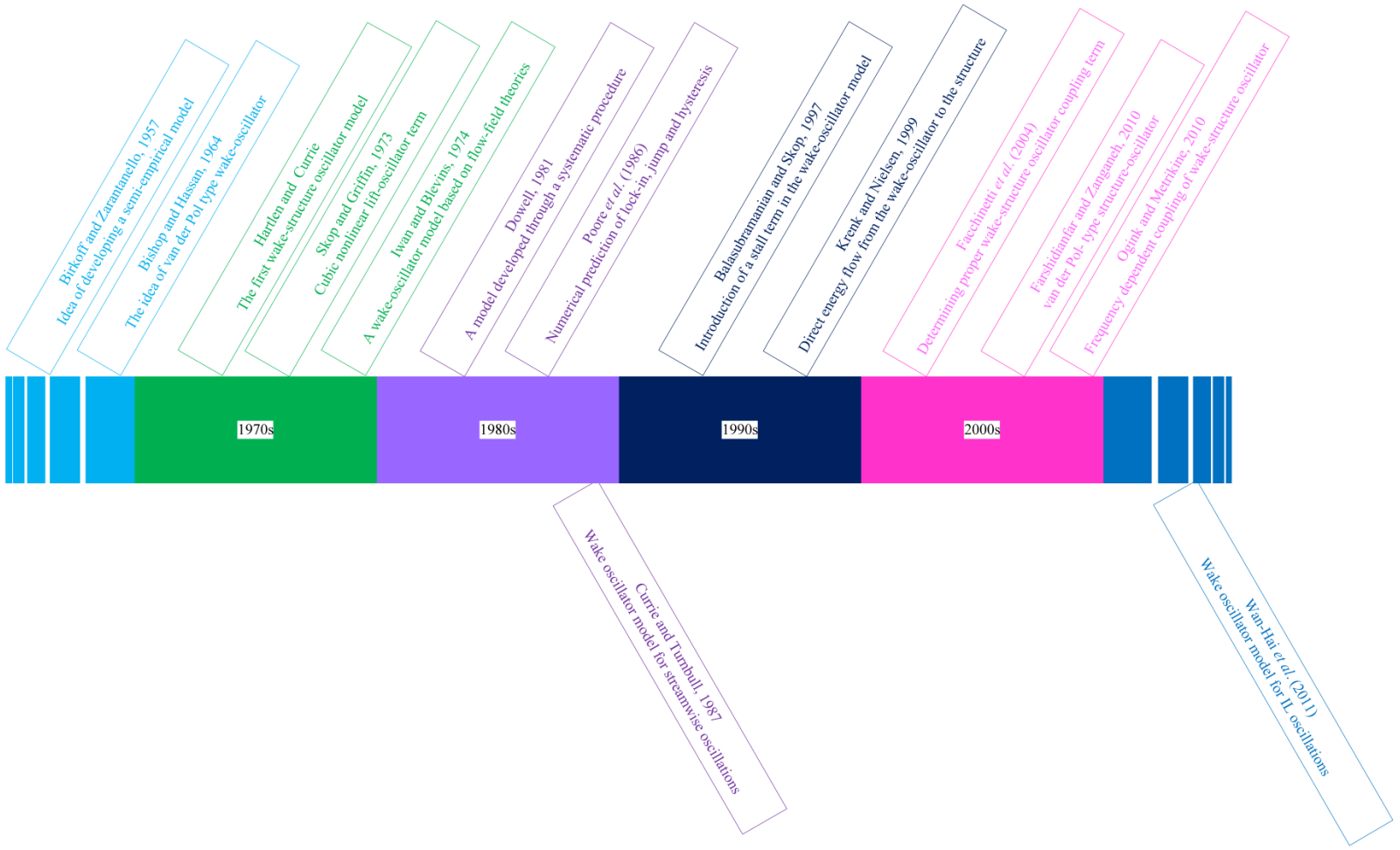

Figure 2.8: A timeline of the major activities in developing CF/IL wake-structure oscillator models [34, 52, 57-68].

- Different types of strategies which have been used to couple wake and structure oscillators.
- Different types of equations (i.e. van der Pol-type or Rayleigh-type) applied for modelling of lift and drag forces.
- Different empirical coefficients which usually have no actual physical interpretation and are evaluated by calibration of the wake oscillator with experimental results.

2.2.3.2 Wake oscillator models: the model by Facchinetti *et al*. [66]

In one of the most influential studies on semi-empirical models, [66] showed that fluctuating lift force exerted to an elastically mounted circular cylinder by vortex-shedding can be modelled via a van der Pol equation as:

$$\ddot{q} + 2\pi\varepsilon f_s(q^2 - 1)\dot{q} + 4\pi^2 f_s^2 q = F \tag{2.15}$$

in which overdots mean derivatives with respect to dimensional time t and q=2C_l/C_{l0} where C_l is the time-varying lift coefficient and ε is one of the empirical coefficients of this wake oscillator model. The other coefficient of this wake oscillator comes from the right-hand-side forcing term F that couples the wake oscillator to the structural oscillator which were supposed to undergo simple harmonic motion as

$$m\ddot{Y} + c\dot{Y} + kY = S \tag{2.16}$$

in which Y is the CF displacement of the cylinder and S is the fluid forcing term which comes from the wake oscillator. To select the best strategy to couple their wake oscillator to the structural oscillators, they examined three scenarios for F to be proportional to (i) the structural displacement Y, (ii) the structural velocity $\dot{Y}$ and (iii) structural acceleration $\ddot{Y}$. Through analytical investigation of their model and comparison of its outcomes with the experimental results, their suggested acceleration coupling and concluded that the acceleration coupling results in predictions with more qualitative resemblance to the experimental results. For example, Figures 2.9, similar to Figure 2.5 (b), depicts the effect of mass ratio on the lock-in range and the corresponding predictions of this semi-empirical model for three aforementioned coupling scenarios. These figures clearly illustrate that while the displacement coupling fails to predict the lock-in range of high mass ratios

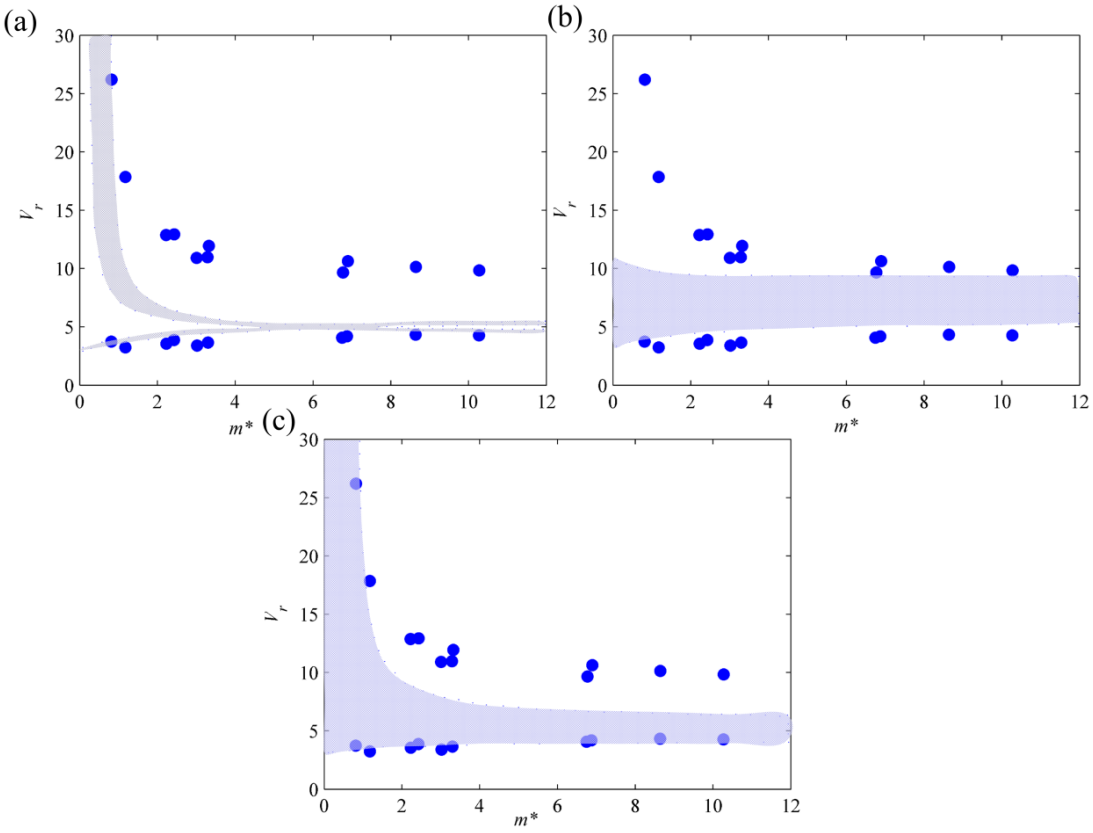

Figure 2.9: Predictions of lock-in domain and critical mass ratio via the semi-empirical model of [66] for different coupling terms. (a), displacement coupling; (b), velocity coupling; (c) acceleration coupling. This figure is a reproduction of the results by [66].

($m^* > m_c^*$) and the velocity coupling fails to capture lock-in forever phenomenon, the results of the acceleration couplings are quite consistent with the experimental results.

2.2.3.3 Wake oscillator models: recent studies and required modifications

Since 2004, the model by [66] has been the backbone of the models which has been developed afterwards. Some general aspects of these models should be summarised:

- A standard linear mass-spring-damper system is used to describe the cylinder oscillation. The effect of structurally geometrical nonlinearities has often been disregarded.
- The coupling of wake and cylinder motions is recognized through a linear term in the wake equation depending on the cylinder acceleration.

- Empirical coefficients in the wake oscillator rely upon the calibration with experimental amplitude data; however, the former are typically assumed as a constant

The above-summarised aspects of wake oscillator models infer that, in these models, the structural and hydrodynamic nonlinearities are neglected. Therefore, it is of great interest to study and investigate the significance and influences of these nonlinearities. Moreover, finding the connection and relation between empirical coefficients of these models and physical parameters can provide more insight into the behavior of such models. This can be done through extensive calibrations, validations and parametric studies. Finally, the results presented in Section 2.2 were based on the assumption that the cylinder can only oscillate in one of the CF or IL directions. However, in real situations and real engineering applications, usually there are no such constraints and the structures are free to vibrate in both directions. The research conducted for investigating simultaneous CF and IL flow-induced oscillations are reviewed in following section. These studies will provide more evidences on the importance of aforementioned required modifications.

2.3 Simultaneous CF/IL VIV of an Elastically-Mounted Cylinder

2.3.1. Early experimental studies: is IL VIV influential?

In spite of many published studies, the vast majority of the research literature has focused on the modelling of pure CF VIV excited by the lift force because of its usually observed largest response [5]. Very little is indeed known about the effect of oscillating drag force, the ensuing IL VIV, the coupling of CF/IL VIV, the dependence on system parameters and how to realistically model these features. Figure 2.10 shows a typical two-dimensional cylinder subjected to a fluid flow of velocity V and is free to vibrate in both CF (Y) and IL (X) directions. Some early research investigations on such structures have evidenced the significant effect of IL VIV [69-71] and have highlighted some interesting features of 2DOF VIV of circular cylinders and meaningful contributions from the IL VIV to the overall dynamics, depending on several control parameters. [70] and [71] observed that the freedom of the system to oscillate in the IL direction can cause an increase of the CF response

amplitude and widen the lock-in range. It has been suggested that these effects may result from an enhanced correlation of the transverse force along the cylinder span. Moreover, [69] reported strong quadratic relationship between IL and CF oscillations and concluded that these motions are not independent. Due to combined lift/drag forces associated with the shedding vortices and the fact that actual underwater structures possess multiple natural frequencies in different directions, a condition of coupled cross-flow/in-line VIV is certainly achievable in most practical situations which can be responsible for the dangerously-amplified dynamics.

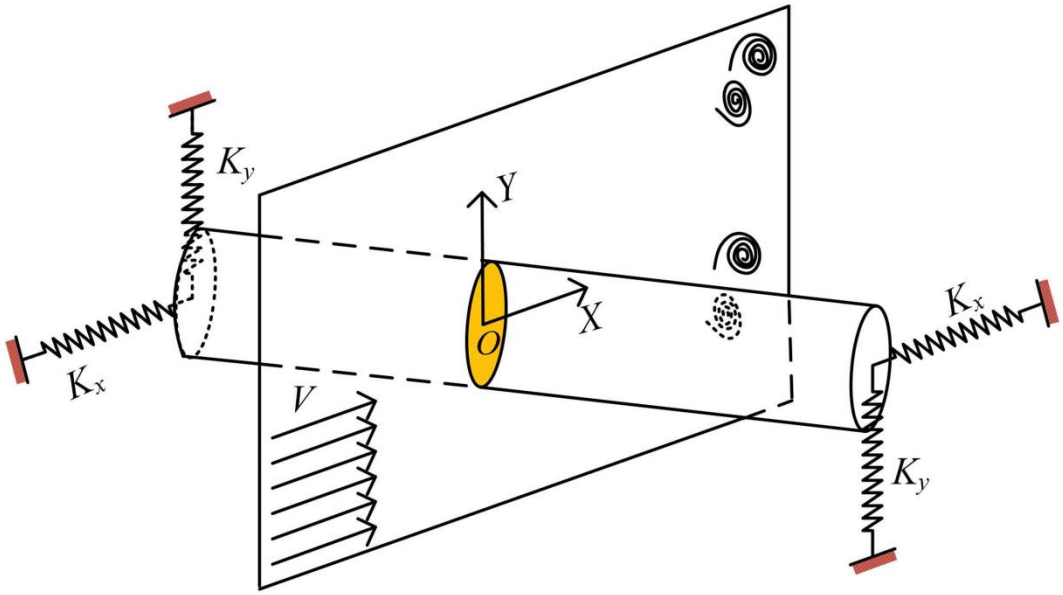

Figure 2.10: A schematic model of a spring-mounted circular cylinder undergoing 2DOF VIV.

One of the primary observations of the early 2DOF VIV experiments which drew the attentions was the prominently periodic Lissajous orbits of the structural displacements with figure-of-8 shapes [72]. Such trajectories require that the ratio of the IL to CF oscillation frequencies be 2:1. When these circumstances are provided, the shape of Fo8 is determined by the phase difference between the two oscillations. For instance, the typical CF and IL vortex-induced displacements of a rigid cylinder, such as that shown in Figure 2.10, can be represented by the equations:

$$y(t) = A_y \sin(\omega t) \tag{2.17}$$

$$x(t) = A_x \sin\left(2\omega t + \theta_{xy}\right) \tag{2.18}$$

in which x (y) is the IL (CF) displacement and A_x and A_y are the oscillation amplitudes in IL and CF directions, respectively. θ_{xy} is the phase difference between IL and CF oscillations and, as it is shown in Figure 2.11, controls the shape of the Fo8 orbits.

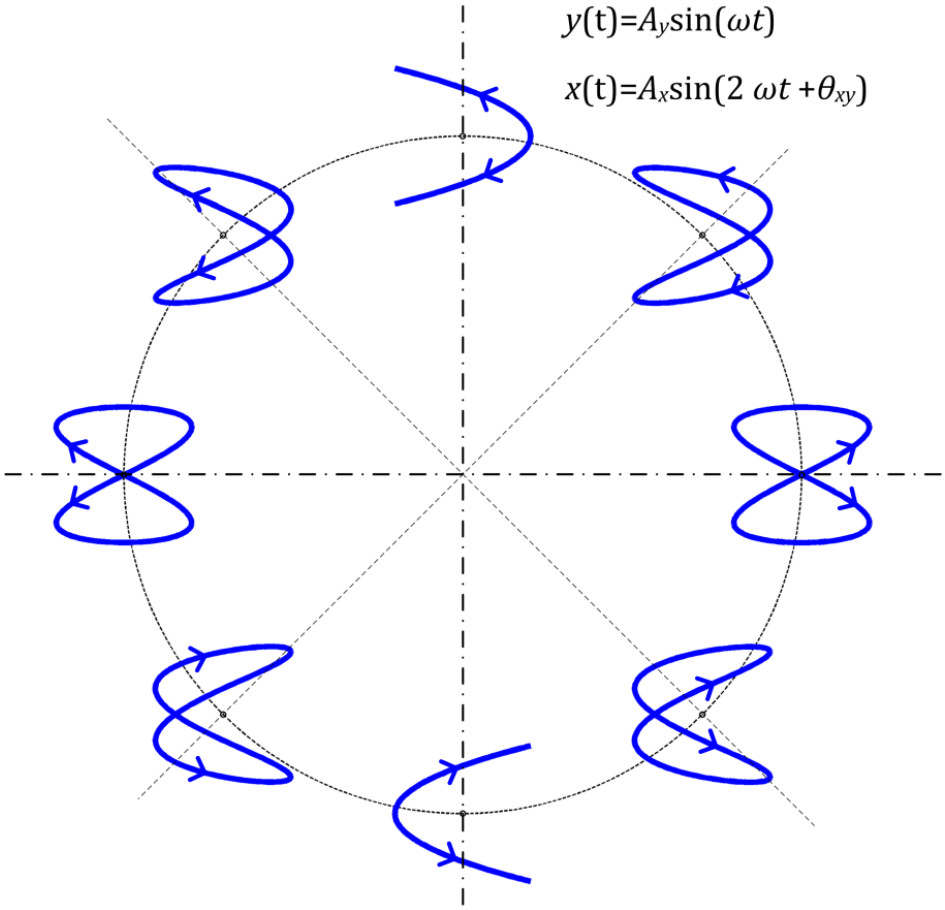

Figure 2.11: Typical Fo8 trajectories as a function of θ_{xy}.

In one of the few forced 2DOF VIV experiments, Jeon and Gharib [73] forced a rigid cylinder to oscillate under Eqs. (2.17) and (2.18). Following the results of free vibration investigations, they chose θ_{xy} to be 0° and 45°. They studied the effects of 2DOF motion on vortex-shedding modes, hydrodynamic coefficients and the energy balance of the system. The comparison of 2DOF results with transverse-only experiments showed, while the vortex-shedding frequency is determined by the frequency of CF oscillations, the addition of the streamwise oscillations to the

motions of the cylinder changes the relative phase of the vortex-shedding and θ_{xy} can control the energy transfer between the wake and the cylinder. They also showed that, even for small A_x, the IL motion delays the transition from 2S to 2P vortex-shedding mode.

The results of Joen and Gharib raised these questions that whether the knowledge obtained over the past decades from transverse-only VIV studies can explain and define the simultaneous CF/IL VIV or not, and what circumstances and factors lead to possible diversions of 2D VIV systems from previously seen behaviours. To provide reliable answers to these questions, over the past decade, more research campaigns have focused on the problem of coupled CF/IL flow-induced oscillations. In this section, a critical review of these studies and their consequent results is presented.

2.3.2 Studies on physical parameters influencing combined CF/IL VIV

Since the fundamental mechanism of two-dimensional VIV is same as that of CF or IL-only VIV described in Section 1, the same parameters must control coupled CF/IL vortex-induced oscillations. However the values of some of these parameters might be different in two directions, that is, CF and IL directions might have different m^*, ξ and f_n. In this thesis, to distinguish between these parameters, they are accompanied with co-subscripts x and y which indicate IL and CF directions, respectively. In addition to the parameters mentioned in Sections 2.1 and 2.2, having different natural frequencies in CF and IL directions results in a new controlling parameter known as the natural frequency ratio f^* which is defined as $f^*=f_{nx}/f_{ny}$. The importance of f^* is more understood if one recall that (i) the excitation frequencies in CF and IL directions are not the same and therefore having different natural frequencies might lead to simultaneous or non-simultaneous CF and IL resonance conditions, and (ii) the real engineering structures can possess multiple frequency ratios. In the next section, the effects of mass ratio, damping ratio and reduced velocity along with this new parameter f^* are studied on two-dimensional VIV of a circular cylinder. Before going any further, it is worth mentioning that, for such a system shown in Figure 2.10, V_r is defined based on f_{ny}.

2.3.2.1 Effects of mass ratio and significance of IL oscillations

In one of the most influential and pioneering studies on combined CF/IL vortex-induced oscillations, Jauvtis and Williamson [9, 74] and Williamson and Jauvtis [75] investigated the significance of the IL oscillations and their effects on the dynamics of an elastically mounted rigid cylinder. Since, in practice, most of the structures have the same mass ratio and natural frequency in both streamwise and transverse directions, they employed a pendulum setup which provided such conditions. They varied the mass ratio of this setup, while $m^*\xi$ was low and almost constant, and compared different aspects of its 1DOF and 2DOF VIV. Figure 2.12 depicts an adaptation of some of their results comparing the amplitude responses of transverse-only and combined transverse/streamwise oscillations at low and high mass ratios, m^*=2.6 and m^*=7, respectively. These results illustrate that:

1. for higher mass ratio, m^*=7
    - both 1DOF and 2DOF elastically mounted rigid cylinders have comparable CF amplitude responses
    - IL oscillations resemble 1DOF streamwise vibrations and have two lock-in ranges corresponding to symmetric and asymmetric vortex-shedding explained in the previous section
2. and when the mass ratio is reduced to m^*=2.6
    - a new response branch with peak-to-peak amplitude of 3D appears in the CF amplitude response which they called it “super-upper branch”
    - the maximum CF amplitude of 2DOF cylinder occurs at higher reduced velocities and is accompanied with jump and hysteresis phenomena
    - in addition to the first and second IL lock-in ranges, a third one appears in the IL amplitude response which coincide with the CF lock-in range

Their investigations, also, revealed that the new high amplitude super-upper branch corresponds to a new vortex-shedding mode in which 2 triplets of vortices shed from cylinder at each cycle of oscillations. They called this new mode 2T and showed that it is accompanied with a considerable third harmonic component in the

lift force [75]. In section 2.3.1 the effects of the phase difference between IL and CF oscillations on the hydrodynamic forces and the energy transfer in the VIV system were discussed; the studies of Jauvtis and Williamson [9] showed that strong third harmonic components occur when the structural displacement trajectories have a crescent shape or there is a phase difference of 270° between CF and IL oscillations. Figure 2.12 also depicts the Fo8 trajectories of the low mass ratio cylinder at different V_r. These highly repetitive trajectories affirm a 2:1 oscillation frequency ratio and illustrate how the shape of these trajectories varies from perfect Fo8 at lower branch to a crescent shape at super upper branch which is associated with 2T vortex modes and strong lift force third harmonic components.

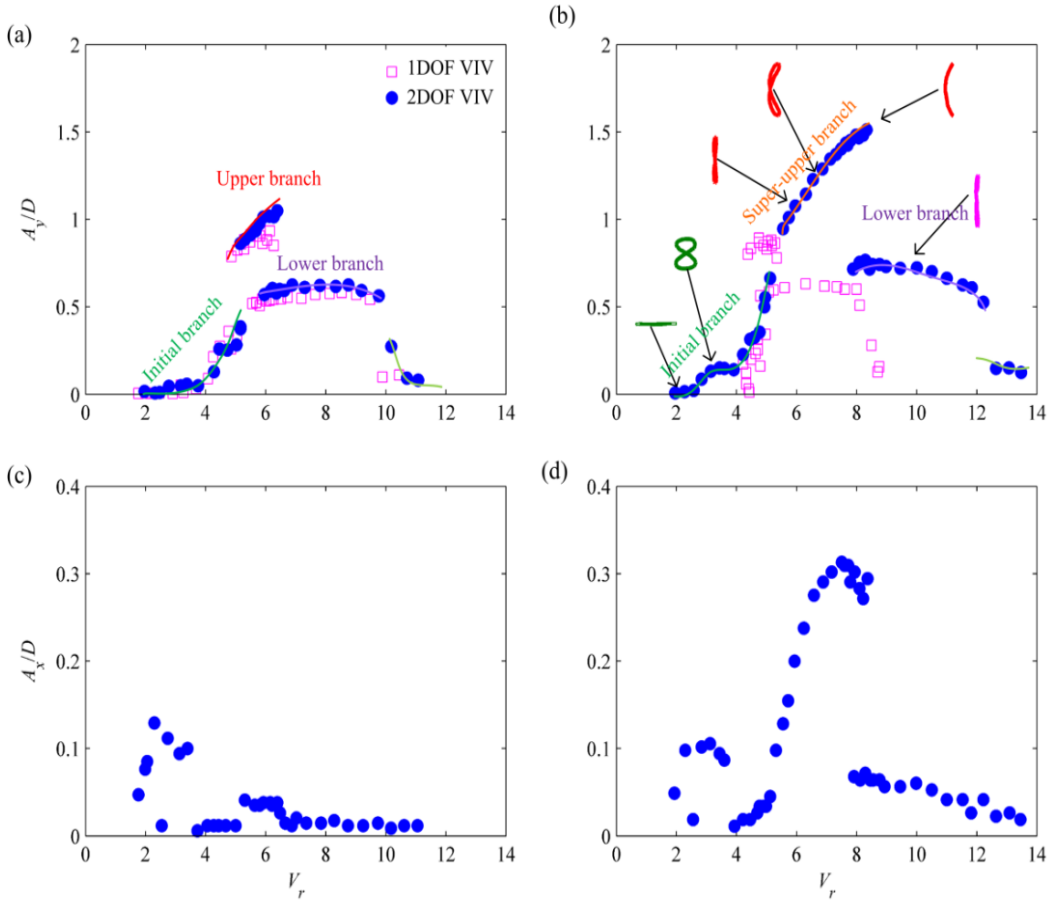

Figure 2.12: CF (a, d) and IL (c, d) amplitude responses for the systems with moderate mass ratio (a,c) m^*=7 and low mass ratio (b, d) m^*=2.6, undergoing 1DOF and 2DOF VIV. The mass-damping parameters of two systems are α=0.0117 for the system with moderate mass ratio and α=0.013 for low mass ratio system. 1DOF results are extracted from [26] and 2DOF results along with the response branch information are taken from [9].

Analogous to the 1DOF VIV discussed in Section 2.2, Jauvits and Williamson checked the existence of critical mass ratio for their experimental setup. They showed that for an elastically mounted rigid cylinder which is free to vibrate in CF and IL directions, the critical mass ratio is equal to 0.52 which is comparable to 0.54 [27] of a 1DOF spring-cylinder system. Moreover, their experimental investigations clarified the circumstances under which IL oscillations become influential. They illustrated that for high and moderate mass ratios ($m^*>6$ as they suggested) the effects of streamwise oscillations are negligible and adding this degree-of-freedom to a spring-cylinder VIV system does not influence its behaviour. However, when $m^*<6$, this extra degree-of-freedom plays a crucial role and dramatically changes the dynamics of the VIV system. The results of Jauvtis and Williamson [9] were, later on, observed in similar studies by [76] which was performed at constant damping and frequency ratios of $\xi=0.006$ and $f^*=1$, respectively. In this experimental study, both CF and IL directions had equal mass ratio which were varied between $2<m^*<13$. However, in addition to the amplitude responses and oscillatory hydrodynamic forces, they reported mean drag coefficients as well.

Figure 2.13 depicts an adaptation of their results showing the comparison between maximum mean drag coefficients of elastically mounted rigid cylinders undergoing transverse-only and combined CF/IL oscillations. In section 2.2.1.3 it was explained that vortex-induced oscillations amplify C_{DT} and this amplification is a linear function of CF oscillation amplitude. The results shown in Figure 2.13 illustrate that as m^* decreases the maximum mean drag of cylinder with two degrees-of-freedom deviates from its one degree-of-freedom counterpart. Following the discussions made in Section 2.2.1.3 and present section, this divergence is the outcome of adding extra DOF to the VIV model which leads to the appearance of the super-upper branch and higher oscillation amplitudes. Although the results of [76] affirms the observations made by [9], there is still a question that whether knowing the mass ratio of a 2DOF system is enough for judging about the significance of IL oscillations. In other words, whether other parameters can affect the importance of IL oscillations or it is just the mass ratio that influences it. The following subsections deal with this question.

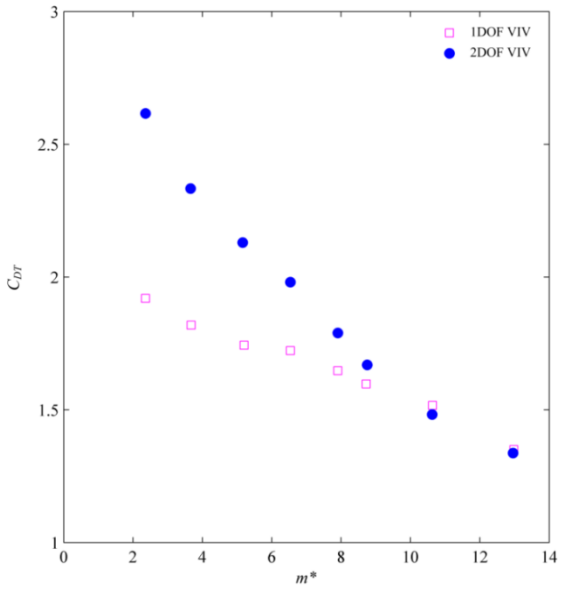

Figure 2.13: Maximum mean drag coefficients of 1DOF and 2DOF VIV systems for different m^*. The experimental results are adopted from [76].

2.3.2.2 Effects of damping ratio: should it be combined with m^*?

Through the experimental results of [30], the effects of damping parameter on 1DOF VIV of an elastically mounted cylinder were explained in Section 2.2.1.3. In this study, in addition to the aforementioned results, they also let the cylinder move in the streamwise direction and investigated the effects of ξ on 2DOF VIV. An adaptation of their experimental results is depicted in Figure 2.14. The comparison between 1DOF and 2DOF VIV results presented in Figures 2.6 and 2.14, respectively, shows that

- the 2DOF VIV results have higher CF amplitudes than their 1DOF results showing that letting the cylinder oscillate in two directions results in higher transverse oscillation amplitudes
- similar to m^*, reducing damping ratio increases the importance of IL oscillations
- at low ξ (ξ<0.02) the third IL lock-in range, coinciding with CF lock-in range, is excited
- at low very ξ, the amplitude response has a new super-upper branch accompanied with jump and hysteresis phenomenon

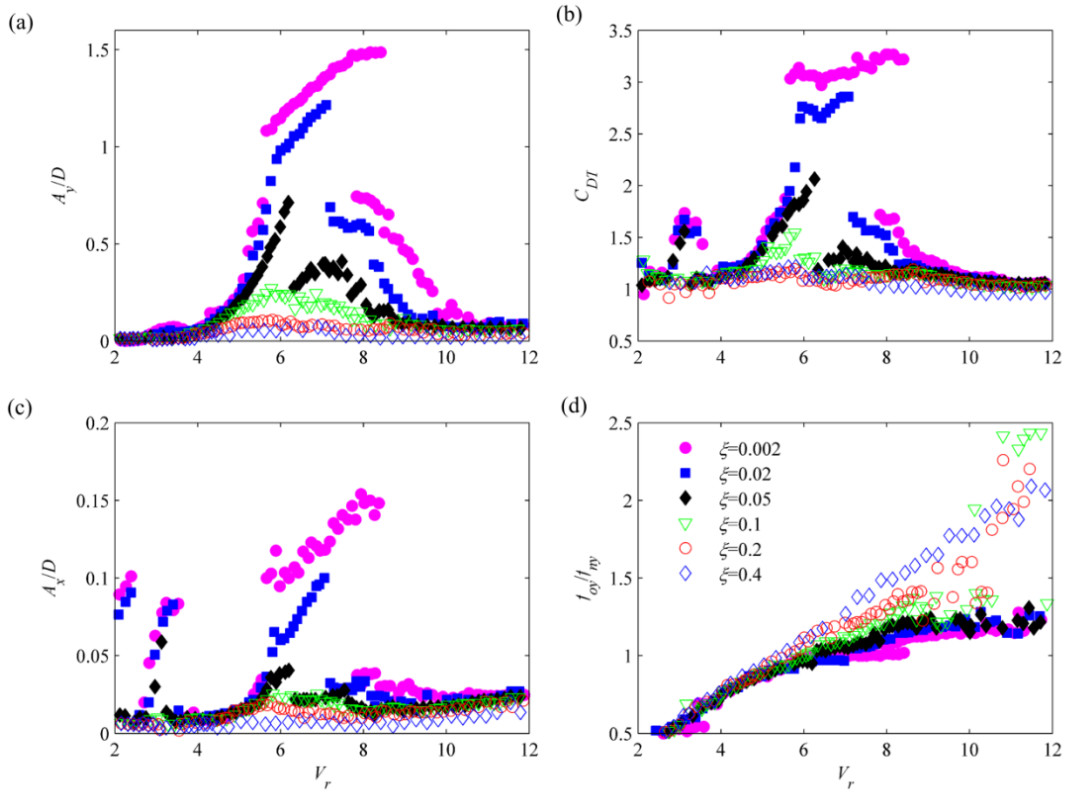

Figure 2.14: (a) CF amplitude response; (b), mean drag coefficient; (c), IL frequency response; (d), frequency response of a rigid cylinder (with m^*=5.4), undergoing combined CF/IL VIV at six different damping ratios. This figure is a reproduction of the experimental results of [30].

These observations suggest that, despite the fact that the experiment is carried out at a constant mass ratio close to 6 (m^*=5.4), the reduction of damping ratio still can increase the significance of the IL oscillations which, similar to the results presented in the Section 2.2.1.2, results in higher maximum attainable CF amplitudes. Hence, for a proper judgment about the effect of the IL motion on the CF oscillations, both m^* and ξ should be taken into account. However, one may ask that whether these two parameters act independently or, similar to transverse-only VIV, it is a combined mass-damping parameter which controls the maximum attainable amplitude of 2DOF VIV. To answer this question, Figure 2.15 depicts the experimental results of [30], obtained at constant $m^*\xi$ and different m^*. The comparison between this figure and Figure 2.7 (a) illustrates that while the maximum amplitude of transverse-only VIV is a function of combined mass-damping parameter, such a parameter does not control the maximum attainable amplitude of

2DOF VIV. Moreover, the results depicted in Figure 2.15 show that reducing m^* causes global effects similar to those observed in transverse-only VIV experiments, e.g. widening of the lock-in range.

2.3.2.3 Effects of frequency ratio and dual resonance

For VIV of an elastically mounted rigid cylinder the frequency ratio is one of the influential physical parameters. However, over the past decades, in few experimental studies, performed at MIT [10, 11, 77], the effect of f^* on 2DOF vortex-induced oscillations have been investigated. In these studies, in contrary to the other experimental results discussed in previous sections, the experimental setup had different mass ratios in streamwise and transverse directions and the values of m_x^* and m_y^* were changed as the f^* varied.

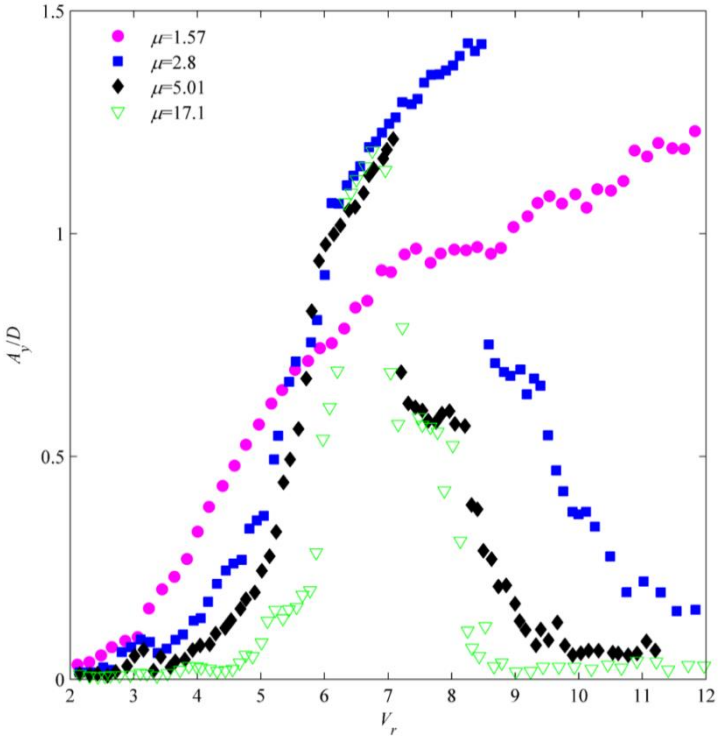

Figure 2.15: Amplitude responses of CF oscillations of rigid cylinders with different mass ratios and similar α'=0.126. This figure is a reproduction of the experimental results of [30].

The experiments by [10] (alongside with the observations such as multiple vortex-shedding modes accompanied with large third harmonics in the lift force which were observed in other experiments) showed that the peak-to-peak amplitude of IL oscillations can reach 1.2D. They also showed that by increasing f^* from 1 to 2

a second peak is excited in the CF amplitude response which was noticed by [71] as well. Moreover, these studies showed that f^* can have interesting effects on Fo8 trajectories. Figure 2.16 depicts these trajectories at different V_r when f^*=1, 1.2, 1.3, 1.5, 1.7 and 1.9 [11]. This figure shows that, while for f^*<1.5 all of the Fo8 trajectories are bent towards downstream, higher frequency ratios contain trajectories which face opposite direction and number of these flipped trajectories increases as f^* increases to 1.9. Knowing that the shape of this Fo8s is determined by the phase difference between CF and IL motions, and remembering this phase difference can have significant effects on the responses of the fluid-structure dynamical system, this figure illustrates the importance of f^*.

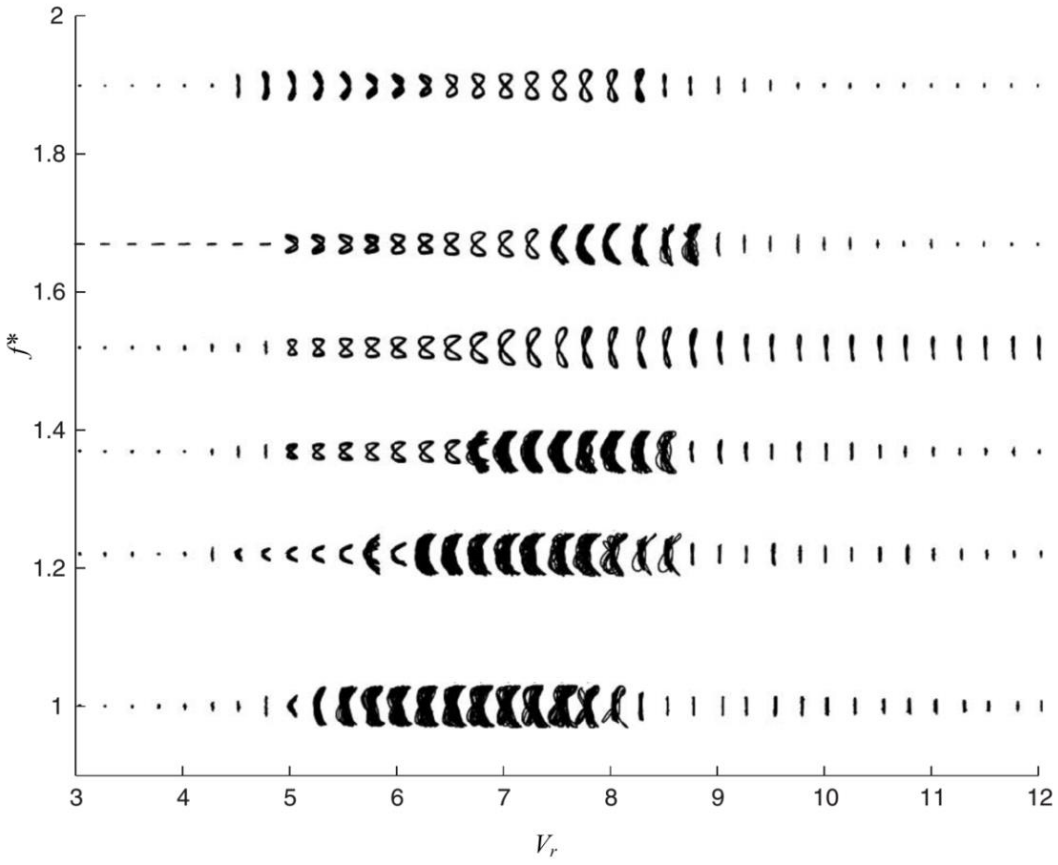

Figure 2.16: Fo8 trajectories of a circular cylinder at different $f^*$and V_r. Adopted from [11].

Dahl *et al.* [77] further highlighted various figure-of-eight patterns in different subcritical and supercritical Reynolds number (Re) ranges ($1.5x10^4$ < Re < $6x10^4$ and $3.2x10^5$ < Re < $7.1x10^5$) and described a figure-eight occurrence as a representation of "dual resonance". Under this dual resonance, the frequencies of the unsteady drag and lift forces are resonantly tuned with the oscillation frequencies (f_{ox} and f_{oy}) of the

cylinder, respectively, such that $f_{ox}/f_{oy} \approx 2$. In addition, a large third harmonic component of the lift force was observed although the main cross-flow response was primarily associated with the first-harmonic lift force.

2.3.2.4 Less-studied parameters and required future experimental studies

Natural frequency ratios different from one can be commonly observed in VIV of slender offshore structures which possess infinite natural frequencies. The mass ratios of such structures in both IL and CF directions are usually equal. However, in spite of the above-mentioned studies, the most practical case of $m_x^* = m_y^*$ and variable f^* has not been thoroughly investigated. For a particular flow with very low Re = 150 and zero structural damping, Bao *et al.* [78] recently have performed direct numerical simulations of a circular cylinder with f^* = 1, 1.25, 1.5, 1.75 and 2. They showed dual resonances in all f^* cases and illustrated how the oscillating drag component is maximized when f^* = 2 with the appearance of the P+S vortex wake mode associated with the maximum in-line response. Nevertheless, apart from this CFD analysis, no other basic studies have been conducted to investigate the effects of f^* variations while m^* is fixed and equal in all directions, and more experimental and numerical investigations in a higher Re range are still needed.

2.3.3 Semi-empirical modelling of combined CF/IL VIV

The experimental and numerical studies discussed in the previous sections showed that how combined transverse/streamwise vortex-induced oscillations of an elastically mounted rigid cylinder can be different from 1DOF VIV. However, despite several wake-oscillator models developed for prediction of CF or IL-only oscillations, a complete set of wake-structure oscillators for simulating the coupling of cylinder CF/IL motions excited by the hydrodynamic lift/drag forces is lacking and is needed. This model, in addition to classic common VIV characteristics and phenomena, such as being self-exciting and self-limiting and lock-in phenomenon, should be able to capture the parameters such as f^* (and behaviours such as Fo8 trajectories, 2:1 oscillation frequency ratio and dual-resonance) which belong to (and are caused by) simultaneous CF/IL oscillations. Moreover, compared to 1DOF VIV, higher oscillation amplitudes accompanied with nonlinear behaviours such as jump

and hysteresis, suggest that linear mass-spring-damper system might no longer be realistic and the effect of structural nonlinearities should be taken into account.

2.4 VIV of Straight Flexible Circular Cylinders

Almost all the engineering structures such as risers, mooring cables and pipelines which are subjected to a fluid flow and may experience vortex-induced oscillations are not rigid and under internal/external loads can deflect and deform. As it was extensively discussed in previous sections, most of the research carried out on VIV has considered rigid structures. This is mostly due to the fact that doing experimental and DNS studies on elastic structures are associated with more practical difficulties such as limitations of test facilities (e.g. limited sizes of towing tanks and water channels and requirement of complicated and expensive measurement systems) and high computational capacities required for 3DOF VIV numerical simulations. Nevertheless, whenever it has been possible, researchers have tried to overcome these limitations and investigate VIV of elastic structures as well [79]. A review of the research studies conducted in this context comes in the following sections.

2.4.1 Influential parameters: elastic vs. rigid cylinder VIV

Many of the behaviours observed in rigid cylinder experiments have been repeated in elastic cylinder tests, as well. For example, Huarte and Bearman [80] in their experiment on a flexible cylinder with aspect ratio of 93.75 (L/D=93.75 where L is the length of the cylinder) which was partially submerged in a water channel and was subjected to a uniform flow, observed dual resonance and 2:1 oscillation frequency ratio accompanied with Fo8 trajectories which their shapes varied along the span of the cylinder. Also, Vandiver *et al*. [81] in their *in situ* tests on a long riser model observed third harmonic lift force components. However, due to intrinsic characteristics of elastic cylinders, VIV in such structures is associated with some new behaviour. The main feature which distinguishes a flexible cylinder from a rigid one is the fact that it possesses infinite number of natural frequencies and vibration modes [82]. For instance, while the natural frequency of an elastically mounted rigid cylinder is $f_n = \sqrt{k/m}$, for an elastic cylinder which is under tension T, f_n can be estimated as [83]:

$$f_{n,i} = \frac{i}{2L}\sqrt{\frac{T}{m} + \left(\frac{i\pi}{L}\right)^2 \frac{EI}{m}} \tag{2.19}$$

where i is the mode number, E is the Young's modulus of elasticity and I is the area moment of inertia. The first consequence of having numerous natural frequencies is that the cylinder might experience multiple lock-in conditions [12, 84, 85]. That is, for a rigid cylinder the lock-in condition ends after certain reduced velocity, while for an elastic cylinder when f_s desynchronizes with one natural frequency (e.g. $f_{n,1}$), it might lock onto another one (e.g. $f_{n,2}$). This circumstances in which just one mode is resonating is called "single-mode" lock-in [85]. On the other hand, since the interval between successive natural frequencies of a flexible cylinder is usually small, it is plausible that the oscillating hydrodynamic forces excite more than one mode at a time and cause multi-mode structural vibrations. For example, Figure 2.17 shows the vibrating modes participated in the CF responses of a bare flexible cylinder of L/D=481 subjected to uniform flow. In this figure, the colours represent the normalised power of modes and illustrate that the structure experiences multi-mode oscillations. For such circumstances that more than one mode is excited, lock-in is defined as one mode dominating the other modes [85]; e.g. in Figure 2.17 the modes with dark red colours are dominant. In flexible cylinder VIV studies, despite VIV studies on rigid cylinders in which just uniform flow velocities are applied, the structure can be subjected to spatially variable flow velocities. Therefore, one can categorise these investigations as (i) studies performed at spatially-uniform flow velocities [86] and (ii) experiments performed at spatially-variable flow velocities [87]. The other feature that distinguishes VIV of elastic structures from that of elastically mounted rigid cylinders is that different geometric layouts and installation configurations of a flexible cylinder, (such as straight, catenary [88], lazy/steep S and lazy/steep wave layouts [89]) lead to different dynamic responses. To be within the scope of this thesis, in the following section, experimental investigations on VIV of straight flexible cylinders, conducted over the past decade, are reviewed.

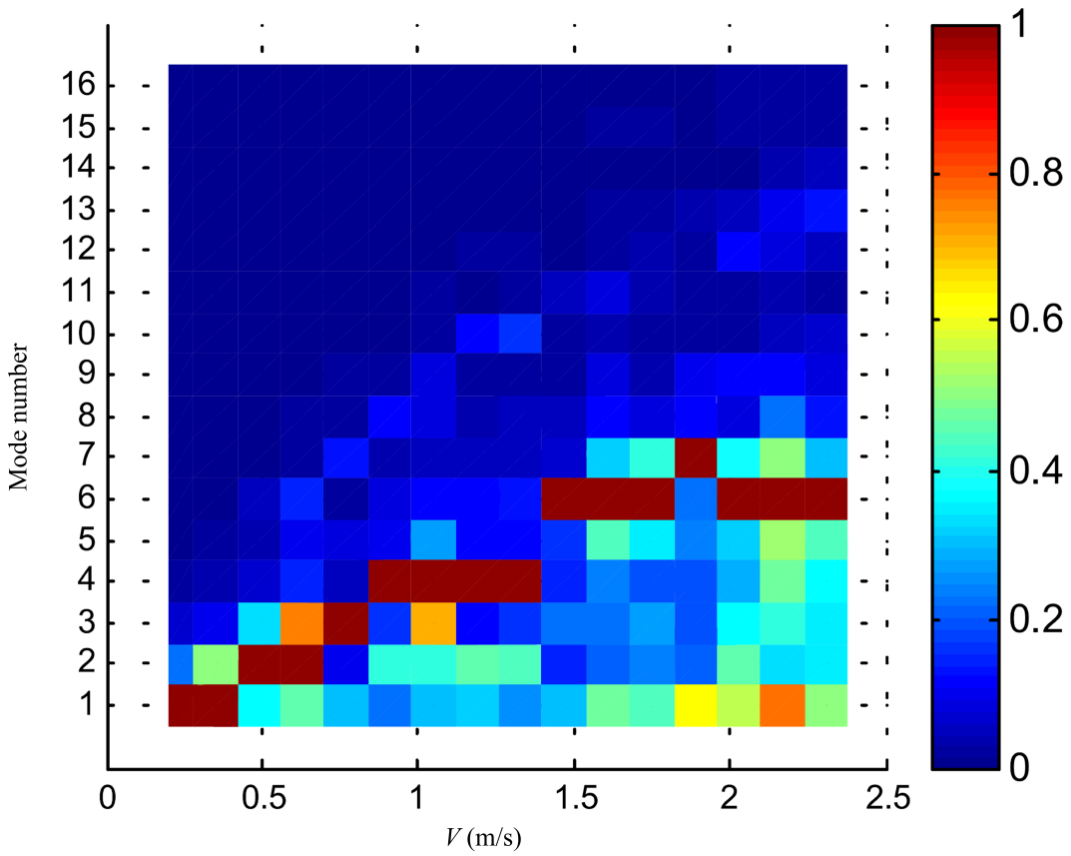

Figure 2.17: Modes contributing in the CF motions of a flexible cylinder subjected to uniform flow of velocity *V*. Adopted from [12].

2.4.2 Experimental studies on VIV of straight flexible cylinders

Table 2.2 shows a chronological summary of some empirical studies on VIV of flexible cylinders which have been accomplished over the past decade. These experiments are chosen in a way to cover a wide range of aspect ratios (i.e. from 30 to 4600) and be performed with both uniform and non-uniform flow velocity profiles at subcritical Reynolds numbers. As it can be seen in Table 2.2, the importance of considering IL oscillations is one of the main findings of most of these studies. Therefore, similar to rigid cylinder studies, these they show that, for a realistic prediction and modelling of VIV of marine risers, combined transverse/streamwise oscillations should be taken into account. The experimental studies also showed that, while the responses of an elastic cylinder subjected to a uniform flow under lock-in condition is dominated by standing waves, sheared flow causes responses dominated by travelling waves.

Table 2.2: A summary of the experimental studies conducted over the past decade on VIV of straight flexible cylinders. The colours represent the applied flow profiles; uniform flow (green), sheared flow (blue) and stepped flow (purple).

Experimental Studies	Flow velocity profile	Test specifications			Main findings
		Re	Aspect ratio	Pretension (N)	
[12, 87]	● ● ○	4000-46000	481.5	700	• Linear increase of oscillation frequencies with the increase of current speed • Multi-mode vibrations; All excited modes oscillate at the same frequency (Strouhal frequency) • Importance of IL oscillations with fatigue damages comparable to CF oscillations • In lock-in condition the responses are dominated by standing waves • Sheared flow causes responses dominated with travelling waves
[90]	● ● ○	70000	1400	4000-6000	• CF and IL have fatigue damages of the same order of magnitude • Mode numbers up to 12 in transverse and 25 in streamwise directions are excited • Sheared flow causes lower oscillation amplitudes

[84]	○ ○ ●	2500-25000	468.6	500-2000	• Multi-mode VIV • Monotonically increase of oscillation amplitude during the lock-in of each mode • Transition from one locked-in mode to the other is accompanied by a drop in oscillation amplitude • Significant amplification of mean drag coefficient
[83]	○ ● ○	36000	3000	3700	• IL mode numbers up to 50; Importance of considering IL oscillations • Non-lock-in VIV • Travelling waves dominate the responses
[91]	○ ● ○	8000-40000	90		• Single-mode lock-in; Transition from lock-in to non-lock-in multi-mode oscillations • Importance of considering IL oscillations
[81, 92]	● ○ ○		4198.3	3225	• Third, fourth and fifth harmonic responses are observed considerable fatigue damage due to higher harmonic responses
[80, 93]	○ ○ ●	1200-12000	93.75	<110	• Dual resonance with Highly repetitive Fo8 trajectories • Significant effect of tension on VIV response branches • Vortex modes depend on the amplitude distribution along the span of the cylinder

[86]	● ○ ○	245000, 106000	32, 59	222.4	• Linearly increase of the frequency response of a tension-dominated cylinder with the increase of flow velocity • Stepped increase of the frequency response of a bending stiffness-dominated cylinder with the increase of flow velocity
[94]	● ○ ○	3000-10000	1750	600-800	• Importance of IL oscillations • Multi-mode vortex-induced oscillations, all mode vibrating at the Strouhal frequency • Asymmetric structural response due to multi-modal VIV and phase lag between involved modes • Higher harmonic components in the VIV response
[95]	● ○ ○	2000-20000	162	73-294	• Increasing pretension lead to: lower oscillation amplitudes, higher lift force, higher mean and dynamic tension
[13]	○ ○ ●	<37400, <28000	158, 187	200-800	• Importance of IL oscillations • High IL and CF oscillation amplitudes up to 1*D* and 3*D* respectively • Large mean drag coefficient up to 4.5

Table 2.2 also infers that pretension force is an influential parameter. the importance of pretension can be inferred from Eq. (2.19) as well. Tension determines the behaviour of the cylinder to be like a cable or like a beam. When the system is tension-dominated, the cylinder behaves like a cable which causes monotonical increase of oscillation frequency and higher modes as the flow velocity increases. On the other hand, when the system is dominated by the bending stiffness, the cylinder behaves like a beam which results in stepped increase of oscillation frequencies and lower excited modes as the flow velocity increases. Along with the experimental studies, computational fluid dynamic studies and direct numerical VIV simulations have been carried out for these years. These studies can provide better understanding of FSI phenomena taking place during VIV and realistically predict VIV [96-104]. However, doing such studies on a high aspect ratio flexible cylinder is very expensive and requires extensive computational capacities. Hence, it is necessary to think of an alternative method that can provide reliable VIV predictions. Similar to rigid cylinders, semi-empirical models such as wake-oscillator models can be the alternative solution. A review of the semi-empirical models applied for prediction of vortex-induced oscillations of elastic cylinders is presented in the following section.

2.4.3 Semi-empirical modelling of VIV of flexible cylinders

The background and features of semi-empirical models were explained in section 2.2.3. Following the scope of this thesis, in this section the wake-oscillator models that over the past decade has been utilised for investigating VIV in elastic structures are reviewed. Generally speaking, these models are similar to the wake-structure oscillator models used for prediction of 1DOF vortex-induced oscillations of an elastically mounted rigid cylinder, except that the equation of simple harmonic motion is replaced with the equation of cable, beam or cable-beam oscillations. These phenomenological models, based on the DOF(s) considered for the structure and the type of the structural equation(s) can be categorised into four groups of wake-structure oscillator models in which (i) linear transverse-only, (ii) nonlinear transverse-only, (iii) combined linear IL/CF oscillations and (iv) coupled axial/CF vortex induced oscillations of an elastic cylinder are modelled.

2.4.3.1 Modelling of linear CF-only VIV

Vortex-induced oscillations and vortex-induced waves of a very slender cylinder subjected to uniform flow were modelled by [105]. In this study, they coupled the phenomenological near-wake model with a cable equation and compared the results of their analysis with DNS and experimental results. The comparison showed that such a model can capture many of important features of VIV and VIW of such structures. For example, Figure 2.18 depicts a comparison between the semi-empirical model and DNS [106] predictions of transverse VIV response of a cable and illustrates that the wake-structure oscillator model can describe the numerical observations such as standing, transient and travelling waves. Using the same system of equations, Mathelin and de Langre [107] considered VIV and VIW a caused by sheared flow and found that, due to a local lock-in, wave packets distribute along the span of the riser. Violette and de Langre [108] added a bending term to the model used in the aforementioned models. They considered an infinite cable subjected to uniform and non-uniform flows and a finite beam subjected to linearly sheared flow.

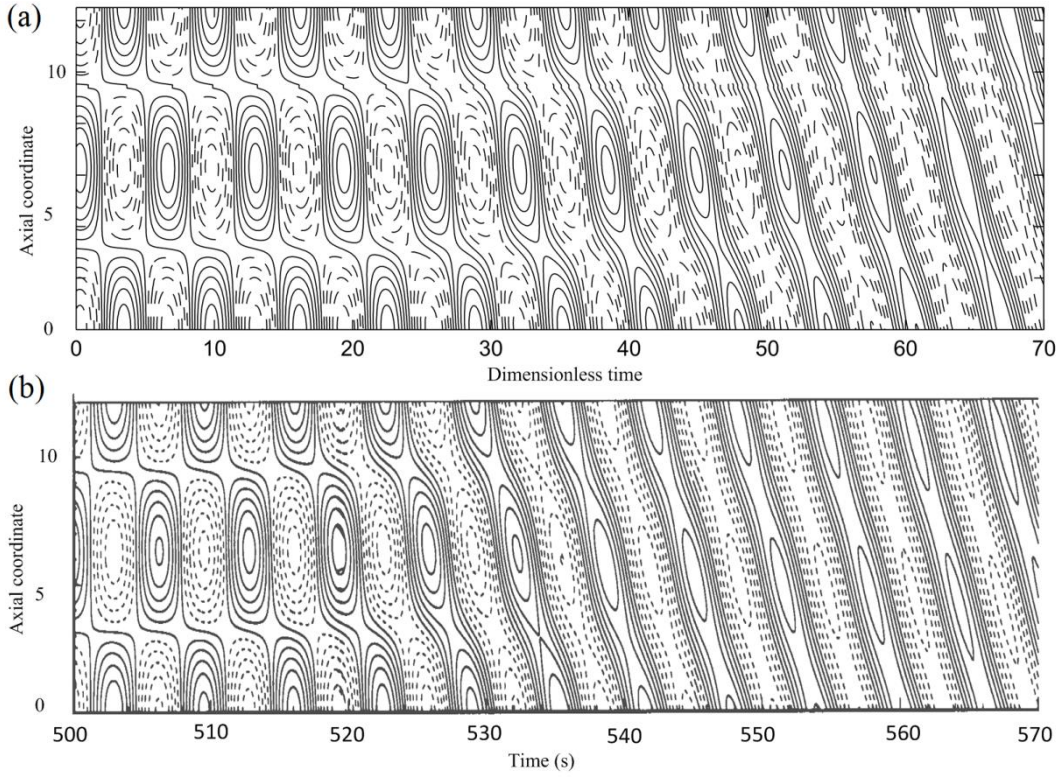

Figure 2.18: Spatio-temporal plot of CF oscillations of a cable undergoing VIV predicted via: (a), semi-empirical model; (b), DNS. Figure (a) is adopted from [105] and figure (b) is taken from [106].

Through comparisons with DNS and experimental results, they showed that their simple model can capture key response characteristics of an elastic cylinder undergoing VIV such as modal content and standing and travelling nature of waves. They also showed that the travelling waves propagate in arbitrary directions along the span of the cylinder. In a latter study [109] they linearized this model to perform a linear stability analysis and using this approach could capture "range of unstable wavenumbers, mode transition or mode switching with flow velocity, time sharing and space sharing". However, due to this simplification and linearization the model couldn't estimate maximum oscillation amplitudes and couldn't capture VIV behaviours caused by nonlinearities.

The importance of tension in determining the behaviour of a flexible cylinder experiencing VIV was discussed in the previous sections. In real engineering practice, the tension along the span of the cylinder may vary due to its weight or the buoyancy force. Srinil [110], using a classic wake oscillator model proposed by [63], investigated the VIV of a vertical riser with variable tension. He could capture multi-mode standing and hybrid standing-travelling waves and observed dominant mode switching in time. In his study, to relate the empirical coefficients of the wake oscillator to physical VIV parameters, using rigid cylinder experimental results, he defined variable wake-oscillator coefficients as a function of Re. The comparison of the model predictions with some experimental results showed qualitative agreement.

2.4.3.2 Modelling of nonlinear CF-only VIV

Although the aforementioned models can model many of experimentally observed behaviours, they do not provide any insight into the nonlinear multi-mode dynamics and interactions of flexible cylinder VIV. To obtain such information, a model should consider both geometric and wake nonlinearities. Srinil [111] developed such a semi-empirical model for a sagged cable and straight cylinder subjected to uniform flow. Similar to his previous study [110], in here as well, he defined the wake coefficients of his model in terms of physical parameters. Through this study, he could model some of the key features of VIV of flexible cylinders such as multi-mode lock-in, mode switching, mode sharing, mode-dependent lock-in bandwidth and added mass. This study also revealed the significant importance of the

geometric nonlinearities for realistic VIV predictions and capturing multi-mode interactions.

Figure 2.19 depicts spatial variation of the root-mean-square (RMS) amplitudes of a flexible cylinder when the geometric nonlinearities are considered (Figure 2.19 (a)) and when these nonlinearities are neglected (Figure 2.19 (b)). The figure illustrates that two models lead to both qualitatively and quantitatively different responses. It can be seen that with the nonlinear model, lower amplitudes are obtained, and due to high multi-mode contributions, a dominant mode cannot be distinguished. On the other hand, the linear model predicts higher oscillation amplitudes and distinguishable dominant modes.

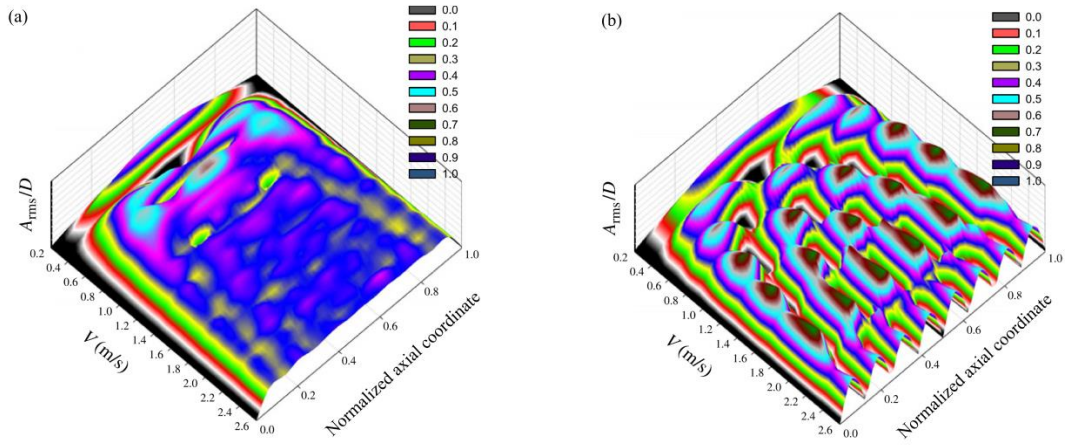

Figure 2.19: Spatial variations of the RMS amplitude of CF oscillations of a flexible cylinder with *V* predicted via (a) a semi-empirical model in which structural geometric nonlinearities are taken into account and (b) a semi-empirical model with linear structure-oscillator. Adopted from [111].

2.4.3.3 Modelling of combined linear CF/IL VIV

The experimental studies reviewed in the previous sections revealed that for a realistic prediction of VIV in flexible cylinders both of the streamwise and transverse oscillations of the cylinder should be taken into account. Following these results, [112] and [113] developed a semi-empirical wake-structure model to study coupled CF/IL oscillations. They considered the structural oscillators of cable-beams which were coupled to wake oscillators. In their model there was no direct coupling between CF and IL structural oscillators and these oscillators were coupled indirectly

through quadratic nonlinear fluid forcing terms [114]. Utilising this model for a cylinder subjected to a uniform flow and comparison between the numerical and experimental results showed that the model could capture similar frequency responses, vibrating modes and standing/travelling wave responses. Changing the flow velocity profile to sheared flow showed significant changes in the characteristics of the VIV response. They also could capture the transitions between multi- and single-mode oscillations.

2.4.3.4 Modelling of coupled axial/CF VIV

For a rigid cylinder which can only oscillate in streamwise and CF directions, it was shown that considering both of these degrees of freedom leads to results different from transverse-only oscillations. When it comes to the elastic cylinders, the structure can take longitudinal oscillations as well. Therefore, this new DOF might have significant effects on the behaviour of the VIV system. The recent studies showed that, as the aspect ratio increases, the axial oscillations which are excited by lateral vibrations (CF and IL vibrations) of the cylinder become more significant [115]. Hence, to study the vortex-induced oscillations of a high aspect ratio riser, [14] used a wake-structure oscillator model in which the structural nonlinearities and the coupling between CF and axial oscillations of the riser were taken into account. They used the classic wake oscillator developed by [66] to model near wake dynamics and utilised this model to study the effect of uniform and sheared flows. Although in this study they considered the axial oscillations of the cylinder, they just reported the CF responses of the structure and did not discuss the axial oscillations.

Overall, while the significance of IL and axial VIV of flexible structures has been proven experimentally and numerically, the majority of semi-empirical models have been focusing on prediction of CF-only VIV of these structures. A few aforementioned coupled models for flexible cylinders are limited to coupled CF-IL or CF-axial VIV in which the interconnection of structural oscillations and geometric nonlinearities are neglected. Moreover, the hydrodynamic nonlinearities of these models are limited to cubic nonlinear terms of wake oscillators, which represent self-exciting and self-limiting nature of VIV, and almost none of these models account

for nonlinear hydrodynamic coupling of wake oscillators and structural equations of motions.

2.5 Conclusions

The extensive and comprehensive review of VIV studies, performed in this chapter, shows the need for a predictive model to analyse the coupled CF/IL VIV of rigid and flexible circular cylinders subjected to uniform and linearly sheared flows. Hence, this study is mainly devoted to developing such fully-nonlinear predictive VIV models. Via such models, it is aimed to capture and explain the aforementioned experimentally observed behaviours, such as dual resonances, higher harmonics, jump and hysteresis, transition between travelling and standing waves, multi and single-mode lock-in conditions, mean drag amplifications and influential hydrodynamic coefficients, as much and accurate as possible. Moreover, the importance of IL and axial oscillations along with the significance of hydrodynamic and geometric nonlinearities are examined to justify the complexity added to the proposed models.

To achieve these objectives, once the mathematical model is developed, appropriate numerical and analytical methods such as Runge-Kutta, finite difference and harmonic balance methods are applied to solve the model. Verification, calibration and examination of the model are achieved via extensive comparisons with experimental results from literature and in-house tests conducted in the towing tank of the Department of Naval architecture, Ocean and Marine Engineering, University of Strathclyde. The in-house experiments are mainly conducted to fulfil the gaps in the literature, explained in Section 2.2.3.4, and will provide new information and observations onto less-studied aspects of VIV whilst being utilised for further calibration and verification of the proposed model.

Chapter 3

Modelling of Coupled CF/IL VIV of Rigid Cylinders

Many studies have typically applied a linear structural spring-mass-damper oscillator and a van der Pol wake oscillator to model a one-dimensional CF vortex-induced vibration. In this chapter, an advanced model for predicting a two-dimensional coupled CF/IL VIV of a flexibly-mounted circular cylinder in a uniform flow is proposed and validated. The ensuing dynamical system is based on double Duffing-van der Pol (structural-wake) oscillators with the two structural equations containing both cubic and quadratic nonlinear terms. The cubic nonlinearities capture the geometrical coupling of CF/IL displacements excited by hydrodynamic lift/drag forces whereas the quadratic nonlinearities allow the wake-cylinder interactions. Some empirical coefficients are calibrated against published experimental results to establish a new generic analytical function accounting for the dependence of VIV on a physical mass and/or damping parameter. By varying flow velocities in the numerical simulations, the derived low-order model is utilised for predicting important VIV characteristics. Using the newly-derived empirical formula, the predicted maximum CF/IL VIV amplitudes and associated lock-in ranges are compared with several experimental results for cylinders with low/high mass or damping ratios. Moreover, the parametric studies are performed to investigate the importance of geometrical nonlinearities through new displacement coupling terms and the ratio of IL to CF natural frequencies of the freely-vibrating cylinder.

3.1 Model with Combined Structural/Hydrodynamic Nonlinearities

A low-order mathematical model simulating the nonlinear 2DOF free vibration of an elastically-supported circular cylinder in a uniform steady flow with a velocity *V* is developed. The cylinder is assumed to be infinitely long such that a mechanical spring-mass-damper system (i.e. the structural oscillator) can be used to model the cylinder dynamic response. As displayed in Figure 3.1 (a), the cylinder of diameter *D* is constrained by a two-directional four-spring system, freely oscillating in both IL (streamwise) *X* and CF (transverse) *Y* directions with *O* at the cylinder centre being the origin of the co-ordinates. In contrast to several existing VIV models which typically consider a linear structural oscillator to describe the cylinder (mostly *Y*) displacement [4], the effect of geometric nonlinearities (i.e. spring nonlinear stiffness or restoring force) of the oscillating cylinder is herein accounted for alongside the hydrodynamic nonlinearities governing the fluctuation of the vortex-induced lift/drag forces.

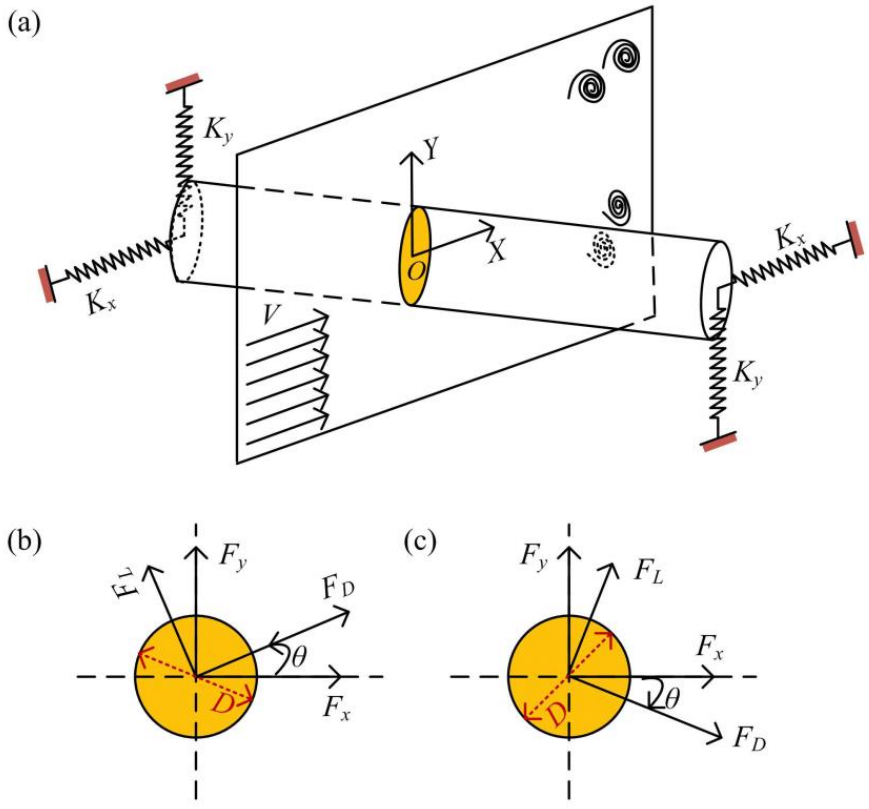

Figure 3.1: A schematic model of a spring-mounted circular cylinder undergoing two-dimensional VIV (a) and associated hydrodynamic force components (b).

By permitting the cylinder to oscillate in both CF/IL directions, experimental results [70, 71] showed that the associated cylinder amplitudes noticeably increase in comparison with the pure CF VIV, owing to the greater influence of fluid-structure interaction. Depending on system parameters, the CF maximum amplitudes in the 2DOF VIV case may achieve such high values as 1.5*D* [11] or even 2*D* [116], being much greater than typical values of about 1*D* observed in the CF-only VIV [26, 117]. According to the large-amplitude response, the axial stretching of the springs may become intrinsically nonlinear, being amplitude-dependent and bi-directionally coupled. Recently, the applied VIV analysis of flexible curved/straight structures has highlighted how the multi-mode interactions in conjunction with structural nonlinearities play a crucial role in both the numerical VIV prediction and comparison with experimental results [111]. Based on these findings, two nonlinearly-coupled structural oscillators in conjunction with two wake oscillators are proposed for the advanced 2DOF VIV modelling and simulation.

3.1.1 Geometrically-nonlinear structural oscillators

The nonlinear equations of motion of the 2DOF freely-oscillating cylinder are derived based on the actual physics of the moving springs, similar to the formulation described by Bellman [118] in a one-directional spring case. By considering four coupled springs as in Figure 3.1 (a), the geometrically-nonlinear structural oscillators governing the IL and CF vibrations of the cylinder may be expressed as

$$\left(m_{sx}+m_{fx}\right)\ddot{X}+\left(c_{sx}+c_{fx}\right)\dot{X}+k_x(X+\alpha_x^*X^3+\beta_x^*XY^2)=F_x \tag{3.1}$$

$$\left(m_{sy}+m_{fy}\right)\ddot{Y}+\left(c_{sy}+c_{fy}\right)\dot{Y}+k_y\left(Y+\alpha_y^*Y^3+\beta_y^*YX^2\right)=F_y \tag{3.2}$$

where a dot denotes differentiation with respect to the dimensional time t, X and Y are dimensional IL and CF displacements, m_s, m_f, c_s, c_f and k the associated cylinder mass, fluid added mass, viscous damping, hydrodynamic damping and spring stiffness coefficients, respectively, with co-subscripts x and y identifying properties in these directions. Herein, we assume $m_{fx} = m_{fy} = m_f$ and $c_{fx} = c_{fy} = c_f$, with $m_f = \pi\rho D^2 C_a/4$ and $c_f = (2\pi \mathrm{St} V/D)\gamma\rho D^2$ [66]. γ is the stall parameter which is directly related to the sectional mean drag coefficient and assumed to be a constant equal to 0.8 [66]. α^*_x, α^*_y, β^*_x, and β^*_y are geometrical coefficients pertaining to the moving

spring-mass system. Note that Eqs. (3.1) and (3.2) are so-called Duffing oscillators [119] whose cubic-type nonlinear terms capture the axial stretching feature (X^3, Y^3) and physical coupling of CF/IL motions (XY^2, YX^2). The use of two coupled Duffing oscillators can also be found in some other scientific applications [120, 121].

The key aspect in the formulation of system equations of motions is to capture the quadratic relationship between in-line and cross-flow displacements [69]. Following Wang et al. [114], the two-directional unsteady fluid forces are exerted on the oscillating cylinder as opposed to the stationary one, by also accounting for the relative velocities between the incoming flow and the cylinder in-line motion. As a result, the instantaneous lift (F_L) and drag (F_D) forces coincide with an arbitrary plane making up an angle of θ with respect to the Y and X axes, respectively. Two cases can be realized depending on whether θ is counterclockwise (Figure 3.1 (b)) or clockwise (Figure 3.1 (c)). From our numerical simulation experience, it has been discovered that such θ direction plays a key role in the ensuing phase difference between cross-flow and in-line oscillations and, correspondingly, the Fo8 appearing shape. In general, the orbital plot exhibits a figure-eight trajectory with tips pointing upstream with a counterclockwise θ model or downstream with a clockwise θ model. As both cases have been experimentally observed in the literature depending on the system parameters, they are herein accounted for in the improved model formulation.

Consequently, by assuming a small θ [7] and omitting the mean drag component, F_x and F_y may be given by [114]

$$F_x = F_D \cos\theta \pm F_L \sin\theta \approx F_D \pm F_L \frac{\dot{Y}}{V} \tag{3.3}$$

$$F_y = F_L \cos\theta \mp F_D \sin\theta \approx F_L \mp F_D \frac{\dot{Y}}{V} \tag{3.4}$$

3.1.2 Phenomenological wake oscillators

Accordingly, the unsteady drag and lift force components are given by

$$F_D = \frac{1}{2}\rho D V^2 C_d, \quad F_L = \frac{1}{2}\rho D V^2 C_l \tag{3.5}$$

where C_d and C_l are the time-varying drag and lift coefficients, respectively. By introducing the reduced vortex lift coefficients as $p = 2C_d/C_{d0}$ and $q = 2C_l/C_{l0}$ [66] in which C_{D0} and C_{L0} are the associated drag and lift coefficients of a stationary cylinder (assumed as C_{D0}=0.2 [52] and C_{L0}=0.3 [7]), the time variation of the fluid vortex variables p and q may follow the self-excitation nature of the van der Pol-based wake oscillators described by

$$\ddot{p} + 2\varepsilon_x\omega_f(p^2 - 1)\dot{p} + 4\omega_f^2 p = S_x \tag{3.6}$$

$$\ddot{q} + \varepsilon_y\omega_f(q^2 - 1)\dot{q} + \omega_f^2 q = S_y \tag{3.7}$$

herein, $\omega_f = 2\pi \mathrm{St}V/D$ is the vortex-shedding angular frequency, S_x and S_y the excitation terms simulating the effect of cylinder motion on the near wake, ε_x and ε_y the wake empirical coefficients. To possibly capture the second and third instability ranges of the stream-wise oscillation [52], the frequency of the wake oscillation in the IL direction (Eq. 3.6) is taken to be twice that in the CF direction (Eq. 3.7). The coupling and interaction between the fluid and the structure is captured through the excitation terms F_x (Eq. 3.1), F_y (Eq. 3.2), S_x (Eq. 3.6) and S_y (Eq. 3.7). Whilst F_x and F_y depend on the projection of oscillating drag/lift forces through Eqs. (3.3-5) accounting for the reduced vortex coefficients p and q, the influence of S_x and S_y may be assumed to be linearly proportional to the displacement [122], velocity [63] or acceleration [66] of the cylinder. Based on 1DOF VIV studies, Facchinetti *et al*. [66] have examined the effect of the coupling S_y term on the VIV modelling and finally suggested the use of acceleration model. Similarly, we assume in the 2DOF VIV modelling that

$$S_x = \Lambda_x \frac{\ddot{Y}}{D}, \quad S_y = \Lambda_y \frac{\ddot{Y}}{D} \tag{3.8}$$

where Λ_x and Λ_y are the empirical coupling parameters adopted equally as Λ_x=Λ_y=12 based on the suggested Λ_y=12 in Facchinetti *et al.* [66]. This assumption would allow us to focus on the scaling and calibration of other control parameters (ε, α, β), see Sections 3.2, 3.3.1 and 3.3.2.

3.1.3 Dimensionless coupled structural-wake oscillators

By introducing the dimensionless time $t' = \omega_{ny}T$, $x = X/D$ and $y = Y/D$, the nonlinearly-coupled Eqs. (3.1), (3.6), (3.2) and (3.7) with four unknown variables (X, p, Y, q) – simulating coupled IL and CF VIV due to fluctuating drag and lift fluid forces – become

$$\ddot{x} + \lambda_x \dot{x} + f^{*2}\left(x + \alpha_x x^3 + \beta_x x y^2\right) = M_D \Omega^2 p \pm 2\pi M_L \Omega^2 q \frac{\dot{y}}{V_r} \tag{3.9}$$

$$\ddot{p} + 2\varepsilon_x \Omega\left(p^2 - 1\right)\dot{p} + 4\Omega^2 p = \Lambda_x \ddot{x} \tag{3.10}$$

$$\ddot{y} + \lambda_y \dot{y} + y + \alpha_y y^3 + \beta_y y x^2 = M_L \Omega^2 q \mp 2\pi M_D \Omega^2 p \frac{\dot{y}}{V_r} \tag{3.11}$$

$$\ddot{q} + \varepsilon_y \Omega\left(q^2 - 1\right)\dot{q} + \Omega^2 q = \Lambda_y \ddot{y} \tag{3.12}$$

where $\Omega = \mathrm{St}V_r$ is equivalent to ω_f/ω_{ny}, being the ratio of vortex-shedding frequency to the cylinder CF natural frequency in still water. The ratio of structural natural frequencies in X and Y directions is given by $f^* = \omega_{nx}/\omega_{ny}$ whose

$$\omega_{nx} = \sqrt{\frac{k_x}{m_{sx} + m_f}}, \qquad \omega_{ny} = \sqrt{\frac{k_y}{m_{sy} + m_f}} \tag{3.13}$$

M_D and M_L are the system mass parameters defined as

$$M_D = \frac{C_{d0}}{2}\frac{1}{8\pi^2 \mathrm{St}^2 \mu_x}, \qquad M_L = \frac{C_{l0}}{2}\frac{1}{8\pi^2 \mathrm{St}^2 \mu_y} \tag{3.14}$$

in which the mass ratios μ_x and μ_y are expressed as [66]

$$\mu_x = \frac{m_{sx} + m_f}{\rho D^2}, \qquad \mu_y = \frac{m_{sy} + m_f}{\rho D^2} \tag{3.15}$$

The damping terms λ_x and λ_y, accounting for the effects of structural viscous damping and fluid added damping (stall term), read

$$\lambda_x = 2\xi_x f^* + \frac{\gamma \Omega}{\mu_x}, \qquad \lambda_y = 2\xi_y + \frac{\gamma \Omega}{\mu_y} \tag{3.16}$$

where ξ_x and ξ_y are the structural reduced damping coefficients [66]. As it was explained in Chapter 2, the mass ratio definition in the literature is variable but it is widely recognized by the notation m^* [6]. In the parametric study, the mass ratio is referred to as m^*; the condition of $m^*_x = m^*_y = m^*$ is applied since practical offshore cylindrical structures generally have a circumferentially-uniform mass. Yet, some experimental studies have considered unequal m^*_x and m^*_y [11, 70] which would make the calibration task more complicated. With the same reason, $\xi_x = \xi_y = \xi$ is assumed. α_x, α_y, β_x, and β_y are the dimensionless counterparts of geometrical parameters α^*_x, α^*_y, β^*_x, and β^*_y, respectively, whose effects will be investigated in Section 4.1.

It is worth emphasizing that Eqs. (3.9) and (3.11) contain cubic (x^3, xy^2, y^3, x^2y) and quadratic ($p\dot{y}, q\dot{y}$) nonlinearities, with the former capturing the axial stretching/structural coupling of x-y displacements whereas the fluid-structure interaction effect is captured through all linear and nonlinear terms in the right-hand side of Eqs. (3.9-12). The maximum cross-flow/in-line amplitudes are unaffected by the choice of θ since the associated velocities are trivial, making $p\dot{y}/V_r \approx q\dot{y}/V_r \approx 0$ Eqs. (3.10) and (3.12). The cylinder natural frequency ratio f^* is also a key physical parameter apart from m^* and ξ which are embedded in M_D, M_L, λ_x and λ_y (Eqs. 3.13-16). The non-linearly coupled Eqs.(3.9-12), based on clockwise θ, are numerically and simultaneously solved using a fourth-order Runge-Kutta scheme with an adaptive time step enabling the solution convergence and stability, and with assigned initial conditions at $t = 0$ of $x = y = 0$, $p = q = 2$ and zero velocities. The numerical results are obtained via standard ODE algorithms of Matlab. On a Dell Optiplex 7010 PC with Intel® Core-i7 3.4 GHz processors and 16 GB of RAM, it takes about 0.3 s for each second VIV simulation with a time step of 10^{-2} s. The case of increasing reduced flow velocity V_r is generally considered. However, if there is a sudden jump of response amplitude, V_r may also be decreasingly varied to capture a possible hysteresis. In all simulation cases, a varying V_r step is sufficiently small being equal to 0.1.

3.2 Identification of Empirical Coefficients

The analysis and prediction of coupled CF/IL VIV of circular cylinders based on Eqs. (3.9-12) depend on several empirical coefficients (ε_x, ε_y, Λ_x, Λ_y) and geometrically-nonlinear parameters (α_x, α_y, β_x, β_y). Fixed values of ε_y and Λ_y have recently been proposed for a 1DOF VIV [66] whereas a new set of ε_x, ε_y, Λ_x, Λ_y, α_x, α_y, β_x and β_y is herein proposed for a 2DOF VIV. For a given m^*, ξ and f^*, these coefficients and parameters can be identified by calibrating the numerically-obtained IL and CF amplitudes (A_x/D and A_y/D) with experimental results and by accounting for some qualitative VIV behaviors. Owing to a large set of variables, it is impractical in a parametric study to capture the system dependence on all of these variables. Accordingly, $\varepsilon_x = 0.3$, $\Lambda_x = \Lambda_y = 12$ [66], and $\alpha_x = \alpha_y = \beta_x = \beta_y = 0.7$ are preliminarily fixed whereas the ε_y-function is determined through the best fits with the 2DOF VIV experiment results in the case of varying (i) ξ [30], (ii) m^* [76] and (iii) $m^*\xi$ [30, 76]. After identifying the ε_y-functions, the sensitivity analysis of other coefficients/parameters will be carried out as in Sections 3.3.1 and 3.3.2.

For a specific $f^* = 1$, Tables 3.1 and 3.2 summarise the test matrix from the two experiments [30, 76] by reporting the assigned ξ (Table 3.1) or m^* (Table 3.2), and the associated $m^*\xi$, along with the tuned ε_y deduced from relevant numerical-experimental calibrations. In the following, only A_y/D are plotted whereas combined A_x/D and A_y/D will be presented in Section 3.3.

3.2.1 Model calibration through experimental results with variable ξ

By first considering the case of varying ξ with a fixed low mass $m^* = 5.4$ [30], Figure 3.2 illustrates a comparison of numerically-predicted (lines) and experimentally-obtained (squares) CF amplitudes for $\xi = 0.002$ (Figure 3.2 (a)), 0.02, 0.05, 0.1, 0.2 and 0.4 (Figure 3.2 (b)). With the lowest $\xi = 0.002$, results with increasing ($\rightarrow$) and decreasing ($\leftarrow$) V_r are plotted in Figure 3.2 (a) which reveals the jump-up and -down response (denoted by dashed lines) and hysteresis of amplitudes around $V_r = 8$. The experimental and numerical maximum $A_y/D \approx 1.5$ and the associated lock-in ranges ($4 < V_r < 8$ or 10) are qualitatively and quantitatively comparable, although the numerical model underestimates the lower-amplitude

branch (V_r > 8). Similar large maximum A_y/D values (1.5 and above) have also been reported by some other experiments, e.g. in Dahl *et al*. [11]. When ξ is increased by one (ξ=0.02, 0.05) or two (ξ=0.1, 0.2, 0.4) order of magnitude, both numerical and experimental results in Figure 3.2 (b) show decreasing A_y/D as expected, being as small as $A_y/D \approx 0.1$ for $\xi = 0.4$. The numerical model also predicts the disappearing jump for high $\xi = 0.05, 0.1, 0.2, 0.4$.

Table 3.1 shows, except $\xi = 0.002$ and 0.4, the increment of ε_y with increasing ξ. From a dynamical viewpoint, the decreasing A_y/D is feasible as ε_y mainly governs the nonlinear damping term (Eq. 3.12) regulating the self-excited and -limiting character of the VIV response [4]; thus, as ε_y increases, the damping effect increases too while keeping other variables unchanged.

Table 3.1: Considered various damping ratios based on experimental input data of [30] for a given m^* = 5.4, along with the numerically-tuned ε_y deduced from associated model simulations.

ξ	$m^*\xi$	ε_y
0.002	0.0108	0.0055
0.02	0.1080	0.0053
0.05	0.2700	0.0067
0.1	0.5400	0.015
0.2	1.0800	0.027
0.4	2.1600	0.02

Table 3.2: Considered various mass ratios based on experimental input data of [76] for a given ξ = 0.006, along with the numerically-tuned ε_y deduced from associated model simulations.

m^*	$m^*\xi$	ε_y
2.36	0.0142	0.0044
3.68	0.0221	0.0062
5.19	0.0311	0.0078
6.54	0.0392	0.0095
7.91	0.0457	0.014
8.76	0.0526	0.017
10.63	0.0638	0.027
12.96	0.0778	0.045

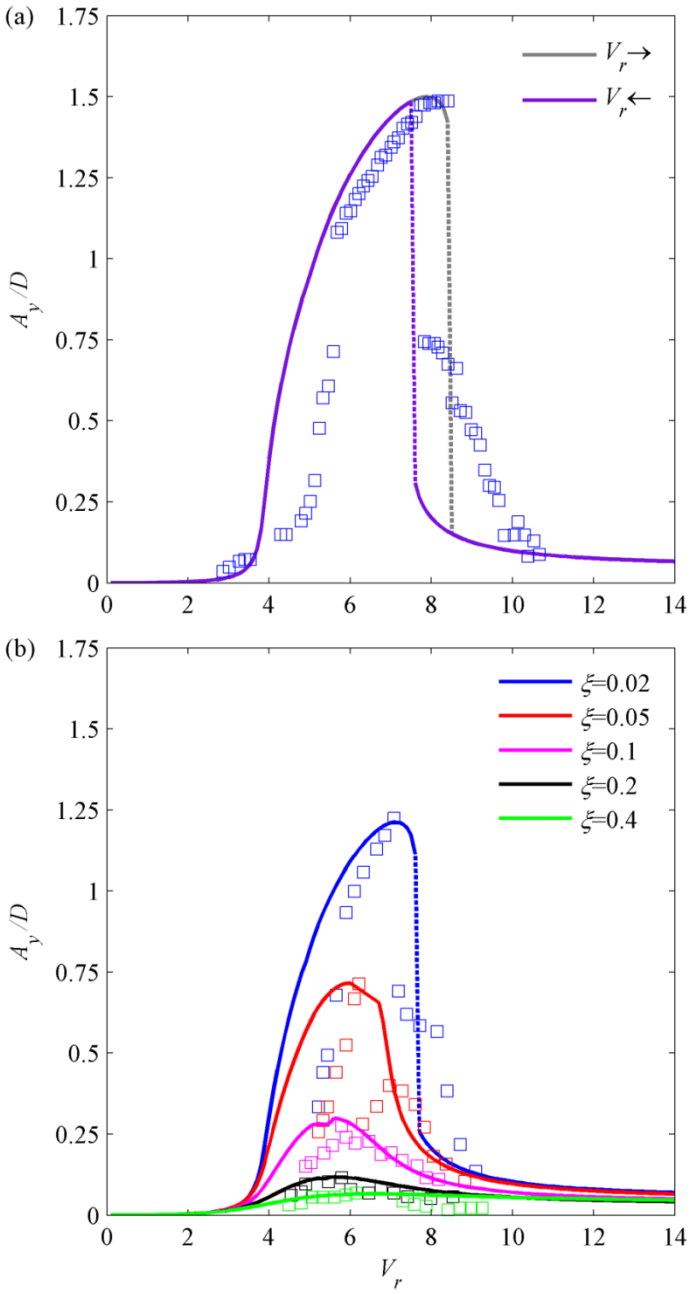

Figure 3.2: Comparison of numerical and experimental [30] cross-flow amplitudes with m^*=5.4 and f^*=1: (a) ξ = 0.002 with increasing (→) and decreasing (←) V_r; (b) varied ξ; squares denote experimental results associated with numerical results (lines) by same colors; dashed lines denote response jumps.

3.2.2 Model calibration through experimental results with variable *m**

For a given low ξ=0.006 [76], Figure 3.3 compares the numerically- (lines) and experimentally-obtained (squares) A_y/D for various m^* = 2.36 (Figure 3.3 (a)), 3.68, 5.19, 6.54, 7.91, 8.76, 10.63 and 12.96 (Figure 3.3 (b)). It is seen that the predicted

jump-up and –down responses occur almost the same V_r in Figure 3.3 (a); nevertheless, the jump disappears in Figure 3.3 (b) for higher m^* = 7.91, 8.76, 10.63 and 12.96, similar to higher ξ cases in Figure 3.2 (b). The maximum A_y/D as well as the associated lock-in ranges decrease as m^* increases, in qualitative agreement with general experimental results [9]. The model predicts a slightly shift in V_r at the jump for high m^* values (Figure 3.3 (b)) but this is considered of secondary importance as far as the primary attention is placed on calibrating maximum amplitudes. By comparing between the case with m^* = 5.4 and ξ = 0.002 in Figure 3.2 (a) and the case with m^* = 5.19 and ξ = 0.006 in Figure 3.3 (b), the former shows a greater maximum A_y/D by about 25 % due to a lower ξ by about 66.7 %. Although both cases have comparable m^*, such comparison emphasizes a role of damping in the VIV as suggested by Klamo *et al*. [29]. Similar to the increasing ξ case in Table 3.1, Table 3.2 shows the increment of tuned ε_y with increasing m^*; i.e. both cases yield the decreasing A_y/D (Figures 3.2 and 3.3).

By plotting and applying a variable curve fitting to the relationship of ξ and ε_y in Table 3.1, a cubic polynomial-based function is chosen as the best-fit $\varepsilon_y(\xi)$ function. The fitted curves are calculated via Curve Fitting toolbox of Matlab this toolbox provides a wide range of pre-defined and user-defined curve types, such as exponential, Sine waves and polynomials, which can be fitted to the desired data. Via this tool, the user is able to view the statistics of each fitting and check the quality of fitting. Using this toolbox $\varepsilon_y(\xi)$ is given by

$$\varepsilon_y = a_3\xi^3 + a_2\xi^2 + a_1\xi + a_0 \tag{3.17}$$

where a_0, a_1, a_2, and a_3 are polynomial coefficients approximately equal to 0.0048, 0.0274, 0.8266 and -2, respectively. In the same way, the curve fitting to the relationship of m^* and ε_y in Table 3.2 entails the best-fit exponential $\varepsilon_y(m^*)$ function as

$$\varepsilon_y = b_1 e^{[b_2 m^*]} \tag{3.18}$$

where b_1=0.00234 and b_2=0.228.

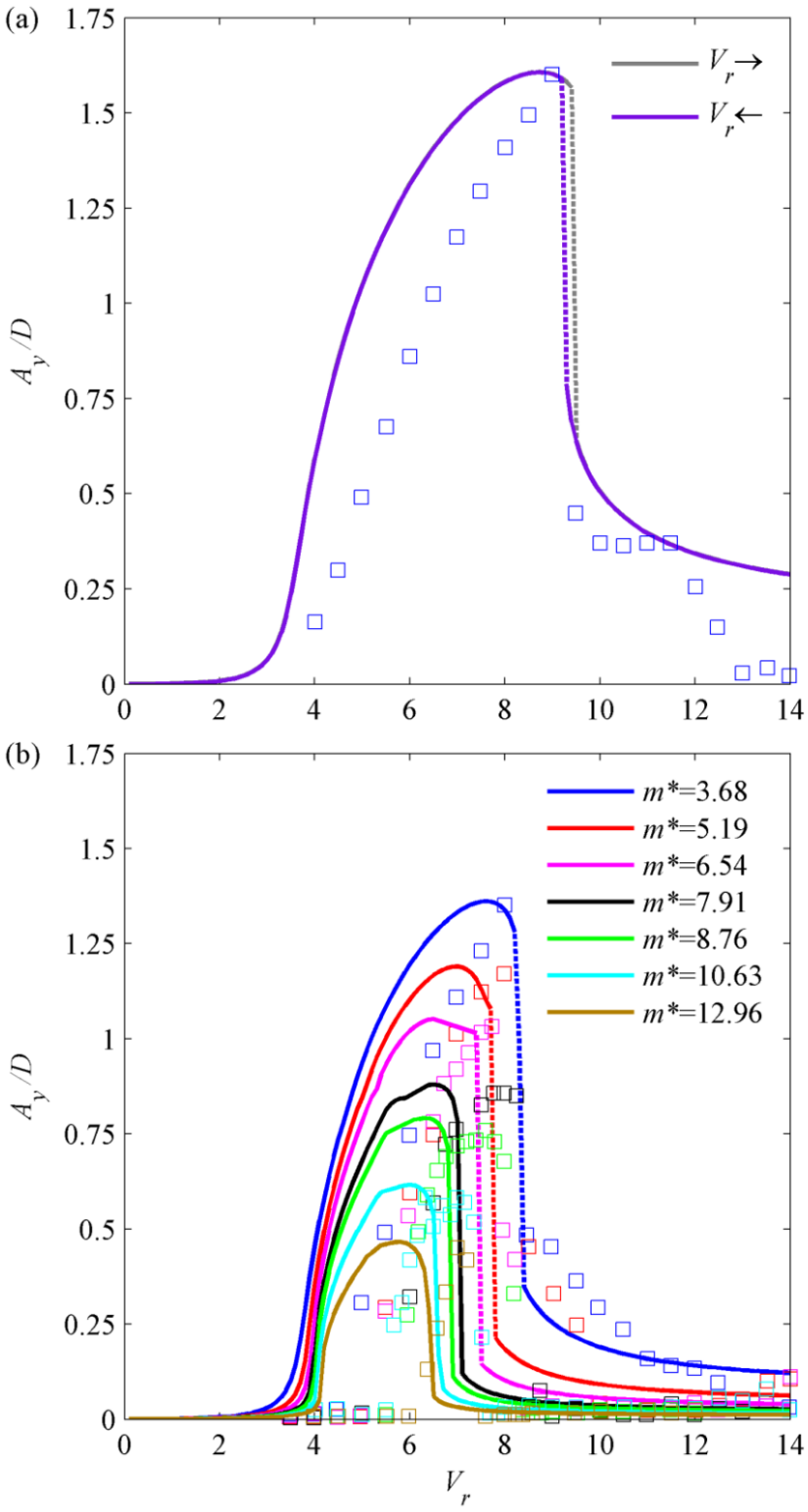

Figure 3.3: Comparison of numerical and experimental [76] cross-flow amplitudes with $\xi = 0.006$ and f^*=1: (a) m^*=2.36 with increasing (→) and decreasing (←) V_r; (b) varied m^*; squares denote experimental results associated with numerical results (lines) by same colors; dashed lines denote response jumps.

3.2.3 Model calibration through experimental results with variable $m^*\xi$

In the third scenario, both m^* and ξ are simply combined as $m^*\xi$ and the relationship of $m^*\xi$ and ε_y taking into account the information from both Tables 3.1 and 3.2 can be described by the best-fit Gaussian $\varepsilon_y(m^*\xi)$ function expressed as

$$\varepsilon_y = c_1 e^{-\left[\frac{m^*\xi - c_2}{c_3}\right]^2} + c_4 e^{-\left[\frac{m^*\xi - c_5}{c_6}\right]^2} \tag{3.19}$$

where c_1=0.0366, c_2=0.0762, c_3=0.02046, c_4=0.02995, c_5=1.464 and c_6=1.103. The above nonlinear functions enable us to capture the dependence of VIV on m^* (Eq. 3.17), ξ (Eq. 3.18) and $m^*\xi$ (Eq. 3.19) through the wake empirical coefficient ε_y.

3.2.4 Identification of the empirical relation proposed for ε_y

To validate the above functions and identify which of them will be utilised in the subsequent studies, we next apply Eqs. (3.17-19) along with Eqs. (3.9-12) to simulate 2DOF VIV responses of a recent experimental model [9] which considered f^* = 1 with two measurement sets: (i) m^* = 2.6 and ξ = 0.0025, (ii) m^* = 7 and ξ = 0.0007. The obtained experimental A_y/D (squares) are plotted against the numerically predicted ones (lines) in Figures 3.4 (a) (case i) and 3.4 (b) (case ii). The corresponding values of $\varepsilon_y(\xi)$, $\varepsilon_y(m^*)$ and $\varepsilon_y(m^*\xi)$ are 0.0048, 0.0042 and 0.0052 in Figure 3.4 (a), whereas they are 0.0048, 0.0116 and 0.0052 in Figure 3.4 (b), respectively. Note that these ε_y values are much smaller than 0.3 given in Facchinetti *et al*. [66]. Overall, a good agreement between experimental results and numerical predictions based on three different functions is found in the higher mass-damping ($m^*\xi$ = 0.0064) case (Figure 3.4 (a)), showing both the response jumps and overall amplitude (initial, upper and lower) branches [9]. However, in the lower mass-damping ($m^*\xi$ = 0.0048) case (Figure 3.4 (b)), discrepancies in maximum A_y/D between experimental and numerical results are remarkable when the latter are based on $\varepsilon_y(\xi)$ and $\varepsilon_y(m^*\xi)$ functions owing to their relevant ε_y values being comparable to 0.0048 and 0.0052, respectively. Based on these observations, the $\varepsilon_y(m^*)$ function based on Eq. (3.18) is preferably used in the following parametric investigations.

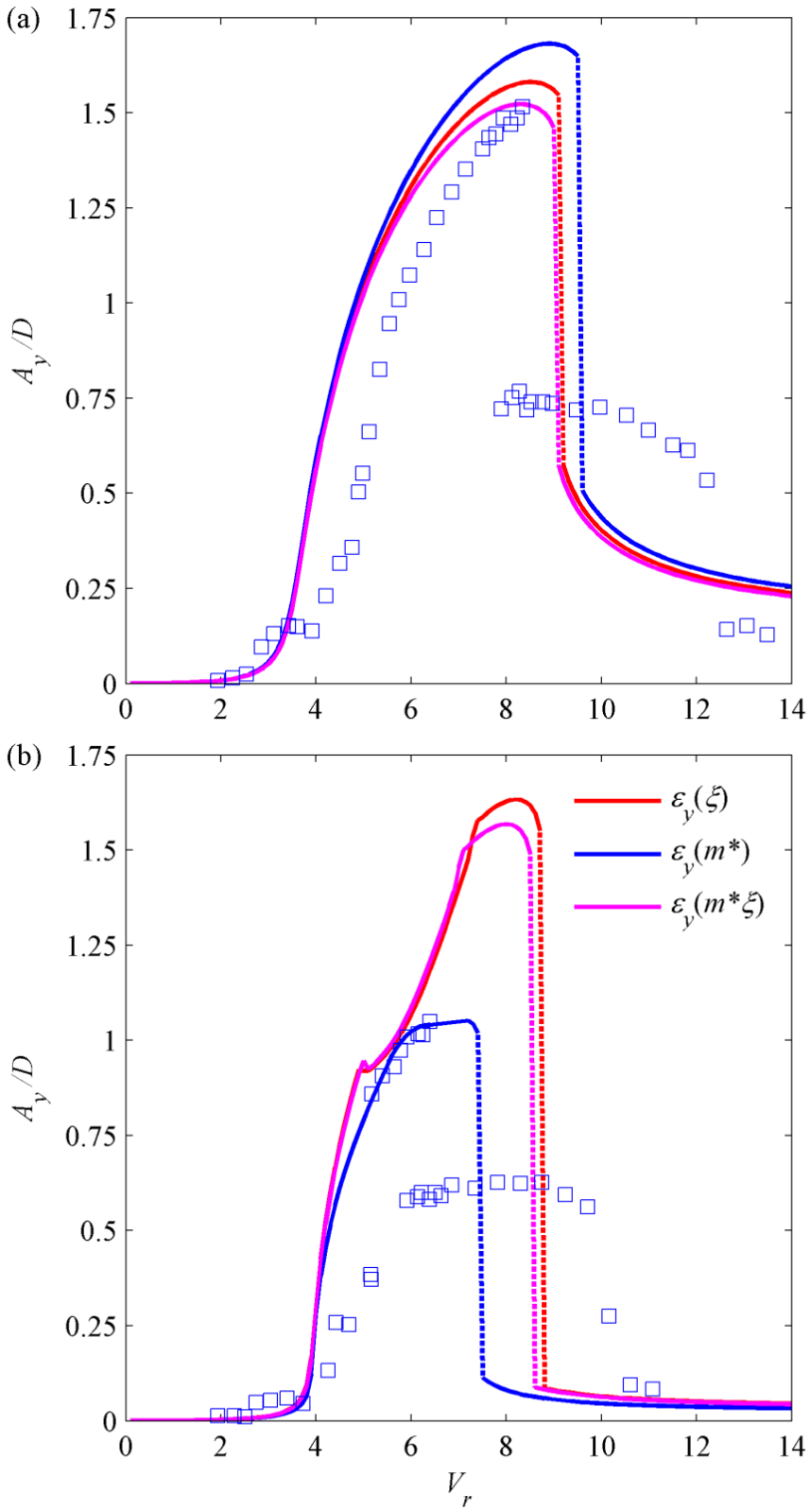

Figure 3.4: Comparison of numerical (lines) and experimental [9] (squares) cross-flow amplitudes by using the derived ε_y functions depending on mass $\varepsilon_y(m^*)$, damping $\varepsilon_y(\xi)$ and mass-damping $\varepsilon_y(m^*\xi)$: (a) m^*=2.6, ξ = 0.0025, f^*=1; and (b) m^*=7, ξ = 0.0007, f^*=1; dashed lines denote response jumps.

3.3 Sensitivity Analysis on Coefficients of the Model

Coupled CF/IL VIV responses of circular cylinders with different m^*, ξ and f^* are now parametrically investigated to highlight the effect of key parameters and several VIV features. By way of examples, experimental input data [9, 11, 30, 76] whose Reynolds numbers are within the sub-critical flow regimes are considered. A reference set of coefficients and parameters in the computation is based on $\varepsilon_x = 0.3$, $\Lambda_x = \Lambda_y = 12$, $\alpha_x = \alpha_y = \beta_x = \beta_y = 0.7$, and the $\varepsilon_y(m^*)$ function deduced from the calibration in Section 3.2.

3.3.1 Influence of geometrical nonlinearities and *f**

The influence of cylinder geometrical nonlinearities is first discussed based on the experimental input data of Stappenbelt *et al*. [76] with low $m^* = 2.36$ and $\xi = 0.006$ (Figure 3.3 (a)). The cubic nonlinearities in Eqs. (3.9) and (3.11) are due to the axial stretching ($\alpha_x x^3$, $\alpha_y y^3$) and displacement coupling ($\beta_x xy^2$, $\beta_y yx^2$). Numerical A_x/D and A_y/D results are plotted in Figures 3.5 and 3.6 for f^*=1 and 2, respectively. In each f^*case, four simulation cases are performed with (i) neglected IL nonlinearities $\alpha_x=\beta_x=0$ (red lines), (ii) neglected CF nonlinearities $\alpha_y = \beta_y = 0$ (green lines), and (iii) neglected IL/CF nonlinearities $\alpha_x = \beta_x = \alpha_y = \beta_y = 0$ (pink lines), in comparison with the full coupling benchmark case (iv) with $\alpha_x = \beta_x = \alpha_y = \beta_y = 0.7$ (blue lines) and experimental results (squares). Note that experimental results in the f^*=2 case are unavailable [76].

Overall, simulation results reveal how omitting CF and/or IL nonlinearities can significantly affect the prediction of A_x/D and A_y/D, depending also on the specified f^*. With f^*=1 and $\alpha_x = \beta_x = 0$ (red vs. blue lines), the IL nonlinearities have a greater effect on A_x/D (Figure 3.5 (a)) than A_y/D (Figure 3.5 (b)). Nevertheless, both bent-to-right responses still qualitatively exhibit the hardening-spring and jump (dashed lines) behaviors as in the full-coupling and experimental cases. When $\alpha_y = \beta_y = 0$ (green vs. blue lines), it is worth remarking some quantitative as well as qualitative changes. Both A_x/D and A_y/D responses increase and appear nearly vertical with a vanishing jump, similar to a typical linear resonant damped response. As a result, the

maximum amplitudes (especially A_x/D) shift towards V_r = 5 lower than V_r = 9 in the benchmark case. By further imposing $\alpha_x=\beta_x=\alpha_y=\beta_y=0$ and comparing with the previous $\alpha_y=\beta_y=0$ case (pink vs. green lines), A_y/D appear unchanged whereas A_x/D noticeably drop. These highlight how the CF (IL) geometric nonlinearities have a significant impact on both *x* and *y* (solely *x*) responses. Overall, the $\alpha_x = \alpha_y = \beta_x = \beta_y =$ 0.7 case provides the best fit to experimental results (squares) [76].

With f^*=2, both IL/CF geometrical nonlinearities now play a significant role in both A_x/D (Figure 3.6 (a)) and A_y/D (Figure 3.6 (b)) diagrams which display distinctive dynamic scenarios amongst all the compared four cases, quantitatively and qualitatively. The maximum A_y/D occurs with the $\alpha_y = \beta_y = 0$ case whereas the maximum A_x/D occurs with the $\alpha_x = \beta_x = \alpha_y = \beta_y = 0$ case. The combined α_y- and β_y-based terms are found to be solely responsible for a response jump as in Figure 3.5 (see blue vs. red lines). With respect to the benchmark case, A_x/D (A_y/D) amplitudes increase (slightly decrease) when varying the cylinder frequency ratio from f^*=1 (Figure 3.5) to f^* = 2 (Figure 3.6), with A_x/D diagram in the f^*=1 case displaying an emergence of a small first resonant peak around V_r = 2.5 (Figure 3.5 (a)). This is possibly due to a primary resonance between the wake and cylinder IL frequencies. Overall, the increasing f^* enhances the coupling and interaction of A_x/D and A_y/D amplitudes through system cubic/quadratic nonlinearities.

3.3.2 Influence of wake-cylinder coupling and IL wake coefficient

The influence of the acceleration coupling terms (Λ_x, Λ_y) and the IL wake coefficient (ε_x) (Eqs. 3.10 and 3.12) on the prediction of 2-D VIV response is next discussed, again based on the experimental input data of Stappenbelt *et al*. [76] with low m^* = 2.36 and ξ = 0.006. By individually varying (i) Λ_y, (ii) Λ_x and (iii) ε_x, a comparison of A_x/D and A_y/D with respect to the benchmark case ($\Lambda_y = \Lambda_x$ = 12 and ε_x = 0.3) is displayed in Figures 3.7 (a) and 3.7 (b) (i), Figures 3.7 (c) and 3.7 (d) (ii), and Figures 3.7 (e) and 7 (f) (iii), respectively.

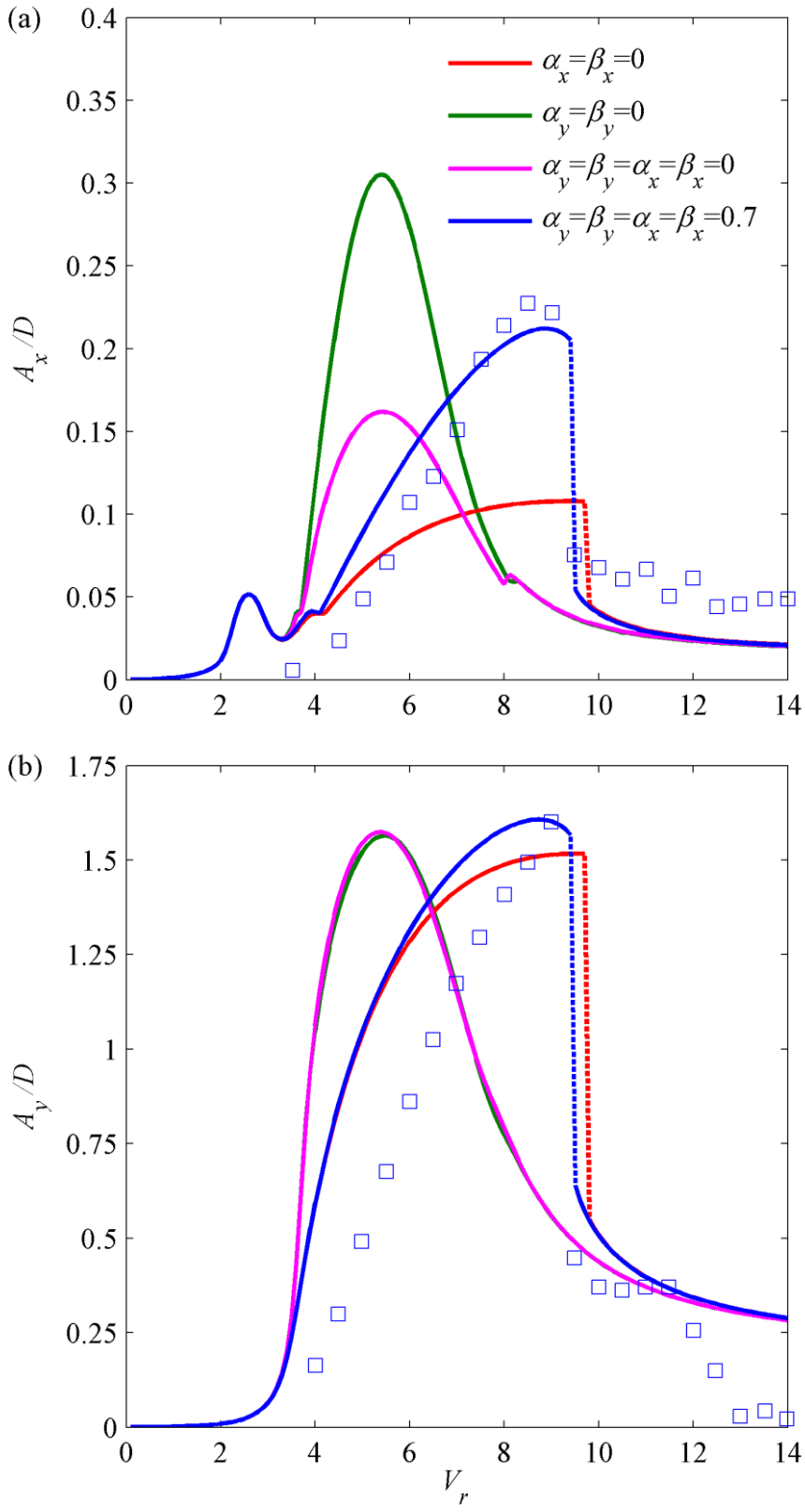

Figure 3.5: Comparison of numerical (lines) and experimental [76] (squares) amplitudes with m^*=2.36, ξ = 0.006 and f^*=1, by considering the effect of geometrical nonlinear terms: (a) A_x/D and (b) A_y/D; dashed lines denote response jumps.

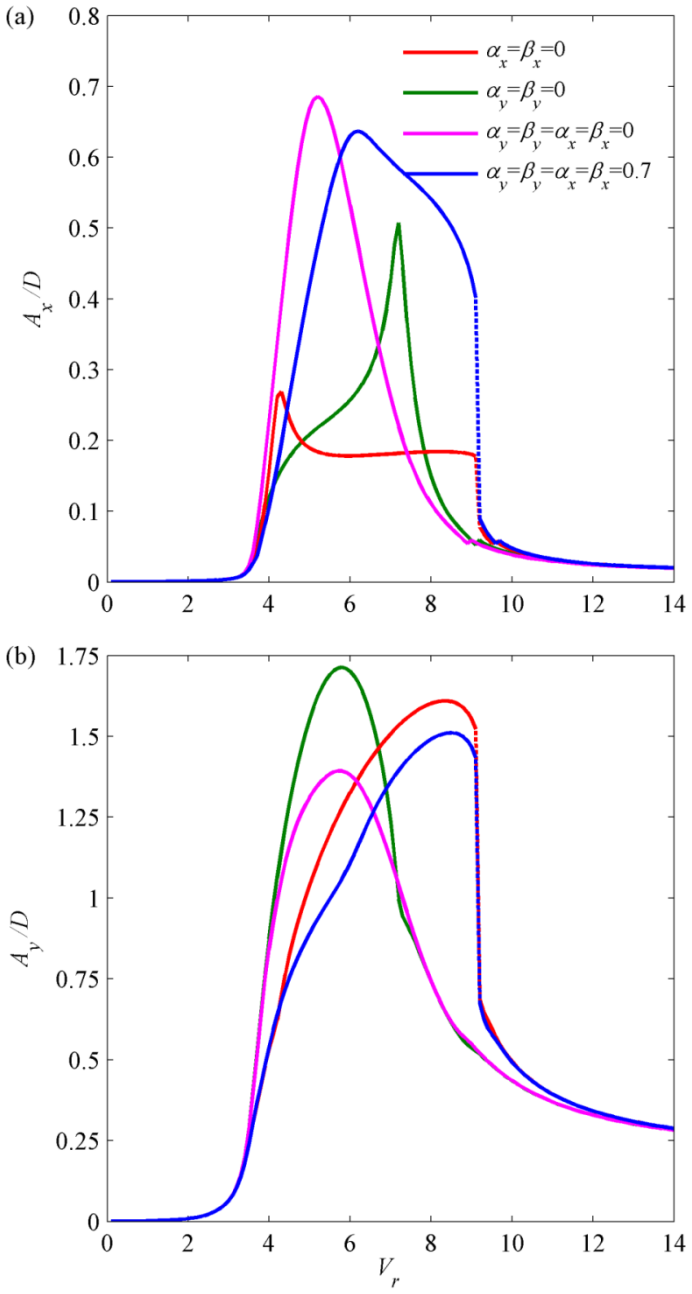

Figure 3.6: Effect of geometrical nonlinear terms based on experimental input data of [76] with m^*=2.36, ξ = 0.006 and f^*=2: (a) A_x/D and (b) A_y/D; dashed lines denote response jumps.

As Λ_y increases, it can be seen in Figures 3.7 (a) and 3.7 (b) that overall amplitudes become greater, widening the associated lock-in ranges. This highlights a role played by the CF acceleration coupling term in Eq. (3.12). On the contrary, the variation of Λ_x has a negligible effect on 2DOF amplitudes as shown in Figures 3.7 (c) and 3.7 (d). This may be attributed to the small A_x/D and, correspondingly, the negligible contribution of cylinder IL accelerations through Eq. (3.10).

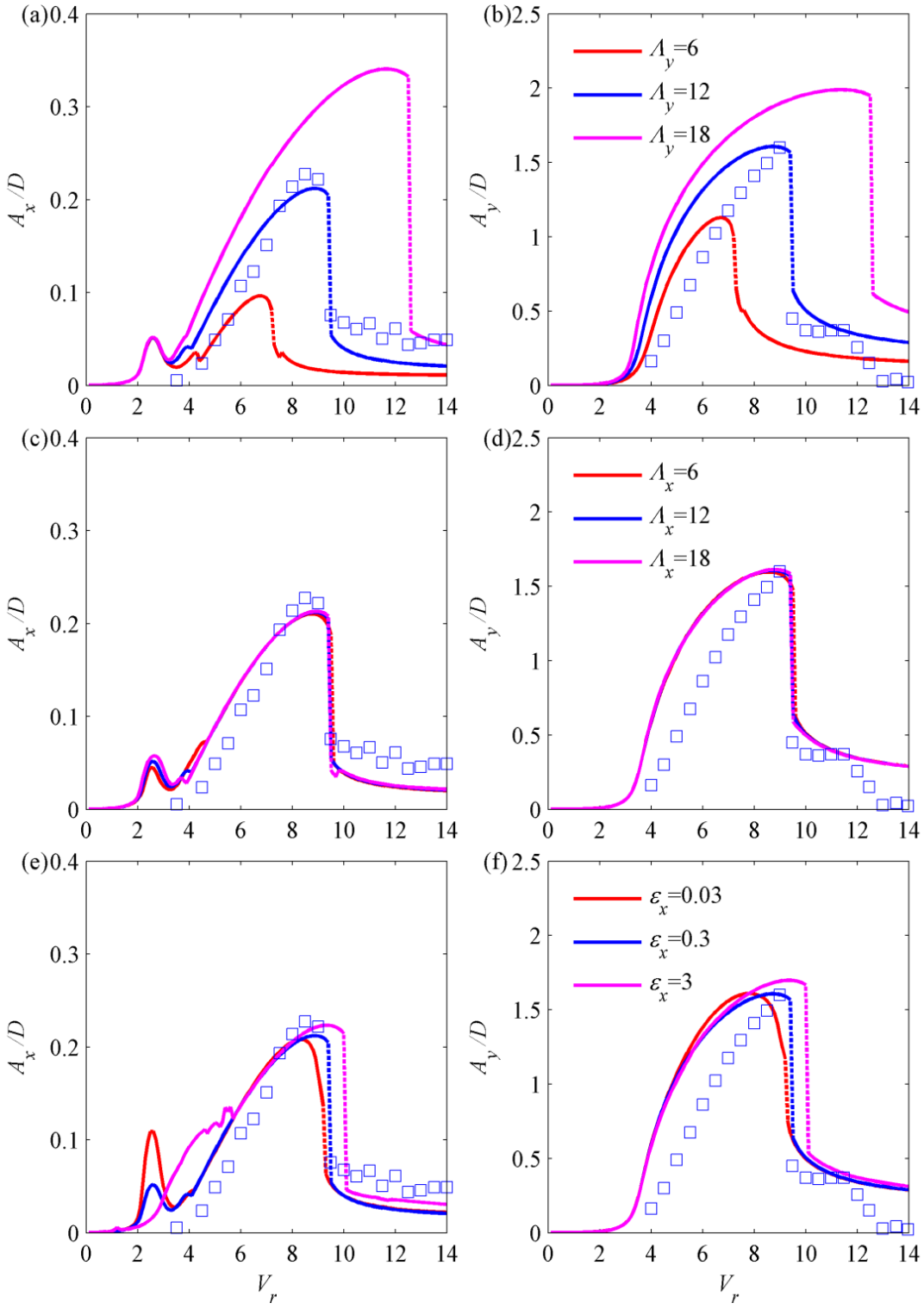

Figure 3.7: Comparison of numerical (lines) and experimental [76] (squares) amplitudes with m^*=2.36, ξ = 0.006 and f^*=1, by considering the effect of wake-cylinder coupling terms and in-line wake coefficient: (a) A_x/D and (b) A_y/D for varied Λ_y, (c) A_x/D and (d) A_y/D for varied Λ_x, (e) A_x/D and (f) A_y/D for varied ε_x; dashed lines denote response jumps.

With regard to the varying ε_x, a noticeable feature should be mentioned via Figure 3.7 (e). In particular, the numerical model predicts two resonant peaks in the IL amplitude diagram (Figure 3.7 (e)) as in Figures 3.5 (a), 3.7 (a) and 3.7 (c), with the first resonant peak occurring at a low reduced velocity range ($2 < V_r < 4$) and increasing with decreasing ε_x. The first and second peaks in Figure 3.7 (e) are reminiscent of the second and third lock-in ranges of IL oscillations, respectively, with the asymmetric vortex shedding in the cylinder wake [9, 52]. As it can be seen in this figure, variations of ε_x influence the behaviour of the system while the cylinder oscillates in the second IL lock-in range. Figure 3.7(e) also illustrates that ε_x with highest order of magnitude (ε_x=3) results in irregularities in the amplitude response in second IL lock-in range. This is mainly due to the fact that such vigorous increase of ε_x makes the dynamical system of Eqs. (3.9-3.12) disordered. And, since ε_x is mainly influential when $2<V_r<4$, such perturbation appears in the second IL lock-in range. Based on some other trial simulations (not shown herein), it has been found that such first peak would disappear if the IL wake frequency in Eq. (3.10) was set equal to the CF wake frequency in Eq. (3.12). As for the main 2DOF lock-in range ($4 < V_r < 10$) [9], numerical results in Figures 3.7 (e) and 3.7 (f) show a small ε_x effect on A_x/D and A_y/D. By comparing overall numerical and experimental results in Figures 3.5-7, the reference set of coefficients $\Lambda_x = \Lambda_y = 12$, $\varepsilon_x = 0.3$ and parameters $\alpha_x=\beta_x=\alpha_y=\beta_y=0.7$ is the preferred option to be assumed in subsequent studies.

Table 3.2 summarises the potential effect of ε_x, ε_y, Λ_x and Λ_y appearing in the wake Eqs. (3.10 and 3.12). It can be seen that both ε_y and Λ_y have a high impact on CF/IL VIV predictions, possibly owing to the associated stronger wake strength and higher amplitude in the CF direction. In contrast, both main CF/IL responses are marginally influenced by a variation of ε_x and Λ_x (Figures 3.7 (c-f)). Nevertheless, the tuning of ε_x could have a high impact on IL VIV with respect to its first-peak resonance (Figures 3.7 (e)). Empirical functions for ε_y have been established (Eqs. 3.17-19) depending on m^* and/or ξ, and it is herein recommended to vary ε_y in the numerical prediction and perform a sensitivity analysis when using the proposed nonlinear wake-structure oscillators. Of course, new experimental tests, calibrations

and validations are needed in order to improve Eqs. (3.17-19) and capture the influence of other important parameters such as f^* and Reynolds number, in terms of both quantitative and qualitative aspects of coupled CF/IL VIV.

Table 3.3: Potential effect of empirical coefficients on 2DOF VIV response prediction.

Coefficients	Potential Effect	
	Cross-flow VIV	In-line VIV
ε_x	Low	High
ε_y	High	High
Λ_x	Low	Low
Λ_y	High	High

3.4 Prediction of IL Oscillations

The proposed wake-structure oscillator model is now used to predict and investigate the effect of m^* and ξ on the IL response. In accordance with CF responses shown in Figures 3.2 (a) and 3.2 (b) (with varying ξ), Figures 3.3 (a) and 3.3 (b) (with varying m^*), Figures 3.4 (a) and 3.4 (b) (with varying $m^*\xi$), the predicted IL responses in the f^*= 1 case are now displayed against experimental results of [30], [76] and [9] in Figures 3.8 (a) (ξ= 0.002, 0.02), 3.8 (b) (m^* = 2.36, 3.68) and 3.8 (c) ($m^*\xi \approx$ 0.0064, 0.0048), respectively.

Overall, there is a good agreement between numerical and experimental results which display two coexisting resonant peaks and maximum A_x/D values about 0.2-0.3 being much smaller than the maximum A_y/D in the range of 1.2-1.5. However, for system with low ξ= 0.002, the numerical model in Figure 3.8 (a) further reveals a third intermediate peak with the highest amplitude (V_r = 6) (see also the corresponding orbital motion in Figure 3.16 (b)). The IL amplitudes as well as associated lock-in ranges are seen to decrease with increasing ξ (Figure 3.8 (a)), m^* (Figure 3.8 (b)) and $m^*\xi$ (Figure 3.8 (c)), in the same way as the CF amplitudes (Figures 3.2-4).

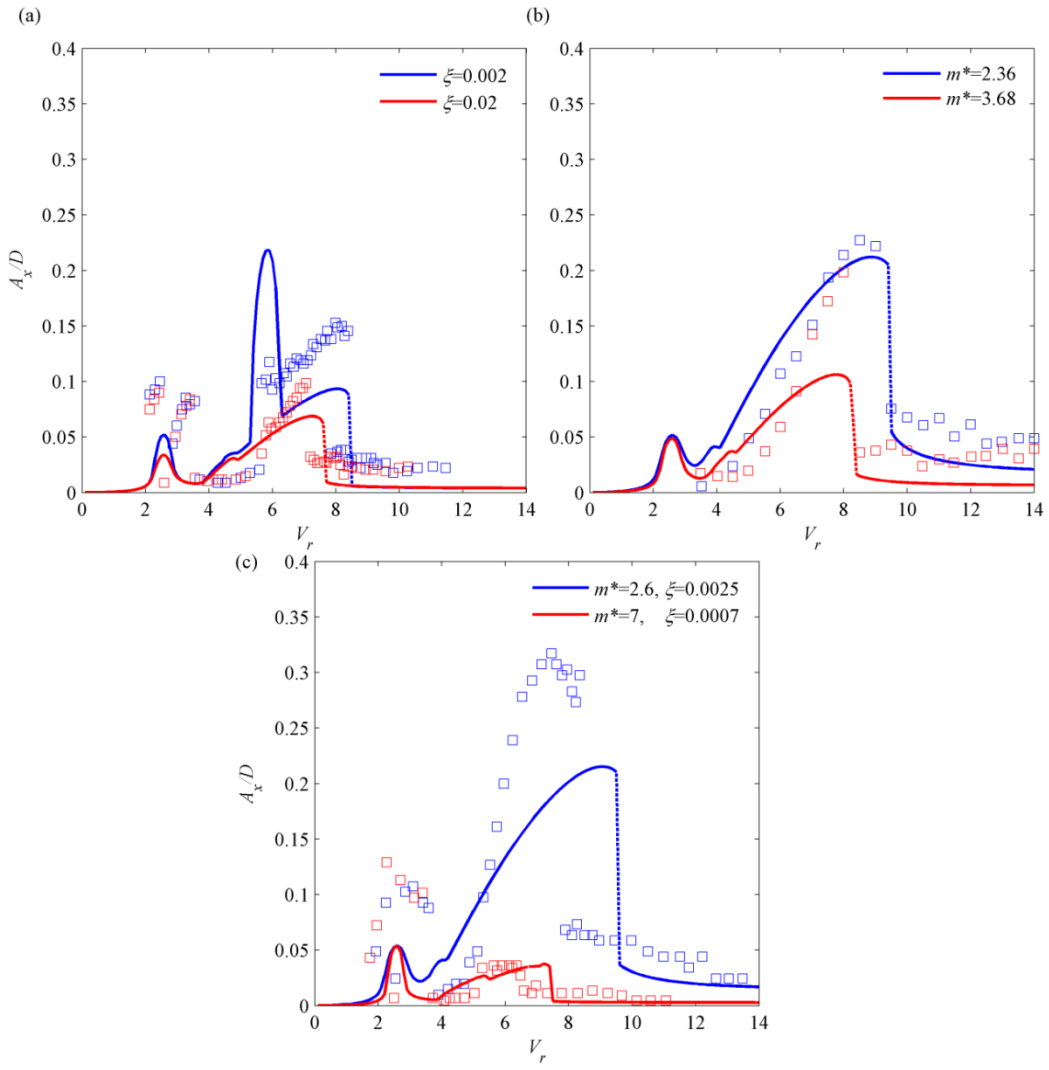

Figure 3.8: Comparison of numerical (lines) and experimental (symbols) in-line amplitudes with (a) m^*=5.4 and f^*=1 [30], (b) ξ = 0.006 and f^*=1 [76], (c) varied $m^*\xi$ and f^*=1 [9]: experimental results associated with numerical results by same colors; dashed lines denote response jumps.

3.5 Influence of Fluid-Structure Parameters

In this section, through numerical predictions of the semi-empirical model of Eqs. (3.9-12), the effects of influential physical parameters, including m^*, ξ and $m^*\xi$, at different V_r and f^* are studied and discussed.

3.5.1 Effects of $m^*\xi$ parameter and discussion

The influence of mass-damping on the 2DOF VIV response is demonstrated via the so-called Griffin plots. As it was explained in Chapter 2, over the last three decades, researchers had a discussion on whether the combined mass-damping, viz.

the Skop–Griffin parameter $S_G=2\pi^3 St^2 m^*\xi$ [6] could reasonably collapse different peak (typically CF) amplitude data of different cylinders in the Griffin plots [36]. For the 2DOF VIV study, observations in [9, 30] and Section 3.3 reveal the response dependence on both m^* and ξ. To further justify this, experimental input data of [30], [76] and [11] are considered; the associated maximum attainable (A_{ym}/D) and IL (A_{xm}/D) amplitudes numerically (solid lines) and experimentally (symbols) obtained are compared in Figures 3.9 (a) and 3.9 (b), respectively. In addition, the associated reduced velocities at which A_{ym}/D and A_{xm}/D take place (V_{rym}, V_{rxm}) are also drawn vs. S_G in Figures 3.9 (c) and 3.9 (d), respectively. Note that, for each given m^* = 2.5 and 7, S_G is varied by altering ξ, and both f^* =1 and 2 are considered. Experimental results of [11] were based on $m_x^* \neq m_y^*$ (in the range of 3.3-5.7) and $\xi_x \neq \xi_y$ (in the range of 1.1-6.2 %), with f^* ranging from 1 to 1.90, those of [30] were based on m^* = 5.4 (varying ξ) and f^* = 1, and those of [76] were based on ξ = 0.006 (varying m^*) and f^* = 1.

It can be seen in Figures 3.9 (a) and 3.9 (b) that, for a specific S_G, numerical results based on different fixed m^* and corresponding ξ are different. Both A_{ym}/D and A_{xm}/D decrease with increasing S_G (or ξ), with f^* = 2 (f^* = 1) case entailing greater IL (CF) responses for both assigned m^*. The difference in A_{xm}/D results between f^* = 1 and 2 cases is quite outstanding particularly for the lower m^*=2.5: these emphasize a combined role played by both f^* and m^* captured by the simulation model. The predicted A_{xm}/D may reach a large value of 0.7 for a low S_G with f^* = 2. Apart from A_{ym}/D and A_{xm}/D, f^* also does affect their corresponding V_{rym} and V_{rxm} as shown in Figures 3.9 (c) and 3.9 (d), respectively. While V_{rym} of A_{ym}/D and V_{rxm} of A_{xm}/D in the case of m^* = 2.5 and f^* = 1 are comparable, those in other cases appear significantly different. The increasing f^* tends to reduce V_{rym} for both m^*. However, V_{rxm} increases (decreases) as f^* increases for m^* = 7 (2.5) due to the greater first-peak (second-peak) A_{xm}/D, see, e.g., in the case of m^* = 7 vs. 2.6 Figure 3.8 (c). As for the experimental comparison, the associated A_{ym}/D and A_{xm}/D, as well as V_{rym} and V_{rxm}, also decrease with increasing S_G either due to the increasing ξ [30] or m^* [76], except some cases in Figures 3.9 (b), 3.9 (c) and 3.9 (d) where $m_x^* \neq m_y^*$ and $\xi_x \neq \xi_y$ [11].

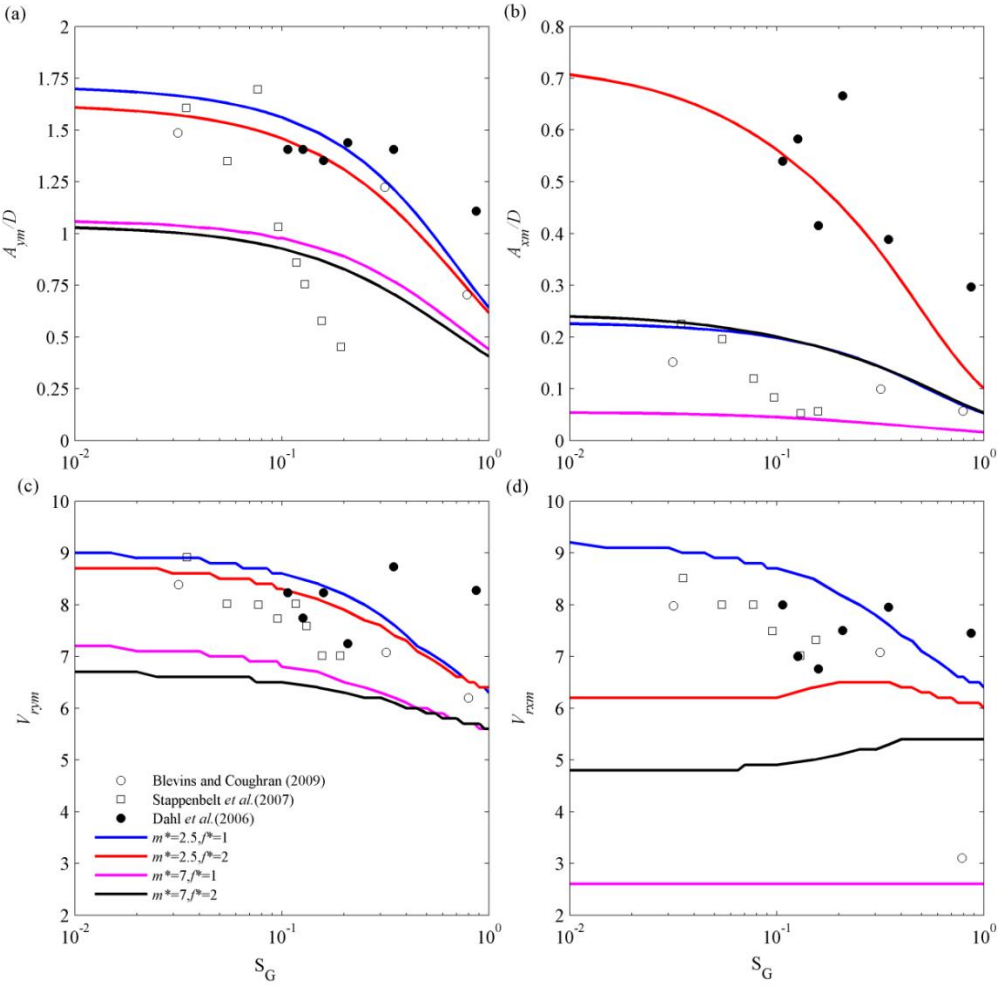

Figure 3.9: Comparison of numerical (lines) and experimental (symbols) maximum attainable amplitudes (a, b) and corresponding reduced velocities (c, d) versus S_G for given m^*=2.5 and 7, f^*=1 and 2: (a) and (b) are so-called Griffin plots.

3.5.2 Effects of mass ratio

3.5.2.1 Maximum attainable amplitudes at constant S_G

By paying attention to the effect of m^*, a different scenario to show the capability of the proposed model in the 2DOF VIV prediction is illustrated in Figure 3.10 (f^*=1) based on two experimental input data of [9] with fixed S_G = 0.0064 and [76] with variable S_G. Experimental results in [9] indicated that, at m^* higher than 6, the variation of m^* does not affect the peak amplitudes in both directions. Our numerical results agree with this but only for the IL response shown in Figure 3.10 (b). For the CF response shown in Figure 3.10 (a), numerical and experimental [9] results are in good agreement within the range $2 < m^* < 6$ showing the decreasing

A_{ym}/D with increasing m^*; for $m^* > 6$, the former yet continues predicting the decreasing A_{ym}/D, instead of a nearly-constant A_{ym}/D by [9]. Although such difference occurs at high m^*, both numerical A_{ym}/D and experimental results of [76] are in good quantitative agreement throughout the considered m^* range. As for A_{xm}/D, Figure 3.10 (b) shows a good correspondence of overall numerical-experimental comparisons.

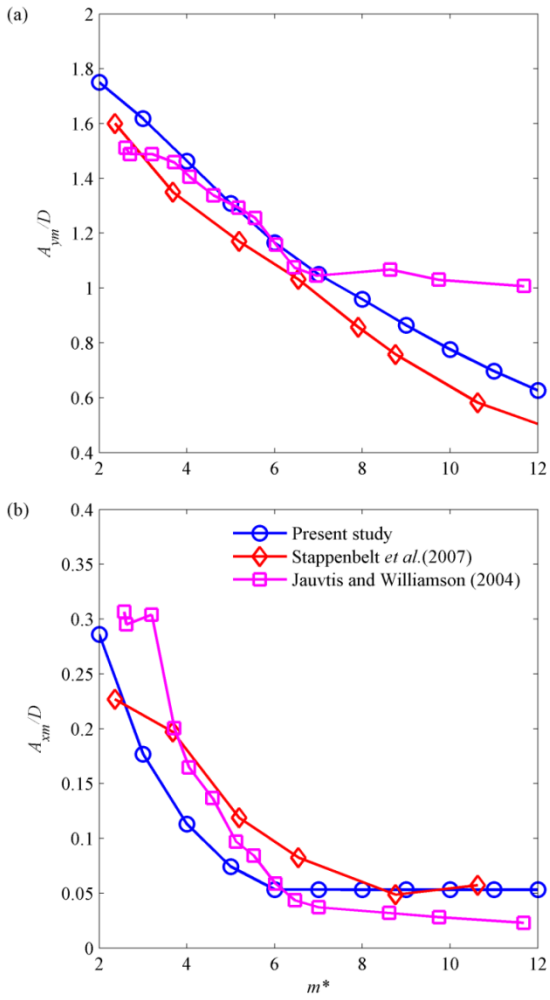

Figure 3.10: Comparison of numerical and experimental maximum attainable (a) cross-flow and (b) in-line amplitudes with varying m^*.

3.5.2.2 Combined effects of m^* and f^*

To further appreciate the combined effect of m^* and f^* on the 2DOF VIV, Figure 3.11 portrays the amplitudes (A_y/D and A_x/D) vs. varying V_r and m^* for a given $f^* = 1$ (Figures 3.11 (a) and 3.11(c)) and $f^* = 2$ (Figures 3.11 (b) and 3.11 (d)), respectively. The fixed low $\xi = 0.001$ is exemplified. It can be summarised that, by

decreasing m^*, overall A_y/D and A_x/D and associated lock-in ranges increase whereby A_{ym}/D and A_{xm}/D occur at higher V_r. With $f^* = 2$, very large A_x/D amplitudes of nearly 1.2 are found in a low m^* range. This is a precarious circumstance since typical marine cylindrical structures have a low mass-damping and their natural frequencies could be tuned such that $f^* = 2$ [111]. In essence, as for a very low $m^* \approx 0.5$, the model with $f^* = 1$ predicts the unbounded lock-in domain whose A_y/D and A_x/D persist throughout the considered V_r range (Figures 3.11 (a) and 3.11 (c)). This occurrence of "resonance forever" [27] is in good qualitative agreement with recent experimental results [9]. However, A_y/D and A_x/D tend to decline at higher V_r in the $f^*=2$ case as shown in Figures 3.11 (b) and 3.11 (d).

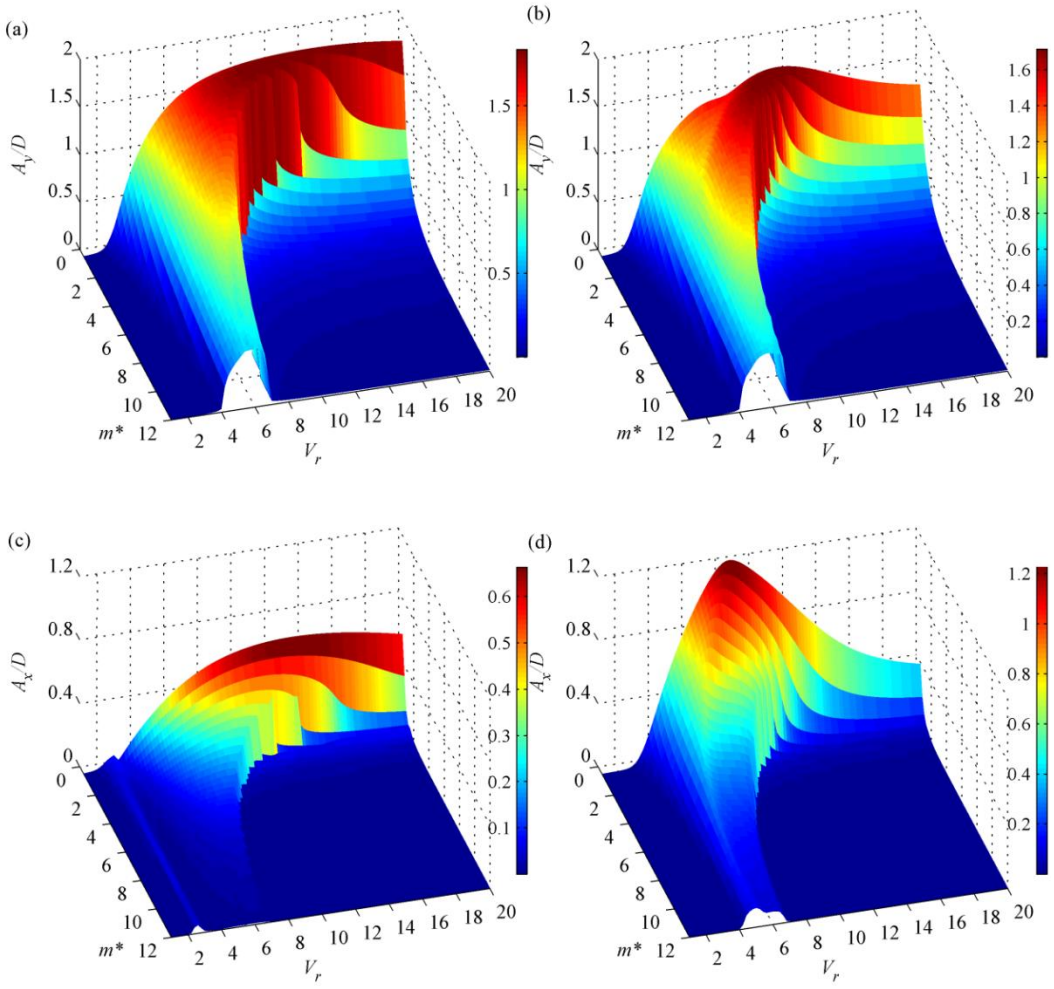

Figure 3.11: Three-dimensional plots of (a, b) cross-flow and (c, d) in-line amplitudes with varied m^* and V_r for given ζ=0.001: f^*=1 (a, c) and f^*=2 (b, d).

3.5.2.3 Lock-in forever and oscillation frequency function

In previous section it was shown that when f^*=1 the model predicts unbounded lock-in ranges at low mass ratios. This lock-in-forever phenomenon is further discussed in this section. In so doing, the contour plots of obtained A_y/D and A_x/D are displayed as a function of both V_r and m^* in Figure 3.12 (a) and 3.12 (b), respectively, with the assigned $\xi_x=\xi_y$ = 0.001 and f^*=1. The onset and the end of the synchronization based on the available *Y*-only VIV experimental data [117] is also given in Figure 3.12 with circle symbols. This synchronization boundary corresponds to the lower-branch amplitude response: it becomes narrower as m^* increases but extends to infinity as m^* decreasingly approaches the critical value of about 0.54 in the case of *Y*-only VIV [117] and 0.52 in the case of 2DOF VIV [9]. Numerical prediction results reveal their good qualitative agreement with experimental results since the lower branches of both A_y/D and A_x/D cease to exist at a very low m^* (< 0.5), thereby resulting in an unbound lock-in domain with their extended upper-branch responses beyond $V_r \approx 25$. Below the critical mass, the predicted A_y/D and A_x/D may achieve a high value greater than 1.8 and 0.75, respectively. On the contrary, for high $m^* > 6$, the contribution from A_x/D response is seen to be negligible as in, e.g., [76].

An analytical function to describe the dominant oscillation frequency (ω) at the maximum response is now derived by also accounting for the m^* effect. To this end, first the oscillation frequencies at maximum attainable amplitudes are evaluated via Matlab FFT algorithm which performs Discrete Fourier Transformation on the time histories of the numerical results. The same algorithm will be utilised in next chapters to evaluate dominant frequencies, frequency responses and higher harmonic components of the responses. When both A_{ym}/D and A_{xm}/D are simultaneously attained, the corresponding values of ω and Ω (i.e. Ω=StV_r) can be evaluated and plotted versus m^* as shown by the sub-figure embedded in Figure 3.12 (a). From these plots, it can be seen that $\omega \approx \Omega$, thus such an assumption (i.e. $\omega=\Omega$) can be made when analytical solutions at the lock-in condition are of interest (e.g. see Section 5.2). Consequently, a best-fit function – describing the oscillation frequency

at the maximum response of the upper or super-upper branch – may be derived, as a function of m^*, as

$$\omega \approx 1.25\sqrt{\frac{m^* + 1}{m^* - 0.52}} \tag{3.20}$$

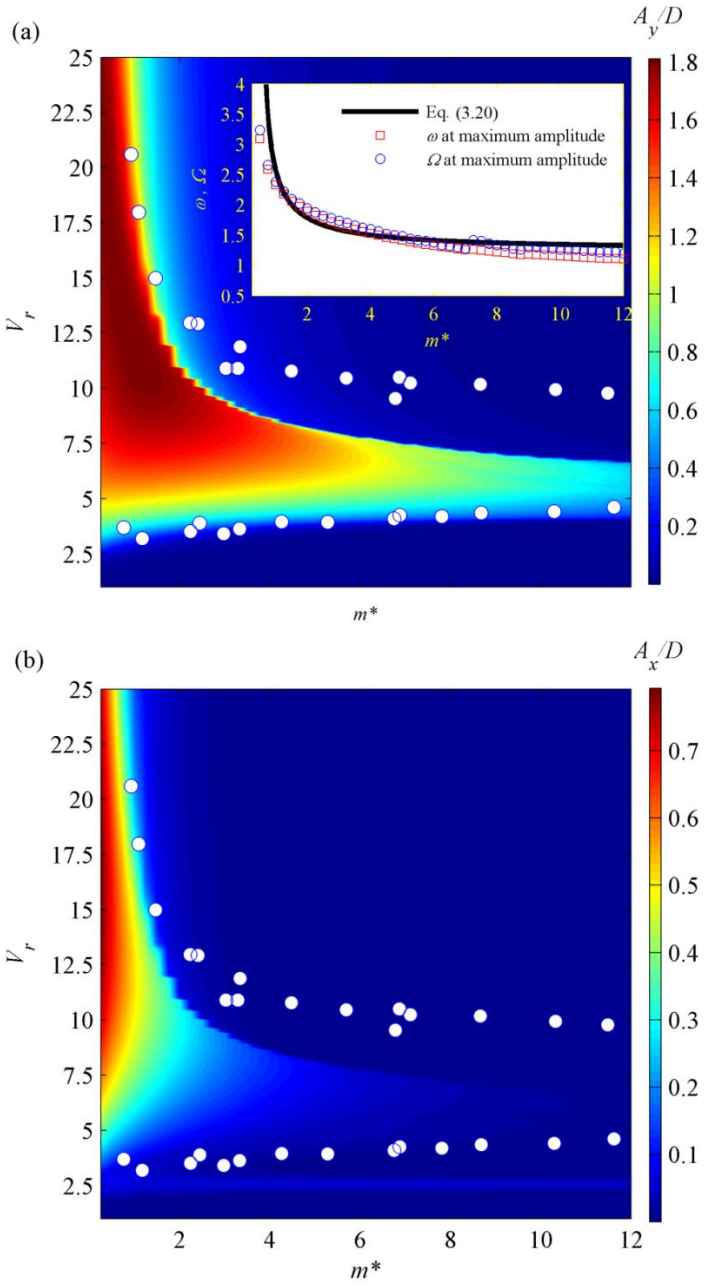

Figure 3.12: Contour plots of (a) A_y/D and (b) A_x/D as functions of m^* and V_r compared with experimental lock-in ranges (circles); plots of ω and Ω as a function of m^* is also depicted in (a).

The above equation is proposed by taking a form similar to the function given by Govardhan and Williamson [117] which described the lower-branch response.

3.5.2.4 Prediction of wake mode regimes

Possible description of the vortex shedding modes in the wake of the oscillating cylinder is now discussed through the numerically obtained transverse responses with varying m^*. The contour plots of A_y/D with specified $\xi_x = \xi_y = 0.001$ and $f^*=1$ (Figure 3.13 (a)) or $f^*=2$ (Figure 3.13 (b)) are drawn as a function of V_r. The associated A_x/D plots can be found in Figure 3.11. In Figure 3.13 (a), the free-vibration A_y/D results are overlaid onto the map of vortex mode regimes produced by Morse and Williamson [123] based on a *Y*-only forced vibration study with a fixed Re = 4000. This map has a higher resolution than the pioneering work of Williamson and Roshko [45], with 2S denoting "two single vortices" and 2P denoting "two vortex pairs". Note that a small region of the overlapping 2S and 2P modes found in [123] is not herein considered.

In Figure 3.13 (a), it is seen that A_y/D and the associated synchronization ranges increase as m^* decreases, with a clear vertical jump from the upper ($m^*>6$ and $A_y/D \leq 1$) or super-upper ($m^*<6$ and $A_y/D>1$) branch to the lower branch when increasing V_r. These features are in good qualitative agreement with recent 2DOF VIV experimental results [9, 76]. A critical line [123] which divides between the 2S and 2P mode regimes passes through the free-vibration response, revealing a reduced V_r range of the 2S mode as m^* (A_y/D) is decreased (increased). For $A_y/D \leq 1$, the vortex mode of the upper branch may be 2P and, for $A_y/D>1$, the vortex mode of the supper-upper branch may be either 2P or 2T (two of vortex triplets) [9]. On the other hand, the P+S mode – which has been defined from the forced-vibration tests [23] – does not correspond to any of the predicted free-vibration amplitudes.

With respect to the jump phenomenon, two new critical (dotted blue) lines are herein proposed in Figure 3.13 (a) ($f^*=1$) and 3.13 (b) ($f^*=2$), one corresponding to the amplitude response just before the jump and the other joining the onset of the lower-branch response, in all m^* cases. The region between these two curves which have no VIV responses is herein suggested to be a non-synchronized wake mode pattern in the case of 2DOF free vibration. As f^* is increased, it is demonstrated in

Figure 3.13 that the no-synchronization region becomes narrower as m^* is decreased. This highlights the coalescence of the super-upper and lower branches towards the critical m^* where the jump disappears, leading to the so-called 'resonance forever' defined in [27]. Nevertheless, more relevant experimental and flow visualization studies are needed to be carried out and confirm this observation.

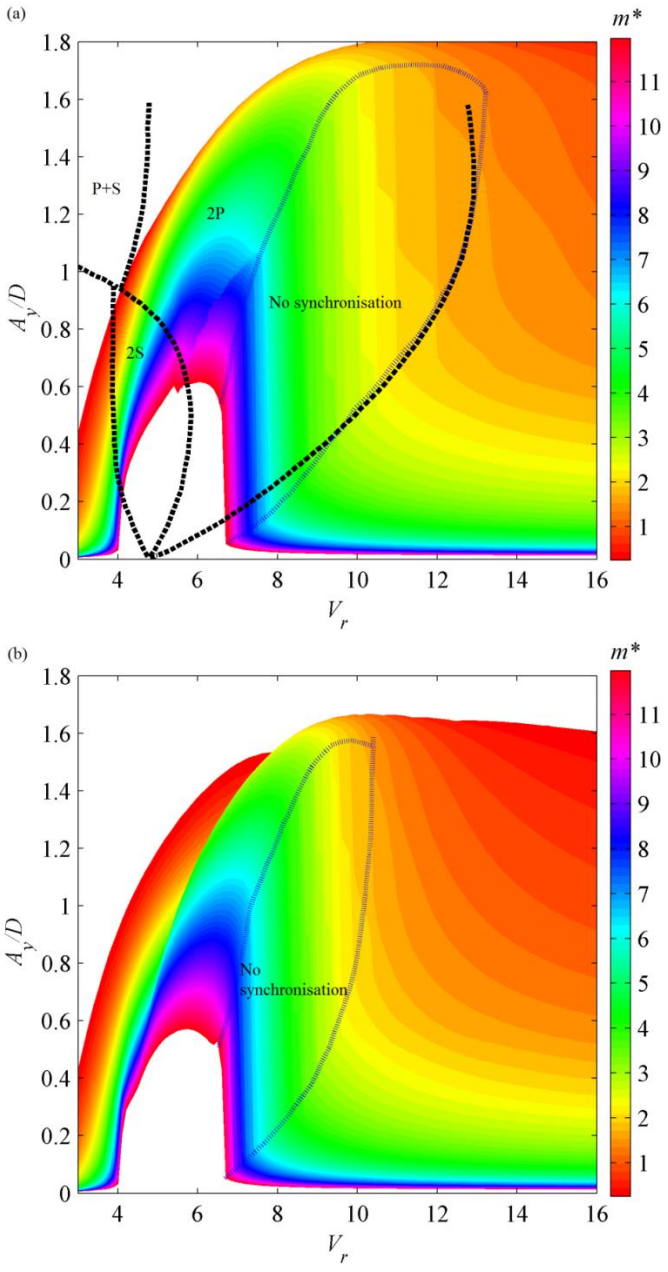

Figure 3.13: Contour plots of A_y/D as functions of m^* and V_r representing the no-synchronisation regions in the case of (a) f^*=1 and (b) f^*=2; maps of vortex-shedding patterns of Morse and Williamson [123] are also overlaid in (a).

3.5.3 Effects of damping ratio

It is now interesting to highlight the combined effect of damping and frequency ratio through Figure 3.14 which plots A_x/D based on m^*=2.5 (3.14 (a), 3.14 (c)) and 7 (3.14 (b), 3.14 (d)), and f^*=1 (3.14 (a), 3.14 (b)) and 2 (3.14 (c), 3.14 (d)).

It is well known that, for f^*=1, CF VIV response (A_y/D) decreases as m^* or ξ increases. This is in agreement with Figures 3.14 (a) and 3.14 (b) for A_x/D. This effect seems to be more evident in the second-peak (or main lock-in) range than in the first-peak range. For f^*=2, overall A_x/D amplitudes in Figures 3.14 (c) and 3.14 (d) become larger than those in Figures 3.14 (a) and 3.14 (b), respectively, in agreement with results presented in section 3.5.2 with varying m^* for a given ξ. As for A_y/D, results are found to be less influenced by the increasing f^*.

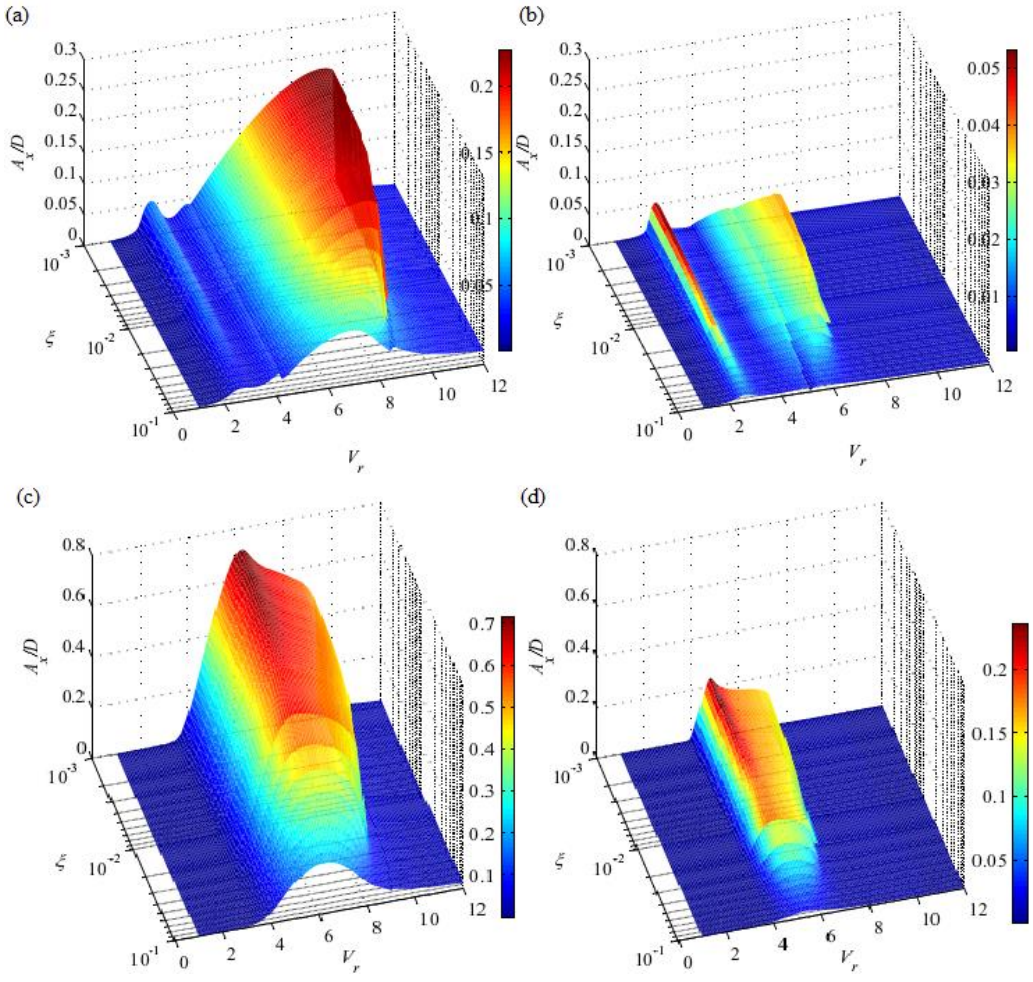

Figure 3.14: Effect of mass ratio (m^*), damping ratio (ξ) and natural frequency ratio (f^*).

3.6 2-D Trajectories and Figures-of-eight

It is now of theoretical and practical importance to construct a 2-D (x-y) trajectory describing the relationship of cylinder IL/CF oscillations based on the proposed numerical model. In so doing, VIV simulations within the last ten cycles yielding steady A_{ym}/D and A_{xm}/D amplitudes are considered for specific V_r values in the neighborhood of hysteresis.

3.6.1 Numerical terms influencing Fo8 trajectories

Corresponding to Figures 3.3 (a) and 3.8 (b) based on the input data of [76] with m^* = 2.36, ξ = 0.006 and f^* = 1, the 2-D orbital motions in the cases of increasing (blue lines) and decreasing (red lines) flow velocities are drawn in Figures 3.15 (a), 3.15 (b) and 3.15 (c) for V_r = 8, 9.25 and 9.45, respectively. Overall, the trajectories exhibit the so-called figures of eight highlighting a tuned 2:1 resonance condition of IL/CF oscillating frequencies although inputting f^* = 1. For a specific V_r, depending on the initial conditions, identical (Figure 3.15 (a)) or two (Figures 3.15 (b) and 3.15 (c)) figures of eight may coexist in different increasing/decreasing V_r cases and with phase differences.It is now worth investigating which numerical terms play an influential role in the figure-8 appearance. Two cases are considered for V_r = 9.45 in comparison with the increasing flow case in Figure 3.15 (c): firstly, the lift and drag wake frequencies in Eqs. (3.10) and (3.12) are assumed to be equal depending on the Strouhal frequency; secondly, the relative velocities between the flow and the cylinder are discarded thereby neglecting the quadratic nonlinear terms in the right-hand side of Eqs. (3.9) and (3.11). The associated simulation results are plotted with solid and dotted lines in Figure 3.15 (d), respectively. It can be seen that both quantitative and qualitative discrepancies occur when neglecting the quadratic nonlinearities: the IL (CF) amplitudes considerably diminish (slightly increase) without showing the Fo8 feature. On the other hand, a similar Fo8 remains even though the wake IL frequency has been altered. Other simulation V_r cases also agree with these observations. This highlights that as the 2:1 resonance and thus the figure of eight is generally associated with quadratic nonlinearities, neglecting the latter ($p\dot{y}, q\dot{y}$) – which capture the wake-cylinder interactions – can lead to the uncoupled IL/CF VIV result.

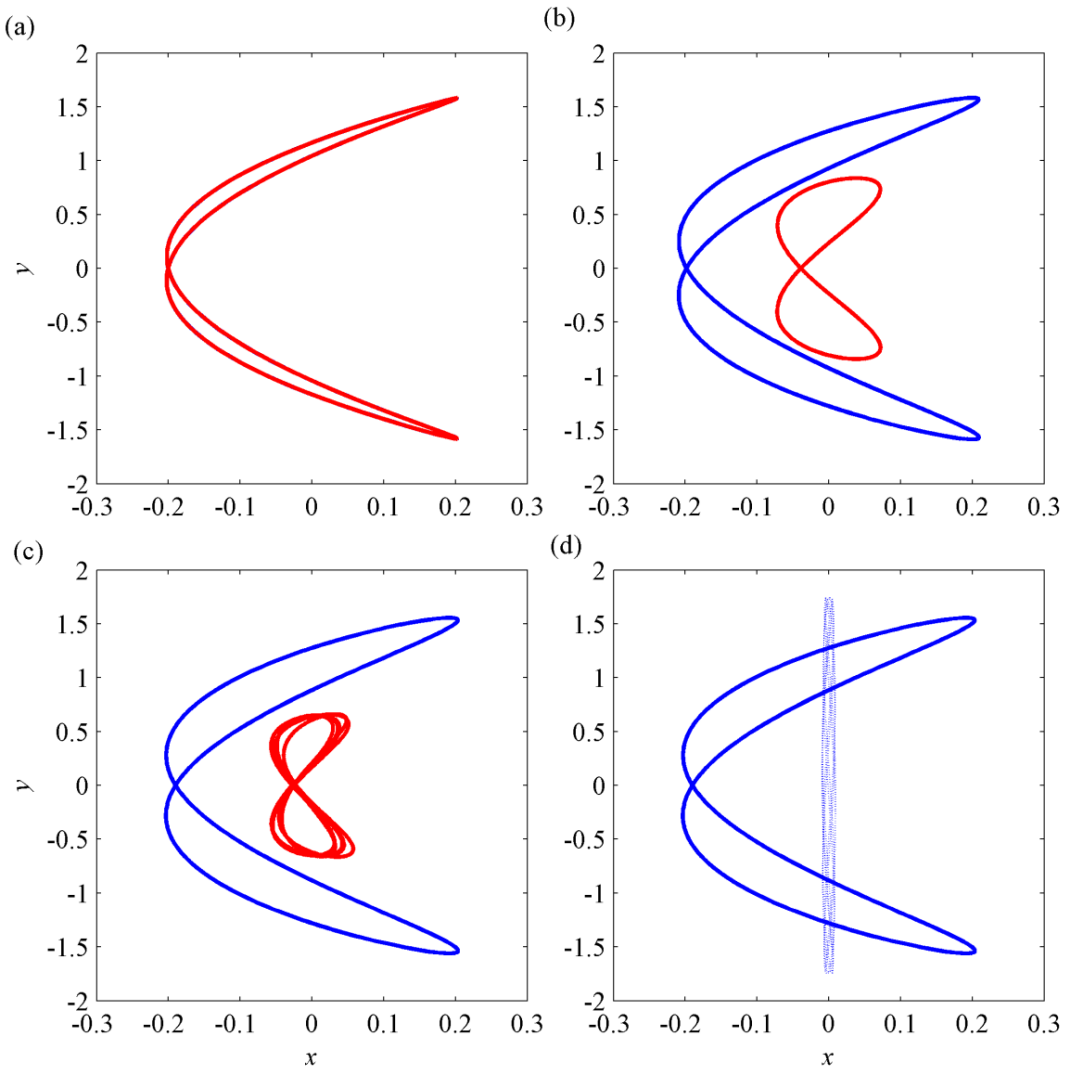

Figure 3.15: 2-D trajectories based on experimental input data of [76] with m^* = 2.36, ξ = 0.006 and f^* = 1: (a) V_r = 8, (b) V_r = 9.25, (c) V_r =9.45, with blue (red) lines denoting increasing (decreasing) V_r case; (d) V_r = 9.45 with assumed equal cross-flow/in-line wake frequencies (blue lines) and neglected quadratic nonlinear terms (dotted lines).

3.6.2 Orbital motion with *f** effect

The influence of f^* on the *x*-*y* trajectories is illustrated in Figure 3.16 based on the experimental input data of [30] with m^* = 5.4 and ξ = 0.002 (Figures 3.2 (a) and 3.8 (a)). Simulation results with V_r = 4.5, 6, 7 and 7.6 are visualized in Figure 3.16 (a-d), respectively, with six successive f^* = 1, 1.2, 1.4, 1.6, 1.8 and 2. It can be seen that, regardless of f^*, most of the *x*-*y* trajectories entail figure-8 orbits. They distinguish themselves depending on the corresponding IL/CF amplitudes, initial

conditions, relative phases and the nearness or tuning of 2:1 resonant oscillating frequencies. These dual resonances confirm some recent experimental 2-D VIV results in [11, 77]. The non-figure-8 trajectories are also found in some cases, for instance in Figure 3.16 (b) with V_r = 6 and f^* = 1 or Figure 3.16 (d) with V_r = 7.6 and f^* = 1.2. Recently in [124], elliptic *x*-*y* trajectories have been found and explained to be subject to a strong structural coupling.

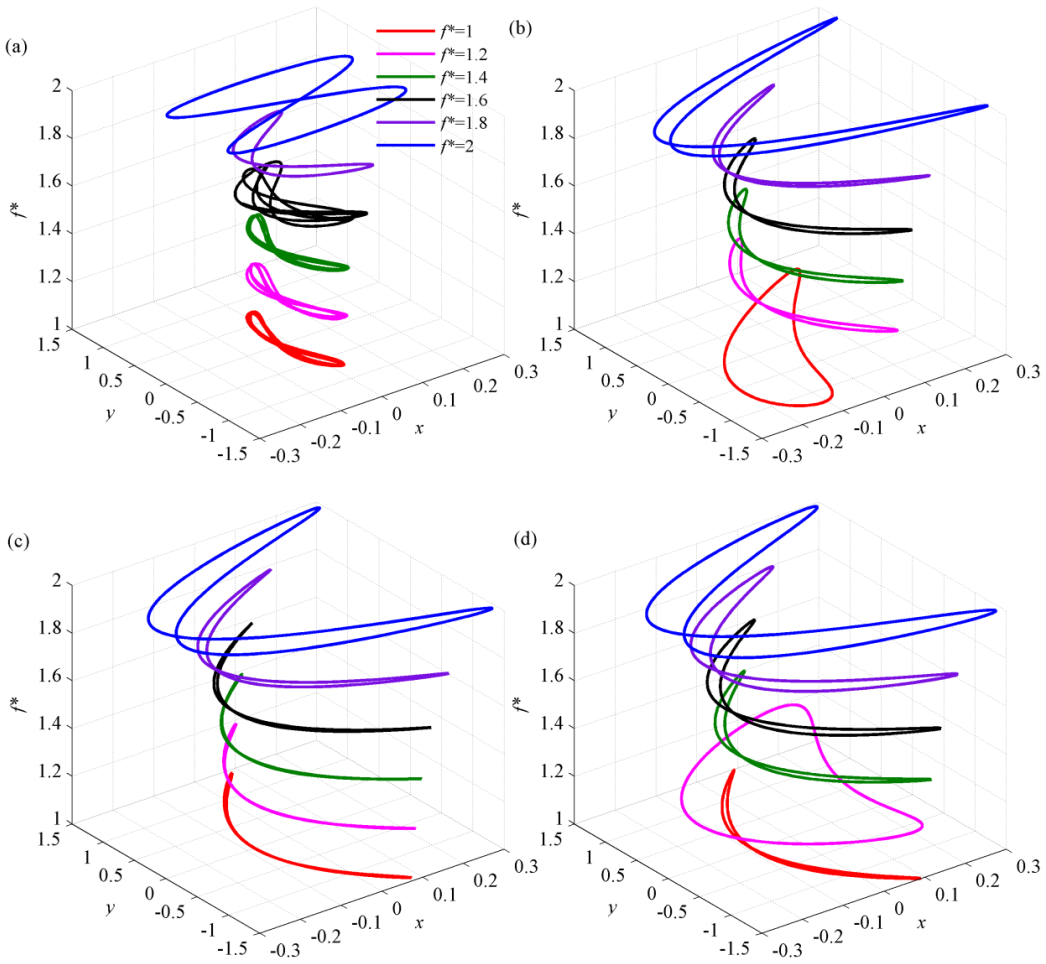

Figure 3.16: 2-D trajectories based on experimental input data of [30] with m^* = 5.4, ξ = 0.002 and various f^*: (a) V_r = 4.5, (b) V_r = 6, (c) V_r =7; (d) V_r =7.6.

The Fo8 trajectory of *x*-*y* motion takes place as a result of a dual 2:1 resonance and its pattern may change with a variable *x*-*y* phase difference as V_r is varied. This implies a differing fluid-structure interaction or energy transfer mechanism between the oscillating cylinder and the hydrodynamic forces. Figure 3.17 illustrates the

normalized x-y phase difference $\theta_{xy} = (\theta_x - 2\theta_y)/\pi$ with $0 \leq \theta_{xy} < 2$ – as well as the corresponding Fo8 – as a function of V_r. To also highlight the effect of f^*, numerical and experimental [10] results with $f^* = 1$ and $f^* \approx 2$ are compared. Note that the associated m^* and ξ values are different: numerical results are based on $m_x^* = m_y^* = 1.4$, $\xi_x = 0.010$ and $\xi_y = 0.016$ (for both $f^* = 1$ and 2) whereas experimental results are based on $m_x^* = 3.3$, $m_y^* = 3.8$, and $\xi_x = \xi_y = 0.022$ (for $f^* = 1$), and $m_x^* = 5$, $m_y^* = 5.7$, $\xi_x = 0.025$ and $\xi_y = 0.062$ (for $f^* \approx 2$). To distinguish different orbital motions, the acronym CCW or CW is also given within 3 regions in Figure 3.17 to specify the counterclockwise or clockwise Fo8 path, respectively, following the motion of the top part of the figure of eight [10].

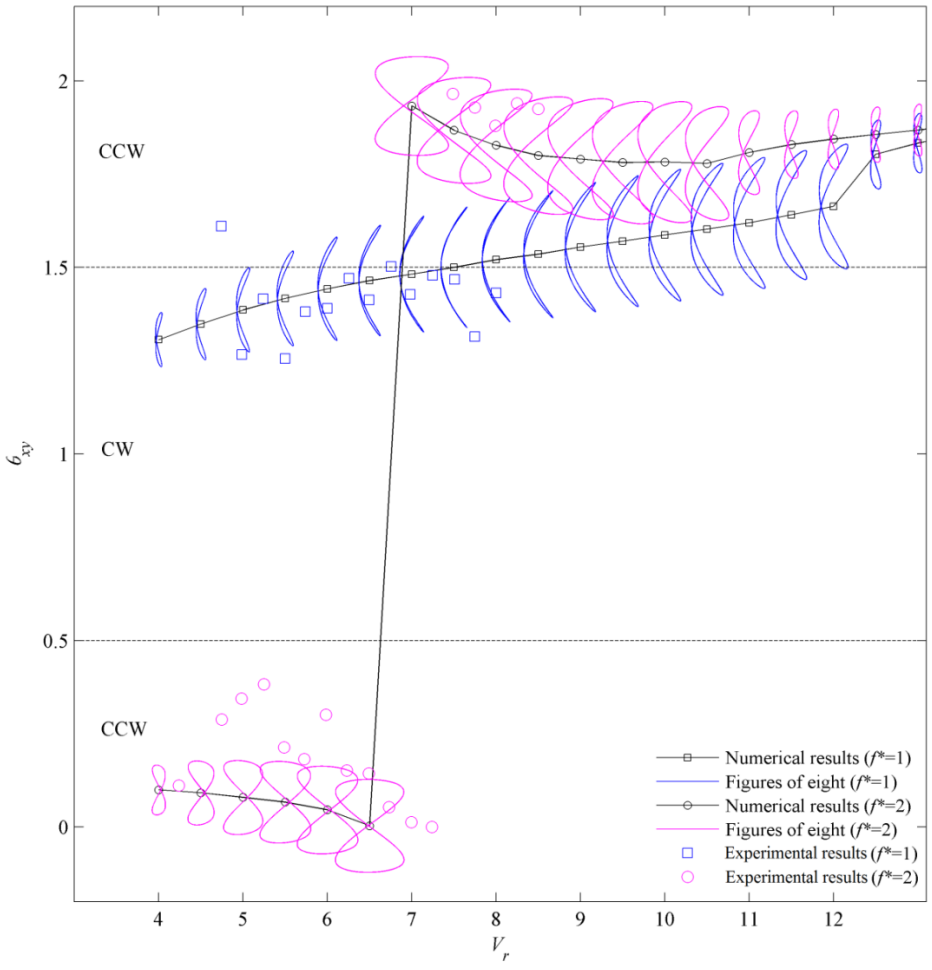

Figure 3.17: Comparison of numerical and experimental [10] x-y phase differences θ_{xy} with f^*=1 and 2 and associated figures of eight: CCW (CW) denotes counter-clockwise (clockwise) orbit.

With increasing V_r, Figure 3.17 exhibits a good qualitative agreement between numerical (lines with symbols) and experimental (symbols) θ_{xy} results, by also showing the influence of f^*. In the f^*=1 case, there is a smooth transition from a CW figure of eight ($1 < \theta_{xy} < 1.5$) to a CCW one ($\theta_{xy} > 1.5$) around $V_r \approx 7$ (see the line with squares) although the tips of all the Fo8 trajectories face towards downstream throughout the V_r range. A crescent-shaped orbit with $\theta_{xy} = 1.5$ occurs at $V_r \approx 7$. On the other hand, in the f^*=2 case, a sudden jump of θ_{xy} (see the line with circles) occurs numerically at $V_r \approx 6.5$ or experimentally at $V_r \approx 7.2$ while maintaining the CCW pattern ($\theta_{xy} < 0.5$ or $\theta_{xy} > 1.5$). Such jump of θ_{xy} leads to a change in the Fo8 lobes from pointing upstream ($\theta_{xy} < 0.5$) to downstream ($\theta_{xy} > 1.5$). Overall, the comparisons shown in Figure 3.17 highlight the capability of the numerical model in qualitatively predicting the variable CW/CCW Fo8 patterns and their transitions with varying V_r and f^* along with the validation of obtained θ_x and θ_y to be used in the subsequent studies in following chapters.

3.7 Conclusions

An advanced model for predicting a 2DOF coupled CF/IL VIV of a flexibly-mounted circular cylinder in a uniform steady flow has been developed, calibrated and validated. The ensuing dynamical system is based on double Duffing-van der Pol (structural-wake) oscillators with the two structural equations containing cubic/quadratic nonlinear terms. The cubic nonlinearities describe the geometrical coupling of CF/IL displacements excited by hydrodynamic lift/drag forces whereas the quadratic nonlinearities allow the wake-cylinder interactions resulting from the relative velocities of the incoming flow and the oscillating cylinder. Some wake empirical coefficients have been identified based on calibration with experimental results in the literature, and new analytical functions accounting for the dependence of VIV on a physical mass and/or damping parameter have been established. These relationships would be useful for a future numerical implementation and experimental VIV analysis. The derived low-order model captures several fundamental VIV characteristics including 2DOF lock-in, hysteresis phenomena and Fo8 trajectories tracing the periodically coupled IL/CF oscillations with their tuned two-to-one resonant frequencies. These figures of eight appear regardless of the

specified ratio of cylinder IL to CF natural frequencies. By making use of a newly-derived empirical formula, the predicted CF/IL VIV amplitudes and associated lock-in ranges compare well with several experiment results for cylinders with low/high mass or damping ratios, by also revealing the occurrence of critical mass whereby maximum amplitudes exhibit the unbounded lock-in scenario. Overall, the parametric investigations highlight the important effect of structural geometrical nonlinearities through new displacement coupling terms and the IL-to-CF natural frequency ratio of the freely-oscillating cylinder.

Chapter 4

Experimental Investigations of Coupled CF/IL VIV of Rigid Cylinders

Slender offshore structures possess multiple natural frequencies in different directions which can lead to different resonance conditions when undergoing vortex-induced vibration (VIV). This chapter presents an experimental and numerical investigation of a two-degree-of-freedom VIV of a flexibly mounted circular cylinder with variable IL-to-CF natural frequency ratio. A mechanical spring-cylinder system, achieving a low equivalent mass ratio in both IL and CF directions, is tested in a water towing tank and subject to a uniform steady flow in a sub-critical Reynolds number range of about 2×10^{3}-5×10^{4}. Experimental results for six measurement datasets are compared with numerical results in terms of response amplitudes, lock-in ranges, oscillation frequencies, time-varying trajectories and phase differences of CF/IL motions. Moreover, comparisons of the newly-obtained and published experimental results are carried out and discussed. Various patterns of figure-of-eight orbital motions associated with dual two-to-one resonances are observed experimentally as well as numerically.

4.1 Experimental Arrangement and Test Facility

For further validation of the model proposed in Chapter 3 and more investigations on less-studied aspects of combined CF/IL VIV of rigid cylinders, e.g. the effects of f^*, a set of experimental studies are conducted. These experiments are performed in the towing tank at the Kelvin Hydrodynamics Laboratory (KHL) of the University of Strathclyde, Glasgow, UK. The characteristics of this experimental facility are explained as follows.

4.1.1 Towing tank and its components

As it was mentioned before, the experiment is conducted in a towing tank which simulates the effects of approaching fluid flow via towing the structure of interest in a tank filled with water. The towing tank of the University of Strathclyde is one of the leading facilities of its kind in the UK with a rich history of performing accurate industrial and academic experimental investigations. A schematic representation of the tank is illustrated in Figure 4.1(a). As it can be seen in this figure, the towing tank consists of four major parts of the (i) water tank (ii) carriage, (iii) wavemaker and (iv) beach.

The water tank has a length of 76 m and is 4.6 m wide. The depth of water, depending on the test requirements can vary from 0.5-2.3 m. The tank is filled with water with a normal temperature of 20^0C. Figure 4.1(b) shows a wide view of the water tank. As shown in Figure 4.1(c), the carriage is mounted on the water tank. This self-propelled carriage can provide towing speeds up to 4 m/s and its acceleration can be increased up to 1 m/s^2. To simulate unsteady hydrodynamic loadings, high-acceleration oscillatory movements or complex flow velocity profiles, a sub-carriage is mounted and implemented onto the carriage which provides such condition. In this experimental study, carriage velocities up to 0.6 m/s are considered.

The KHL is equipped with a state-of-art wavemaker which consists of four paddles which can be adjusted vertically. The wavemaker can generate regular and random waves of up to 0.6m height. Since this thesis deals with VIV of circular cylinders subjected to uniform flows, the wavemaker is not applied in this test.

Figure 4.1(d) shows four paddles of the wavemaker. The beach is primarily designed to absorb and prevent reflections of generated waves. To allow conducting experiments in different water depths, the beach is vertically moveable. Figure 4.1(e) shows the wave-absorbing beach of the KHL.

Figure 4.1: Towing tank of the Kelvin Hydrodynamic Laboratory (a) schematic representation, (b) water tank, (c) carriage, (d) wavemaker and (e) beach of the towing tank.

4.1.2 Experimental test rig

A new experimental test rig for the study of 2DOF VIV of a flexibly mounted, smooth and rigid circular cylinder subject to a uniform steady flow has been developed for use in the KHL towing tank. The design of this rig was motivated by a recent collaborative work conducted at the University of Sao Paulo, Brazil [125]. As the schematic drawing of Figure 4.2 shows, the rig consists of a long pendulum which via a low-friction universal joint is suspended from a stiff metal frame and a rigid cylinder is attached to its other end. Furthermore, four linear springs (two in IL and two in CF direction) connect the pendulum to the frame and provide restoring forces for the system. More detailed specification of each of these parts is described in following.

4.1.2.1 Test cylinder

Figure 4.3 shows the test cylinder adopted in the present study. This cylinder is made of thick-walled cast nylon tube, having an outer diameter (D) of 114 mm, a fully submerged length (L_c) of 1.037 m and a dry weight of 10.85 kg. Commonly, to prevent the effects of end conditions and maintain the two-dimensionality of vortex-shedding, end-plates are attached to test cylinders. However, for configurations such as the one used in this study, the bottom of the tank can be considered as a very long end-plate and no end-plates are attached to the test cylinder [30, 76, 125]. Moreover, in this experiment, the lower end of the cylinder is located 50 mm from the bottom of the tank, and the upper end is located 50 mm beneath the static free surface. Such lower end condition was deemed to produce a negligible effect on the peak amplitudes [126]. Finally, the aspect ratio (L_c/D) of the cylinder is about 9 being comparable to L_c/D in some recent studies [9, 76, 127].

4.1.2.2 Long aluminium pendulum

The upper end of the test cylinder is connected to a long aluminium pendulum with the total length of about 4.1 m (L_p) and weight of 13.25 kg. The total length of the system (L_p+L_c) is chosen to minimize the pendulum motion effects. In other words, the pendulum effect on the uniformity of the local flow field is believed to be insignificant since the maximum roll and pitch angles of the cylinder about the universal joint were found to be only about 2 degrees in all tests. Figures 4.4(a-d)

depict the aluminium pendulum used in this experimental study and its lower and upper ends connected to the test cylinder and the universal joint, respectively. The universal joint will allow the pendulum to undertake low-damping combined CF/IL oscillations.

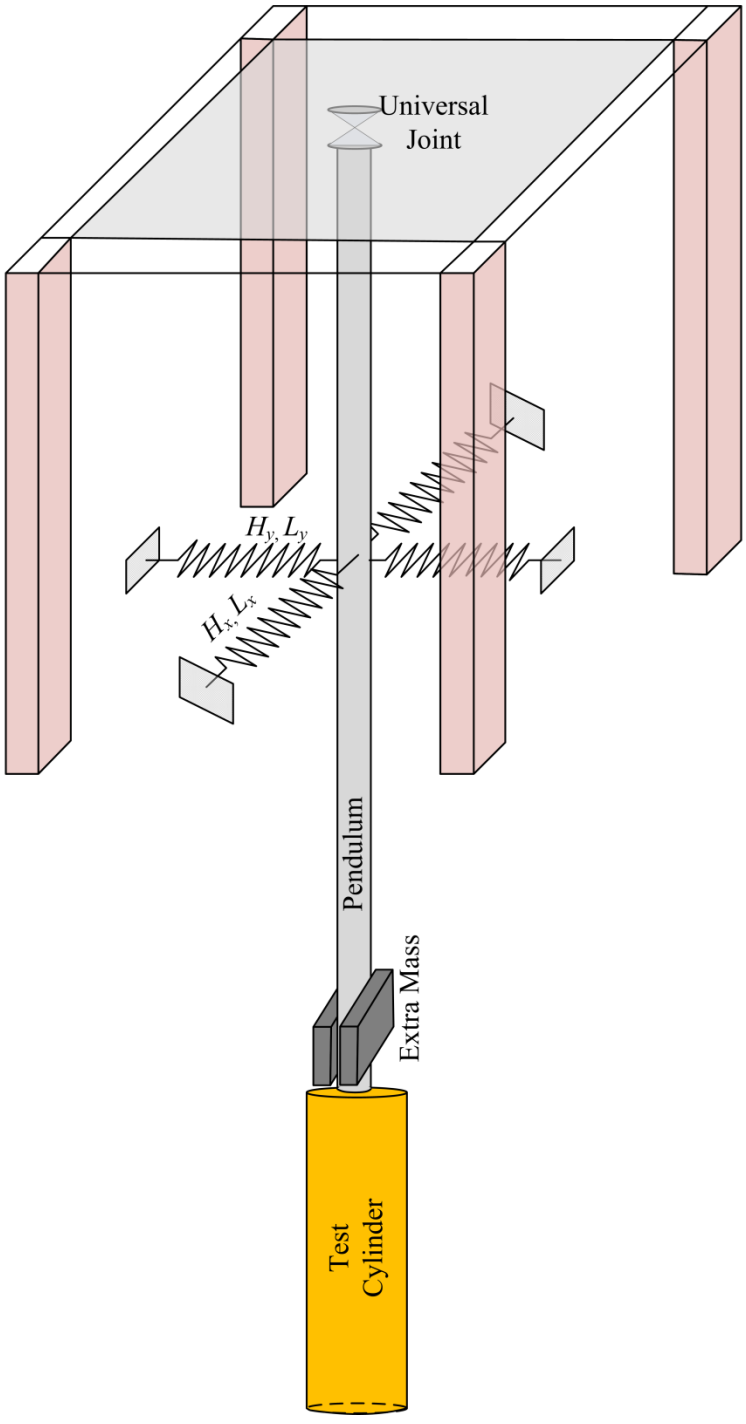

Figure 4.2: Schematic representation of the test rig.

4.1.2.3 Extra masses

To change the mass ratio of the model, lumped masses are attached to the pendulum. These masses are mounted on the pendulum close to the test cylinder to produce maximum moment of inertia and above the water surface to avoid unexpected contact with water. Figure 4.5 shows how these masses are installed. In this study, lumped masses of the total weight of 30kg are added to the system whose mass ratio along with those of other tests will be shown in next Sections.

Figure 4.3: Test cylinder from different angles.

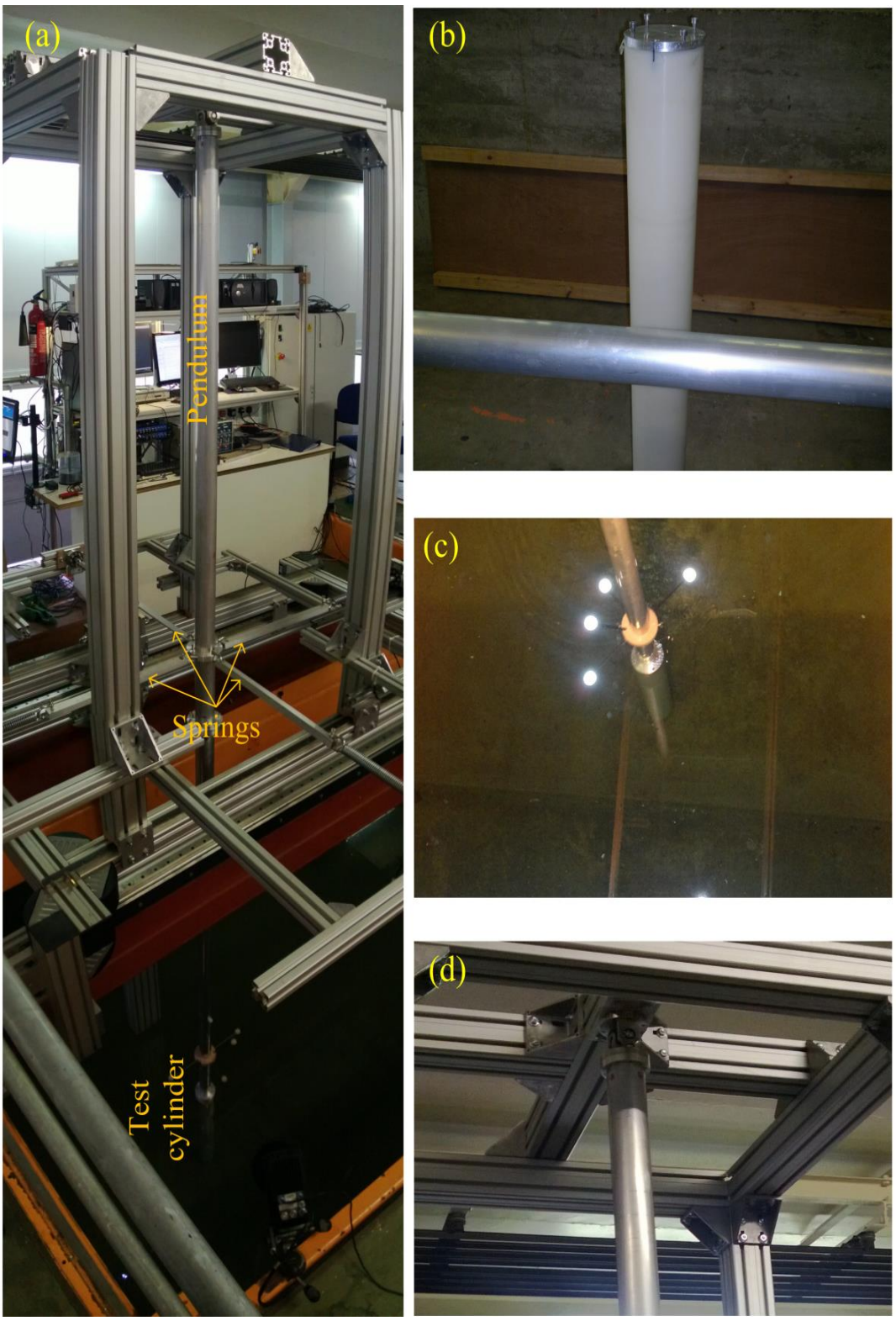

Figure 4.4: Aluminium pendulum; (a) panoramic photo of the aluminium pendulum hanged from the supporting frame; (b) aluminium pendulum (horizontal) compared to the test cylinder (vertical); (c) bottom end of the pendulum; (d) top end of the pendulum.

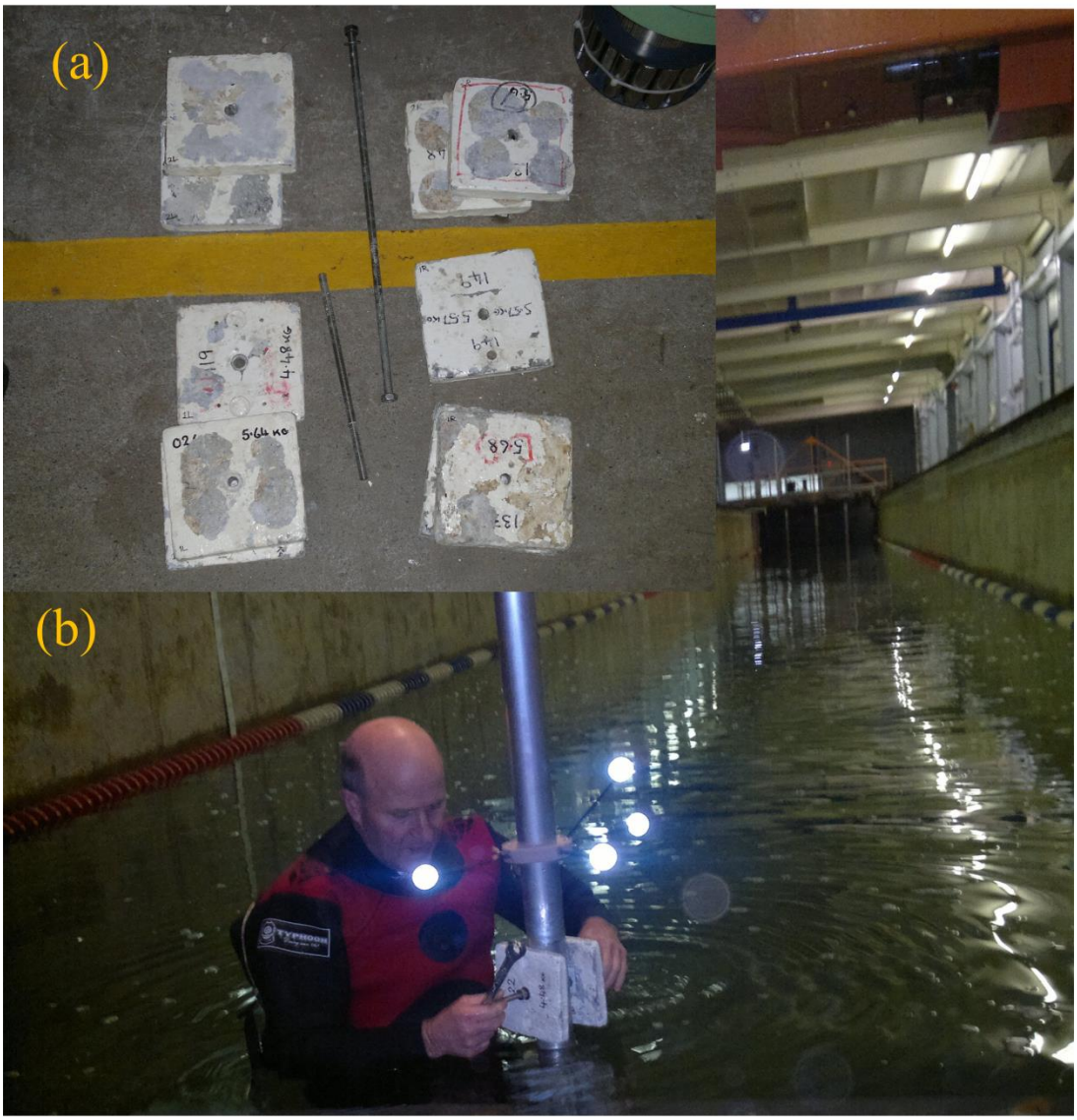

Figure 4.5: (a) Extra masses; (b) attaching extra masses to the pendulum.

4.1.2.4. Linear tensile coil springs

The main objective of this experimental study is to study the effects of f^* variations on 2DOF VIV of an elastically mounted rigid cylinder. Variations of f^* are achieved through the utilisation of different sets of spring. Figure 4.6 shows the springs used in this study and their position on the test rig. These springs are selected in a way that their stiffness satisfies the desired f^*. To this end, first, using Newton's second law of motion and after basic calculations [128], the natural frequency of a system similar to the one depicted in Figure 4.2 is analytically obtained as:

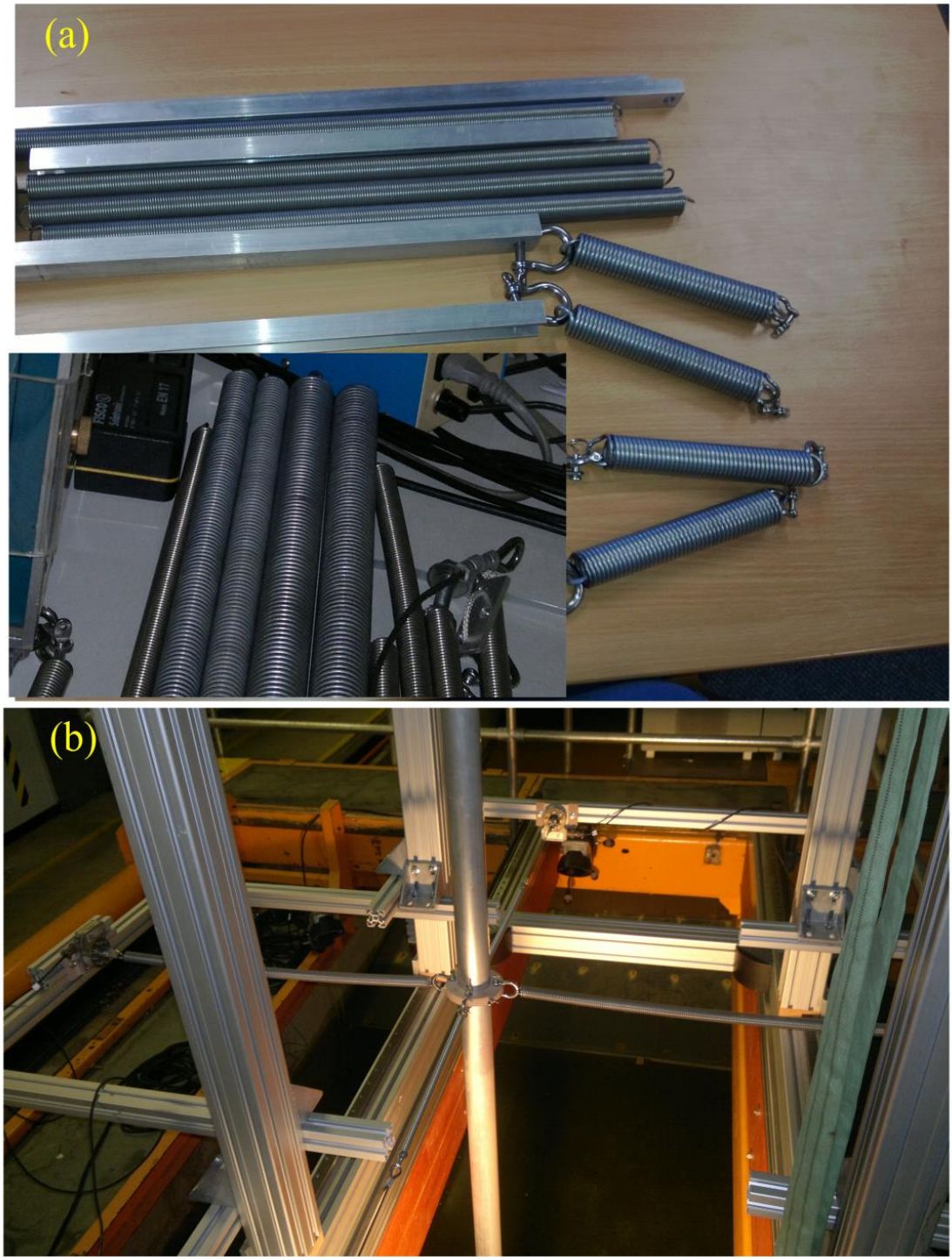

Figure 4.6: (a) Tensile springs; (b) springs attached to the pendulum.

$$f_{nx} = \frac{1}{2\pi}\sqrt{\frac{2k_x L_s^2 + 2k_y L_s^2\left(1 - \frac{L_y}{H_y}\right) + \frac{1}{2}m_p g L_p + m_c g\left(L_p + \frac{L_c}{2}\right)}{\frac{1}{3}m_p L_p^2 + \frac{1}{12}m_c L_c^2 + mc\left(L_p + \frac{L_c}{2}\right)^2}} \tag{4.1}$$

$$f_{ny} = \frac{1}{2\pi}\sqrt{\frac{2k_y L_s^2 + 2k_x L_s^2\left(1-\frac{L_x}{H_x}\right) + \frac{1}{2}m_p g L_p + m_c g\left(L_p + \frac{L_c}{2}\right)}{\frac{1}{3}m_p L_p^2 + \frac{1}{12}m_c L_c^2 + mc\left(L_p + \frac{L_c}{2}\right)^2}} \quad (4.2)$$

where L_s, measured from the universal joint, is the location in which springs are attached to the pendulum, m_p the total mass of the pendulum, m_c the mass of the test cylinder, L_x and L_y the free length of the springs, and H_x and H_y are the distances between centre of vertical pendulum and the wall where the springs are attached to. Then, knowing the desired range of the reduced velocity and f^*, and via Eqs. (4.1) and (4.2), the stiffness of the springs are calculated. The mechanical system is restrained to allow the cylinder to oscillate freely with arbitrary amplitudes in both IL (X) and CF (Y) directions by using two pairs of coil springs (with lengths of about 50 cm) rearranged perpendicularly in the horizontal X-Y plane. Each spring obeys Hooke's law (i.e. with a linear constant stiffness); nevertheless, as the cylinder oscillates two-directionally due to VIV, the assembly creates the geometrically nonlinear coupling of CF/IL displacements. These non-linear effects were accounted for in the numerical prediction model presented in Chapter 3 and Eq. (1) and (2).

To verify Eq. (4.1) and (4.2) sets of free-decay tests are conducted in air while different sets of springs are utilised. Figure 4.16 shows the time histories of these test with k_x=k_y=74 N/m (Figures 4.7(a) and (b)), k_x=k_y=352 N/m (Figures 4.7(c) and (d)) and k_x=352, k_y=74 N/m (Figures 4.7(e) and (f)) and the measured and calculated natural frequencies are reported in each figure. As these figures illustrate, in all cases the natural frequency is predicted with less than 3.5% error.

4.1.2.5 Mean IL position-adjusting mechanism

When the cylinder is towed, the mean drag causes a mean IL displacement of the cylinder in the flow direction; however, only the fluctuating displacements are of main interest. In order that the mean position of the cylinder for the measurements is vertical in the IL direction to avoid the possible cylinder inclination effect on VIV, this displacement was initially adjusted by pre-tensioning the upstream IL spring, such that the cylinder mean position, remains nearly vertical during the VIV test. Figure 4.8 shows the mechanism used for adjusting mean IL position of the pendulum.

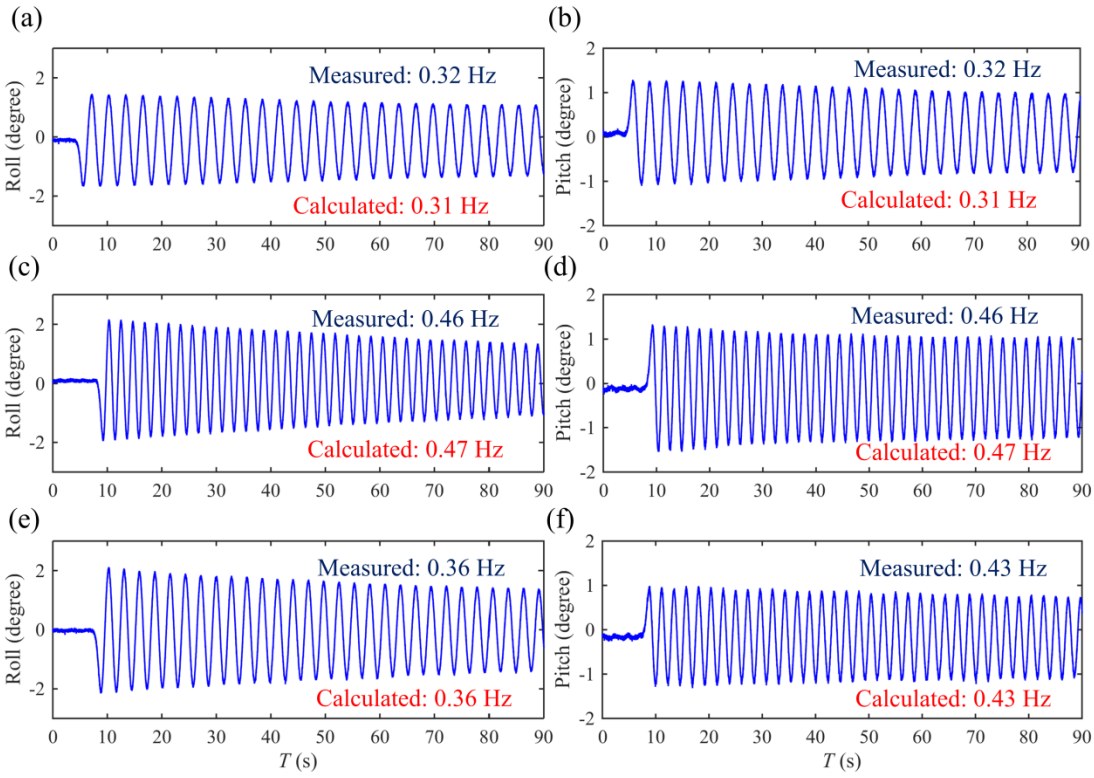

Figure 4.7: Time histories of free decay tests in air when (a) and (b) k_x=k_y=74 N/m, (c) and (d) k_x=k_y=352 N/m, (e) and (f) k_x=352, k_y=74 N/m.

4.1.3 Data acquisition

Measurement of cylinder motions was carried out using a Qualisys optical motion capture system with a fixed sampling frequency of 137 Hz. Four infrared cameras were used to identify and optimize the three-dimensional positions of four reflective markers mounted on the pendulum, and calibration was performed with an average residual across all cameras of less than 0.3 mm. Key outputs were the roll and pitch angles with a degree resolution of 0.001. Figure 4.9 shows the location of these cameras on the rig and also the reflective balls which are used for motion tracking. In contrast with traditional displacement measurement instruments, the non-contact nature of this system ensures that no unwanted additional damping or restoring forces are applied to the pendulum. Note that establishing the systematic uncertainty of measurements of the optical motion-tracking systems is more challenging than the contact-based measurements since this uncertainty depends upon the position and orientation of both the cameras and the reflective markers.

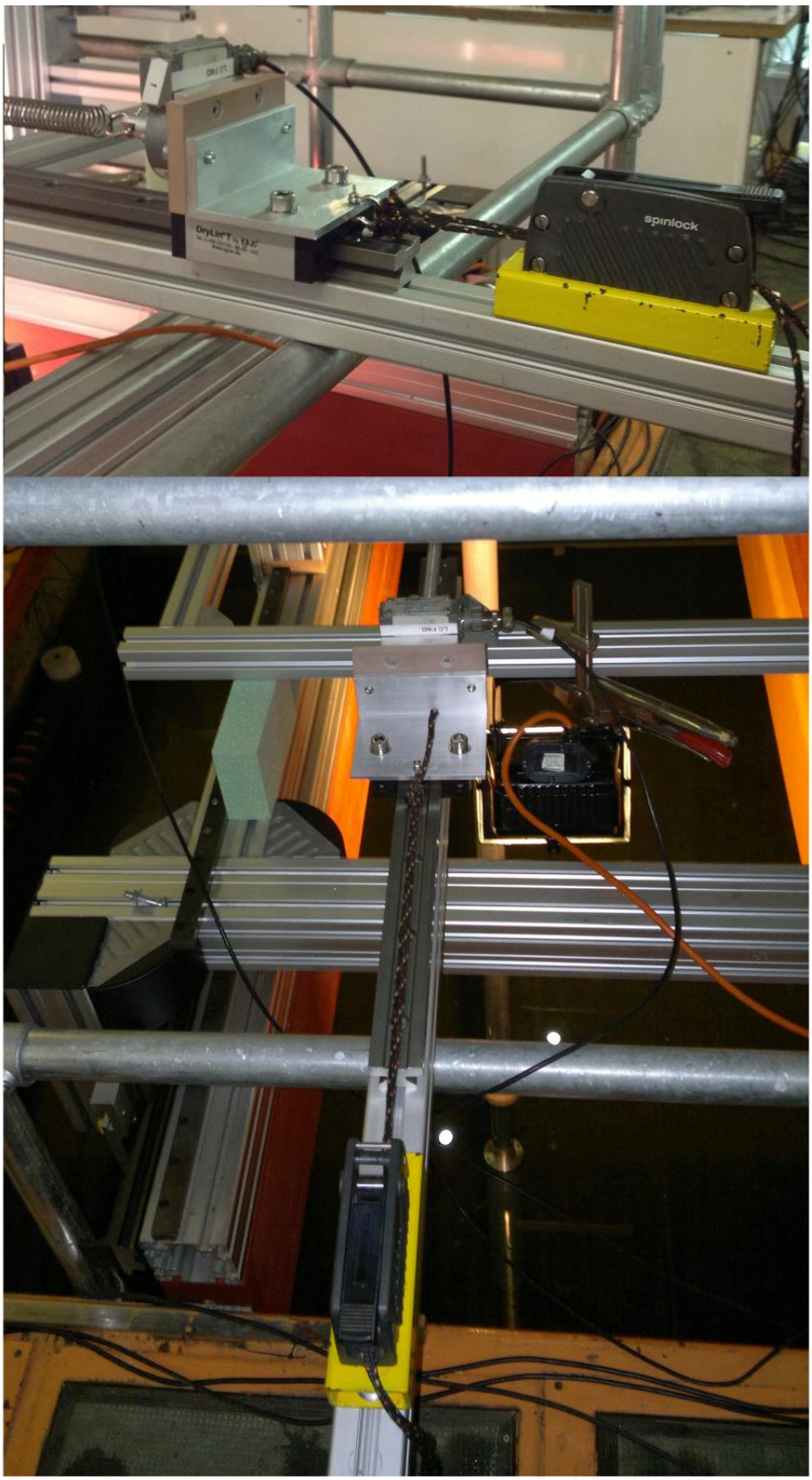

Figure 4.8: Mean IL position adjustment mechanism.

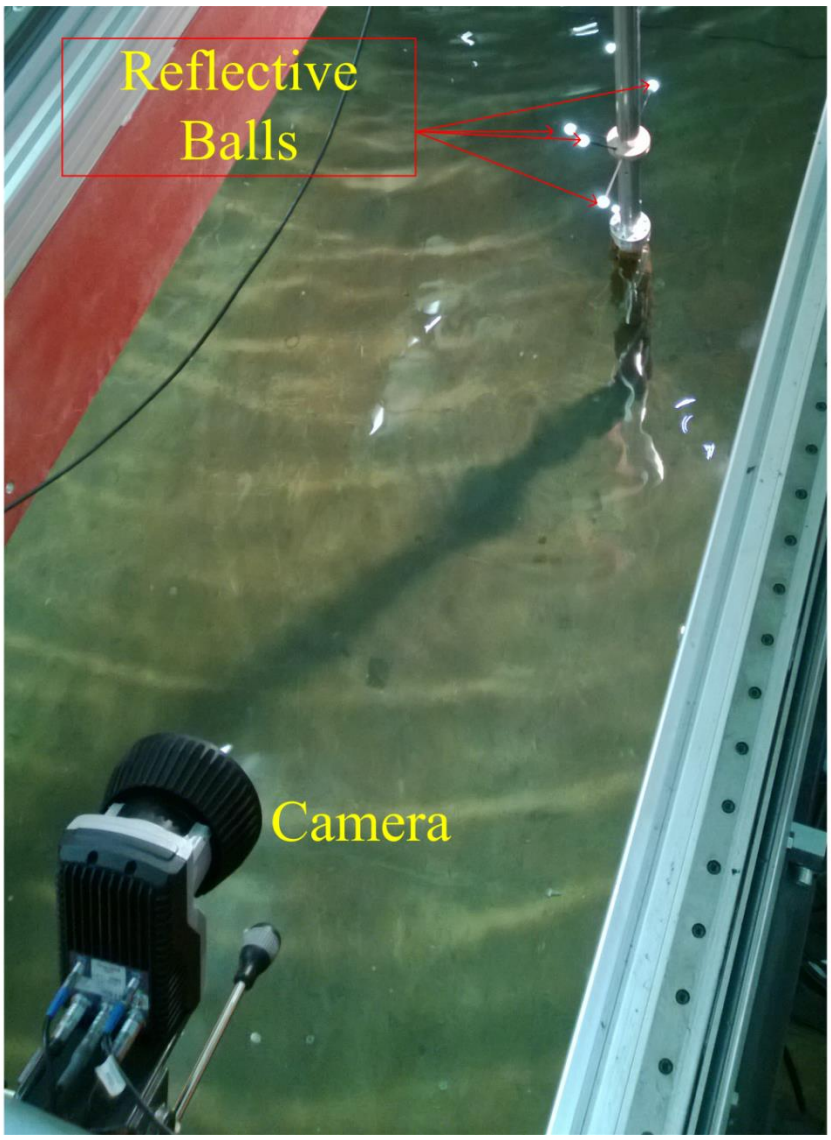

Figure 4.9: The Qualisys optical motion capture system; one of the cameras and the reflective balls can be seen in the photo.

4.1.4 Free-decay tests in water

Each VIV test was initiated with a series of free decay tests in calm water were performed to identify f_{nx}, f_{ny} and the associated damping ratios (ξ_x, ξ_y) in both X and Y directions. Small initial displacements were assigned independently in each X or Y direction to ensure that no geometric nonlinear coupling took place. Moreover, each test was repeated three times to ensure repeatability and reliability of measured signals. f_{nx} and f_{ny} were obtained from the free damped responses whose maximum amplitudes were about 0.1 of the diameter in all datasets. The damping obtained from

free-decay test is the total damping of the system which contains both structural and fluid added damping. The representative ξ_x and ξ_y values have been evaluated by subtracting the fluid damping component ξ_f from the total damping of the system. To evaluate fluid added damping in still water, Eq. (8.69) of [16] is applied:

$$\xi_f = \frac{\rho D^2}{4\pi(m+m_f)}\frac{8}{3}C_D\frac{A}{D} \tag{4.3}$$

The results of these tests (labeled as KHL1-KHL6) are summarised in Table 4.1. The average value of the results presented in Table 4.1 will be used as the structural damping in numerical modelling which will be explained in following Sections.

Table 4.1: Data from KHL free-decay tests in still water.

Dataset	f_{ny} and f_{nx}		Total damping in water		ξ_{fy} and ξ_{fx}		ξ_y and ξ_x	
	Y	*X*	*Y*	*X*	*Y*	*X*	*Y*	*X*
KHL1	0.31	0.31	0.009	0.045	0.003	0.003	0.006	0.042
			0.012	0.050	0.003	0.003	0.010	0.047
			0.012	0.033	0.003	0.003	0.010	0.029
KHL2	0.218	0.291	0.016	0.014	0.003	0.003	0.013	0.011
			0.018	0.013	0.003	0.003	0.015	0.010
			0.018	0.013	0.003	0.003	0.015	0.010
KHL3	0.262	0.419	0.017	0.015	0.003	0.003	0.014	0.013
			0.019	0.013	0.003	0.003	0.016	0.010
			0.019	0.013	0.003	0.003	0.016	0.010
KHL4	0.203	0.376	0.018	0.016	0.003	0.003	0.016	0.013
			0.020	0.015	0.003	0.003	0.018	0.012
			0.020	0.015	0.003	0.003	0.018	0.012
KHL5	0.192	0.192	0.039	0.029	0.002	0.002	0.036	0.027
			0.022	0.033	0.002	0.002	0.020	0.031
			0.022	0.033	0.002	0.002	0.020	0.031
KHL6	0.223	0.223	0.018	0.037	0.005	0.006	0.013	0.031
			0.020	0.029	0.005	0.006	0.015	0.023
			0.020	0.024	0.005	0.006	0.015	0.018

In addition to free decay tests in water, as it was mentioned earlier in this chapter, free decay tests in air were conducted on the experimental apparatus with and without the cylinder-spring system and it was found to be lightly damped at around 0.5 % and 0.2 % of the critical damping, respectively.

4.1.5 VIV tests investigating effects of *f**

Following the preliminary free decay tests which provided natural frequencies and damping of the system in air and water, self-excited VIV experiments were conducted for different f^* and m^*. Table 4.2 summarises test matrix of these experiments in which two mass ratios ($m_x^* = m_y^* = m^*$=1.4 and 3.5) of the cylinder are considered. These m^* were considered to be low, being less than 6 [9], to encourage the effect of IL VIV and the overall large-amplitude responses. Due to the amplitude-dependence nature of the structural and fluid-added damping in water, variable ξ_x and ξ_y values (between 1-5 %) are reported. The combined mass-damping values are in the range of $0.014 < m^*\xi < 0.081$. The $m^* = 1.4$ case (KHL1-KHL5) corresponds to the initial apparatus setup, whilst in later tests m^* was increased by adding lump masses to the rig system such that $m^* = 3.5$ (KHL6). Such an increased m^* case allows us to evaluate the prediction model (Chapter 3) whose empirical coefficients have been calibrated based on the experiments with varying m^* [76]. For $m^* = 1.4$, five tests with different $f^* \approx 1.0$, 1.3, 1.6 and 1.9 were performed to justify the occurrence of a dual 2:1 resonance regardless of f^* and as the drag fluctuation has double the frequency of the lift fluctuation. In all datasets, the reduced velocity V_r range in which $V_r = V/f_{ny}D$ was about $0 < V_r < 20$, corresponding to $2\times10^3 < \mathrm{Re} < 5\times10^4$ of the sub-critical flows and the flow speed V of 0.02-0.6 m/s. This considered range encompassed a V_r value at which the peak amplitude occurred. The acquisition time for each steady-state response was about 2 minutes and the waiting time between each two consecutive measurements was about 5 minutes. A trailing wheel of very accurately defined circumference was attached to the carriage, and the angular velocity of the wheel was determined using a high-precision magnetic encoder and a counter-time which outputs the velocity signal representing the carriage speed.

With the aim of comparing our experimental results with other published studies by also focusing on the variation of f^*, the experimental model performed at the MIT towing tank [11] is herein considered. Their test matrix, comprising 6 datasets (labeled as MIT1-MIT6) with L_c/D of 26, $0.041 < m^*\xi < 0.353$, and $11\times10^3 < \mathrm{Re} < 6\times10^4$, is given in Table 4.3 in comparison with KHL datasets in Table 4.2. It

is worth noting that both experiments have similar ξ_x and ξ_y values in the range of about 1-6 %. Apart from being different in the experimental arrangement and procedure, in L_c/D, and variable ξ and f^* values, the main distinction between KHL and MIT datasets is due to the specified mass ratios: $m_x^* = m_y^*$ in this study whereas $m_x^* \neq m_y^*$ in Dahl *et al*. [11]. This aspect along with other observations will be taken into account in the comparison of results in Section 4.3.

Table 4.2: KHL experimental data with variable m^*, ξ and f^*.

Dataset	f_{ny} (Hz)	f_{nx} (Hz)	ξ_y (%)	ξ_x (%)	$\boldsymbol{m_y^*}$	$\boldsymbol{m_x^*}$	f^*
KHL1	0.312	0.316	1.0	4.7	1.4	1.4	1.01
KHL2	0.218	0.281	1.5	1.0	1.4	1.4	1.29
KHL3	0.262	0.419	1.6	1.0	1.4	1.4	1.60
KHL4	0.203	0.376	1.8	1.2	1.4	1.4	1.85
KHL5	0.192	0.192	2.0	3.1	1.4	1.4	1.00
KHL6	0.223	0.223	1.5	2.3	3.5	3.5	1.00

Table 4.3: MIT experimental data with variable m^*, ξ and f^*.

Dataset	f_{ny} (Hz)	f_{nx} (Hz)	ξ_y (%)	ξ_x (%)	$\boldsymbol{m_y^*}$	$\boldsymbol{m_x^*}$	f^*
MIT1	0.715	0.715	2.2	2.2	3.8	3.3	1.00
MIT2	0.799	0.975	1.3	1.7	3.9	3.8	1.22
MIT3	0.894	1.225	1.1	2.5	3.9	3.7	1.37
MIT4	0.977	1.485	1.6	3.2	4.0	3.6	1.52
MIT5	0.698	1.166	2.6	2.9	5.5	5.3	1.67
MIT6	0.704	1.338	6.2	2.5	5.7	5.0	1.90

4.1.6 Post-processing of experimental results

The data acquisition system installed on the carriage provided text file for each test run containing measured signals of the test including carriage velocity and pitch and roll motions of the pendulum. The whole processes of analysing these signals were performed by Matlab software and its toolboxes. In the first stage, the signals were filtered to remove any noises which might appear in the signals and could have influenced the accuracy of the results. To this end, using the Fast Fourier Transform (FFT) and Inverse Fast Fourier Transform (IFFT) algorithms of Matlab, the signals

first were transferred to frequency domain and then were brought back into the time domain. Such consecutive transformations result in smooth signals while no phase difference, between original and filtered signals, was imposed to resultant time histories. Figure 4.10 exemplifies the time histories of CF and IL oscillations of the pendulum system at V_r =8.6 and their corresponding filtered signals.

In the next stage of processing the test signals, the desired quantities such as amplitude and frequency responses and Fo8 trajectories are extracted from filtered signals. The reported experimental CF (A_y/D) and IL (A_x/D) amplitudes normalized by the cylinder diameter are referred to as the displacements at the bottom tip of the cylinder and include both maximum and RMS of the displacement signals. These quantities are extracted from steady state part of each time history. It is worth noting that, to evaluate such quantities in IL direction, the drift which appears in the signals due to mean drag, was subtracted. The frequency response of each dataset is obtained via FFT algorithm of Matlab. Finally, to produce the plots of Fo8 trajectories, filtered time histories of CF oscillations are plotted against IL motions. When Fo8 orbits of tests at different V_r plotted in a single figure are of interest, the value of the magnitude of V_r is added to its corresponding IL signal.

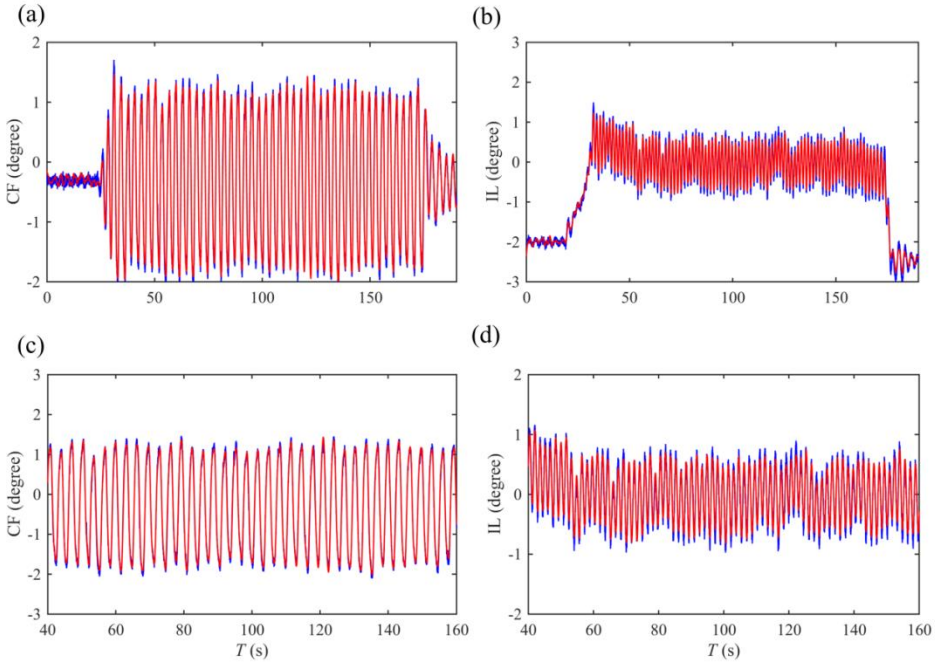

Figure 4.10: Original (blue) and filtered (red) signals of (a) and (c) roll (CF) and (b) and (d) pitch (IL) oscillations of system for KHL1 dataset at V_r=8.6.

4.1.7 Limitations, uncertainties and repeatability of tests

As 2DOF VIV of a flexibly mounted circular cylinder depends on several system fluid-structure parameters in both CF and IL directions, it is a very challenging task to keep all of these parameters under control. Hence, to assure the reliability of the measurements, for each datasets repeatability tests were performed and some tests were repeated in the neighbourhood of peaks and response jumps. Figure 4.11 depicts the time histories of repeatability tests for KHL1 and 3 conducted at Vr=8.6 and Vr=7.2, respectively. As it can be seen, in terms of flow velocity, maximum amplitudes and oscillation frequency and periodicity of the signals, time histories are highly comparable. Despite all the attention paid to the accuracy and precision of the measurements, yet there are aspects of uncertainties which, in particular, can affect quantitative match between numerical prediction results and experimental measurements. One of these aspects deals with the difference between the numerical model idealization and the real experimental setup. For the sake of generality, the cylinder is theoretically postulated to be infinitely long such that the flow field might be approximated to be two-dimensional. However, during the experiment, the three-dimensional flow field along with the free surface around the oscillating cylinder with a finite length could play an influential role.

One of the main reasons suggested is that some of the key variables were not assessed with sufficient confidence during the testing campaign. In particular, values of the structural damping in water – used as one of the inputs in the numerical model – were found to be sensitive to the initial displacement condition, the change of springs' stiffness and the apparatus arrangement leading to some repeatability issues in determining total and fluid-added damping from the free decay tests in water. This observation was in contrast to the measurements made in air for which the estimated damping was highly repeatable. As a consequence, the damping ratios ξ_x and ξ_y appeared variable and $\xi_x \neq \xi_y$ when comparing and calibrating all datasets with different f*. To overcome this constraint, an improved means to assess and control equivalent damping values in both directions [129] or a systematic approach to measure system uncertainties [130, 131] should be implemented.

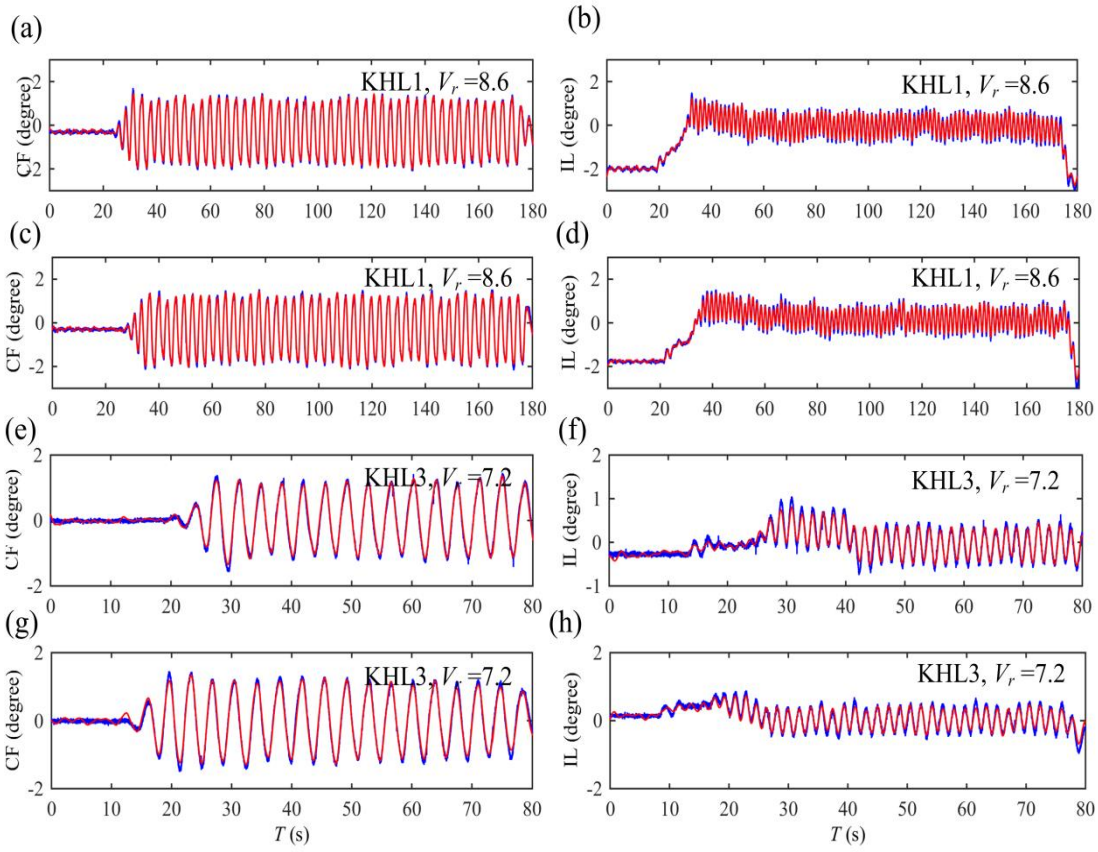

Figure 4.11: Repeatability tests for (a-d) KHL1 dataset at V_r=8.6 and (e-h) KHL3 dataset at V_r=7.2.

As a final remark, due to a finite length of the tank, it is presently unfeasible to perform a perfect sweeping test where a towing speed (i.e. V) is altered during a single run of the carriage. As this change (whether increasing or decreasing V) would require the time for the transient dynamics to die out in order to achieve steady-state responses (especially for large-amplitude 2DOF vibrations in the neighbourhood of the hysteresis), the carriage would reach the end and be terminated before the cylinder steady-state response takes place. Hence, possible coexisting responses associated with the jump and hysteresis – as usually observed in a water flume facility [9] – were not ascertained in our towing tank tests although the proposed numerical model can capture such important behaviours. Depending on system parameters and initial conditions, the jump and hysteresis phenomena should be further experimentally investigated in the framework of a 2DOF VIV of a circular cylinder with variable f^* and in a higher Re range.

4.2 Comparisons of Experimental and Numerical Results

Experimental and numerical prediction results are now compared based on KHL data in Table 4.2. To facilitate the comparison and discussion, two sets of results are classified depending on f^*: (i) f^*=1 (KHL1, KHL5, KHL6) and (ii) variable f^* with f^*=1.29 (KHL2), 1.60 (KHL3) and 1.85 (KHL4). Both maximum and root-mean-squared (RMS) values of CF (A_y/D) and IL (A_x/D) amplitudes are evaluated.

4.2.1 Amplitude responses and time histories

Results in the f^*=1 cases are plotted in Figure 4.12 which illustrates a fairly good qualitative comparison of numerical (lines) and experimental (symbols) responses. From the experiments, pure IL responses are observed in a marginal range of about $2 < V_r < 4$ (Figure 4.12 (b), (d) and (f)) whereas coexisting CF/IL VIV responses take place in the range of about $4 < V_r < 17.5$ (Figure 4.12 (a) and (c)) or $4 < V_r < 12.5$ (Figure 4.12 (e)), depending on m^*. As expected from both a numerical and experimental viewpoint, both KHL1 and KHL5 datasets with the lower m^*=1.4 exhibit a wider synchronization region. With increasing V_r, some jumps of peak amplitudes from upper to lower branches (Figures 4.12 (c-f)) are experimentally as well as numerically (denoted by vertical dashed lines) observed. These jumps are in agreement with several recently published experimental results of 2DOF VIV with f^*=1 [9, 30, 76].

In view of quantitative comparisons, the highest values of experimental and numerical RMS amplitudes are found to be comparable in the range of about 0.9-1.25 for A_y/D (Figures 4.12 (a), (c) and (e)) and 0.1-0.3 for A_x/D (Figures 4.12 (b), (d) and (f)), depending on the system mass and damping. As regards the maximum attainable responses (A_{ym}/D, A_{xm}/D), Figure 4.12 shows a better comparison in the CF VIV than in the IL VIV, with both experimental and numerical responses providing $1.4 < A_{ym}/D < 1.75$. The numerical model apparently underestimates A_{xm}/D although it predicts well the associated RMS values. These outcomes could be influenced by the temporal modulation of A_y/D and A_x/D. To exemplify this aspect, experimental (dashed blue lines) and numerical (solid pink lines) time histories of y and x

responses of KHL1 data with V_r = 10.9 (Figure 4.12 (a) and (b)) and KHL5 data with V_r = 11.7 (Figure 4.12 (c) and (d)) are plotted in Figure 4.13 (a-b) and 4.13 (c-d), respectively. It is found that, in spite of the nearly-zero mean values of the time-varying x (about 0.046 in Figure 4.13 (b) and 0.013 in Figure 4.13 (d)), experimental IL responses are seen to have a higher modulation when compared to the associated numerical ones. In contrast, both experimental and numerical y responses (Figure 4.13 (a) and (c)) are comparable, exhibiting a much less fluctuating signal.

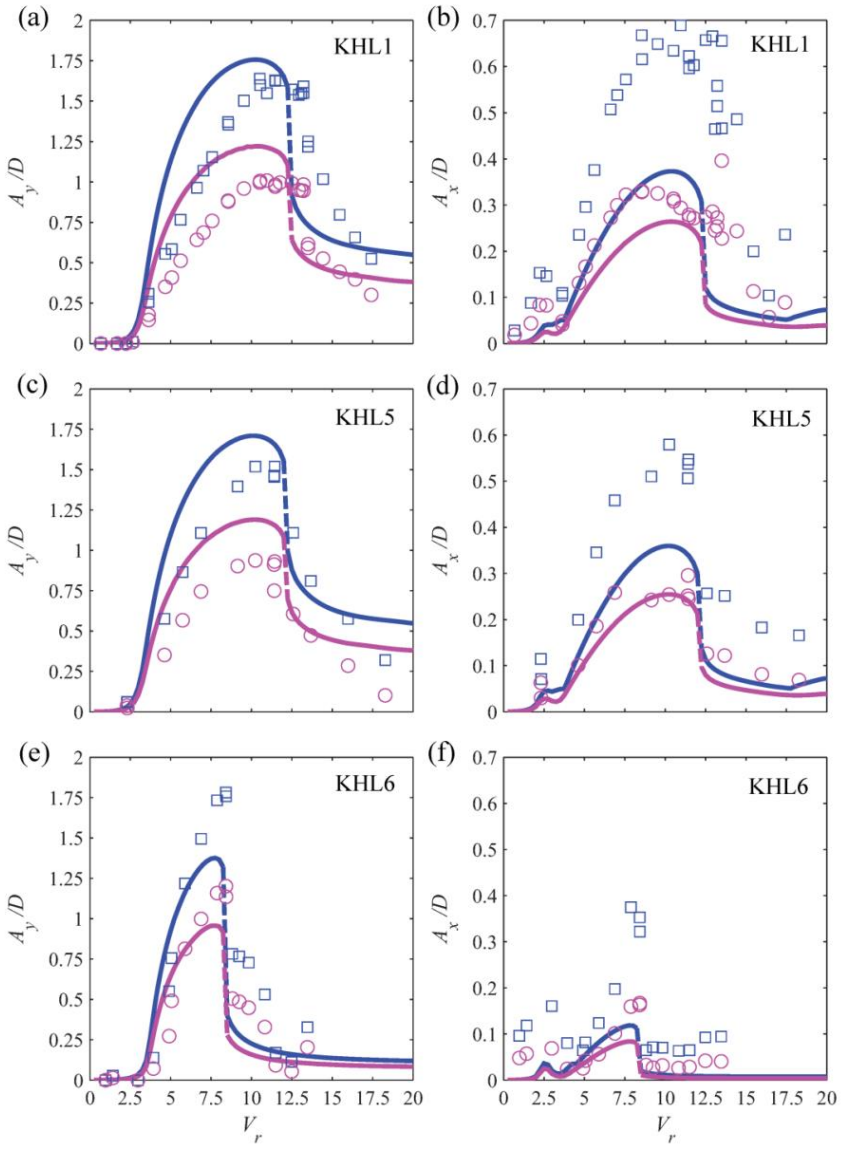

Figure 4.12: Comparison of numerical (lines) and experimental (symbols) cross-flow and in-line amplitude responses based on KHL data with f^*=1: blue lines and squares (pink lines and circles) denote maximum (RMS) values; dashed lines denote numerical response jumps.

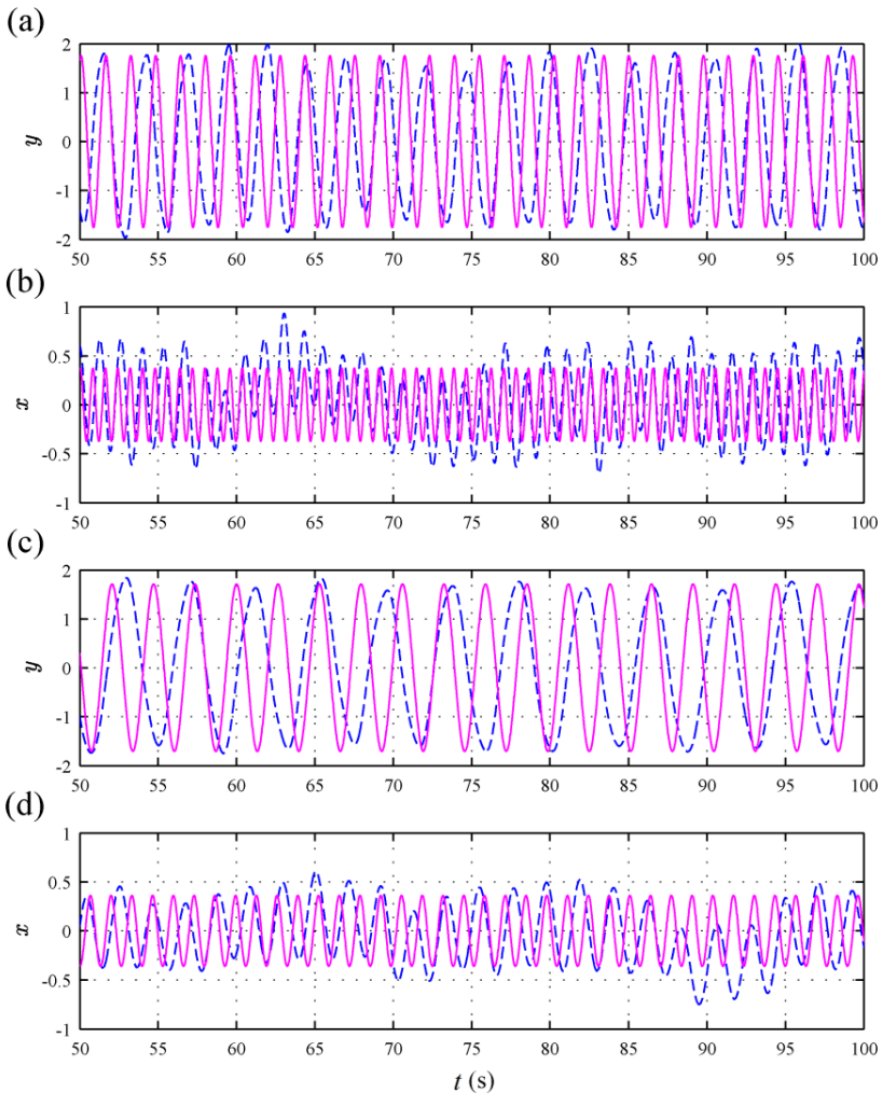

Figure 4.13: Comparison of numerical (pink solid lines) and experimental (blue dashed lines) cross-flow (a, c) and in-line (b, d) time histories: KHL1 data with V_r = 10.9 (a, b) and KHL5 data with V_r = 11.7 (c, d).

In the case of $f^*\neq1$, experimental and numerical comparisons of A_y/D and A_x/D are shown in Figure 4.14. To also demonstrate the effect of empirical coefficients, two sets of numerical results are plotted: one based on $\Lambda_x = \Lambda_y = 12$ (solid lines) and the other based on $\Lambda_x = \Lambda_y = 15$ (dashed lines), while keeping other parameters unchanged. This change in Λ_x and Λ_y has been motivated by a possible variation of both lock-in ranges and ensuing amplitudes. With increasing f^*, some VIV behaviors are noticed experimentally. First, the IL-only responses seem to disappear with increasing f^* = 1.6 (Figure 4.14(d)) and f^* = 1.85 (Figure 4.14(f)). This is in

agreement with the numerical prediction. Secondly, both CF and IL responses in Figure 4.14(c) and 4.14(d) (f^* = 1.6) and Figure 4.14(e) and 4.14(f) (f^* = 1.85) reveal the flattening slopes of their upper branches with amplitudes starting from $V_r \approx 2.5$ and ending at $V_r \approx 12.5$. These amplitude profiles are qualitatively similar to the experimental results of Assi *et al*. [132] with f^* = 1.93.

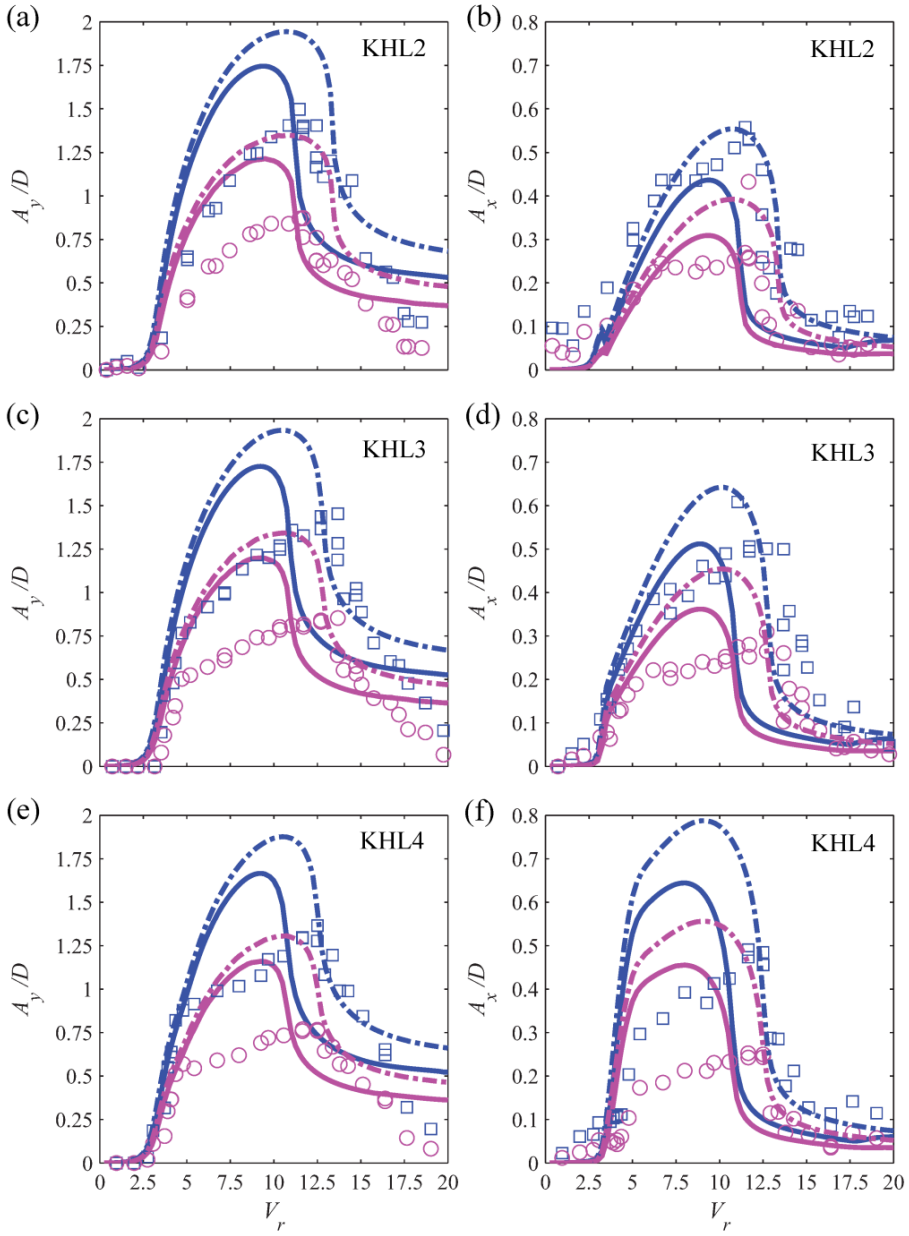

Figure 4.14: Comparison of numerical (lines) and experimental (symbols) cross-flow and in-line amplitude responses based on KHL data with $f^* \neq 1$: blue lines and squares (pink lines and circles) denote maximum (RMS) values; dashed (solid) lines with $\Lambda_x = \Lambda_y = 15$ (12).

Nevertheless, overall experimental results show $A_{ym}/D \approx 1.5$ and $A_{xm}/D \approx 0.5$, and the associated excitation ranges are quite comparable, in all f^* cases. Given the similar values of $m^*\xi$, these imply the negligible effect of varying f^* on the maximum response outcomes based on this pendulum-spring-cylinder system. With respect to numerical comparisons, the predicted A_{ym}/D and A_{xm}/D are found to be overestimated and the associated upper branches show higher slopes being typical for resonance diagrams. These reflect the difficulty in matching numerical and experimental results in which several coefficients control the dynamic responses and some of the influential parameters are variable, i.e. $\xi_x \neq \xi_y$. However, with a demonstrated small increment of Λ_x and Λ_y, the qualitative prediction of lock-in ranges appears to be satisfactorily improved. Hence, values of $\Lambda_x = \Lambda_y = 15$ are hereafter considered.

4.2.2 Sensitivity analysis on geometric coefficients

Next, it is of practical importance to carry out a sensitivity study on the numerical model in order to understand the influence of varying parameters on the 2DOF VIV prediction and the dependence of the latter on f^*. To also capture possible qualitative and quantitative changes, as it was shown in Chapter 3, the sensitivity analysis should be performed with respect to the parameters related to the greater y response. By ways of examples, the geometrical coefficient α_y or β_y is varied in the numerical simulations with $f^* = 1.3$, 1.6 and 2. In each f^* case, $m_x^* = m_y^* = 1.4$ and the averaged $\xi_x = 1.6$ % and $\xi_y = 1$ % (based on KHL2-4 datasets) are assigned. Contour plots of A_y/D and A_x/D are displayed in Figures 4.15 and 4.16 in the varying α_y and β_y cases, respectively.

For each f^*, it is seen in Figure 4.15 that A_{ym}/D increases (Figure 4.15 (a-c)) whilst A_{xm}/D decreases (Figure 4.15 (d-f)) as α_y increases, with the associated peaks locating at higher V_r values. These reflect both the quantitative and qualitative influence of the cubic nonlinear stretching term which results in the bent-to-right response as $\alpha_y y^3$ becomes greater. On the other hand, it is found in Figure 4.16 that, as β_y increases, both A_{ym}/D (Figure 4.16 (a-c)) and A_{xm}/D (Figure 4.16 (d-f)) decrease; the associated peaks are slightly bent for lower f^* (Figure 4.16 (a) and (d))

or nearly vertical for higher f^* (Figure 4.16 (b-c) and 4.16 (e-f)). These show the mostly quantitative effect of the geometric coupling $\beta_y yx^2$ term. Based on the above observations, the similar experimental response patterns with comparable ξ_y and ξ_x in Figure 4.14 might be more influenced by the displacement coupling terms than the stretching nonlinearities. For this reason, a suitable new fixed β_y value (e.g. 1.5) based on Figure 4.16 may be suggested to improve the numerical quantitative comparison with experimental results in Figure 4.14 whose $A_{ym}/D \approx 1.5$ and $A_{xm}/D \approx 0.5$ in all f^* cases. These sample contour plots might be applicable to a future prediction analysis once exact geometrical parameters are practically known.

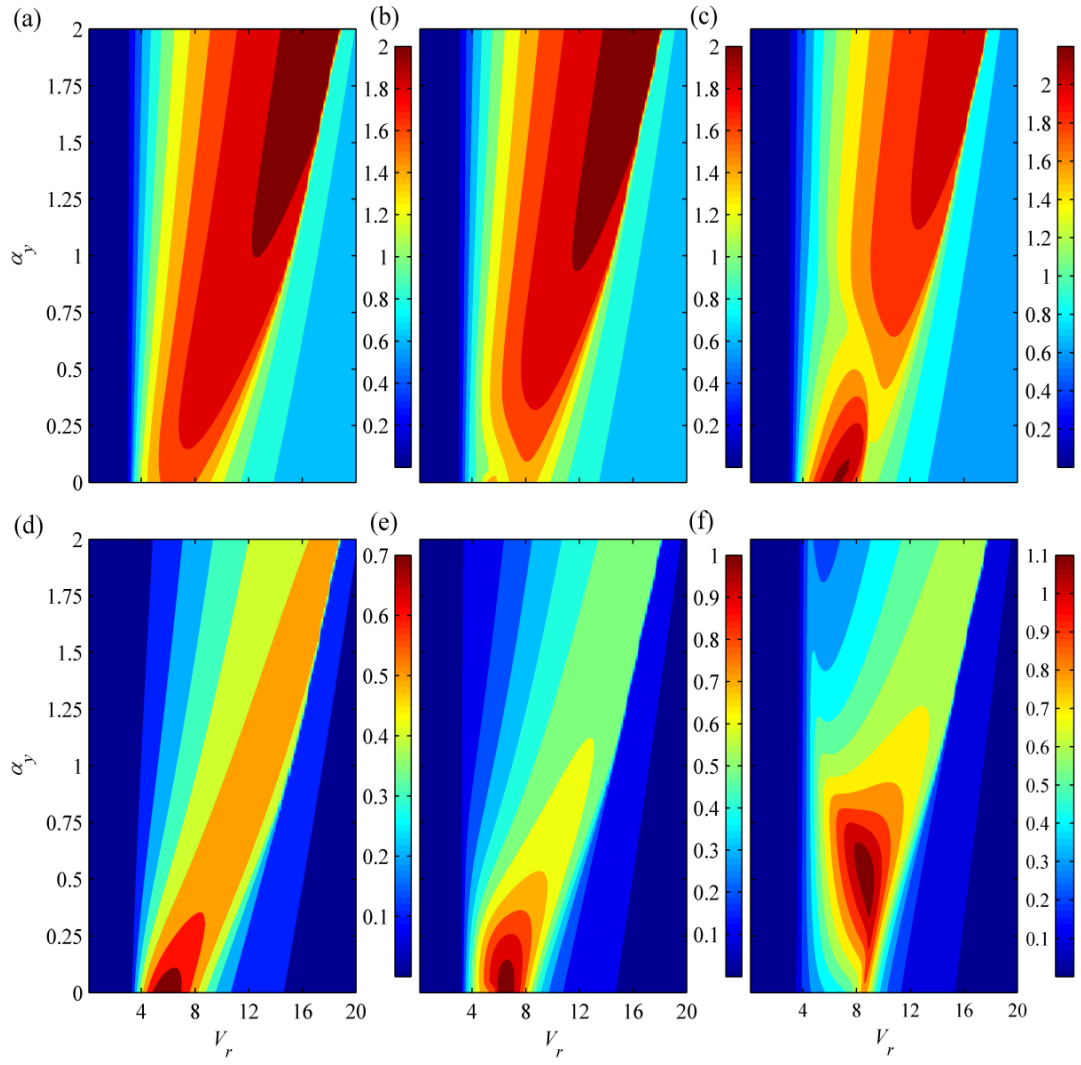

Figure 4.15: Sensitivity analysis showing the influence of geometrical parameter αy on cross-flow (a-c) and in-line (d-f) amplitude responses: f^*=1.3 (a, d), f^*=1.6 (b, e), f^*=2 (c, f).

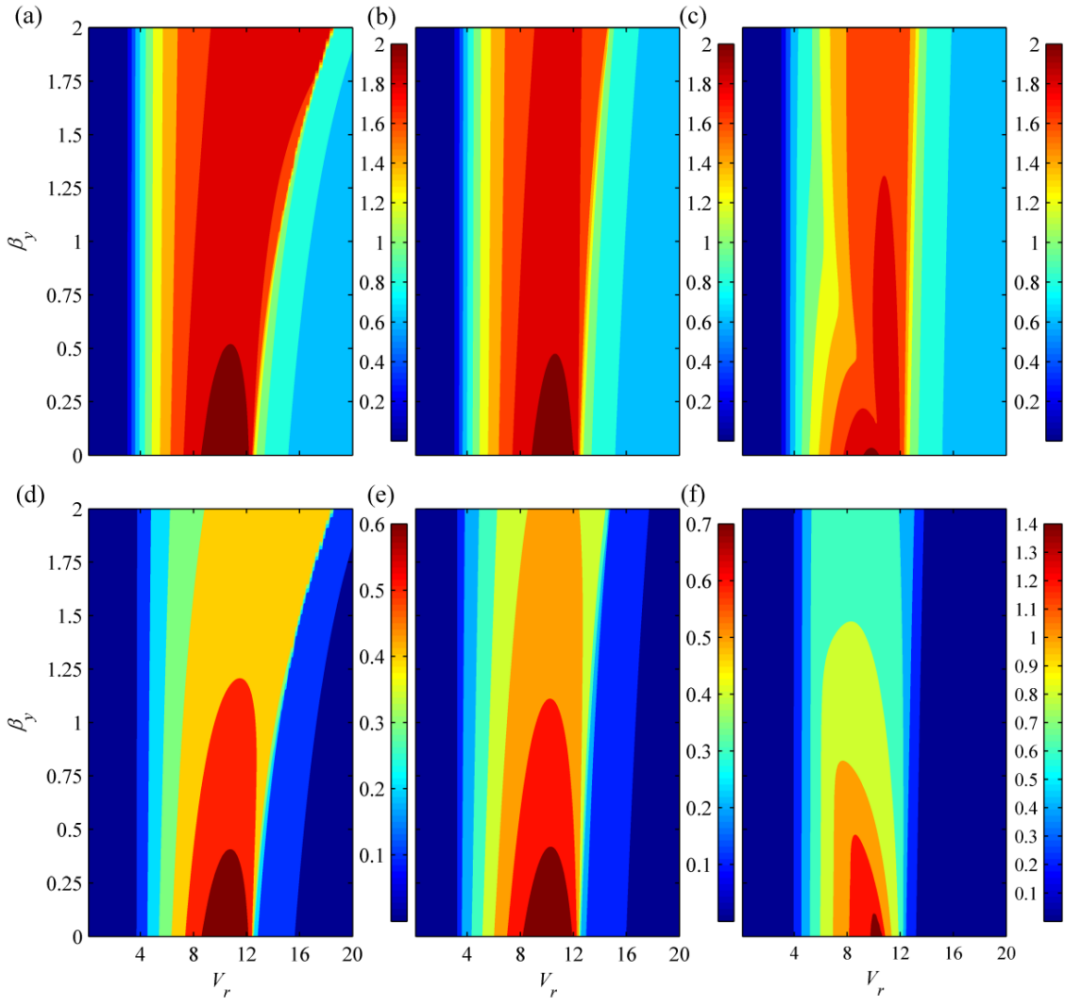

Figure 4.16: Sensitivity analysis showing the influence of geometrical parameter β_y on cross-flow (a-c) and in-line (d-f) amplitude responses: f^*=1.3 (a, d), f^*=1.6 (b, e), f^*=2 (c, f).

4.2.3 Figure-of-eight trajectories with effect of frequency ratio

Now, it is interesting to perform numerical and experimental comparisons of the time-varying orbital *x*-*y* motions as well as phase angles because this information could shed some light on how the fluid-cylinder interaction affects the resulting vortex-shedding modes. Corresponding to KHL1-6 results in Figures 4.12 and 4.14, the *x*-*y* trajectory plots within several cycles of the oscillation are displayed in Figure 4.17 (a) with some chosen V_r. The normalized *x*-*y* phase differences $(\theta_x\text{-}2\theta_y)/\pi$ of KHL3 and KHL4 datasets are also exemplified in Figure 4.17 (b). Depending on f^*, m^* and ξ (Table 4.2) and initial conditions in both numerical simulations and experiments, various characteristics of figure-of-eight trajectories appear with

variable phase differences between x and y motions. In particular, the crescent shapes are evidenced in the experiments (see blue lines in Figure 4.17 (a)) with their tips pointing mostly downstream (all KHL datasets) and occasionally upstream (KHL3 and KHL4 for V_r < 10). Similar orbital motions have been found in recent 2DOF VIV experiments of rigid circular cylinders [9, 11, 30, 77, 133], and the present study confirms these studies with both experimental and numerical results.

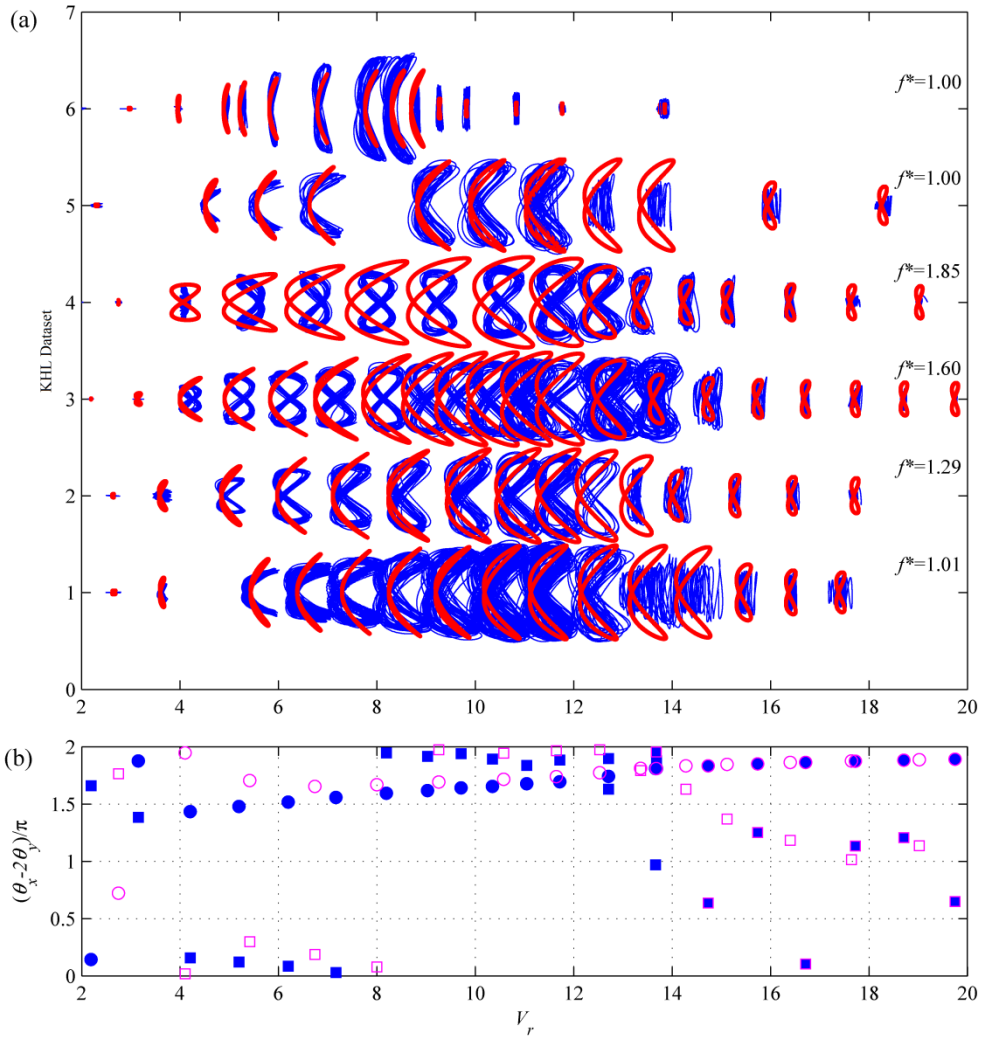

Figure 4.17: (a) Comparison of numerical (red lines) and experimental (blue lines) *x*-*y* trajectories based on KHL datasets with variable *f**; (b) comparison of numerical (circles) and experimental (squares) *x*-*y* phase differences for KHL3 (filled symbols) and KHL4 (open symbols) dataset.

It is worth noting that experimental orbital motions exhibit a high modulation feature of amplitudes whereby the oscillating cylinder does not follow the same path

from cycle to cycle. This suggests a strong fluid-structure interaction effect associated with a 2:1 resonance during the test. On the contrary, numerical orbital motions are perfectly repeatable which justify the limit cycle character of the two pairs of coupled Duffing and van der Pol oscillators for which stable periodic solutions are attained. The numerical model is found to predict quite well overall qualitative behaviors of the figure-eight appearance which, as it was discussed in Chapter 2, is due to the associated quadratic nonlinearities [69]. The experimental (squares) and numerical (circles) comparisons of phase differences in Figure 4.17 (b) also reveal their good agreement in the range of about $8<V_r<14$ where response amplitudes are maximized (Figure 4.14). By following the cylinder movement at the top of the Fo8 [134], several figures of eight of KHL3 and KHL4 datasets can be defined as counterclockwise ($0 < \theta_x-2\theta_y < \pi/2$ and $3\pi/2 < \theta_x-2\theta_y< 2\pi$) or clockwise ($\pi/2<\theta_x-2\theta_y<3\pi/2$) paths.

Experimental results in Figure 4.17 (a) suggest similar vortex formation patterns for KHL1, KHL5 and KHL6 with $f^* = 1$ since the associated Fo8 are qualitatively similar in all V_r cases. When increasing f^* to be about 1.3 (KHL2), 1.6 (KHL3) and 1.9 (KHL4), the Fo8 orbits corresponding to some particular V_r cases are noticed to be modified and these imply the possible change in the vortex formation patterns [78].

4.2.4 Comparisons of experimental and numerical frequency responses

A comparison of experimental and numerical oscillation frequencies (f_{oy}, f_{ox}) obtained from the amplitude responses within the main excitation ranges (Figures 4.12 and 4.14) and normalized by the associated f_{ny} is exemplified in Figure 4.18 based on the selected KHL1 ($f^* \approx 1$), KHL3 ($f^* = 1.6$) and KHL4 ($f^* \approx 1.9$) data. Overall good qualitative agreement is appreciated, with x (Figure 4.18 (b), (d) and (f)) and y (Figure 4.18 (a), (c) and (e)) frequency responses exhibiting their dual 2:1 resonances irrespective of the specified f^*. For the tested cylinder with low $m^*=1.4$, the oscillation frequencies of all dataset increase with increasing V_r due to the decreasing value of the hydrodynamic added mass. This justifies the fundamental mechanism of 2DOF VIV [23, 33].

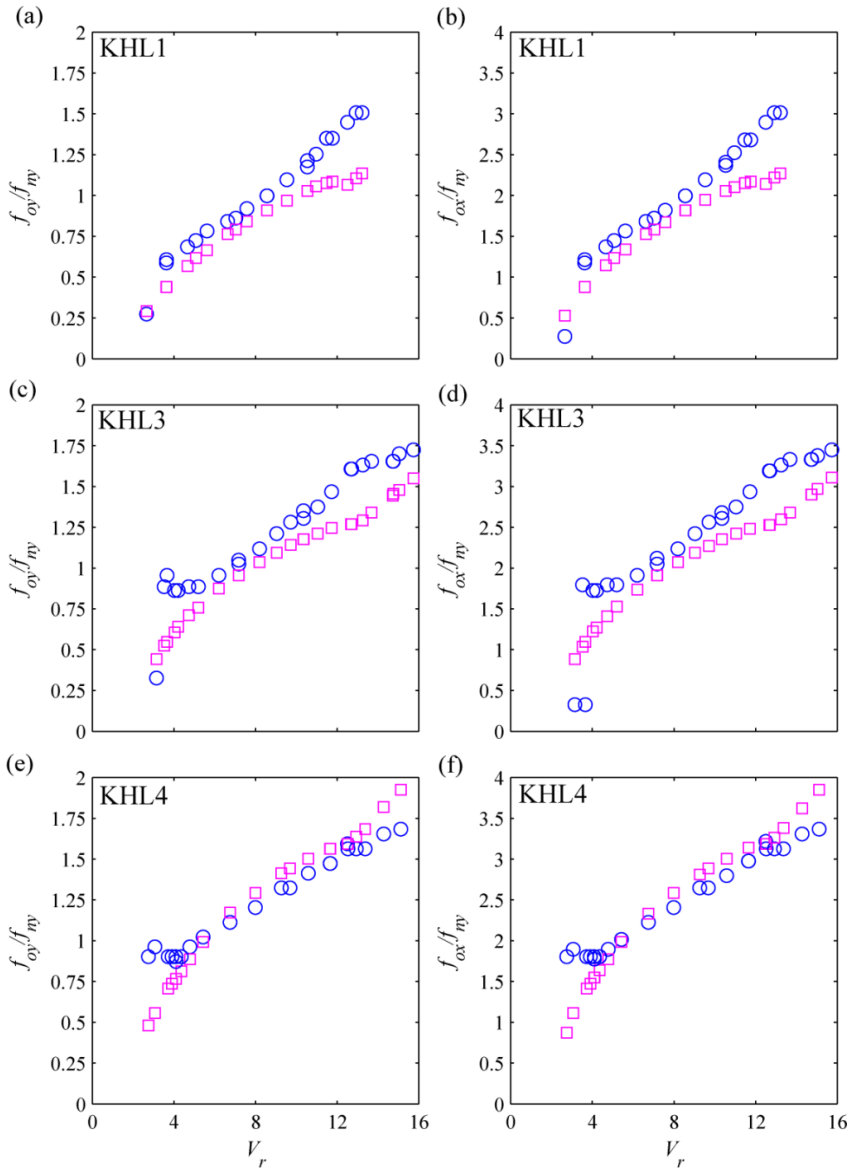

Figure 4.18: Comparison of experimental (circles) and numerical (squares) cross-flow/in-line oscillation frequencies as function of V_r for selected KHL datasets with variable f^*.

4.3 Experimental Comparisons with Other Studies

It is of considerable theoretical and practical importance to understand the extent to which 2DOF VIV results are sensitive to the various arrangements of test rigs and measurement procedures. A comparison is now presented between the results of the present study and those obtained by Dahl *et al.* [11] at MIT using a very different test rig. The comparison between KHL (Table 4.2) and MIT (Table

4.3) experimental data are considered by categorizing the results into four groups depending on the comparable values of f^* as follows:

a) KHL1, KHL5, KHL6 vs. MIT1, all with $f^* \approx 1$,

b) KHL2 vs. MIT2 and MIT3, all with the averaged $f^* \approx 1.3$,

c) KHL3 vs. MIT4 and MIT5, all with the averaged $f^* \approx 1.6$,

d) KHL4 vs. MIT6, all with $f^* \approx 1.9$.

Comparisons are made in terms of A_y/D and A_x/D diagrams (Figure 4.19), the associated oscillation-to-natural frequency ratios f_{oy}/f_{ny} and f_{ox}/f_{ny} (Figure 4.20) and the Griffin plots (Figure 4.21) of peak amplitudes vs. the Skop-Griffin parameter $S_{GX} = 2\pi^3 St^2 m_x^* \xi_x$ and $S_{GY} = 2\pi^3 St^2 m_y^* \xi_y$ [63]. Note that the value of A_{ym}/D with MIT apparatus was limited to 1.35 [11]. f_{ox} and f_{oy} are the dominant oscillation frequencies obtained from the fast Fourier transform analysis of relevant response time histories.

4.3.1 Comparisons of experimental amplitude responses

With $f^* \approx 1$, overall response amplitudes of KHL1, KHL5, KHL6 and MIT1 data show a variation of A_{ym}/D in the range of about 1.35-1.75 (Figure 4.19 (a)) and A_{xm}/D in the range of about 0.4-0.8 (Figure 4.19 (b)). This disparity of peak responses may in part be due to the influence of variable ξ_y and ξ_x whose values are mostly $\xi_y \neq \xi_x$ (except MIT1). The KHL6 and MIT1 results with comparable m^* (3.3-3.8) provide a good qualitative agreement with a similar lock-in range of $4 < V_r < 12$ in which both A_y/D and A_x/D are simultaneously excited. Good qualitative agreements are also appreciated by the comparison of KHL1 and KHL5 data.

In the lower $m^* = 1.4$ cases, the lock-in range is noticed to be broader ($4 < V_r < 18$). This influence of varying m^* on the 2DOF lock-in range has recently been highlighted by the experiments of Stappenbelt *et al*. [76]. With the averaged $f^* \approx 1.3$ and $f^* \approx 1.6$, the comparison of KHL2, MIT2 and MIT3 data (Figure 4.19 (c) and (d)) and that of KHL3, MIT4 and MIT5 data (Figure 4.19 (e) and (f)) reveal their good qualitative agreement of A_{ym}/D and A_{xm}/D in a small range of about 1.35-1.5 and 0.4-

0.6, respectively. As previously mentioned, a difference in the lock-in range between KHL and MIT results is possibly due to their different m^* values, apart from assigning whether $m_x^* = m_y^*$ (KHL) or $m_x^* \neq m_y^*$ (MIT). The effect of variable damping – which has been found to control the response amplitude rather than the lock-in range [30] – might in part again be responsible for the difference in response peaks as in the previous case of $f^* = 1$.

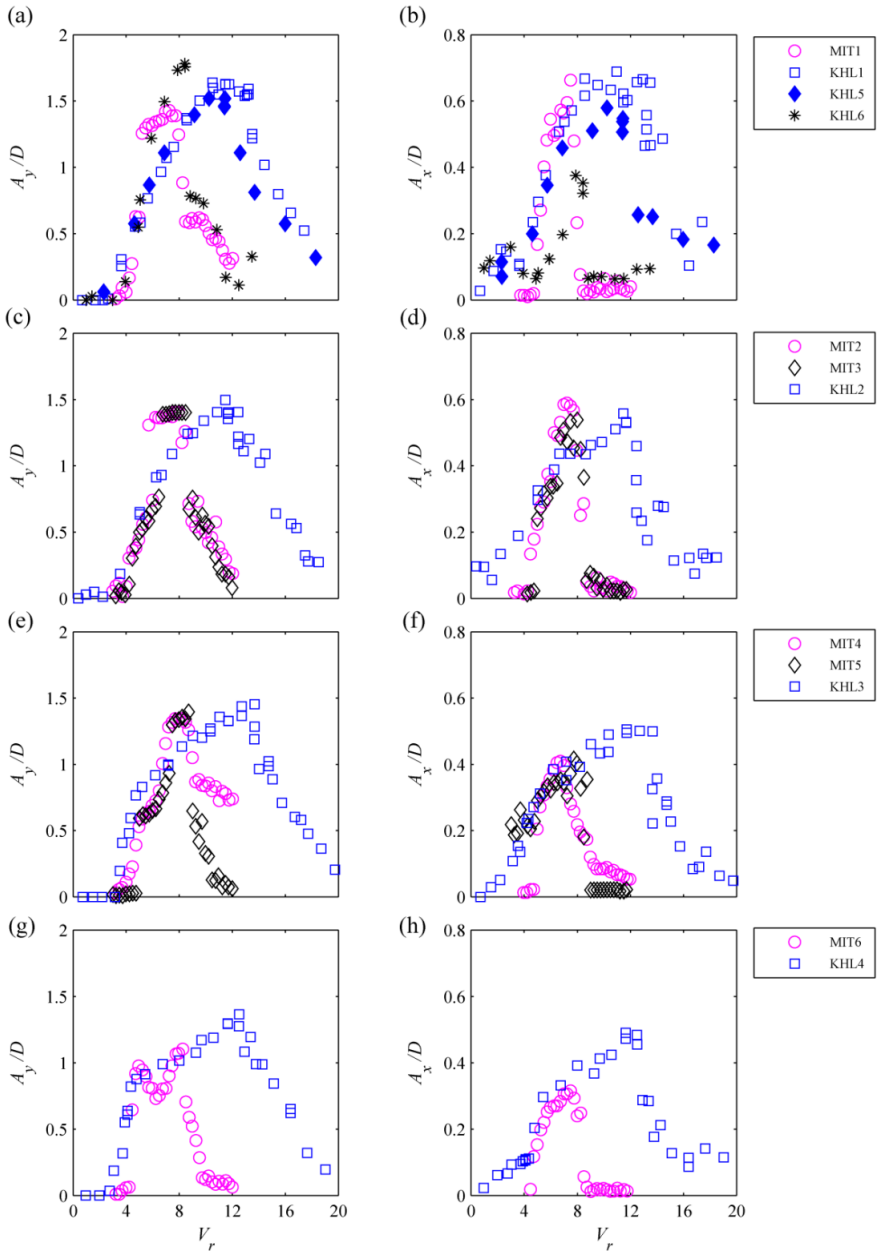

Figure 4.19: Experimental comparisons of cross-flow and in-line amplitudes between KHL and MIT data with variable f^*.

Both qualitative and quantitative differences are now realized when considering the results with the averaged f^*≈1.9. For the MIT6 data with $m_x^* \neq m_y^*$ and $\xi_y \neq \xi_x$, results reveal a two-peak CF response (Figure 4.19 (g)) – similar to those reported in Sarpkaya [71] with $f^* = 2$ (although therein m^* and ξ were not reported) – with the two A_{ym}/D≈1 and 1.1 taking place at $V_r \approx 5$ and 8, respectively. Note that the MIT6 IL response still exhibits a single peak of $A_x/D \approx 0.3$ at $V_r \approx 8$ (Figure 4.19 (h)). These observations are in contrast with KHL4 results with $m_x^* = m_y^*$ and $\xi_y \neq \xi_x$ which show single-peak responses in both CF and IL responses. Recent numerical studies by Lucor and Triantafyllou [101] have also found only single-peak responses with $m_x^* = m_y^*$ and $\xi_y = \xi_x$. Owing to the lower m^* and ξ of KHL4 data, the associated $A_{ym}/D \approx 1.3$ (Figure 4.19 (g)) and $A_{xm}/D \approx 0.5$ (Figure 4.19 (h)) are greater and the associated lock-in range is wider of about $4 < V_r < 18$. These qualitatively justify the present experimental results.

4.3.2 Comparisons of experimental frequency responses

In Figure 4.20, overall comparisons of f_{oy}/f_{ny} (a, c, e and g) and f_{ox}/f_{ny} (b, d, f and h) plots highlight good correspondence between KHL and MIT results. In general, f_{oy}/f_{ny} values vary from 0.5 to 2 and f_{ox}/f_{ny} values vary from 1 to 3, with increasing V_r. These imply the variation of hydrodynamic added mass caused by VIV; that is, its value is first positive when $f_{oy}/f_{ny} < 1$ and $f_{ox}/f_{ny} < 2$, being zero at $f_{oy}/f_{ny} \approx 1$ and $f_{ox}/f_{ny} \approx 2$, and then becoming negative when $f_{oy}/f_{ny} > 1$ and $f_{ox}/f_{ny} > 2$. Regardless of the assigned f^*, the f_{ox}/f_{oy} values in Figure 4.20 are nearly commensurable to 2:1 ratios in various V_r cases. These confirm the existence of dual resonance conditions [11, 77, 78] and demonstrate the intrinsic quadratic relationships between IL and CF responses [69] corresponding to the various Fo8 orbital motions traced out in Figure 4.17 (a) in comparison with numerical prediction results. These outcomes also confirm other recent experimental results of circular cylinders undergoing 2DOF VIV with $f^* = 1$ [9, 30, 127].

4.3.3 Maximum CF/IL amplitudes and the Griffin plots

Comparisons of various experimental 2DOF VIV results [11, 30, 76, 77] with A_{ym}/D vs. S_{GY} and A_{xm}/D vs. S_{GX} are now discussed through the Griffin plots in

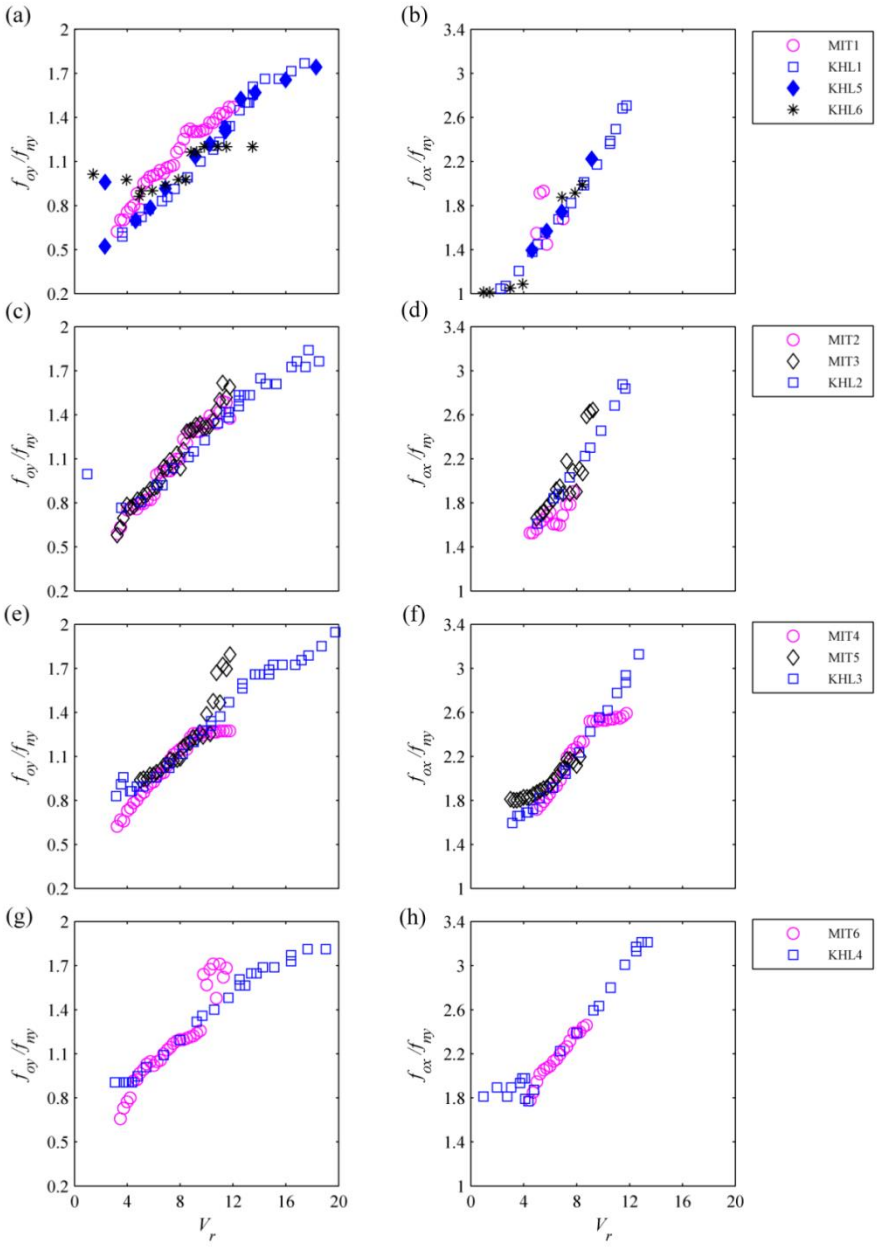

Figure 4.20: Experimental comparisons of normalized cross-flow and in-line oscillation frequencies between KHL and MIT data with variable *f**.

Figure 4.21. Numerical prediction results with specified $m_x^* = m_y^* = m^* = 1.4$ (lowest value from KHL data) and 5.7 (highest value from MIT data), and *f** = 1 and 2 in each of these cases are also given. The numerical variation of S_{GY} and S_{GX} values (from 0.01 to 1) is performed by varying ξ_y and ξ_x, respectively, with a small increment. A general qualitative agreement can be seen in Figure 4.21 where both A_{ym}/D and A_{xm}/D decrease as S_{GY} and S_{GX} increase. However, for a specific S_{GY} =

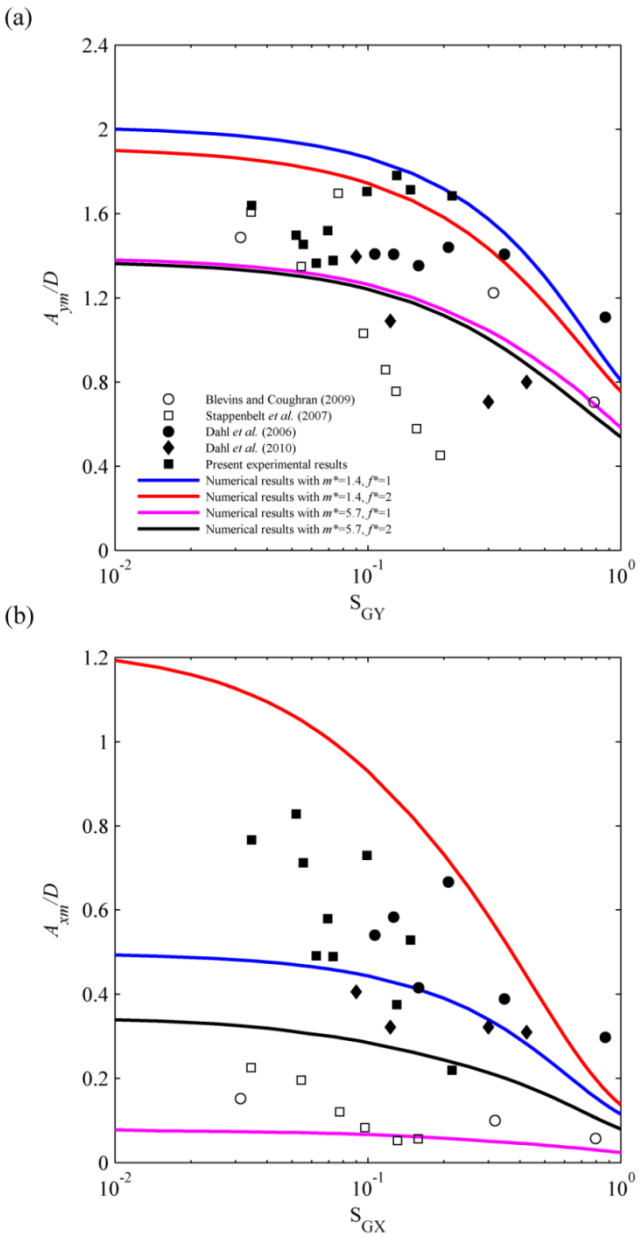

Figure 4.21: Griffin plots of maximum attainable cross-flow and in-line amplitudes based on several 2DOF VIV experimental (symbols) and numerical prediction (lines) results.

S_{GX}, experimental results with different values of m^*, ξ and f^* are scattered. The Re range might also play a role [36] although the majority of the experimental results in Figure 4.21 were based on the subcritical Re flows, except for some results in a supercritical Re range of Dahl et al. [77]. These imply how the combined mass-damping parameter fails to collapse different experimental 2DOF VIV data.

Numerical results also capture these quantitative effects, by also providing the approximate ranges of peak amplitudes and highlighting a possibly influential role of f^*. From a prediction viewpoint, both A_{ym}/D and A_{xm}/D increase as m^* decreases; however, for a higher m^*= 5.7 value, the variation of A_{ym}/D is slightly influenced by the varying f^*. This observation is reminiscent of the experimental study of Jauvtis and Williamson [9] where there was a slight influence on the CF response with m^* > 6 when comparing the results obtained between 1 and 2DOF models. In contrast, numerical A_{xm}/D values are found to be susceptible to any change of system m^*, ξ and f^* parameters. The above-mentioned discussion and comparisons deserve further experimental explorations before we could draw a firm conclusion on whether and how each – or the combination – of these parameters actually governs the 2DOF VIV of circular cylinders.

4.4 Conclusions

Experimental investigations of 2DOF VIV of a flexibly mounted circular cylinder with a low equivalent mass ratio (m^*=1.4 and 3.5) and variable IL-to-CF natural frequency ratio ($f^* \approx$ 1, 1.3, 1.6, 1.9) have been performed in a water towing tank. The VIV experiments cover a sub-critical Re range of about 2×10^3-5×10^4. The results of this experimental study have been compared with the numerical results of the semi-empirical model presented in Chapter 3 and have been utilised for calibration of the model empirical coefficients. Some important aspects in the 2DOF VIV have been numerically captured which are in good qualitative agreement with experimental observations. With low values of m^*=1.4 equally in both directions, the two-dimensional VIV excitation ranges have been experimentally found to be in a broad range of the reduced velocity parameter, $4<V_r<17.5$, with maximum attainable CF and IL amplitudes achieving high values of about 1.25-1.6 and 0.5-0.7, respectively, depending on the level and combination of the *x*-*y* structural damping ratios in all f^* cases. This damping parameter along with the two-directionally geometrical coupling coefficients might in part be responsible for the disparity of response amplitudes and the quantitative differences between experimental and numerical results, apart from the fact that actual three-dimensional features of the flow around the finite cylinder cannot be presently captured by the numerical model.

As regards experimental comparisons, the present measurement results and MIT published data based on similar Re and mass-damping ratio ranges exhibit fairly good agreement with comparable response amplitudes, lock-in ranges and oscillation frequencies. However, there is no appearance of two-peak CF response found in the present testing campaign as a result of the equivalent m^* in the two motion directions. Regardless of the specified f^* and overall hydro-geometric nonlinearities, various features of Fo8 orbital motions have been experimentally as well as numerically observed in a wide V_r range. These evidence the fundamental characteristics of dual 2:1 resonances of coupled IL/CF VIV responses. The proposed numerical model of Chapter 3 is able to capture these dual resonances associated with quadratic nonlinearities in addition to the reasonable estimation of response amplitudes, lock-in ranges and oscillation frequencies.

Chapter 5

Characterisation of Two-Dimensional Hydrodynamic Coefficients

Hydrodynamic forces and maximum amplitudes in the vortex-induced vibration (VIV) of circular cylinders can be practically useful in the analysis and design of underwater flexible structures subject to current flows. This study presents a combined analytical and numerical approach to systematically characterise the hydrodynamic coefficients and maximum achievable responses of a flexibly mounted circular cylinder undergoing a two-dimensional coupled cross-flow/in-line VIV with a dual two-to-one resonance. Depending on oscillation amplitudes, frequencies and phase relationships, analytical closed-form expressions governing the dual-resonant harmonic responses are derived and applied to parametrically evaluate key coefficients of the unsteady hydrodynamic forces including the fluid excitation, damping, inertia and added mass components in both cross-flow and in-line directions. The amplification of the mean drag coefficient caused by VIV is also ascertained. Numerical results are compared and discussed against available published experimental data. Moreover, new contour plots which relate the maximum dual-resonant responses to the independent mass and damping ratios are constructed. Various parametric investigations are performed in the case of varying flow velocities, highlighting the important effects of system geometric coupling nonlinearities, mass, damping and in-line-to-cross-flow natural frequency ratios. Several maps of fluid force coefficients can be beneficial to a practical analysis tool and provide new benchmarks for comparisons with other experimental and computational studies.

5.1 Analytical Solution for Hydrodynamic Coefficients

Several analytical expressions for estimating hydrodynamic coefficients have been proposed in the literature but most of them have mainly focused on the CF-only VIV [23, 33]. A few recent studies have dealt with both CF/IL VIV [9, 77]; however, the potential nonlinear effects of geometrical and wake-cylinder couplings were disregarded from their formulations. In this study, these effects are herein accounted for in the derivation of analytical closed-form solution applicable to the extraction of hydrodynamic properties from the two-dimensional VIV.

In a wide range of V_r, several experimental VIV tests have shown how the *x*-*y* response trajectories of the oscillating cylinder exhibit the Fo8 periodic motions owing to the two-dimensional lock-in conditions and dual 2:1 resonances [30, 77]. To assess the hydrodynamic coefficients of such dynamic system, both the cylinder CF motion (y) and the associated force (q) may be approximated to be sinusoidal at a resonant oscillation frequency ω whereas both the cylinder IL motion (x) and the associated force (p) may be approximately sinusoidal at 2ω. By considering a primary harmonic function, the steady-state solutions for x, p, y and q in Eqs. (3.9)-(3.12) are postulated as

$$x = x_0 \sin(2\omega t' + \theta_x), \quad p = p_0 \sin(2\omega t' + \theta_p) \tag{5.1}$$

$$y = y_0 \sin(\omega t' + \theta_y), \quad q = q_0 \sin(\omega t' + \theta_q) \tag{5.2}$$

in which x_0, p_0, y_0 and q_0 are the dimensionless amplitudes and θ_x, θ_p, θ_y and θ_q are the associated phase angles. Note that the higher harmonics of the lift and drag forces could be important in some V_r cases but these are herein neglected since attention is given to a dual resonant motion responding periodically at a fundamental frequency [9].

By substituting Eqs. (5.1) and (5.2) into Eqs. (3.9)-(3.12), applying the harmonic balance method and decomposing both linear and nonlinear forcing terms in Eqs. (3.9) and (3.11) into their excitation and inertia force counterparts, the system nonlinear equations governing the time-dependent variables can be rewritten as

$$\ddot{x} + \lambda_x \dot{x} + f^{*2} x + f^{*2} \left(\frac{3}{4}\alpha x_0^2 + \frac{1}{2}\beta y_0^2\right) x - \frac{f^{*2}}{4} \beta x_0 y_0^2 \sin\left(\theta_x - 2\theta_y\right)$$
$$= \left(-\frac{M_D \Omega^2 p_0 \cos\left(\theta_p - \theta_x\right)}{4\omega^2 x_0}\right.$$
$$\left. - \pi \mathrm{St} M_L \Omega \frac{q_0 y_0 \cos\left(\theta_q + \theta_y - \theta_x\right)}{4\omega x_0}\right) \ddot{x}$$
$$+ \left(\frac{M_D \Omega^2 p_0 \sin\left(\theta_p - \theta_x\right)}{2\omega x_0}\right.$$
$$\left. + \pi \mathrm{St} M_L \Omega \frac{q_0 y_0 \sin\left(\theta_q + \theta_y - \theta_x\right)}{2x_0}\right) \dot{x}$$
$$+ \pi \mathrm{St} M_L \Omega q_0 y_0 \omega \sin\left(\theta_q - \theta_y\right)$$

(5.3)

$$\ddot{p} + 2\varepsilon_x \Omega \left(\frac{p_0^2}{4} - 1\right) \dot{p} + 4\Omega^2 p = \Lambda_x \ddot{x}$$

(5.4)

$$\ddot{y} + \lambda_y \dot{y} + y + \left(\frac{3}{4}\alpha y_0^2 + \frac{1}{2}\beta x_0^2\right) y$$
$$= \left(-\frac{M_L \Omega^2 q_0 \cos\left(\theta_q - \theta_y\right)}{\omega^2 y_0}\right.$$
$$\left. + \pi \mathrm{St} M_D \Omega \frac{p_0 \cos\left(\theta_p - 2\theta_y\right)}{\omega}\right) \ddot{y}$$
$$+ \left(\frac{M_L \Omega^2 q_0 \sin\left(\theta_q - \theta_y\right)}{\omega y_0} - \pi \mathrm{St} M_D \Omega p_0 \sin\left(\theta_p - 2\theta_y\right)\right) \dot{y}$$

(5.5)

$$\ddot{q} + \varepsilon_y \Omega \left(\frac{q_0^2}{4} - 1\right) \dot{q} + \Omega^2 q = \Lambda_y \ddot{y}$$

(5.6)

It is worth remarking a key ability of the presented nonlinear structural model in explicitly capturing an IL drift leading to a new equilibrium of the cylinder as opposed to the traditional linear structural model. This is highlighted through Eq. (5.3) where two new time-independent drift terms appear. The drift term in the left-hand side is seen to be solely dependent on the structural cubic nonlinearities ($x_0 y_0^2$) whereas the drift term in the right-hand side is subjected to the cylinder-wake quadratic nonlinear coupling ($q_0 y_0$). Both terms should be recognized in the post-processing analysis of numerical and experimental results based on a two-directional spring-cylinder system. However, from a modeling viewpoint, only the cylinder-

wake interaction term is accounted for in the evaluation of VIV-induced mean drag force (see Eq. (5.9)). This is feasible since experimental studies reported the dependence of mean drag on the CF response [31, 135]. As shown in Section 5.3.2, the q_0y_0–based term entails a positive drag coefficient which is realistically relevant to the physical downstream translation of the cylinder in a uniform steady flow.

To obtain hydrodynamic coefficients, the vortex-induced forces exerted on the oscillating cylinder in CF (f_x) and IL (f_y) directions, normalized by $(m_s+ m_f)\omega^2_{ny}D$, may be described and decomposed into the time-varying (x and y) and mean-valued (x) components as

$$f_x = \frac{1}{2}\rho DV^2\left[\frac{C_x\sin(2\omega t+\theta_x-\delta)+C_{dv}}{(m_s+m_f)\omega_{ny}^2 D}\right] = -\frac{V_r^2}{8\pi^2\mu}\left(\frac{C_{ax}}{4\omega^2 x_0}\right)\ddot{x}-\frac{V_r^2}{8\pi^2\mu}\left(\frac{C_{vx}}{2\omega x_0}\right)\dot{x}+\frac{V_r^2 C_{dv}}{8\pi^2\mu} \tag{5.7}$$

$$f_y = \frac{1}{2}\rho DV^2\left[\frac{C_y\sin(\omega t+\theta_y-\varphi)}{(m_s+m_f)\omega_{ny}^2 D}\right] = -\frac{V_r^2}{8\pi^2\mu}\left(\frac{C_{ay}}{\omega^2 y_0}\right)\ddot{y}-\frac{V_r^2}{8\pi^2\mu}\left(\frac{C_{vy}}{\omega y_0}\right)\dot{y} \tag{5.8}$$

where C_{dv} is the coefficient of the mean drag induced by VIV, C_x and C_y are the oscillatory force coefficients in the IL and CF directions, δ and φ are the associated phase angles between the forces and the displacements, and C_a and C_v (with x or y subscript) are the corresponding components of forces in-phase with the cylinder acceleration and velocity, respectively. These time domain equations, along with Eqs. (5.3) and (5.5) can be utilised to derive closed-form expressions for the hydrodynamic coefficients. To this end, the right-hand-side terms in Eq. (5.3) are equated with Eq. (5.7) and those in Eq. (5.5) with Eq. (5.8) which yield:

$$C_{dv} = \frac{8\pi^2\mu}{V_r^2}\left[\pi \mathrm{St} M_L \Omega q_0 y_0 \omega \sin(\theta_q-\theta_y)\right] \tag{5.9}$$

$$C_{ax} = \frac{8\pi^2\mu}{V_r^2}\left[M_D\Omega^2 p_0\cos(\theta_p-\theta_x) + \pi \mathrm{St} M_L \Omega q_0 y_0 \omega \cos(\theta_q+\theta_y-\theta_x)\right] \tag{5.10}$$

$$C_{vx} = \frac{8\pi^2\mu}{V_r^2}\left[-M_D\Omega^2 p_0 \sin\left(\theta_p - \theta_x\right) - \pi \mathrm{St} M_L \Omega q_0 y_0 \omega \sin\left(\theta_q + \theta_y - \theta_x\right)\right] \tag{5.11}$$

$$C_{ay} = \frac{8\pi^2\mu}{V_r^2}\left[M_L\Omega^2 q_0 \cos\left(\theta_q - \theta_y\right) - \pi \mathrm{St} M_D \Omega p_0 y_0 \omega \cos\left(\theta_p - 2\theta_y\right)\right] \tag{5.12}$$

$$C_{vy} = \frac{8\pi^2\mu}{V_r^2}\left[-M_L\Omega^2 q_0 \sin\left(\theta_q - \theta_y\right) + \pi \mathrm{St} M_D \Omega p_0 y_0 \omega \sin\left(\theta_p - 2\theta_y\right)\right] \tag{5.13}$$

If the inertia force is scaled based on the cylinder acceleration, in place of the dynamic pressure ($\rho V^2/2$) in Eqs. (5.7) and (5.8), see, e.g., [136], the added mass coefficients due to VIV in the IL (C_{Ax}) and CF (C_{Ay}) directions may be obtained from

$$C_{Ax} = \frac{4\mu}{\pi}\left[\frac{M_D\Omega^2 p_0 \cos\left(\theta_p - \theta_x\right)}{4\omega^2 x_0} + \pi \mathrm{St} M_L \Omega \frac{q_0 y_0 \cos\left(\theta_q + \theta_y - \theta_x\right)}{4\omega x_0}\right] \tag{5.14}$$

$$C_{Ay} = \frac{4\mu}{\pi}\left[\frac{M_L\Omega^2 q_0 \cos\left(\theta_q - \theta_y\right)}{\omega^2 y_0} - \pi \mathrm{St} M_D \Omega \frac{p_0 \cos\left(\theta_p - 2\theta_y\right)}{\omega}\right] \tag{5.15}$$

Overall, Eqs. (5.9)-(5.15) highlight (i) the important effect of quadratic nonlinear coupling (q_0y_0, p_0y_0) and (ii) the dependence of hydrodynamic coefficients on the system amplitudes (x_0, y_0, p_0, q_0), phases (θ_x, θ_y, θ_p, θ_q), oscillation frequency (ω) and parameters (St, μ, M_D, M_L, V_r). Their positive or negative signs which imply the excitation or damping mechanism depend on the phase angles relationships. All the numerical amplitudes and phases can be obtained *a priori* from numerical results of Eqs. (3.9)-(3.12), by applying a spectral approach to the steady-state dynamic responses. In Section 5.3, understanding of the contributions from each linear and nonlinear forcing term and key insights into the hydrodynamic excitation mechanism will be discussed.

5.2 Analytical Solution for Maximum Dual-Resonant Responses

It is of theoretical and practical importance to develop an efficient analytical solution for estimating the maximum achievable amplitudes of the cylinder undergoing combined CF/IL VIV with dual resonances. By way of examples, the f^*=1 case which has some experimental data available for comparisons is considered.

By substituting Eqs. (5.1) and (5.2) into Eqs. (3.9)-(3.12), expanding the relevant trigonometric terms and equating the coefficients of $\sin\omega t$ ($\sin 2\omega t$) and $\cos\omega t$ ($\cos 2\omega t$) separately, the ensuing coupled equations governing the fluid-structure interaction system with four unknown amplitudes (x_0, p_0, y_0, q_0) and phases (θ_x, θ_p, θ_y, θ_q) can now be expressed as

$$2\lambda_x \omega x_0 = M_D \Omega^2 p_0 \sin(\theta_p - \theta_x) - \pi \mathrm{St} M_L \Omega q_0 y_0 \omega \sin(\theta_q + \theta_y - \theta_x), \tag{5.16}$$

$$\begin{aligned} &\left(1 + \frac{3}{4}\alpha x_0^2 + \frac{1}{2}\beta y_0^2 - 4\omega^2\right) x_0 \\ &= M_D \Omega^2 p_0 \cos(\theta_p - \theta_x) \\ &- \pi \mathrm{St} M_L \Omega q_0 y_0 \omega \cos(\theta_q + \theta_y - \theta_x) \end{aligned} \tag{5.17}$$

$$\varepsilon_x \Omega \left(\frac{p_0^2}{4} - 1\right) p_0 = \Lambda_x \omega x_0 \sin(\theta_p - \theta_x) \tag{5.18}$$

$$(\omega^2 - \Omega^2) p_0 = \Lambda_x \omega^2 x_0 \cos(\theta_p - \theta_x) \tag{5.19}$$

$$\lambda_y \omega y_0 = M_L \Omega^2 q_0 \sin(\theta_q - \theta_y) + \pi \mathrm{St} M_D \Omega p_0 y_0 \omega \sin(\theta_p - 2\theta_y) \tag{5.20}$$

$$\begin{aligned} &\left(1 + \frac{3}{4}\alpha y_0^2 + \frac{1}{2}\beta x_0^2 - \omega^2\right) y_0 \\ &= M_L \Omega^2 q_0 \cos(\theta_q - \theta_y) + \pi \mathrm{St} M_D \Omega p_0 y_0 \omega \cos(\theta_p - 2\theta_y), \end{aligned} \tag{5.21}$$

$$\varepsilon_y \Omega \left(\frac{q_0^2}{4} - 1\right) q_0 = \Lambda_y \omega y_0 \sin(\theta_q - \theta_y) \tag{5.22}$$

$$(\omega^2 - \Omega^2) q_0 = \Lambda_y \omega^2 y_0 \cos(\theta_q - \theta_y) \tag{5.23}$$

Within the lock-in or resonance range where a maximum amplitude is attained, it can be realized that $\omega \approx \Omega$: this resonant frequency of the wake and the cylinder is variable, being different from the assumed ω = 1 in [66] pertaining to the Strouhal law. Consequently, the linear terms in Eqs. (5.18), (5.19), (5.22) and (5.23) entail that θ_p-θ_x = θ_q-θ_y = π/2. These phase relations are equivalent to the obtained numerical results which will be shown in Section 5.3.1 (see Fig. 5.3 (a) and (c)) where maximum attainable amplitudes take place. Apart from validating the

numerical solution, the condition of θ_p-θ_x = θ_q-θ_y = $\pi/2$ entails the reduced system of equations which read

$$x_0 = \frac{\varepsilon_x}{\Lambda_x}\left(\frac{p_0^2}{4} - 1\right)p_0, \tag{5.24}$$

$$y_0 = \frac{\varepsilon_y}{\Lambda_y}\left(\frac{q_0^2}{4} - 1\right)q_0, \tag{5.25}$$

$$\left(1 + \frac{1}{\tan^2(\theta_q + \theta_y - \theta_x)}\right)(2\lambda_x\omega x_0 - M_D\omega^2 p_0)^2 = (\pi \mathrm{St} M_L q_0 y_0 \omega^2)^2, \tag{5.26}$$

$$\left(1 + \frac{1}{\tan^2(\theta_p - 2\theta_y)}\right)\left(\lambda_y\omega y_0 - M_L\omega^2 q_0\right)^2 = (\pi \mathrm{St} M_D p_0 y_0 \omega^2)^2. \tag{5.27}$$

By substituting Eqs. (5.24) and (5.25) into Eq. (5.26), solving the latter for p_0 and substituting overall results of x_0, y_0 and p_0 into Eq. (5.27), a highly-nonlinear equation describing the variation of σ – which is now solely dependent on the transverse wake force q_0 (viz., $\sigma = (q_0^2/4) - 1$) – can be derived as

$$k_{pq}\left(a_1\left(a_2\sigma - a_3\right)^2 - a_4\sigma^2 - a_5\sigma^2\right)^2\left(a_2\sigma - a_3\right)^2 = a_6\sigma^8\left(\sigma + 1\right)^2, \tag{5.28}$$

in which the system coefficients (a_1- a_6, k_{pq} and k_q) are given, respectively, by

$$a_1 = 2\lambda_x\omega\frac{\varepsilon_x}{\Lambda_x}k_q, \qquad a_2 = \lambda_y\omega\frac{\varepsilon_y}{\Lambda_y}, \quad a_3 = M_L\omega^2 \tag{5.29}$$

$$a_4 = 2\lambda_x\omega\frac{\varepsilon_x}{\Lambda_x}\left(2\pi \mathrm{St} M_D\omega^2\frac{\varepsilon_y}{\Lambda_y}\right)^2, \quad a_5 = M_D\omega^2\left(2\pi \mathrm{St} M_D\omega^2\frac{\varepsilon_y}{\Lambda_y}\right)^2$$

$$a_6 = \lambda_y\omega\frac{\varepsilon_y}{\Lambda_y}, \quad a_7 = M_L\omega^2, \quad a_8$$

$$= 256\left(\pi \mathrm{St} M_D\omega^2\frac{\varepsilon_y}{\Lambda_y}\right)^6\left(\pi \mathrm{St} M_L\omega^2\frac{\varepsilon_y}{\Lambda_y}\right)^2$$

$$k_{pq} = \left(1 + \frac{1}{\tan^2(\theta_q + \theta_y - \theta_x)}\right)k_q, \quad k_q = \left(1 + \frac{1}{\tan^2(\theta_p - 2\theta_y)}\right)$$

Depending on the assigned system parameters and empirical coefficients summarised in Eq. (5.29), Eq. (5.28) can be iteratively solved for several real and

complex numbers of q_0. However, only a positive real-valued q_0 – which entails a unique set of positive real p_0, x_0 and y_0 – is selected. If the system nonlinearities are omitted from the structural equations of motions (Eqs. (3.9) and (3.11)), a_4, a_5 and a_6 are trivial and k_{pq} becomes k_q. As a result, the linearlized closed-form solutions for p_0, q_0, x_0 and y_0 can be readily derived, respectively, as

$$p_0 = 2\sqrt{1+\frac{\Lambda_x}{\varepsilon_x}\frac{M_D\omega}{2\lambda_x}} \tag{5.30}$$

$$q_0 = 2\sqrt{1+\frac{\Lambda_y}{\varepsilon_y}\frac{M_L\omega}{\lambda_y}} \tag{5.31}$$

$$x_0 = \frac{M_D\omega}{\lambda_x}\sqrt{1+\frac{\Lambda_x}{\varepsilon_x}\frac{M_D\omega}{2\lambda_x}} \tag{5.32}$$

$$y_0 = \frac{2M_L\omega}{\lambda_y}\sqrt{1+\frac{\Lambda_y}{\varepsilon_y}\frac{M_L\omega}{\lambda_y}} \tag{5.33}$$

Moreover, if the accerelation coupling terms in Eqs. (3.10) and (3.12) are neglected, both Eqs. (5.30) and (5.31) give rise to a limit cycle with a finite (p_0, q_0) amplitude of 2, guaranteeing a generic feature of the self-excited oscillators [119].

By introducing the so-called Skop-Griffin parameter [63] $S_G=8\pi^2St^2\mu\xi$, which is equivalent to $C_{l0}\xi/2M_L$ [66], Eq. (5.33) can be rewritten as

$$y_0 = \frac{\frac{C_{l0}\omega}{2}}{S_G+4\pi^2St^2\gamma\omega}\sqrt{1+\frac{\Lambda_y}{\varepsilon_y}\frac{\frac{C_{l0}\omega}{4}}{S_G+4\pi^2St^2\gamma\omega}} \tag{5.34}$$

If the Strouhal condition with ω = 1 is further applied, Eq. (5.34) becomes identical to Eq. (35) in [66] regarding the CF-only VIV ($\varepsilon_y \rightarrow \varepsilon$ and $\Lambda y \rightarrow A$ in [66]). This validates the present analytical formulation when omitting system nonlinearities and IL motion effect. In Section 5.4, illustrative examples comparing between linear (Eqs. (5.30)-(5.33)) and nonlinear (Eqs. (5.24)-(5.29)) structural models will be discussed along with the contour plots of maximum attainable responses (A_{xm}/D and A_{ym}/D) as functions of m^* and ξ. Moreover, Eq. (3.18), together with Eq. (3.20), enable one to incorporate the key effect of m^* into the

analytical expressions of Eqs. (5.28)-(5.29) and explore parametrically the peak responses and associated hydrodynamic coefficients as in Section 5.4.

5.3 Two-Dimensional Hydrodynamic Coefficients

Variable hydrodynamic forces exerted on an elastically-mounted circular cylinder experiencing two-dimensional VIV are composed of (i) the oscillatory components in CF/IL directions (C_{vx}, C_{vy}, C_{ax}, C_{ay}, C_{Ax}, C_{Ay}) and (ii) the mean component in the IL direction (C_{dv}). Based on the derived closed-form expressions in Eqs. (5.9)-(5.15), coefficients of the hydrodynamic forces in phase with the cylinder velocities and accelerations are now systematically investigated and compared with relevant experimental results. By assigning $\xi_x=\xi_y=\xi$, attention is paid to the effect of varying V_r, m^* and f^*. For given input parameters (μ, M_D, M_L, St), overall coefficients depend on the maximum amplitudes (x_0, p_0, y_0, q_0), oscillation frequencies (ω), phase angles (θ_x, θ_p, θ_y, θ_q) and wake-structure coupling terms (p_0y_0, q_0y_0). To validate prediction results, the numerical predictions are compared with available experimental measurements of two-dimensional hydrodynamic coefficients. However, as it was explained in Chapter 2, few experimental studies are performed on combined CF/IL VIV and not all of them have reported the desired hydrodynamic coefficients. Hence, in cases where the values of hydrodynamic coefficients have not been explicitly reported, e.g. for C_{vx}, C_{vy}, C_{ax} and C_{ay}, these values are extracted from experimental results via post-processing approach suggested by [9, 135].

5.3.1 Phase relationships of wake and cylinder motions

Prior to evaluating the hydrodynamic coefficients, it is worthwhile to qualitatively understand how each linear and nonlinear forcing term plays a role in the IL and CF VIV response, as well as to analytically describe the fluid excitation and damping mechanism, through the phase relationships of the fluid-structure interaction system. In accordance with Eqs. (5.9)-(5.13), plots of the normalized phase differences including (i) $(\theta_p-\theta_x)/\pi$, (ii) $(\theta_q+\theta_y-\theta_x)/\pi$, (iii) $(\theta_q-\theta_y)/\pi$ and (iv) $(\theta_p-2\theta_y)/\pi$ are displayed (with regard to the left axis) vs. V_r in Figure 5.1 (a), (b), (c) and (d) (circles), respectively, based on the assigned m^*=1.5, ξ = 0.001 and f^*=1. Note

that the (i) (Figure 5.1 (a)) and (iii) (Figure 5.1 (c)) relations govern the linear terms – as commonly considered in the literature – whereas the (ii) (Figure 5.1 (b)) and (iv) (Figure 5.1 (d)) relations govern the newly-introduced nonlinear terms. In the background of Figure 5.1, the associated A_x/D and A_y/D are also displayed by dashed lines (with regard to the right axis) to describe relevant x and y response branches and excitation ranges. Moreover, by recognizing the signs in the force decomposition of Eqs. (5.7) and (5.8), the ensuing sign of each velocity-based (acceleration-based) force is visualized by the left (right) color bands, with the pink and green color representing the positive and negative output, respectively.

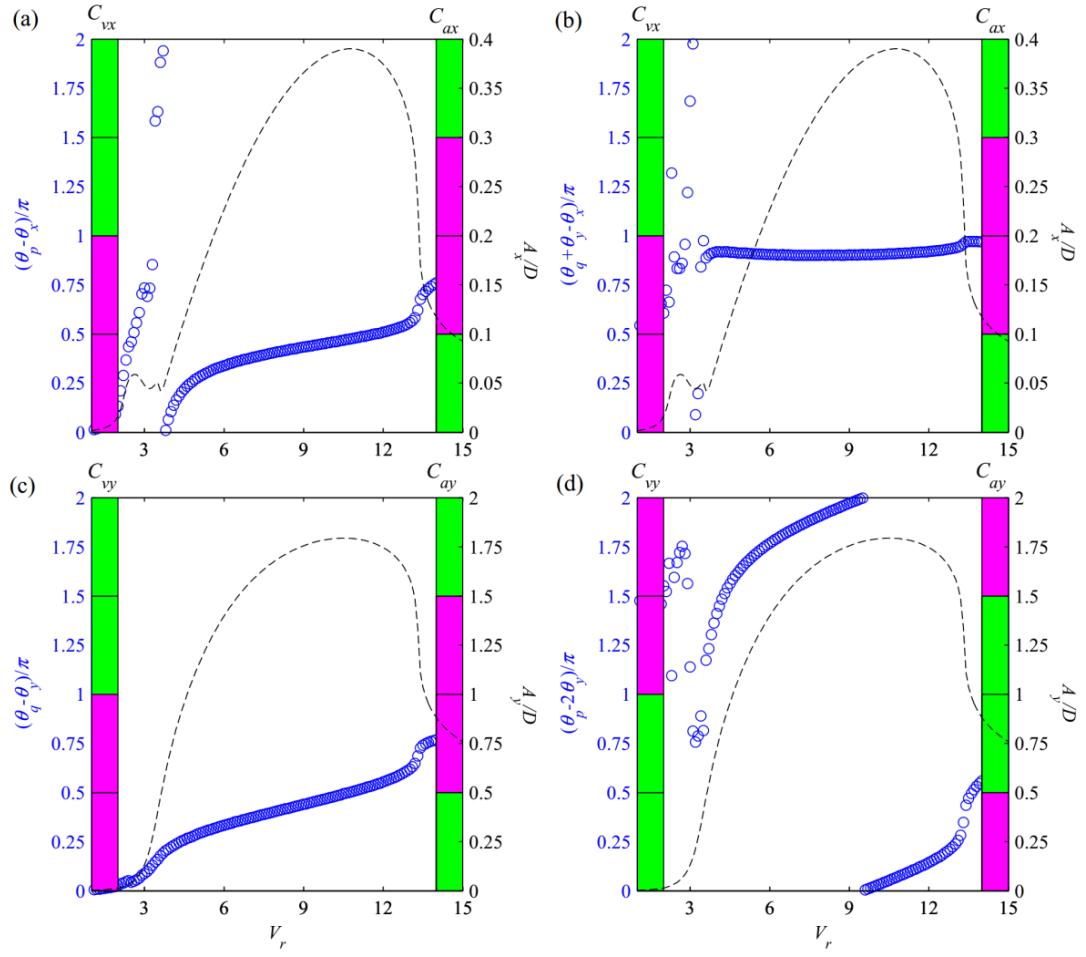

Figure 5.1: Plots of system phase differences (circulars) governing hydrodynamic coefficients as functions of A_x/D or A_y/D (dashed lines) and V_r: (a) and (c) ((b) and (d)) correspond to linear (nonlinear) fluid forces; pink (green) denotes positive (negative) output through Eqs. (5.7) and (5.8).

For purely IL VIV which occurs in a very small region of about $2.5 < V_r < 3$ ($A_{xm}/D \approx 0.05$), it can be seen that the relative phases are about $0.5 < (\theta_p-\theta_x)/\pi < 1$ in Figure 5.1 (a) and mostly $0.5< (\theta_q+\theta_y-\theta_x)/\pi < 1$ in Figure 5.1 (b). These results in both linear and nonlinear excitation forces through C_{vx} in Eq. (5.11). However, as the CF VIV and thus the associated q_0y_0-based nonlinear term are negligible in this range, the coefficient C_{vx} responsible for the peak A_x/D is mainly due to the oscillating drag p_0-based linear term. As regards the relative phase which influences C_{ax}, Figure 5.1 (a) reveals a sign change at $(\theta_p-\theta_x)/\pi \approx 0.5$ associated with the linear term in Eq. (5.10). This change of added mass sign across a resonance justifies the occurrence of peak IL VIV in the so-called second instability range involving asymmetric vortices [52].

For coexisting CF/IL VIV in the lock-in range of about $4<V_r<12$ ($A_{xm}/D \approx 0.38$, $A_{ym}/D \approx 1.8$), the quadratic nonlinearities now play an influential role. For IL oscillation, both $(\theta_p-\theta_x)/\pi$ (Figure 5.1 (a)) and $(\theta_q+\theta_y-\theta_x)/\pi$ (Figure 5.1 (b)) terms guarantee how the energy is transferred from the fluid flow to the cylinder system through both p_0-based linear and q_0y_0-based nonlinear terms in Eq. (5.11) for C_{vx}. For CF oscillation, the linear q_0- and $(\theta_q-\theta_y)/\pi$-based term in Eq. (5.13) for C_{vy} is seen to be responsible for the excitation throughout the $4<V_r<12$ range (Figure 5.1 (c)). Nevertheless, there are two consecutive regimes (centered around $V_r \approx 9$) where the associated p_0y_0- and $(\theta_p-2\theta_y)/\pi$-based nonlinear force changes its sign (Figure 5.1 (d)) from being positive ($4<V_r<9$) to negative ($9<V_r<12$). In the $4<V_r<9$ range, A_y/D grows due to the combined linear and nonlinear excitation forces (i.e. leading to a definite negative C_{vy}, see, e.g., Figure 5.4 (a)). In the $9 < V_r < 12$ range, the quadratic nonlinearities contribute such that the effective transverse force produces a damping effect and, hence, controls the self-limiting character of VIV whereby the peak A_y/D is achieved at about $V_r \approx 10.5$.

As regards the relative phases which influence C_{ax} and C_{ay}, Figure 5.1 (a) and (c) show a sign change from being negative to positive of the $(\theta_p-\theta_x)/\pi$ and $(\theta_q-\theta_y)/\pi$-based linear terms across the resonance or peak at $V_r \approx 10.5$. Thereafter, these forces remain positive throughout the remaining V_r range. On the contrary, while the

(θ_q+θ_y-θ_x)/π-based nonlinear force in Figure 5.1 (b) is in general positive for C_{ax}, the (θ_p-2θ_y)/π-based nonlinear force in Figure 5.1 (d) changes its sign for C_{ay} from being positive to negative when a response jump is experienced at V_r≈13. Depending on oscillation amplitudes, these distinctive phase relations show how the quadratic nonlinearities can affect the resulting added mass coefficients and their signs for achieving dual resonances (Section 5.3.4). As a final remark, prior to the jump occurrence of *x*-*y* responses, θ_p-θ_x and θ_q+θ_y-θ_x values at the peak A_x/D are approximated to be equal to π/2 (Figure 5.1 (a)) and 9π/10 (Figure 5.1 (b)) whereas θ_q-θ_y and θ_p-2θ_y values at the peak A_y/D are approximated to be equal to π/2 (Figure 5.1 (c)) and π/10 (Figure 5.1 (d)), respectively. Since these numerically-obtained phase differences are found to be valid in a wide m^* range, θ_p-θ_x = θ_q-θ_y ≈ π/2, θ_q+θ_y-θ_x ≈ 9π/10 and θ_p-2θ_y ≈ π/10 will be again utilised in Section 5.4 for obtaining maximum responses and associated hydrodynamic coefficients based on closed-form expressions.

5.3.2 Mean hydrodynamic drag coefficients

Coefficients of the amplified mean drag in the IL direction are now evaluated by considering the case of f^*=1. Previous experiments [31, 135] introduced an empirical relationship between the total mean drag coefficient (C_{DT}) and A_y/D of the form $C_{DT} \approx \bar{C}_d\left(1 + k'A_y/D\right)$ where *k'* is a curve fitting parameter. In this study, through the use of wake oscillators, $C_{DT} \approx \bar{C}_d + C_{dv}$ is purposed where the mean drag coefficient of a stationary cylinder $\bar{C}_d$ is assumed as 1.2 for sub-critical flows [7], and C_{dv} is based on Eq. (5.9) depending on the transverse wake-cylinder (q_0y_0) coupling. To obtain a realistic mean drift downstream (Eq. (5.7)), C_{dv} should be positive according to the sine term; this is justified by the numerical results of $0 < \theta_q$-$\theta_y < \pi$ displayed in Figure 5.1 (c).

Figure 5.2 (a) compares experimental and numerical C_{DT} as a function of V_r based on the experimental models with m^*=5.4 and ξ=0.002 [30], and m^* = 2.6 and ξ = 0.007 [137]. Overall comparisons reveal their agreement in a similar lock-in range of about 4<V_r<9. The numerical model overestimates the maximum C_{DT} in the lower m^* = 2.6 case. Similar to the A_y/D response (e.g. Figure 5.1 (c)), a jump in the

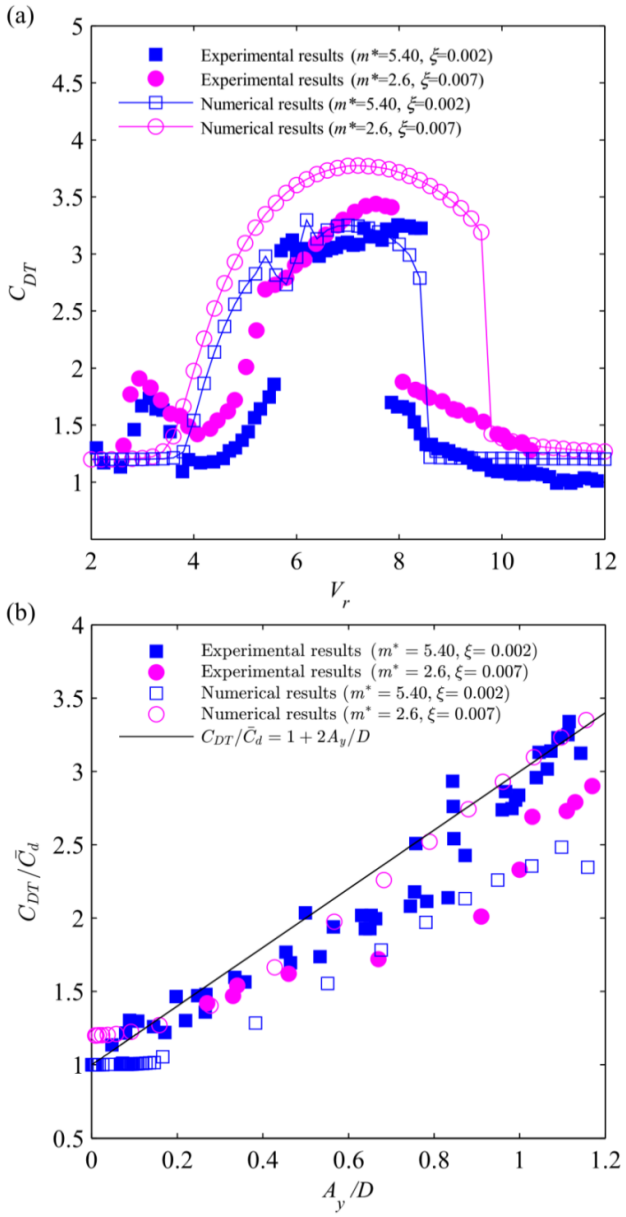

Figure 5.2: Comparison of numerical and experimental ([30], m*=5.4 and [137], m*=2.6) mean drag coefficients as function of (a) V_r and (b) A_y/D in which the black line represents the empirical relation by [31].

C_{DT} plot is noticed both numerically and experimentally. Outside the lock-in range where A_y/D is diminished, C_{DT} is comparable to $\bar{C}_d$ of the non-oscillating cylinder. As it was explained in Chapter 3, under the discussion of Figures 3.2 and 3.3, in some cases the proposed model of Eqs. (3.9-3.12) underestimates the amplitude responses in "lower branch". This is mainly due to the fact that this model is calibrated in comparison with upper and super-upper branches of amplitude

response. Consequently, the predicted hydrodynamic coefficients may be underestimated. Such circumstances occur in Figure 5.2 where the magnitudes of mean drag coefficients at lower branch are lower than their experimental counterparts. Corresponding to Figure 5.2 (a), Figure 5.2 (b) shows the $C_{DT}/\bar{C}_d$ plots as a function of A_y/D, illustrating how numerical and experimental results follow the well-known empirical formula with k' = 2 [31]. With varying V_r, Figure 5.3 displays the contour plots of numerical C_{DT} as a function of m^* (Figure 5.3 (a)) and associated A_y/D (Figure 5.3 (b)), in the case of f^* = 1 and ξ = 0.001. As expected, numerical results highlight a strong dependence of

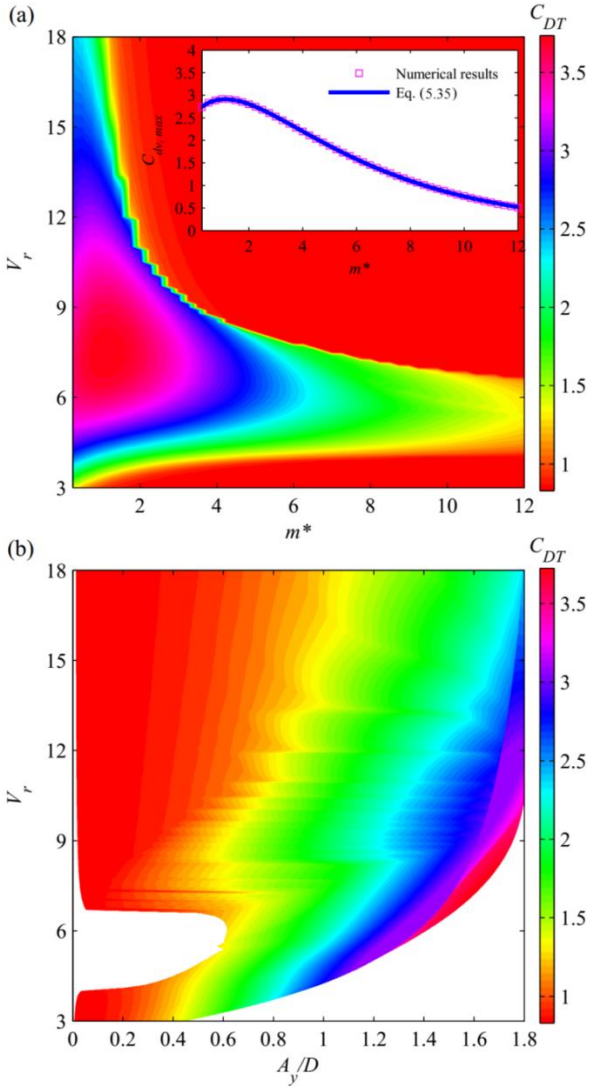

Figure 5.3: Contour plots of C_{DT} as functions of (a) m^* and (b) A_y/D with varying V_r: plots of $C_{dv,\max}$ as function of m^* is also depicted in (a).

C_{DT} on A_y/D; generally speaking, the lower the m^*, the greater the A_y/D and, thus, the C_{DT}. For $m^* > 6$ and $A_y/D < 1.1$, C_{DT} slightly changes with varying V_r. Therefore, in this high m^* range, a nearly constant C_{DT} may be uniquely identified. On the contrary, when $m^* < 6$ towards a critical value of 0.52 [9] and $A_y/D > 1.1$, there is a greater variation in C_{DT} when varying V_r. In this higher-amplitude range, C_{DT} is dependent exclusively on both m^* and V_r, and the overall maximum C_{DT} does not necessarily correspond to the maximum A_y/D at the lowest m^*. For a fixed $\bar{C}_d$, the best-fit function for the maximum C_{dv} suggests, based on results in Figure 5.3 (a) and using "curve fitting" toolbox of Matlab, that

$$C_{dv,max} = 5.14e^{-0.19m^*} - 2.54e^{-0.64m^*} \tag{5.35}$$

5.3.3 Hydrodynamic forces in phase with cylinder velocities

Coefficients of the hydrodynamic forces in phase with the cylinder velocities (C_{vx}, C_{vy}) are now discussed. For a given $m^* = 2.6$, $\xi = 0.007$ and $f^*=1$, results of C_{vy} and C_{vx} with varying V_r are plotted in Figure 5.4 (a) and (b), respectively. To validate prediction results, C_{vy} and C_{vx} plots based on the 2DOF VIV experiments [137] and a post-processing approach in [9] are compared. In Figure 5.4, experimental and numerical results reveal similar qualitative behaviors: both C_{vx} and C_{vy} are negative with their minimum values corresponding to the upper-branch range. There is also a discontinuity in C_{vx} and C_{vy} plots with a jump phenomenon as observed in the 2DOF amplitude diagrams [9]. Following the numerical sign convention imposed, the range with $C_{vx} < 0$ and $C_{vy} < 0$, with the former being greater than the latter, is referred to as an excitation region which indicates how the energy is transferred from the fluid to the structure, rendering the growing response as V_r is increased towards a location of peak amplitudes where C_{vx} and C_{vy} achieve their minimum values.

For a given $\xi = 0.001$, Figure 5.5 illustrates the influence of varying m^* and V_r on both C_{vy} and C_{vx} in the case of $f^*=1$ (Figure 5.5 (a) and (b)) and $f^*=2$ (Figure 5.5 (c) and (d)). With $f^* = 1$, C_{vy} in Figure 5.5 (a) and C_{vx} in Figure 5.5 (b) are seen to increase as m^* increases. These are valid since VIV responses of a high-mass cylinder ($m^* > 6$) are generally small for A_y/D or even negligible for A_x/D [9]. On the contrary, as m^* is decreased towards a critical value of about 0.52 [9], both C_{vx} and C_{vy} become persistently negative throughout the considered V_r range. This justifies

the so-called ‘resonance forever’ occurrence [27] where the lower-branch CF/IL responses disappear and the lock-in ranges of the upper-branch amplitudes are considerably extended. The influence of f^* on the C_{vy} and C_{vx} prediction is discussed by comparing the results with $f^* = 2$ (Figure 5.5 (c) and (d)) to those with $f^* = 1$ (Figure 5.5 (a) and (b)). It is seen that the excitation range for the IL response is increased when $f^* = 2$ since the overall area of negative C_{vx} is grown (Figure 5.5 (d) vs. (b)), spanning across the whole m^* range. With Figure 5.5 (c) vs. (d), C_{vy} values and their isoline patterns are seen to be slightly influenced by the increased f^*. These entail comparable A_y/D responses with f^*=1 and 2.

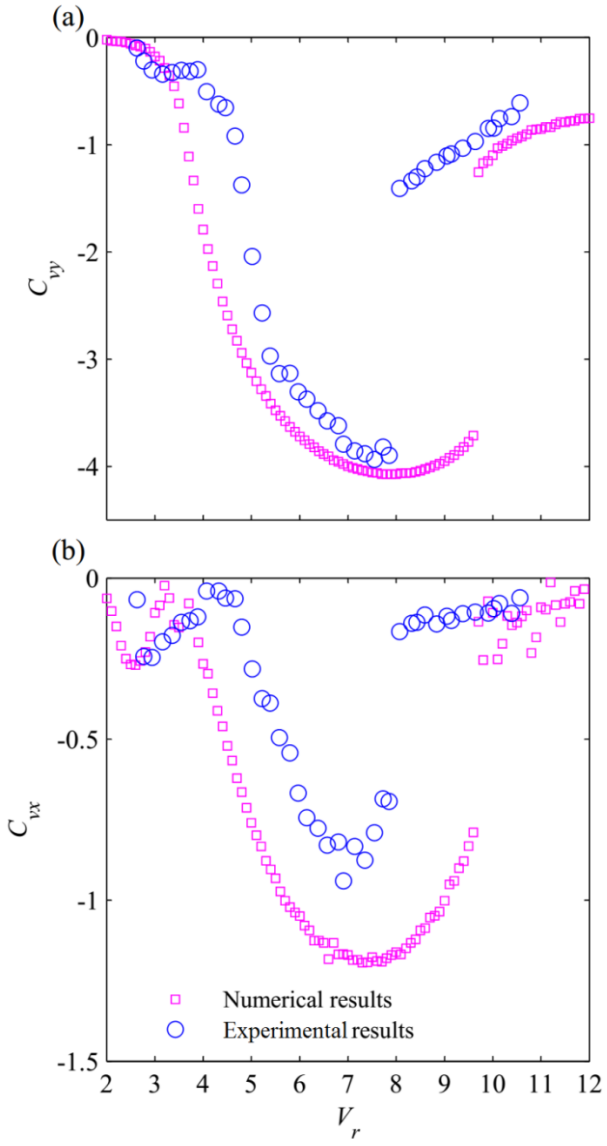

Figure 5.4: Plots of (a) C_{vy} and (b) C_{vx} as function of V_r with experimental comparisons.

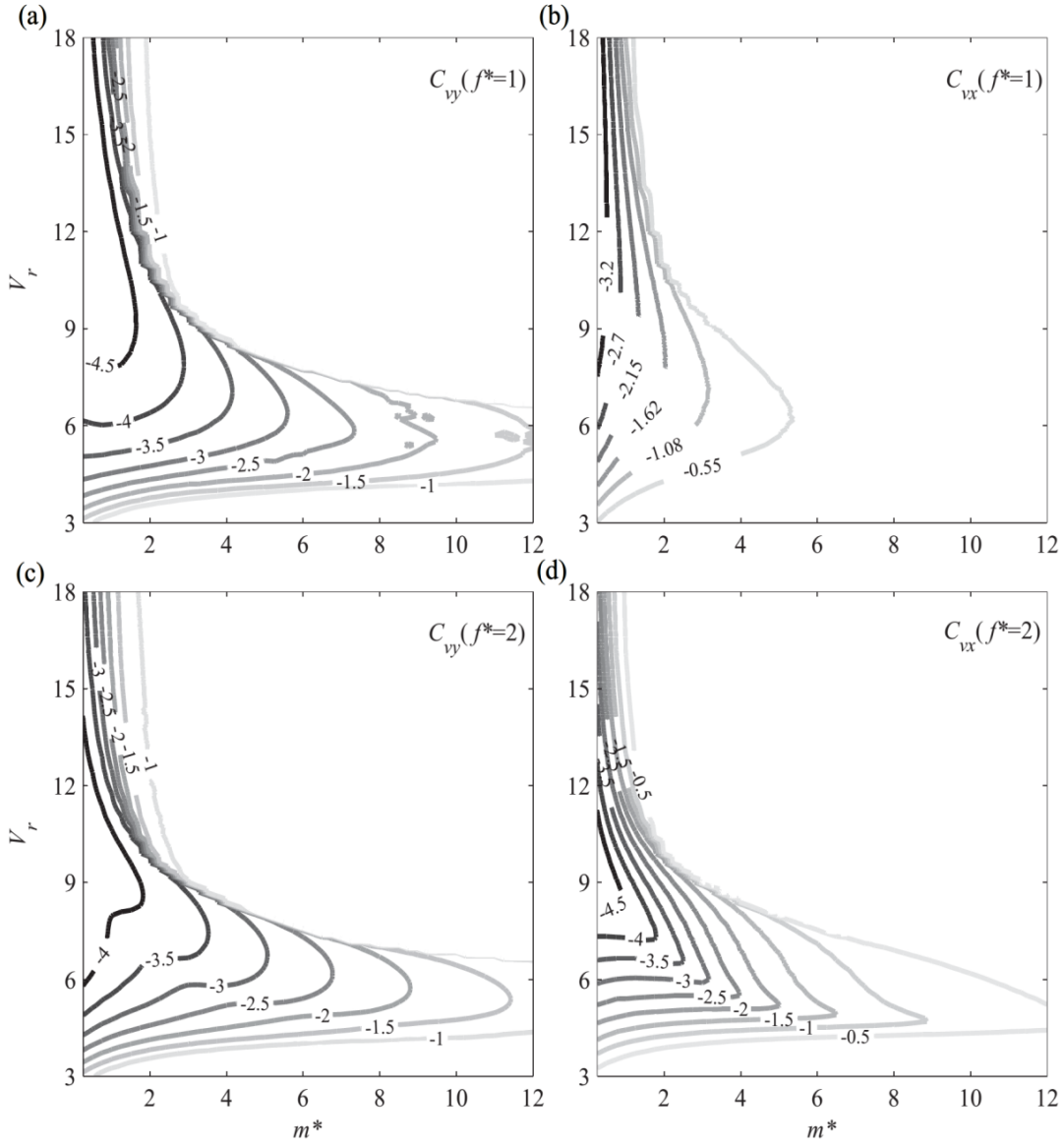

Figure 5.5: Maps of (a, c) C_{vy} and (b, d) C_{vx} as functions of m^* and V_r: (a, b) f^*=1 and (c, d) f^*=2.

5.3.4 Hydrodynamic forces in phase with cylinder accelerations

Coefficients of the hydrodynamic forces in phase with the cylinder acceleration (C_{ax}, C_{ay}) as well as the corresponding effective added mass coefficients (C_{Mx}, C_{My}) where $C_{Mx} = C_{Ax}+C_a$ and $C_{My} = C_{Ay}+C_a$ ($C_a \approx 1$ for a circular cylinder [7] having been incorporated into Eqs. (3.9) and (3.11)) are now evaluated based on Eqs. (5.10), (5.12) and (5.14)-(5.15). Throughout the lock-in range, these amplitude-dependent coefficients are variable, thereby influencing the dual-resonant *x*-*y* oscillation frequencies.

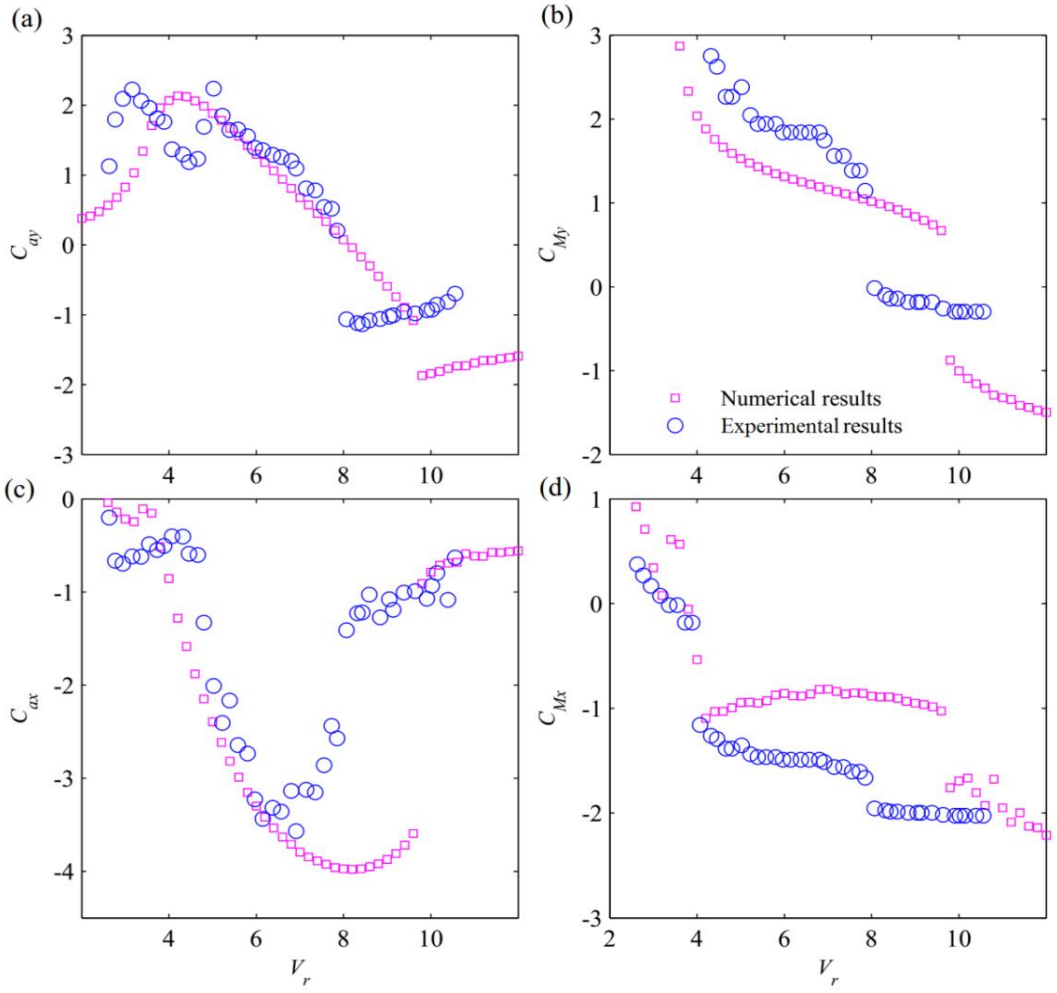

Figure 5.6: Plots of (a) C_{ay}, (b) C_{My}, (c) C_{ax} and (d) C_{Mx} as function of V_r with experimental comparisons.

By assigning the same m^* and ξ as in Figure 5.4, numerical results of C_{ay}, C_{My}, C_{ax} and C_{Mx} are plotted as a function of V_r in Figure 5.6 (a-d), respectively. Experimental results of [137] based on the post-processing approach in [9] are also compared in Figure 5.6. In the CF direction, a qualitative agreement between numerical and experimental results can be noticed with, approximately, $-2 < C_{ay} < 2$ and $-2 < C_{My} < 3$, revealing a transition from a positive to negative C_{ay} and C_{My} as V_r is increased. When the associated C_{vy} in Figure 5.4 (a) achieves its minimum value ($V_r \approx 7$ experimentally and $V_r \approx 8$ numerically), the inertia component C_{ay} in Figure 5.6 (a) becomes zero and changes its sign across the resonance. This indicates the decreasing effective added mass C_{My} as shown in Figure 5.6 (b) and confirms an increment in the effective oscillation frequency of a low mass-damping cylinder as V_r

is increased [9, 76]. In the IL direction, C_{ax} plots in Figure 5.6 (c) reveal their negative values throughout the considered V_r range. This results in a lower effective added mass C_{Mx} in Figure 5.6 (d) than C_{My} in Figure 5.6 (c): this seems feasible since dual 2:1 resonances require a considerable augmentation in the IL oscillation frequencies in the case of f^*=1. Recent computational fluid dynamics study also revealed negative effective added masses whose values are as low as nearly -2, depending on f^* [78]. For a given ξ = 0.001 as in Figure 5.5, the influence of varying m^* and V_r on both C_{ay} and C_{ax} is now illustrated in Figure 5.7 with f^* =1 and 2. For f^* =1, C_{ay} plots throughout the considered range of m^* display a typical transition from being positive to negative when increasing V_r (Figure 5.7 (a)). As m^* is increased, such transition regime becomes apparently limited with decreasing absolute C_{ay} values, owing to the reduced A_y/D response and its synchronization range. These overall observations also hold in the case of f^* = 2 (Figure 5.7 (c)). On the contrary, the isolines of C_{ax} reveal both quantitative and qualitative differences between the cases of f^* = 1 and 2. In the f^* = 1 case (Figure 5.7 (b)), C_{ax} are overall negative, as discussed above, and the absolute values of C_{ax} are greater than those of C_{ay} as m^* decreases towards the resonance forever regime ($m^* \approx 0.52$). In the f^* = 2 case, the C_{ax} isolines in Figure 5.7 (d) now reveal the patterns similar to those of C_{ay} in Figure 5.7 (a) and (c) with positive (low V_r), zero and negative (high V_r) coefficients. This is in qualitative agreement with the recent study of Bao et al. [78]. It is also worth remarking that the zero C_{ay} and C_{ax} lines suggest the reduced velocities at maximum attainable responses depending on m^*. As m^* is decreased, A_{ym}/D and A_{xm}/D occur at higher V_r due to the increased lock-in range.

5.4 Maximum Dual-Resonant Responses

It is well known that the maximum amplitude of CF-only VIV (A_{ym}/D) is a function of the combined $m^*\xi$ parameter [23, 33]. However, this is no longer valid in the case of CF/IL VIV where maximum amplitudes (A_{ym}/D, A_{xm}/D) are functions of m^* and ξ [30]. In this study, a new alternative way of representing A_{ym}/D and A_{xm}/D versus varying m^* and ξ is presented through the analytical solution derived in Section 5.2 (Eqs. (5.24-29)).

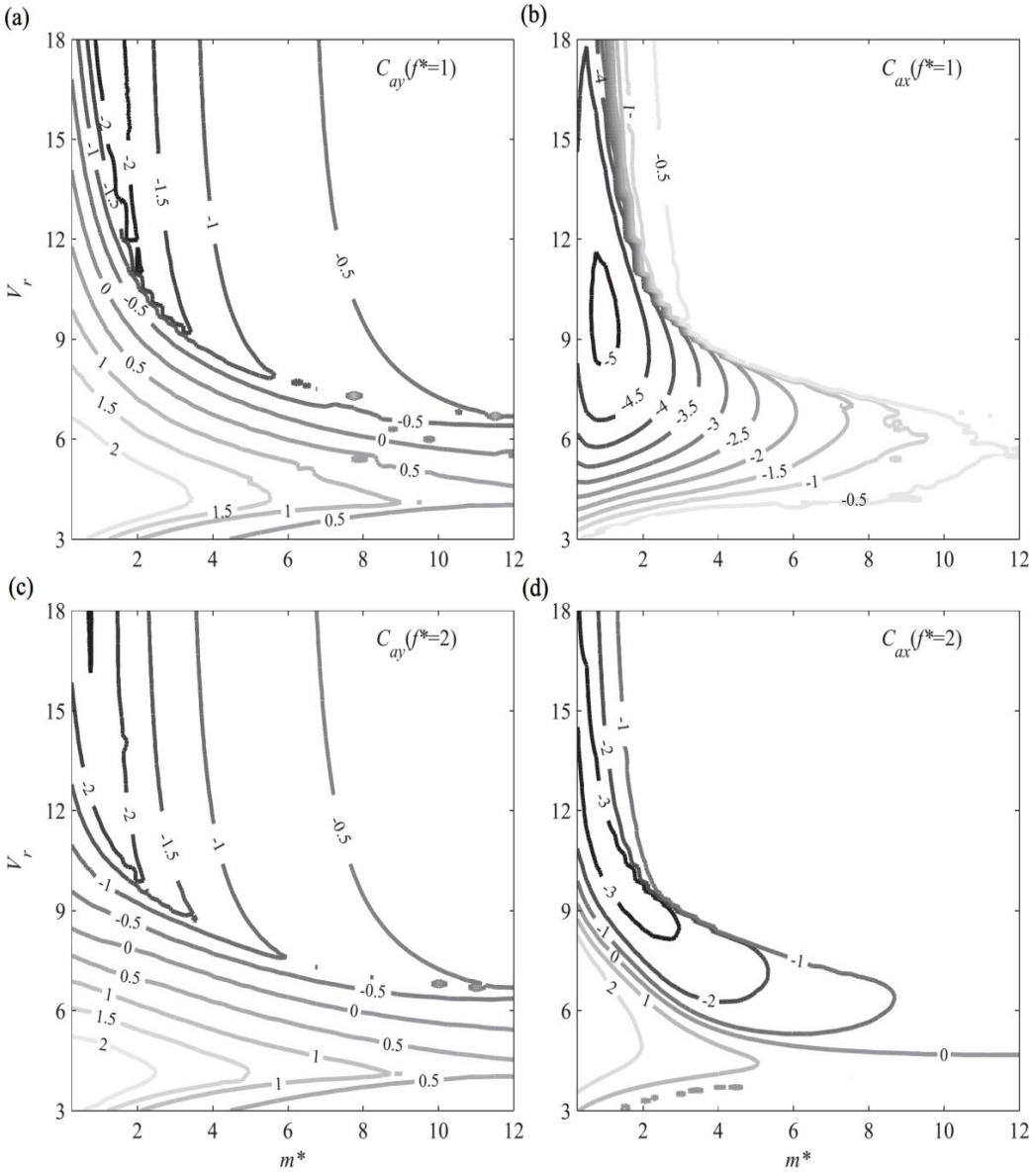

Figure 5.7: Maps of (a, c) C_{ay} and (b, d) C_{ax} as functions of m^* and V_r: (a, b) f^*=1 and (c, d) f^*=2.

5.4.1 Maximum attainable amplitudes and hydrodynamic coefficients

Based on the deduced oscillation frequency function (Eq. (3.20)) and phase relations (θ_p-θ_x = θ_q-θ_y ≈ π/2, θ_q+θ_y-θ_x ≈ 9π/10 and θ_p-2θ_y ≈ π/10) from Section 5.3.1 (Figure 5.1), contour plots of A_{ym}/D and A_{xm}/D in the f^* = 1 case are illustrated in Figure 5.8. At maximum responses, contour plots of the unsteady lift (C_l = $C_{l0}q$/2), unsteady drag (C_d = $C_{d0}p$/2) and amplified mean drag (C_{dv}) coefficients are illustrated in Figure 5.9.

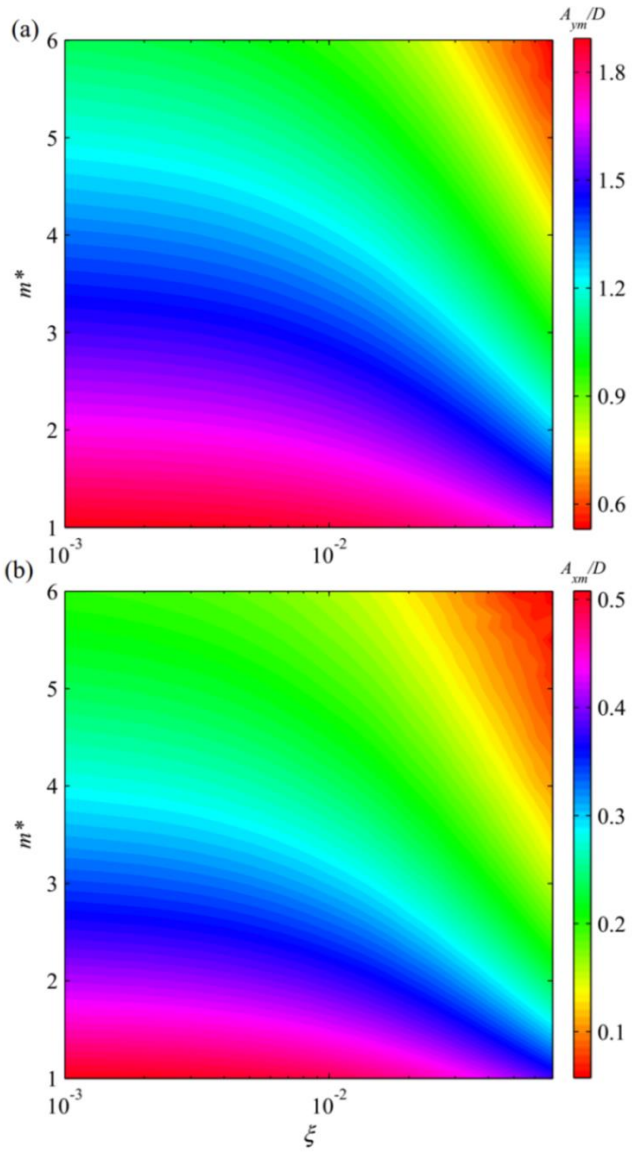

Figure 5.8: Contour plots of maximum dual-resonant responses as functions of m^* and ξ: (a) A_{ym}/D and (b) A_{xm}/D.

Figures 5.8 and 5.9 highlight how the variation of m^* and ξ has a significant effect on A_{ym}/D (Figure 5.8 (a)) and A_{xm}/D (Figure 5.8 (b)) as well as on C_L (Figure 5.9 (a)) and C_d (Figure 5.9 (b)). In general, A_{ym}/D, A_{xm}/D, C_l and C_d values increase as m^* or ξ decreases. The variation of m^* for a given ξ is seen to have a greater influence – as exhibited by the multi-colour response when noticing vertically – on the maximum responses and hydrodynamic coefficients than the variation of ξ for a given m^*. For the considered $1 \leq m^* \leq 6$ (where the effect of IL response is meaningful [9]) and $0.001 \leq \xi \leq 0.07$, the estimated ranges of analytically-obtained

values are as follows: $0.5 < A_{ym}/D < 2$, $0 < A_{xm}/D < 0.5$, $2 < C_l < 5$ and $0.3 < C_d < 0.5$. Hence, there is a considerable magnification of the unsteady lift and drag coefficients of the oscillating cylinder at the maximum response when compared to those (e.g. $C_{l0} = 0.3$ [7], $C_{d0} = 0.2$ [52]) of the stationary cylinder. This is in qualitative agreement with what have recently been experimentally [77] and numerically [78] observed.

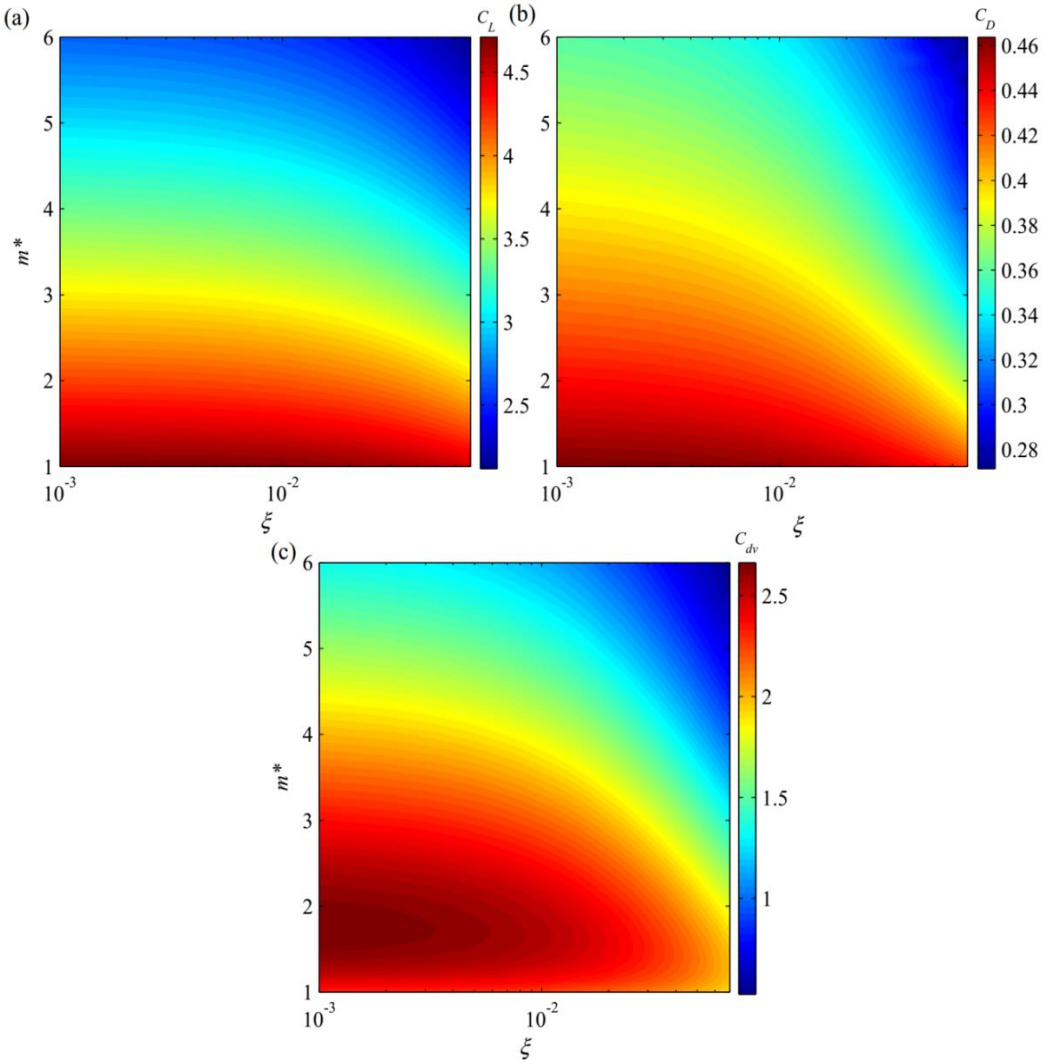

Figure 5.9: Contour plots of (a) C_l, (b) C_d and (c) C_{dv} as functions of m^* and ξ, associated with Figure 5.8.

With regard to the VIV-induced mean drag, the features of C_{dv} contours in Figure 5.9 (c) are generally similar to those in Figure 5.8 (a) due to the dependence of C_{dv} on A_y/D. The position of the peak $C_{dv} \approx 2.7$ is found to appear at $m^* \approx 1.8$ and $\xi \approx 0.001$. This analytically-obtained C_{dv} (2.7) is found to be comparable to that (2.8)

numerically obtained from Eq. (5.35). In practice, the design near such a low $m^*\xi$ should be avoided since the associated peak C_{dv} could render a large downstream equilibrium of the structure, the associated bending or axial stress due to the additional displacement and a possible collision or wake interference with the adjacent structural system.

5.4.2 Effects of structural nonlinearities and empirical coefficients

Next, a shortcoming of using the linear structural oscillators in the 2DOF VIV prediction is underlined through Figure 5.10 in comparison with Figure 5.8, by accounting for the effect of m^* and ξ. When system nonlinearities are omitted from Eqs. (3.9) and (3.11), analytical results of A_{ym}/D and A_{xm}/D in Figure 5.10 are obtained based on Eqs. (5.30)-(5.33). To also appreciate the effect of a model empirical coefficient, two cases are analysed: (i) ε_y is based on the calibrated function in Eq. (3.18) depending on m^* (Figure 5.10 (a) and (c)) and (ii) $\varepsilon_y = 0.3$ [66] is fixed (Figure 3.10 (b) and (d)). In the first case, both quantitative and qualitative discrepancies in the IL response are evident when comparing Figure 5.10 (c) (linear model) to Figure 5.8 (b) (nonlinear model). Due to the lack of CF/IL coupling terms, the predicted A_{xm}/D values are very low. On the contrary, the effect of CF nonlinearities on A_{ym}/D is seen to be negligible (Figure 5.10 (a) vs. 5.8 (a)) when applying Eq. (3.18) to the analysis case of $f^*=1$. Nevertheless, this would not hold when $f^*\neq 1$. In the second case, by specifying $\varepsilon_y = 0.3$, both quantitative and qualitative differences in both CF and IL responses are remarkable when comparing Figure 5.10 (b) and (d) (linear model) to Figure 5.8 (a) and (b) (nonlinear model). Since $\varepsilon_x = \varepsilon_y = 0.3$ and the linear y and x structural oscillators are identical, contour plots in Figure 5.10 (b) and (d) appear qualitatively similar with highly underestimated A_{ym}/D and A_{xm}/D. These results emphasize the importance of accounting for the system coupling nonlinearities and the dependence of empirical coefficients on a system parameter (e.g., m^*) in the modelling and prediction of combined CF/IL VIV.

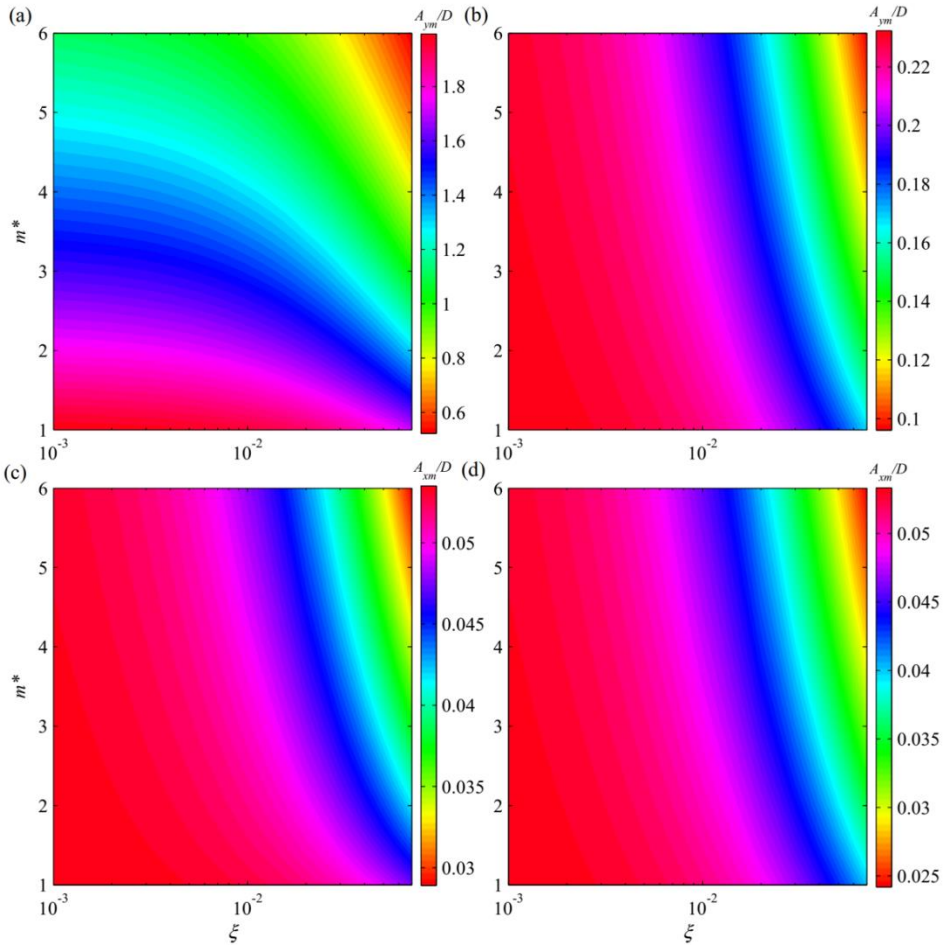

Figure 5.10: Contour plots of (a, b) A_{ym}/D and (c, d) A_{xm}/D as functions of m^* and ξ: (a, c) models with neglected nonlinearities and variable ε_y depending on m^* (Eq. 3.18); (b, d) model with neglected nonlinearities and fixed ε_y.

5.5 Conclusions

By accounting for cubic and quadratic nonlinearities of the proposed semi-empirical model, analytical closed-form expressions have been derived to parametrically characterize key coefficients of the unsteady hydrodynamic forces comprising the fluid excitation, inertia and added mass components and the amplification of the mean drag. The dependence of hydrodynamic properties on the quadratic coupling of transverse amplitude and fluid wake motion is underlined. Some numerical comparisons with available experimental results have been discussed.

Overall two-dimensional hydrodynamic coefficients of the oscillatory forces in phase with the cylinder velocities and accelerations depend on the system fluid-structure parameters, oscillation amplitudes, frequencies and phase relationships. The natural frequency ratio influences on the IL hydrodynamic mechanism. This is quite noticeable with respect to the force in phase with the cylinder acceleration and associated added mass, justifying a greater modification of the IL oscillation frequency during the lock-in or dual resonance exhibiting a variable figure-of-eight pattern. The mass ratio plays a significant role in both CF and IL hydrodynamics. The fluid excitation ranges are increased with decreasing mass ratio, becoming unbounded when approaching the very low-mass region. Some useful best-fit formulae as a function of mass ratio have been introduced to describe the maximum VIV-induced mean drag coefficient. New analytical contour plots of maximum dual-resonant responses and associated lift/drag force coefficients as functions of mass and damping ratios have been constructed. A shortcoming of using a linear structural oscillator model or a fixed empirical coefficient in the wake oscillator model for the 2DOF VIV prediction is highlighted.

Chapter 6

Three-dimensional VIV of Flexible Cylinders Subjected to Uniform Flow

In this chapter, a semi-empirical predictive model for vortex-induced vibrations (VIV) of a flexible cylinder subjected to a uniform flow is developed. The model consists of nonlinear equations of CF, IL and axial structural oscillations which, through fully-nonlinear lift/drag forces, are coupled to van der Pol-type wake-oscillators modelling fluctuating fluid forces. The geometric nonlinearities of the equations of the motions let the model capture interconnected structural vibrations and axial oscillations induced by lateral VIV of the cylinder. Solving the model via a finite difference numerical scheme, three-dimensional VIV responses of the cylinder are predicted. The model predictions are analysed through time and frequency domain, modal and stress analyses. Furthermore, the importance of considering the geometric and hydrodynamic nonlinearities is studied. Finally, a quantitative validation of the numerical results is performed as well.

6.1 Description of the Model and Evaluation of System Parameters

Deepwater explorations require risers with higher aspect ratios (length-to-diameter ratio, *L*/*D*) which are VIV-prone and can experience very high amplitude oscillations owing to vortex shedding. Figure 6.1 (a) shows a schematic representation of such a riser subjected to a uniform and unidirectional flow. The riser is supposed to have spatially uniform properties including mass/length (*m*), damping (*c*), diameter (*D*), bending stiffness (*EI*) and axial stiffness (EA_r). For the VIV system of a slender cylinder like this, structural geometric nonlinearities, including nonlinear coupling between lateral (CF and IL) and axial motions, and the impact of longitudinal oscillations become important [14]. Also, for a reliable and realistic prediction of VIV in offshore applications, both of IL and CF vibrations must be considered simultaneously [9]. That is, for an accurate and dependable prediction of slender marine risers' behaviours, a three-dimensional nonlinear structural model is required.

6.1.1 Structural equations of motions

The dimensional nonlinear partial-differential equations of the three-dimensional coupled lateral and axial motions of a flexible cylinder can be expressed as [138]:

$$\begin{aligned}(m+m_a)\ddot{u} + c\dot{u} + EIu^{(IV)} - (Tu')' &= EA_r(v''u' + v'u'') \\ &+ \frac{1}{2}EA_r\left(3u''u'^2 + u''v'^2 + 2v''v'u' + u''w'^2\right. \\ &\left. + 2w''w'u'\right) + F_x\end{aligned} \tag{6.1}$$

$$\begin{aligned}(m+m_a)\ddot{v} + c\dot{v} + EIv^{(IV)} - (Tv')' &= EA_rv'' + 2EA_rv''v' + EA_r(u''u' + v''v' + w''w') \\ &+ \frac{1}{2}EA_r\left(v''u'^2 + 2u''u'v' + 3v''v'^2 + v''w'^2\right. \\ &\left. + 2w''w'v'\right)\end{aligned} \tag{6.2}$$

$$(m+m_a)\ddot{w}+c\dot{w}+EIw^{(IV)}-(Tw')' \tag{6.3}$$
$$=EA_r(v''w'+v'w'')$$
$$+\frac{1}{2}EA_r\left(w''u'^2+2u''u'w'+w''v'^2+2v''v'w'\right.$$
$$\left.+3w''w'^2\right)+F_z$$

where u, v and w denote dynamic displacement in IL (X), axial (Y), and CF (Z) directions. The overdot and prime symbols show derivatives with respect to time t and space Y, respectively. m is the structural mass per unit length and m_a is the fluid added mass per unit length defined. E is the modulus of elasticity, I the area moment of inertia, A_r the cross-sectional area and T the space-related tension. Despite other physical parameters which are supposed to be spatially constant, T is considered to be variable. For a vertical riser with a top tension of T_{top}, variation of the tension along the span of the riser can be expressed as [110] $T=T_{top}-g(m-b)(L-Y)$ where g is the gravitational acceleration and $b=\pi/4g\rho D^2$ is the buoyancy force. For a horizontal riser, as it is the case for the experimental results of [94] and [139] which will be used in this paper, there is no tension variation due to weight of the riser and the buoyancy force. Hence, for a horizontal riser $T= T_{top}$.

6.1.2 Fluid forces, wake oscillators and empirical coefficients

Axial oscillations of the Eq. (6.2), through geometric nonlinear coupling terms, are induced by the IL and CF lateral motions of the slender cylinder which are excited by the unsteady fluid forces, caused by vortex shedding, denoted as F_x and F_z in Eqs. (6.1) and (6.3), respectively. These forces can be expressed as:

$$F_x=\frac{1}{2}\rho DV^2C_x \tag{6.4}$$

$$F_z=\frac{1}{2}\rho DV^2\,C_z \tag{6.5}$$

where C_x and C_z are the force coefficients in IL and CF directions, respectively. For a stationary cylinder, Figure 6.1 (b), these coefficients are corresponding to the drag and lift coefficients, respectively. When the cylinder oscillates, Figure 6.1 (c), due to its relative motion, the drag and lift forces are no longer in X and Z directions. In this case, as it is explained in previous chapters, these coefficients can be obtained in terms of lift and drag coefficients as:

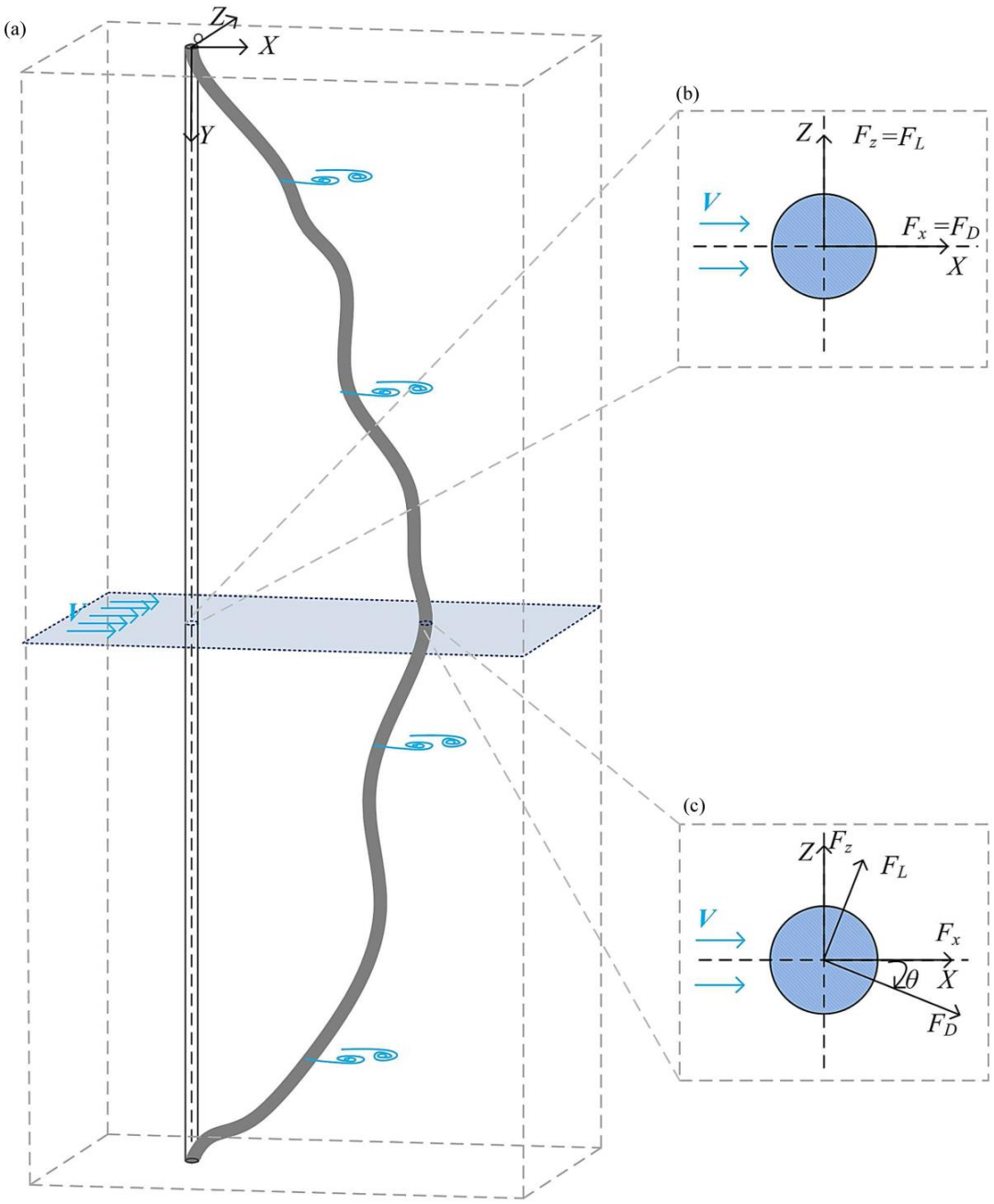

Figure 6.1: (a) Schematic of a riser at rest (hollow cylinder) and during VIV (filled grey cylinder); (b) fluid forces on an arbitrary section of the stationary riser; (c) fluid forces on an arbitrary section of the oscillating riser.

$$C_x = (C_D \cos\theta + C_l \sin\theta)\left(\frac{V_{rel}^2}{V^2}\right) \tag{6.6}$$

$$C_z = (C_l \cos\theta - C_D \sin\theta)\left(\frac{V_{rel}^2}{V^2}\right) \tag{6.7}$$

in which

$$\sin\theta = \frac{\frac{\dot{w}}{V}}{\sqrt{\left(1-\frac{\dot{u}}{V}\right)^2+\left(\frac{\dot{w}}{V}\right)^2}} \tag{6.8}$$

$$\cos\theta = \frac{1-\frac{\dot{u}}{V}}{\sqrt{\left(1-\frac{\dot{u}}{V}\right)^2+\left(\frac{\dot{w}}{V}\right)^2}} \tag{6.9}$$

where C_l is the time-dependent lift coefficient and $C_D = \bar{C}_d + C_d$ is the drag coefficient in which $\bar{C}_d = 1.2$ [7] is the mean drag coefficient of a stationary cylinder and C_d is the oscillatory drag coefficient. Substituting Eqs. (6.6)-(6.9) into Eqs. (6.4) and (6.5) yields

$$F_x = \frac{1}{4}\rho D V_{rel} C_{d0} p(V-\dot{u}) + \frac{1}{2}\rho D V_{rel}\bar{C}_d(V-\dot{u}) + \frac{1}{4}\rho D V_{rel} C_{l0} q\dot{w} \tag{6.10}$$

$$F_z = \frac{1}{4}\rho D V_{rel} C_{l0} q(V-\dot{u}) - \frac{1}{4}\rho D V_{rel} C_{d0} p\dot{w} - \frac{1}{2}\rho D V_{rel}\bar{C}_d\dot{w} \tag{6.11}$$

where V_{rel} is the relative velocity and is defined as:

$$V_{rel} = V\sqrt{\left(1-\frac{\dot{u}}{V}\right)^2+\left(\frac{\dot{w}}{V}\right)^2} \tag{6.12}$$

In the literature, for the sake of simplicity and deriving analytical solutions, it is usually supposed that the structural velocities compared to flow velocity are small which leads to the linearization and simplification of these nonlinear forcing terms [114]. Moreover, as it has been shown previous chapters, the models with such forcing terms are capable of explaining and predicting some of the important experimentally observed phenomena, for example, higher harmonics, dual resonance and mean drag amplification due to VIV [79]. In this chapter to keep the generality of the model, the fully nonlinear versions of these fluid forces are utilised.

The fluctuating time-dependent nature of the oscillatory lift and drag coefficients, as it was done for the rigid cylinder model, can be replicated by van der Pol equations which through acceleration terms are coupled to the equations of structural oscillations [66, 105, 112]:

$$\ddot{p} + 2\varepsilon_u \omega_f (p^2 - 1)\dot{p} + 4\Omega_f^2 p = \frac{\Lambda_u}{D}\ddot{u}, \tag{6.13}$$

$$\ddot{q} + \varepsilon_w \omega_f (q^2 - 1)\dot{q} + \Omega_f^2 q = \frac{\Lambda_w}{D}\ddot{w}, \tag{6.14}$$

where St=0.18 is the Strouhal number and ε_u, ε_w, Λ_u and Λ_w are empirical coefficients which can be obtained through calibration of the model with the experimental results. As it is explained in Chapters 2 and 3, there is no clear physical interpretation of these coefficients; however, to make the comparison with the previous results possible, following the rigid cylinder model presented in previous chapters, here ε_u=0.3, Λ_u=12 and Λ_w=12. Also, to relate one of these coefficients to the important physical parameters of the VIV system, using the Eq. (35) of [66] and Eq. (6.2) of [36], ε_w can be expressed as:

$$\varepsilon_w = \frac{\Lambda_w}{4\frac{S_G + 1.3}{C_{l0}}\left(2\frac{S_G + 1.3}{C_{l0}}(1 + 1.12\alpha + 0.3\alpha^2)\log 0.41\mathrm{Re}^{0.36}\right)^2 - 1} \tag{6.15}$$

6.1.3 Coupled wake-structural oscillators and numerical scheme

Substituting the nonlinear fluid forcing terms of Eqs. (6.10) and (6.11) into the Eqs. (6.1) and (6.3), respectively, and utilising the empirical coefficients introduced in previous section in the wake oscillator equations, a system of nonlinear partial differential equations is formed which is employed for prediction and description of the behaviour of a tensioned marine riser undergoing VIV. To this end, similar to [105], [108] and [14], these equations are solved via a stable centred finite difference scheme in both space and time domains for a beam-cable with pinned-pinned boundary conditions which initially is at rest; and wake oscillators with initial conditions of p=2 and q=2. This numerical solution is developed via Matlab programming language. To assure that the numerical results are accurate, convergence tests are done. Using this code, on a Dell Optiplex 7010 PC with Intel® Core-i7 3.4 GHz processors and 16 GB of RAM, each second of the numerical VIV simulations, wit a time step of 10^{-4} s, takes 23 and 76 s long for cases considered in Chapters 6 and 7, respectively. In next sections, the results of the numerical solution of the model are qualitatively and quantitatively compared with experimental results. These comparisons, apart from validating the model predictions, investigate that

whether the values and relations suggested for the empirical coefficients of the model are correct. This is important because all the phenomenological models have empirical coefficients which are used for calibration of the model with the experimental results. However, in this chapter, to make it possible to compare the results with the other similar models, the values of these parameters are chosen from the literature and for one parameter, ε_w, a relation is introduced, Eq. (6.15). Hence, the capability of the model in replication of the experimental results would validate the suggested values and relations.

6.2 Model Predictions and Discussion

The semi-empirical model presented in the previous section is solved numerically based on the experimental riser model of [94, 140]. The properties and given parameters of this experiment are summarised in Table 6.1. The model predictions are discussed and are qualitatively compared with experimental observations. Moreover, in the cases where the comparison are made between numerical predictions at different flow velocities, the velocities are chosen to be V=0.3, 0.4, 0.8, 1 m/s to capture more aspects of three-dimensional VIV of elastic cylinders.

Table 6.1: Parameters of the riser models used for validation of the semi-empirical model.

Parameters	Experiment by [94, 140]
Length, m	28
Inner diameter, m	0.016
Outer diameter, m	0.015
Mass ratio	1.0
Bending stiffness, N.m^2	153.7
Axial stiffness, N	5.11×10^6
Pretension, N	700
Range of Reynolds number	3000-10000

6.2.1 Space-time variations of structural oscillations

Figure 6.2 shows the model predictions of normalised three-dimensional displacements of the riser model in the space-time domain. Moreover, these results illustrate that the frequency of oscillations in the IL and axial directions are almost

twice of that in the CF direction, e.g. see section AA of Figure 6.2 (a), (e) and (i). These higher oscillation frequencies caused by higher excitation frequencies infer that the structure might undergo higher vibration modes in the IL and axial directions. The spatio-temporal plots of structural oscillations at V=0.3 m/s and V=0.4 m/s clearly confirm this. The comparison between the results at these moderate velocities, also, suggest that in the CF direction the riser undergoes single-mode oscillations while in the IL and axial directions more than one mode contributes to the responses. To investigate which modes contribute to the structural responses, a proper modal analysis is required which will be performed and presented in the following sections. However, as it was mentioned earlier, the results of Figure 6.2 can provide some visual information such as higher vibrating mode of IL and axial oscillations.

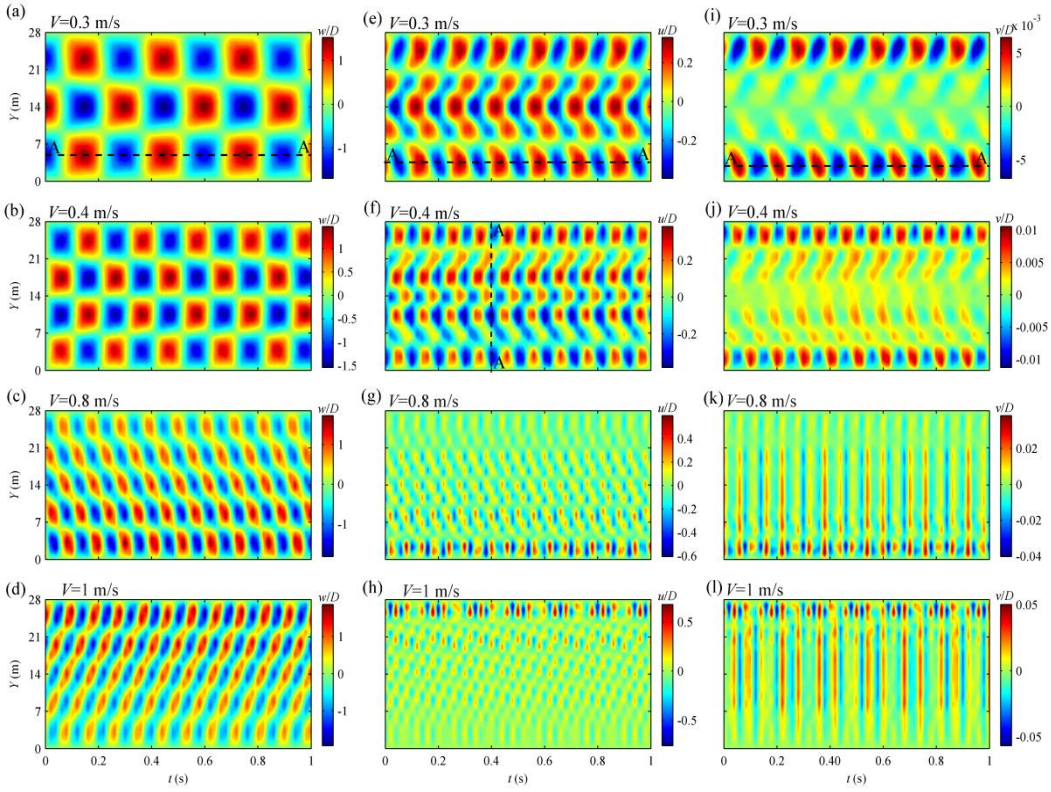

Figure 6.2: Spatio-temporal plot of: (a-d) CF oscillations; (e-h) IL oscillations; (i-l) axial oscillations.

Experimental studies have shown that the higher the oscillation mode be, the more probable the travelling waves are [141]. This deduces that travelling waves appear in the IL direction prior to CF direction. In the present results of Figure 6.2, at

V=0.3 m/s the responses are heavily dominated by the standing waves. As the flow velocity increases to V=0.4 m/s, while the standing waves still dominate the responses, transition to travelling wave starts in the IL response. For example, by following the variation of colours along the section A-A (dashed line) in Figure 6.2 (f), this transitional response can be distinguished. At higher velocities, higher vibrating modes are excited which consequently make the occurrence of travelling waves more probable. Therefore, at V=0.8 and 1 m/s which the excitation frequency is high enough, the responses are dominated by the travelling waves. In Figure 6.2 (c), (g) and (k) these travelling waves propagate towards the bottom end boundary of the riser model and in Figure 6.2 (d), (h) and (l) they propagate in the other direction. This is consistent with the results of [108] in which they reported arbitrary propagation directions.

The overall comparison between the spatio-temporal plots of Figure 6.2, also, demonstrates that the amplitudes of oscillations increase as V increases. However, while this increase in the CF and IL directions is gradual, in the axial direction it happens with a higher rate and results in considerable longitudinal oscillations at high flow velocities (Figure 6.2 (k) and (l)). Hence, the importance of axial motions is fortified at higher flow velocities. Moreover, at moderate velocities where the standing waves dominate the responses, maximum axial displacement occurs near two ends of the riser and the midsection of the riser has no longitudinal displacements. On the other hand, at high V that travelling waves are dominating, the amplitude of longitudinal oscillations increases monotonically towards the direction of wave propagation. Further investigation of the results depicted in Figure 6.2, will draw a clearer picture of the observations made in here. The frequency domain analysis of these results is presented in the next section.

6.2.2 Frequency domain analysis and higher harmonics

The results presented in the previous section suggested that the frequencies of IL and axial oscillations are almost twice of that in the CF directions. The frequency domain analysis of those spatio-temporal results is depicted in Figure 6.3. This figure shows the power spectrum of the structural oscillations along the span of the cylinder and confirms that the structure in the IL and axial directions vibrates at frequencies

twice of the frequency of CF oscillations. Moreover, these figures show that the dominant frequency of the three-dimensional structural oscillations increases as the flow velocity increases. However, the most important observations which can be made in these figures are the appearance of higher harmonics in the structural responses. These higher harmonics are specified and highlighted by rectangles surrounding them. Figure 6.3 (a-d) illustrates that in the transverse direction the structure oscillates under one dominating strong basic frequency and a third harmonic component which is identified by a black square. In the IL direction, Figure 6.3 (e-h), the frequency domain analysis confirms the existence of fourth higher harmonics. These results, also, illustrate that the contribution of the fourth higher harmonics to the IL oscillations is more than that of third harmonics to the CF oscillations. For example, the colour intensities of the higher harmonics in Figure 6.3 (a) and (e) shows that higher harmonics have more contributions to the IL oscillations than the CF motions.

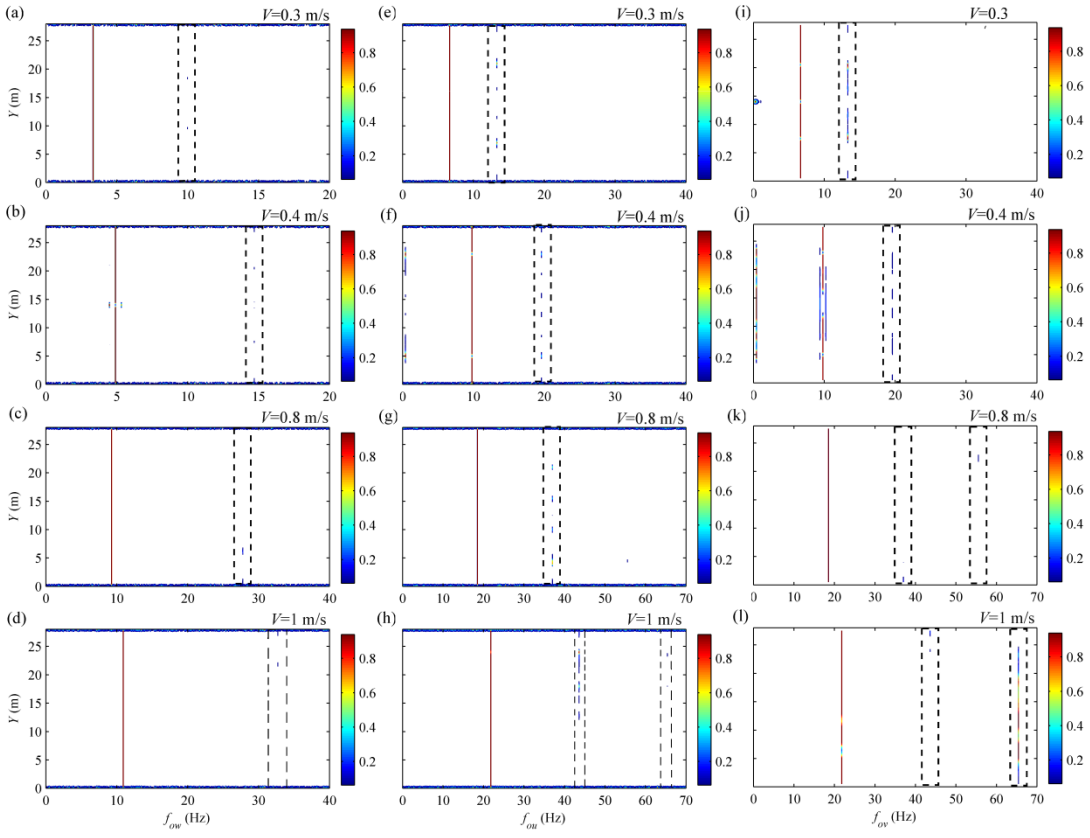

Figure 6.3: Frequency domain analysis of the numerical predictions of the structural oscillations in (a-d) CF direction; (e-h) IL direction and (i-l) axial direction.

The analysis of the axial oscillations, Figure 6.3 (i-l), shows that at the moderate flow velocities of V=0.3 and 0.4 m/s the cylinder experiences axial oscillations with fourth higher harmonics involved. At higher flow velocities, V=0.8 and 1 m/s, in addition to the fourth higher harmonics, the sixth higher harmonics are involved as well. Moreover, the results suggest that the importance of this sixth harmonic component is fortified as the flow velocity increases. For instance, the comparison between sixth harmonic components of Figure 6.3 (k) and (l) shows that at V=1 m/s this harmonic component is more significant. Likewise, the comparison between second and sixth harmonic components of Figure 6.3 (l) shows that at some sections along the span of the cylinder the higher harmonics dominate the response. These findings along with the results shown in previous section and the experimental results suggesting considerable contribution of the higher harmonics to the fatigue damage of an elastic cylinder [81, 142], show the importance of considering axial oscillations.

It is worth mentioning that in the experimental results, the higher harmonics are observed in both forces and structural responses. However, since in semi-empirical models both of the wake oscillator and the structure oscillate at the same frequencies; here just the frequency domain analyses of the structural responses are presented. Development of higher harmonics in the fluid forces can be explained, as it is proven by [79], through nonlinear fluid forcing terms of Eqs. (6.10) and (6.11). These nonlinear forcing terms, apart from higher harmonics, make the prediction of amplification of mean drag caused by VIV and the dual resonance and 2:1 oscillation frequency ratios possible, as well (see Chapter 5). These 2:1 oscillation frequency ratios result in highly repetitive Fo8 trajectories which have been experimentally observed and proven to be controlling the appearance of higher harmonics [9, 77]. Therefore, to predict the interconnection of higher harmonics and Fo8 trajectories, the nonlinear fluid forcing terms applied in the present model should be considered. In the next Section, the variation of the Fo8 orbits along the span of the riser and variations of mean IL displacements due to VIV are presented.

6.2.3 Fo8 orbits, dual resonance and mean drag amplification

Figure 6.4 show the mean position of the riser model at different flow velocities and depicts the Fo8 trajectories at different elevations along the span of the riser. Due to existence of dual resonance response, all of the trajectories are highly repetitive and similar to experimental and numerical results from rigid cylinder VIV studies (see Chapter 4), almost all of them are towards downstream (the direction of incoming flow is shown with an arrow) . It, also, can be observed that the trajectories at different locations on the riser model have different shapes. In some cases, such as the one specified by blue colour in Figure 6.4 (d), the shapes are affected by the higher harmonics frequencies involved in the responses. The shape of these trajectories is controlled by the phase difference between IL and CF oscillations which controls the higher harmonics in the structural responses [79]. Therefore, appearance of higher harmonic responses at some sections of the riser does not necessarily mean that all the sections along the span of the cylinder have higher harmonic responses. This is important when it is known that the contribution of these higher harmonics in the fatigue damage can be quite considerable [142] and consequently the overestimation of damages might lead to over-conservative costly riser designs. Apart from the variation of Fo8 trajectories, Figure 6.4 illustrates that mean IL deflection of the riser model increases with the increase of flow velocity, Figure 6.4 (e). This increase is due to mean drag amplification which in here displaces the riser model in IL direction up to 30 diameter [143]. The mean drag coefficient for a cylindrical structure undergoing VIV, compared to a stationary cylinder at similar flow velocity, is amplified. It is proven that this amplification can be expressed in terms of CF vibration amplitude [7, 135]. Moreover, in Chapter 5 it was shown that the IL nonlinear fluid forcing terms, under periodic assumed solutions, produce a constant forcing term which is a function of CF amplitude and can be interpreted as VIV-induced drag force. Therefore, as the flow velocity increases the structure oscillates at higher CF amplitudes which in turn amplifies the mean drag coefficient and increases the mean IL displacement of the structure. The present model, through the nonlinear forcing terms, is able to capture these interrelated and interactive behaviours.

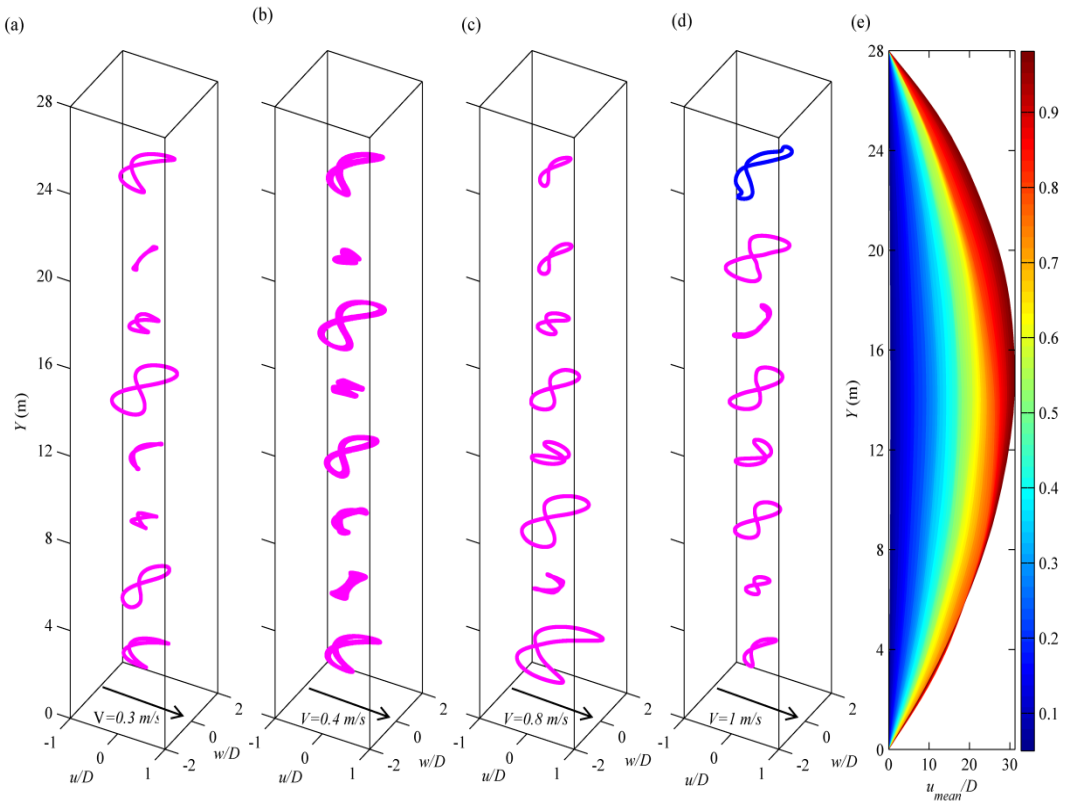

Figure 6.4: (a-d), Variation of Fo8 trajectories along the span of the riser; (e), mean IL displacement at different flow velocities.

6.2.4 Modal decomposition: multi-mode vibrations and mode switching

For a pined-pined riser model, the time-varying shape of the model can be defined as a summation of sinusoidal mode shapes [83]:

$$\begin{bmatrix} u(t,Y) \\ v(t,Y) \\ w(t,Y) \end{bmatrix} = \sum_{n=1}^{\infty} \begin{bmatrix} W_{un}(t)\varphi_n(Y) \\ W_{vn}(t)\varphi_n(Y) \\ W_{wn}(t)\varphi_n(Y) \end{bmatrix}, \quad Y \in [0, L] \tag{6.16}$$

where n is the mode number, W the modal weight and $\varphi_n(Y)=\mathrm{Sin}(n\pi Y/L)$ the mode shape. Via this assumption, the mode/modes which are involved in the structural oscillations in all directions can be extracted.

Figure 6.5 shows the first five dominant vibration modes which are involved in the structural responses of the semi-empirical model. In each figure, the horizontal axis is the mode number and the vertical axis shows the power of vibration modes which are normalized with the power of first dominant mode in the corresponding

direction and flow velocity (each figure also shows the magnitude of maximum power in dB/Hz). The analysis of the responses at moderate flow velocities, as it could be deduced from the time histories of Figure 6.2, shows that the CF motions are single-mode oscillations while in the IL and axial directions the cylinder undergoes multi-mode VIV which was observed in many experimental studies [12, 81, 83]. These results also suggest that at V=0.3 m/s, where the responses are dominated by standing waves, in the IL direction only the symmetric modes (1,3,5,…) are excited and only even modes are involved in the axial motion. The analytical explanation of such behaviour can be found in the literature of cable dynamics which is out of the scope of the present paper [144]. However, in the following sections, where the effects of the geometric and hydrodynamic nonlinearities are studied, it will be explained that which terms are responsible for this behaviour. With the increase of flow velocity to V=0.4 m/s and transition of responses to travelling waves, the vibrating modes other than symmetric (antisymmetric) can involve in IL (axial) oscillations, as well. Following this trend, at high flow velocities of V=0.8 and 1 m/s, in which the travelling waves dominate the responses in all CF, IL and axial directions, multi-mode VIV with symmetric and antisymmetric modes contributing collectively occurs in all these three directions. The experimental studies have shown that when a structure undergoes multi-mode VIV, the dominant mode of oscillations can momentarily switch from one mode to another [84]. Figure 6.6 depicts the time variation of modal weights of first five dominant modes of structural oscillations presented in Figure 6.5. As these plots illustrate, most of the time, one particular mode which is presented with blue colour dominates the response. However, there are some special moments in which other modal weights overtake the blue line. For instance, in Figure 6.6 (e), the colourful dashed lines indicate the moments when the mode with the corresponding colour temporarily becomes dominant. Moreover, these time histories infer that almost all of the vibrating modes contributing to the structural responses oscillate with first and second harmonic frequencies in the CF and IL/axial directions, respectively. However, in some cases, the excited mode oscillates at higher frequency equal to the frequency of the higher harmonics involved in the structural responses. For example, in Figure 6.6 (a), (e) and (i), the modes represented with purple colour oscillate with

the frequency of third, fourth and fourth harmonics, respectively. Furthermore, at V=1 m/s the dominant mode of axial oscillations clearly vibrates at three frequencies which, based on the results presented in the previous section, are the second, fourth and sixth harmonics.

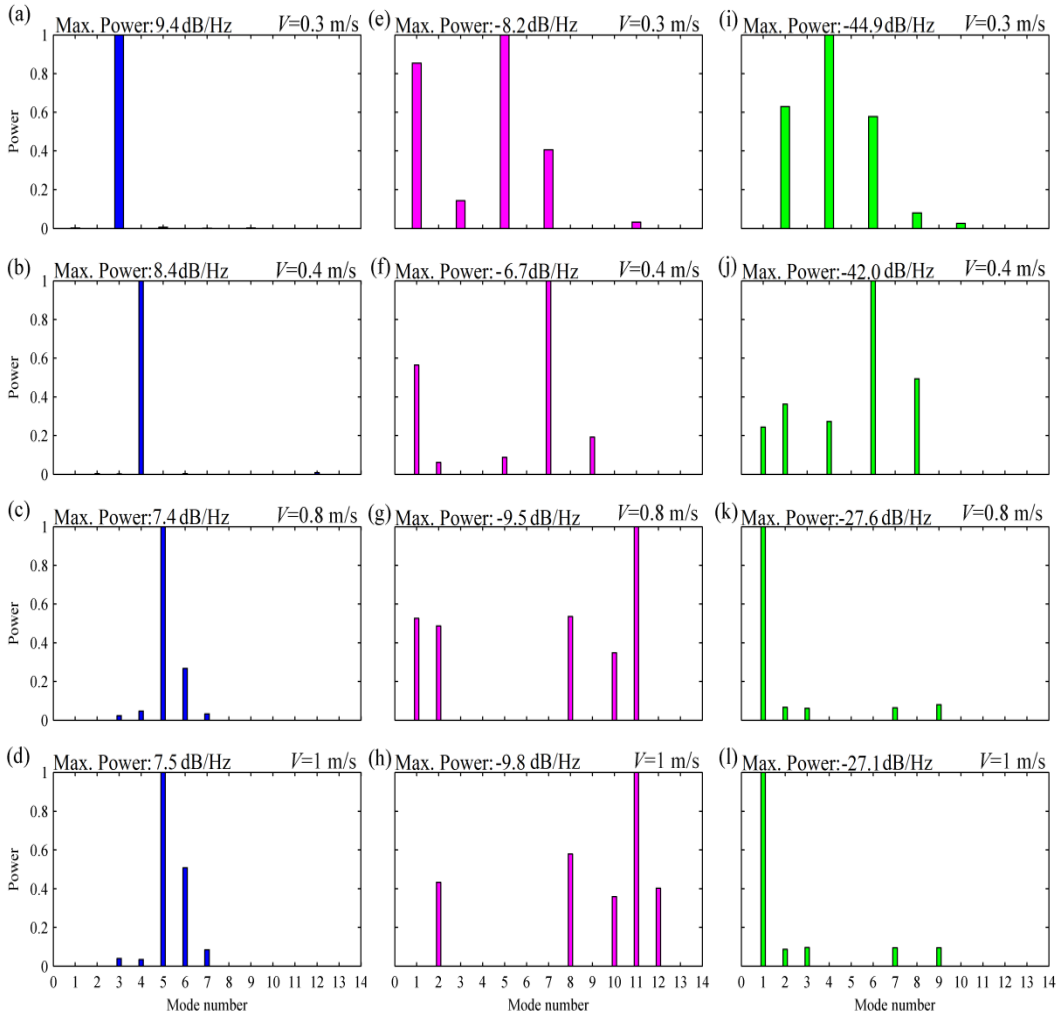

Figure 6.5: Modal decomposition of structural responses in (a-d) CF direction; (e-h) IL direction; (i-l) axial direction.

6.2.5 Stress analysis: bending, axial stresses and dynamic tension

The numerical predictions of the structural responses can be utilised for stress analysis and finding space-time variation of dynamic stresses. To this end, approximations of bending stresses induced by CF and IL oscillations, σ_w and σ_u, respectively, are [142]:

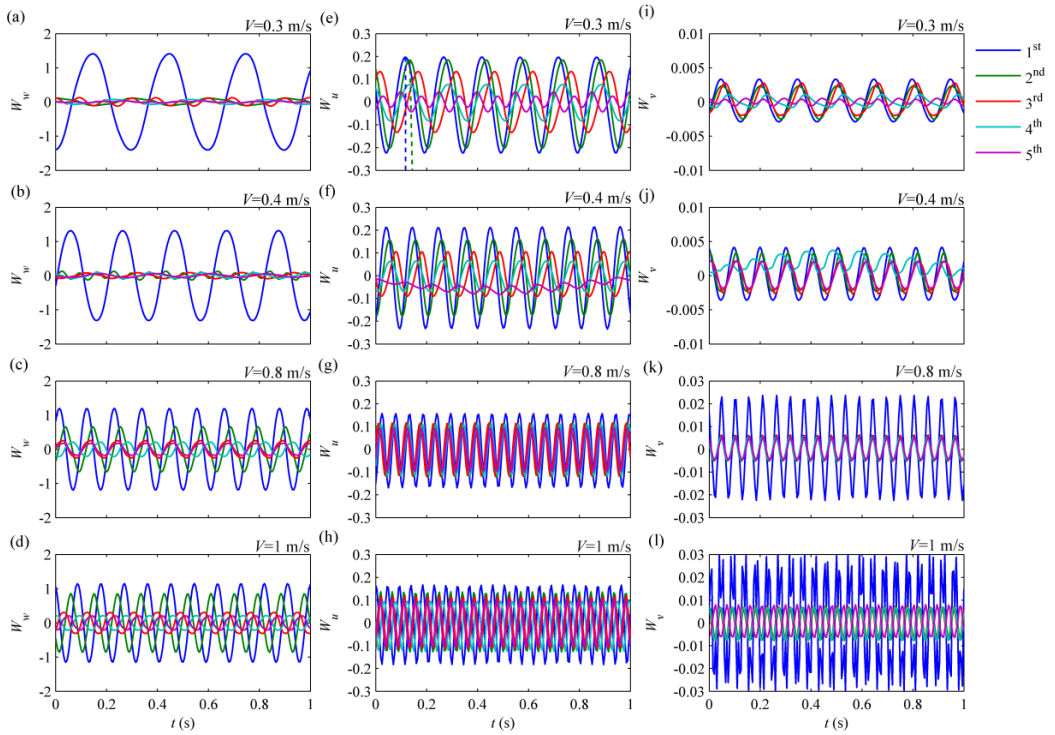

Figure 6.6: Modal weights of the first four dominant modes involved in the responses of: (a-d) CF oscillations; (e-h) IL oscillations; (i-l) axial oscillations.

$$\sigma_w(Y,t) \approx \frac{D}{2} E w''(Y,t) \tag{6.17}$$

$$\sigma_u(Y,t) \approx \frac{D}{2} E u''(Y,t) \tag{6.18}$$

and the axial stress σ_v, can be accurately approximated as [145]:

$$\sigma_u(Y,t) \approx E \frac{1}{1+x'^2}\left(v' + u'x' + \frac{1}{2}(u'^2 + v'^2 + w'^2)\right) \tag{6.19}$$

in which $x(Y)$ is the mean in-line position of the riser under VIV. Figure 6.7 shows the spatio-temporal plots of each of these bending and axial stresses.

An alongside comparison of CF bending stresses at moderate flow velocities with Figure 6.2 (a) and (b) illustrates that maximum stresses occur in the peaks while in nodes the bending stress is zero. To draw a clearer picture of the system behaviour, the variation of dynamic CF bending stresses, in Figure 6.7 (a), along the specified sections of A-A, B-B, and C-C is described. In section A-A stress variations along the span of the riser model in a certain moment of time is seen and it can be observed that the structure is vibrating in symmetric modes. The time

variations of σ_w in one of the modal peaks are followed in section B-B which shows how it interchanges from tensile to compressive stress. And section C-C illustrates that dynamic tension in the modal node constantly remains zero. However, in Figure 6.7 (a) and (b) new patterns can be distinguished which were not observed in Figure 6.2 (a) and (b). For instance, following the variation of σ_w along the D-D section shows that even though the cylinder vibrates in the third mode, in this particular moment of time, a 6^{th}-mode-like behaviour can be observed [143]. Moreover, a comparison between time variations of stresses at sections B-B and E-E shows that in each period of oscillation the modal peak three times goes through maximum absolute stresses while at section E-E the structure for six times experiences the maximum stress corresponding to that section. Although the maximum stress at section E-E is lower than section B-B, since it occurs in higher frequency it may cause more severe fatigue damages. The same analysis of CF bending stresses at high flow velocities, Figure 6.2 (c) and (d), shows that some of the aforementioned observations can be made in here as well. For example, although at V=0.8 m/s the fifth mode dominates the responses, following the fluctuations of σ_w along the section A-A of Figure 6.7 (c), a 10^{th}-mode-like behaviour can be identified. However, despite moderate flow velocities in which some sections of the cylinder experience stress fluctuations with frequencies twice of the structural oscillations, e.g. section E-E of Figure 6.7 (a), at high flow velocities no such section can be distinguished. This is due to the fact that at high flow velocities travelling waves dominate the CF structural responses. Moreover, owing to the same reason, no unstressed sections similar to section C-C of Figure 6.7 (a) can be found at high flow velocities.

Figure 6.7 (e-h) depicts the bending stresses in the IL direction. In this direction and at moderate V, despite CF bending stresses, there is no section on the riser which constantly undertakes zero stresses, and the maximum stresses do not necessarily occur at the modal peak. This may be due to the fact that CF oscillations are single-mode vibrations while in the IL direction multi-mode VIV happens. Figure 6.7 (e) and (f) together with Figure 6.2 (e) and (f) show that spatio-temporal variations of the IL bending stresses at moderate velocities resemble oscillations at the highest excited mode. For instance, at V=0.3 m/s, Figure 6.2 (e) and Figure 6.7

(e), 1st, 3rd , 5th and 7th vibration modes are excited and the bending stresses vary in a 7th -mode-like manner. Also, Figure 6.7 (e) and (f) compared with Figure 6.6 (e) and (f) show that the maximum IL bending stresses occur when two of these dominant vibration modes have equal modal weights. For example, in Figure 6.7 (e), sections A-A and B-B indicate the moments when the maximum compressive and tensile stresses occur, and Figure 6.6 (e) shows that at these moments two of dominant modes have similar modal weights. The analysis of IL bending stresses at V=0.8 and 1m/s shows that the same trends can be distinguished at higher flow velocities as well.

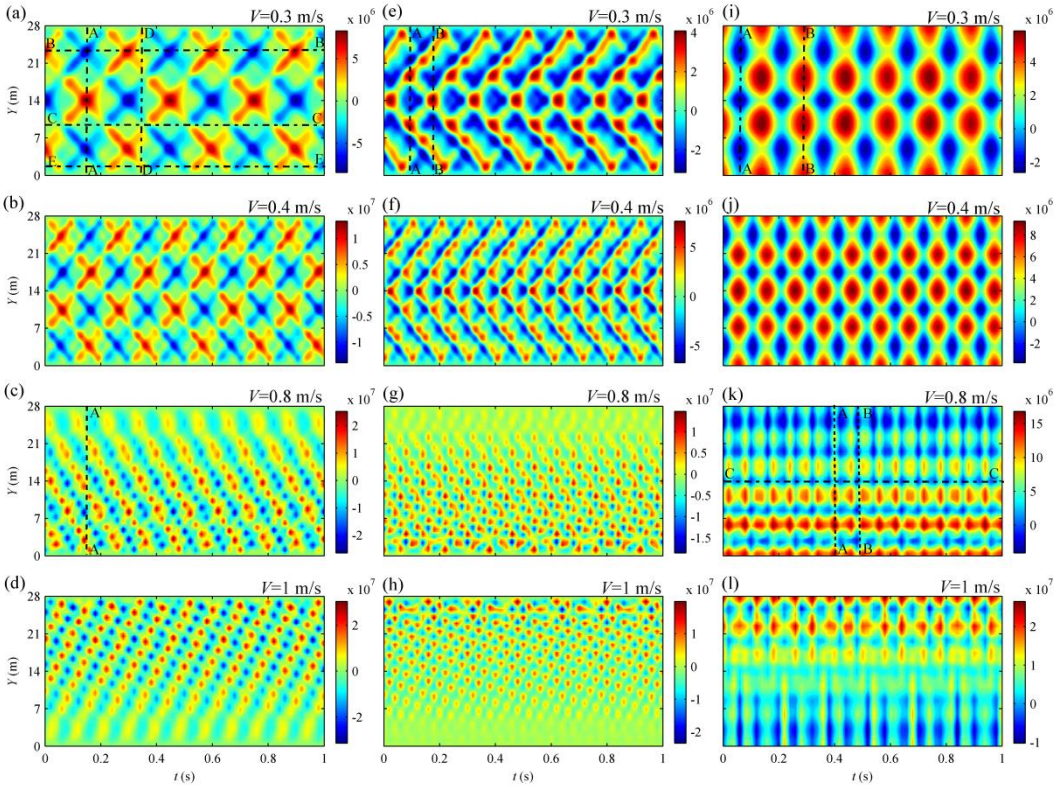

Figure 6.7: Spatio-temporal plots of (a-d) CF bending stress; (e-h) IL bending stress; (i-l) axial stress.

The time variations of axial stresses along the span of the riser model are plotted in Figure 6.7 (i-l). The figures show that in all velocities there is a mean axial stress which escalates as the flow velocity increases and can be interpreted as the effect of mean drag force and its consequent mean IL displacement. Previously in Eq. (6.2) it was shown that the axial motion is induced by CF and IL oscillations, hence the effect of these oscillations can be seen in axial stresses, as well. The

comparison of Figure 6.7 (i-j) with Figure 6.2 shows that the maximum compressive axial stresses occur at the location of CF modal peaks when in this direction the structure is at rest and in the IL direction has its maximum deflection, e.g. see section A-A of Figure 6.7 (i). Moreover, the maximum tensile axial stresses occur at CF modal nodes when the structure in both CF and IL directions has maximum deflection, e.g. see section B-B of Figure 6.7 (i). The results depicted in Figure 6.7 (k) and (l) confirms that the same behaviour occurs at high velocities as well, for instance, see sections A-A and B-B of Figure 6.7 (k). Moreover at high flow velocities in which the travelling waves are dominating, the axial stress increases in the direction of wave propagation. In other words, the areas of the cylinder with small oscillation amplitudes mostly experience compressive stresses while the sections undergoing larger oscillation amplitudes, where the wave propagates towards them, are mostly under tensile stresses. For instance, see the sections of the axial stresses above and below the section C-C of Figure 6.7 (k). Finally, the overall comparison between stresses in CF, IL and axial directions illustrates that although the oscillation amplitudes in these directions are not the same, the stresses in all directions have the same order of magnitude. Moreover, while the increase in CF and IL bending stresses with the increase of V is gradual, the axial stress grows rapidly and at V=1 m/s it reaches a maximum value similar to its corresponding CF bending stress. These results indicate the importance of axial oscillations and infer that their corresponding fatigue damages might be very similar [143].

The axial stresses shown in Figure 6.7 (i-l) can be expressed as dynamic tensions, $T_d=\sigma_v A$, as well. Analytical investigation of cable dynamics demonstrated that increase of the amplitude of CF and IL oscillations can cause outstanding increases in the dynamic compressive/tensile tensions. That is, the model riser might momentarily experience negative total tension, $T_t=T_0+T_d$, which results in impulsive motions, snapping and buckling responses. Hence, it is important to monitor the spatio-temporal variations of total tension. Figure 6.8 depict these variations and illustrate that in all velocities the mean total tension, $\bar{T}_t$, is more than the pretension at the end and grows as the flow velocity increases. This increase of $\bar{T}_t$ caused by the mean drag forces, in the experimental results, appears as mean end tension amplification [94]. Moreover, Figure 6.8 show that the amplitude of dynamic tension

fluctuations increases with the increase of flow velocity. As it can be seen, for the present cases, this amplitude is always less than T_0. However, it can be predicted that for lower pretensions or for vertical risers with variable pretensions, at similar flow velocities, the amplitude of compressive dynamic tensions may reach T_0 and cause negative total tensions. Therefore, choosing a proper pretension through checking $\bar{T}_t$ would be of substantial importance.

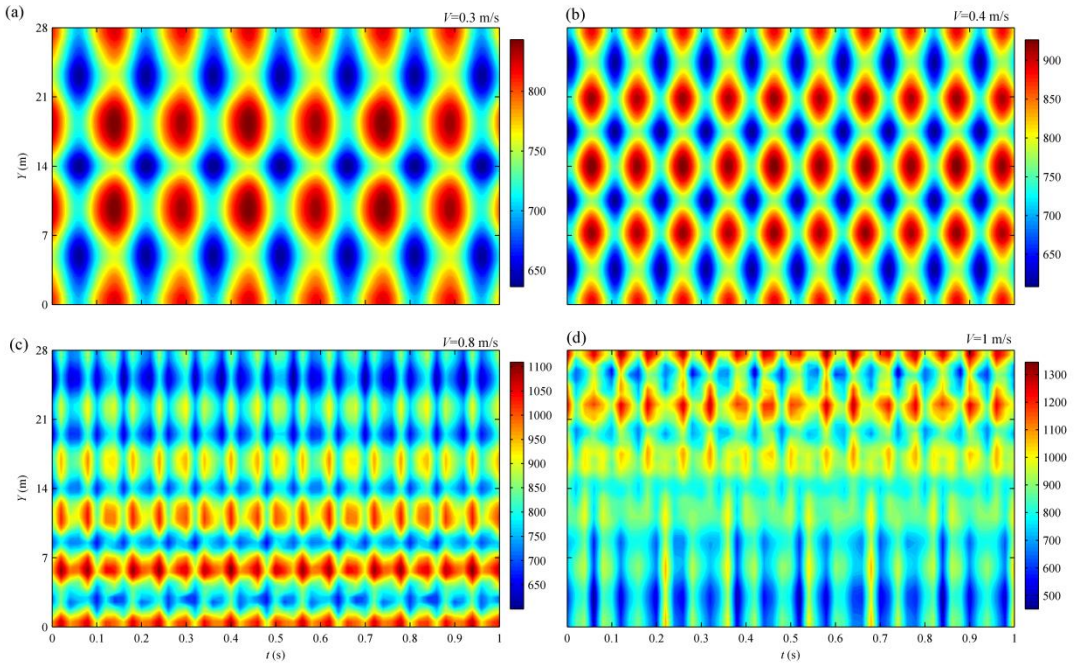

Figure 6.8: Spatio-temporal plots of the total tension, T_t=T_0+T_d.

6.3 Importance of Nonlinearities and Axial Motions

The results discussed in previous sections showed that increasing flow velocity fortifies the significance of the axial motions such that they can become as damaging to a slender structure as the CF motions. Moreover, the results illustrated the model capabilities in capturing number of experimentally observed phenomena such as multi-mode structural oscillations, dual resonance, variations of Fo8 trajectories along the span of the cylinder, mean drag amplification due to VIV, higher harmonics of the responses and transition from standing-wave-dominated to travelling-wave-dominated responses. Some of these phenomena, e.g. dual resonance and VIV-induced mean drag amplification, have been observed in experiments performed on elastically mounted rigid cylinders as well. In Chapter 5 it was shown

that, to capture these behaviours for a rigid cylinder undergoing VIV, the quadratic nonlinear fluid forcing terms of Eqs. (6.10) and (6.11) should be taken into account. In this section, the importance of considering geometric and hydrodynamic nonlinearities and axial oscillations, for predicting the aforementioned behaviours, is studied.

Figure 6.9 show the root mean square (RMS) amplitude of CF and IL vibrations and the mean IL deflection of the riser in three cases of fully nonlinear model (blue circles), neglecting the axial oscillations (purple squares) and neglecting geometric nonlinear terms (black diamonds). Since the importance of considering longitudinal oscillations and structural/hydrodynamic nonlinearities at high flow velocities was illustrated in the previous sections, the results in Figure 6.9 are obtained at low and moderate flow velocities of V=0.1, 0.15, 0.3 and 0.4 m/s. The comparison of the results illustrates that when the flow velocity is low, V=0.1 and 0.2, all three cases end up with similar predictions of the structural responses. At V=0.3, the axial oscillations yet have no considerable effect on the results whereas neglecting geometric nonlinearities results in the prediction of higher dominant modes for CF and IL oscillations and excessively high mean IL deflection. As the flow velocity increases to V=0.4, the previously seen effects of the geometric nonlinearities are fortified and axial oscillations become more influential. For example at this velocity neglecting the axial motions considerably affects the amplitudes of the IL oscillations. Hence, following the trends observed in Figure 6.9 and as it was shown in the previous sections, both of axial motions and geometric nonlinearities become more influential at higher velocities.

The effect of geometric nonlinearities at low and high flow velocities along with the influence of nonlinear forcing terms are further studied in Figure 6.10. To obtain these results, in Figure 6.10 (a-c), (e-g), (i-k) and (m-o) a model with nonlinear equations of motions and linear fluid forcing terms at V=0.25, 0.3 and 0.8 m/s, and in Figure 6.10 (d), (h), (l) and (p) a model with linear equations of motions and linear fluid forcing terms at V=0.8 m/s, are considered, respectively. Figure 6.10 (a-b), (e-f), (i-j) and (m-n) illustrates that when the quadratic nonlinear forcing terms are neglected, the structure in both CF and IL directions undergoes single-mode

oscillations which can be either a symmetric or antisymmetric mode and are dominated by standing waves. Such a model at V=0.8 m/s, Figure 6.10 (e), (g), (k) and (o), which higher modes are excited and travelling waves are more probable, predicts IL and CF responses which are dominated by travelling waves. Hence, it can be concluded that the quadratic hydrodynamic forcing terms in addition to the mean drag amplification, 2:1 oscillation frequency ratio and dual resonance are the causes of the symmetric-mode-only IL VIV and asymmetric-modes-only longitudinal oscillations at moderate flow velocities which were observed in Figure 6.2 and 5. Moreover, these results infer that the transition to travelling-wave-dominated responses is modelled through the geometric nonlinear terms. Further linearization of the model and neglecting geometric nonlinearities, Figure 6.10 (d), (h), (l) and (p), result in predicting dominating standing waves which contradict experimental observations. Thus, considering geometric nonlinearities for capturing transition to travelling waves at high flow velocities is necessary.

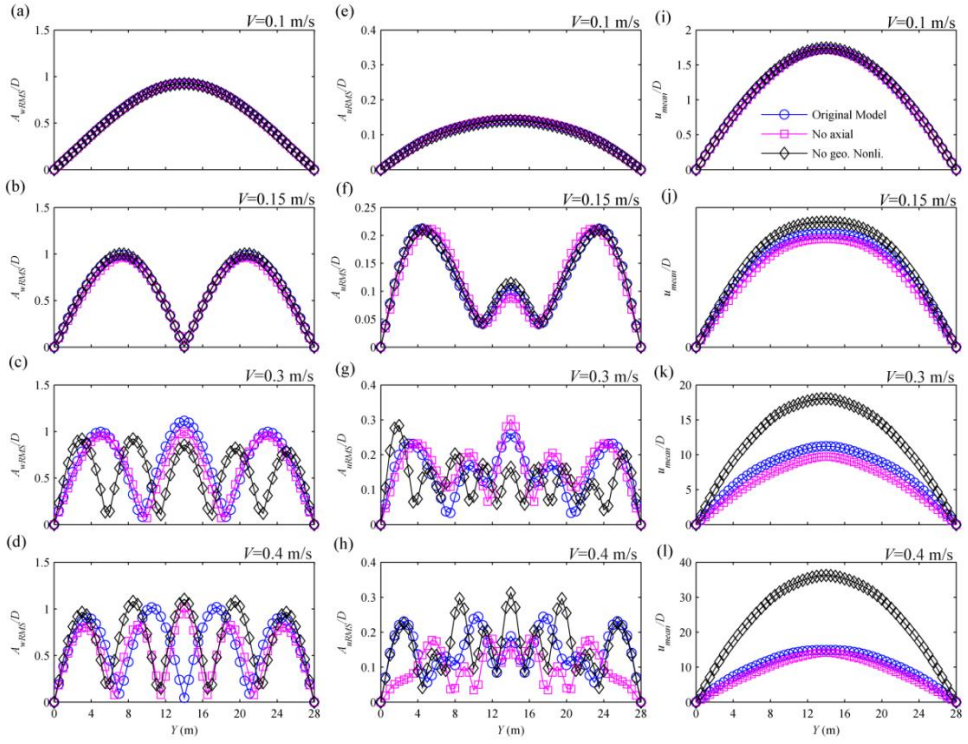

Figure 6.9: Effect of geometric nonlinearities and axial motions on the predictions of the model, (a-d) RMS value of the amplitude of CF oscillations along the span of the riser model; (e-h) RMS value of the amplitude of IL oscillations along the span of the riser model; (a-d) Mean IL displacement along the span of the riser.

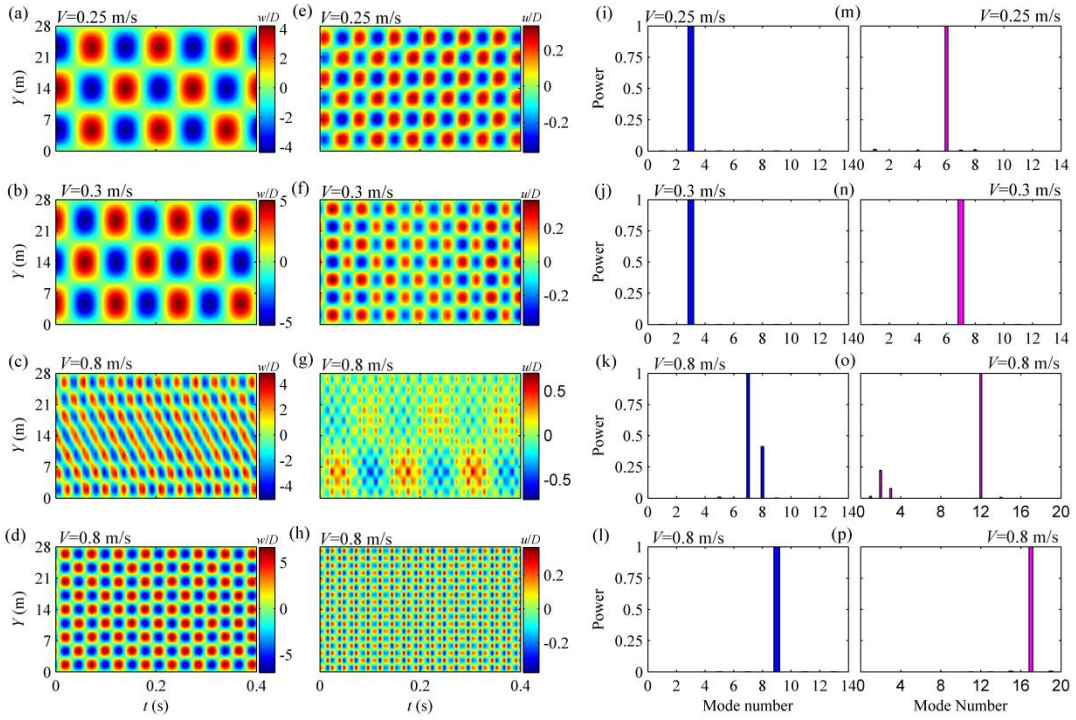

Figure 6.10: Effect of geometric/hydrodynamic nonlinearities on the model predictions. (a-d), CF oscillations; (e-h), IL oscillations; (i-l), modal decomposition of CF structural responses; (m-p), modal decomposition of IL structural responses.

6.4 Validation of The Proposed Model

The results presented in previous sections illustrated the qualitative agreement of the model predictions with the experimental observations. In the following sections, the numerical predictions of the amplitude and frequency responses and the dominant vibrating modes are quantitatively compared with the experimental results of [94, 140].

6.4.1 Amplitude responses

Figure 6.11 (a) and (b) shows the comparison between the maximum amplitude of CF and IL oscillations (A_{wM}/D, A_{uM}/D) of the experimental set of Table 6.1 and their corresponding numerical predictions. In both of experimental and numerical results, overall, the maximum amplitude increases with the increase of fellow velocity. This amplitude augmentation, as it is explained in [36], can be interpreted as the effect of the Reynolds number. However, with taking a closer look at both of the experimental and numerical results, a sawtooth behaviour can be distinguished

which in Figure 6.11 (a) is shown with the dashed lines (for the numerical results) and colours (for the experimental results). In other words, although the general trend of the amplitude response is to increase with the increase of flow velocity, when the response switches from one branch (dashed line or colour) to the other, first the amplitude drops and then continues to grow. The results which will be presented and discussed in the following sections will provide more explanation for this behaviour.

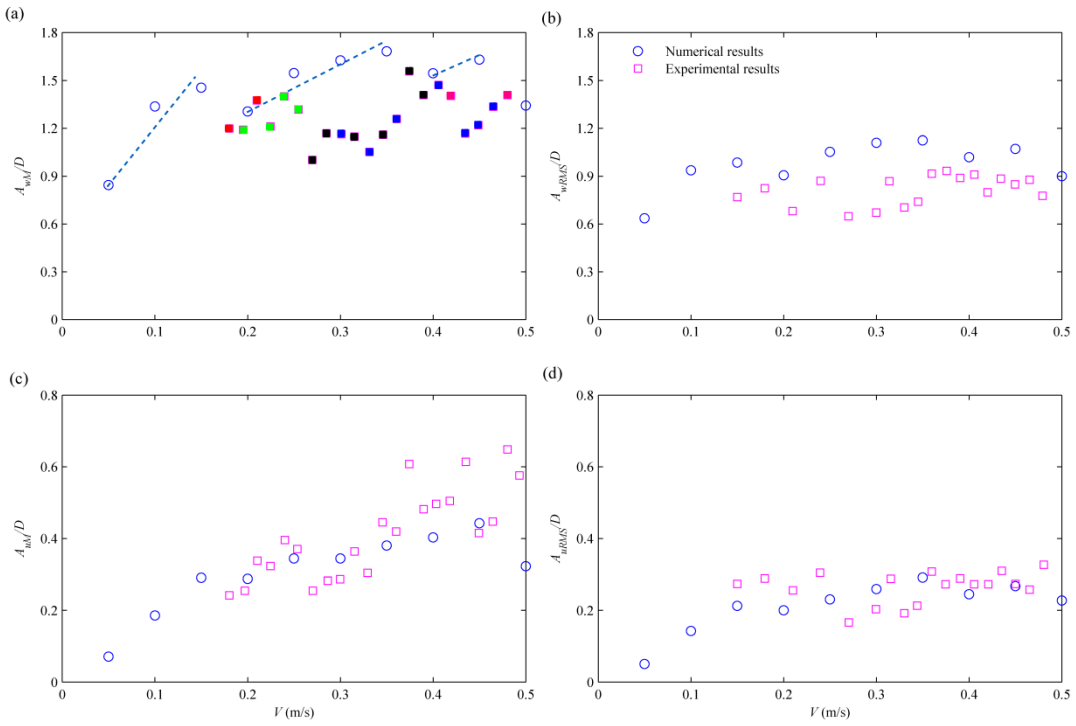

Figure 6.11: Comparison of numerical amplitude responses with their corresponding experimental results; (a) CF maximum amplitude responses; (b) IL maximum amplitude responses; (c) CF root mean square amplitude response; (d) IL root mean square amplitude response.

The comparison between numerical and experimental results depicted in Figure 6.11 (a) and (b) shows that experimental (numerical) results predict maximum amplitude responses up to 1.6*D* (1.7*D*) for the CF oscillations and 0.7*D* (0.5*D*) in the IL direction, respectively. Experimental evaluation of maximum VIV amplitudes of an elastic cylinder is usually involved with "large statistical uncertainties" [139]. These uncertainties, which are boosted at higher flow velocities, along with inevitable practical imperfections, such as the deviation from the presumed perfectly uniform flow, result in the values at high velocity cases which might be "a little overestimated"[94]. Hence, usually the RMS value of the oscillation amplitude is

reported. The corresponding RMS values of the numerical and experimental results of Figure 6.11 (a) and (b) (A_{wrms}/D, A_{urms}/D) are shown in Figure 6.2 (c) and (d), respectively. These figures depict less-scattered experimental results and more-quantitatively-comparable numerical results. Overall, the model provides predictions which both qualitatively and quantitatively resemble the experimental results. For a more in-depth investigation on the validity of the semi-empirical model predictions, beside the amplitude responses, the frequency response and dominating vibrating modes are checked, as well.

6.4.2 Frequency responses and dominant vibrating modes

Figure 6.12 depict the comparison between the experimental CF and IL oscillation frequencies of with their corresponding numerical predictions, respectively. In both of the experimental and numerical results, and in both CF and IL directions, the oscillation frequency linearly increases with the increase of flow velocity. The comparison of Figure 6.12 (a) and (b) show that the frequency of the IL oscillations is twice of the frequency of the CF motion. In other words, while the structure undergoes resonance CF motions with frequency of f_s (vortex-shedding frequency), in the IL direction the resonance motions occur at the frequency of $2f_s$. This phenomenon is known as the "dual resonance", observed in the VIV experiments on elastically-mounted rigid cylinders with two degrees of freedom [77], and infers that the dominant mode of the IL oscillations of the riser must be higher than that of the CF oscillations; and can be checked through modal analysis of the numerical predictions.

The dominant mode of CF and IL vibrations from the experimental set of Table 6.1 along with the numerical results of the semi-empirical model are depicted in Figure 6.12 (b). This figure, as it was deduced from the analysis of the frequency responses in Figure 6.12 (a), illustrate that IL oscillations are dominated by modes almost twice of the dominating mode of CF oscillations. Moreover, it can be seen that the dominant mode gradually increases with the increase of the flow velocity. The numerical results, as well, resemble this qualitative behaviour. However, the comparison shows that the dwell of the semi-empirical model in some dominant modes is longer than experimental results. For instance, based on the experimental

results of [94], the third mode dominates CF oscillations just when 0.2<V<0.25 m/s, while for the numerical results it happens when 0.2<V<0.35 m/s. Similar statements can be made for the IL oscillations, as well. These differences might be due to the fact that in the semi-empirical model all of the parameters which can influence the natural frequencies of the riser model, such as pretension and fluid added mass, are fixed and equal to the theoretical values, while in the experimental results some of these parameters are difficult to be kept constant and some are different from their theoretical values.

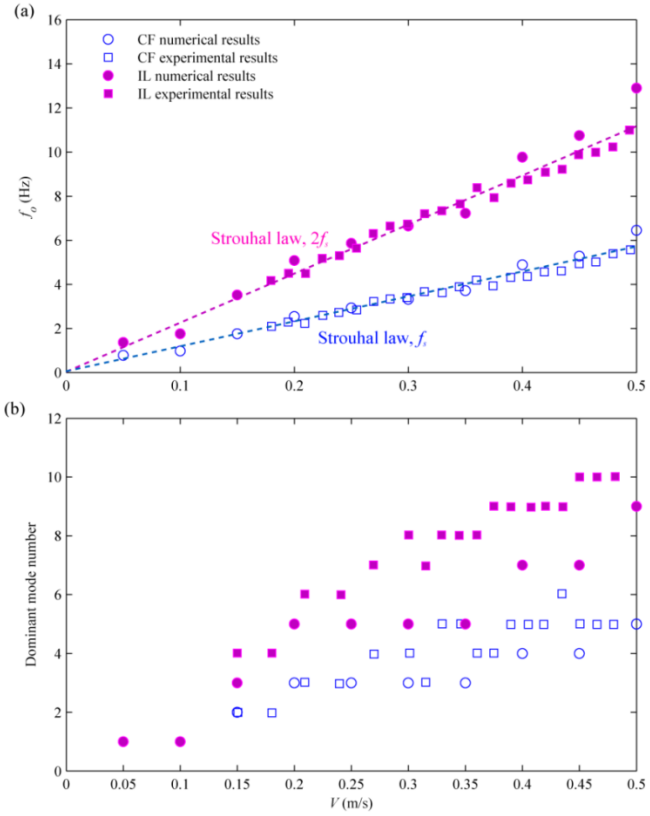

Figure 6.12: Comparison between numerical predictions of (a) CF/IL dominant oscillation frequencies; (b) CF/IL dominant vibration modes and their corresponding experimental results.

6.4.3 CF and IL amplitudes vs. reduced velocity

Hitherto, the experimental data and numerical predictions have been presented with respect to the flow velocity, V. In the literature, particularly for VIV of rigid cylinders, instead of V, results are expressed with respect to reduced velocity, $V_r=V/(f_nD)$ in which f_n is the natural frequency of the structure in CF direction. For

an elastic cylinder, the structure has infinite natural frequencies; therefore different definitions of reduced velocity can be adopted. Two of these possible definitions are $V_{r1}=V/(f_1D)$ and $V_{ri}=V/(f_iD)$ where f_1 is the first natural frequency of the structure and f_i is the natural frequency of the dominant mode of CF oscillations at corresponding current velocity. Figure 6.13 depict the experimental CF and IL amplitude responses and their numerical counterparts with respect to V_{ri}, Figure 6.13 (a) and (b), respectively. To evaluate the reduced velocities, the experimental value of natural frequencies reported in Table 2 of [94] are utilised.

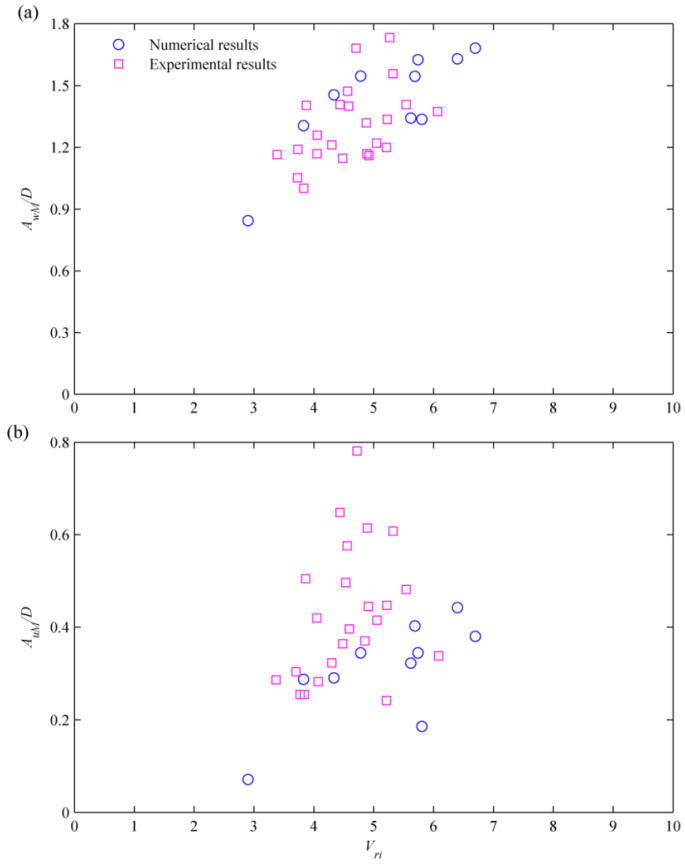

Figure 6.13: Numerical and experimental amplitude responses presented vs. reduced velocities defined based on the natural frequency of the dominant mode of the CF oscillations, V_{ri},; (a) CF amplitude vs. V_{ri}; (b) IL amplitude vs. V_{ri}.

Figure 6.13 illustrate that, although the results are obtained in different velocities, all collapse in a confined range of reduced velocity. For the present results, this range is $3<V_{ri}<7$ which is comparable to the ranges reported by [12, 143]. That is, when the structure vibrates in a particular mode, the increase of flow

velocity increases V_{ri}, which means higher oscillation amplitudes. And when the structure switches to higher oscillation modes, although the flow velocity is increased, the reduced velocity corresponding to the new mode decreases which means lower oscillation amplitudes and produces the sawtooth trends observed in Figure 6.11 (a). While all of the results can collapse in a narrow range of V_{ri}, the overall maximum amplitude of oscillations at each dominant mode increases as the dominant mode increases. This is due to the fact that higher modes occur at higher Reynolds numbers and higher Reynolds numbers cause higher amplitudes [36]. Structural oscillations at higher Reynolds numbers, and consequently at higher modes, are accompanied with the appearance of higher harmonics in the structural responses [79] which were discussed in previous sections.

6.5 Conclusions

Three-dimensional coupled CF/IL/axial VIV of an elastic cylinder subjected to uniform fluid flow is modelled via a semi-empirical model in which structural geometric nonlinearities are taken into account and fully-nonlinear fluid forcing terms have been applied. Having solved the model via a finite difference method, numerical results were compared with experimental results which showed qualitative and quantitative resemblance of the model predictions with the empirical observations. The numerical analyses illustrated model capabilities in capturing dual resonance accompanied with highly repetitive Fo8 trajectories and higher harmonic components of structural responses. Single-mode and multi-mode VIV oscillations and transitions from standing-wave-dominated responses to travelling-wave-dominated responses were predicted. The modal and stress analyses performed on the numerical results provided more insight into VIV mechanism of slender cylinders and significance of IL and axial oscillations. Moreover, the sensitivity analyses performed revealed that the importance of geometric nonlinearities and axial oscillations increases as the flow velocity increases. Finally, interconnection between rigid and elastic VIV models was discussed. The presented semi-empirical model, with the less possible simplifications and manipulations of the empirical parameters, can provide the designers with practical predictions of VIV in offshore risers and mooring cables which would be beneficial for early stages of the design process.

Chapter 7

Three-dimensional VIV of Flexible Cylinders Subjected to Linearly Sheared Flow

Figure 7.1 shows a flexible cylinder which is subjected to a linearly sheared flow and undergoes vortex-induced oscillations. In this Chapter, three-dimensional laterals and axial VIV of such fluid-structure system is studied. To this end, the equations of structural motions and fluctuating hydrodynamic forces introduced in previous Chapter, when the flow velocity linearly varies along the span of the cylinder, are solved through a finite difference scheme. Then the numerical results obtained in different flow velocities are investigated via time/frequency domain, modal and stress analyses and are qualitatively and quantitatively compared with experimental results.

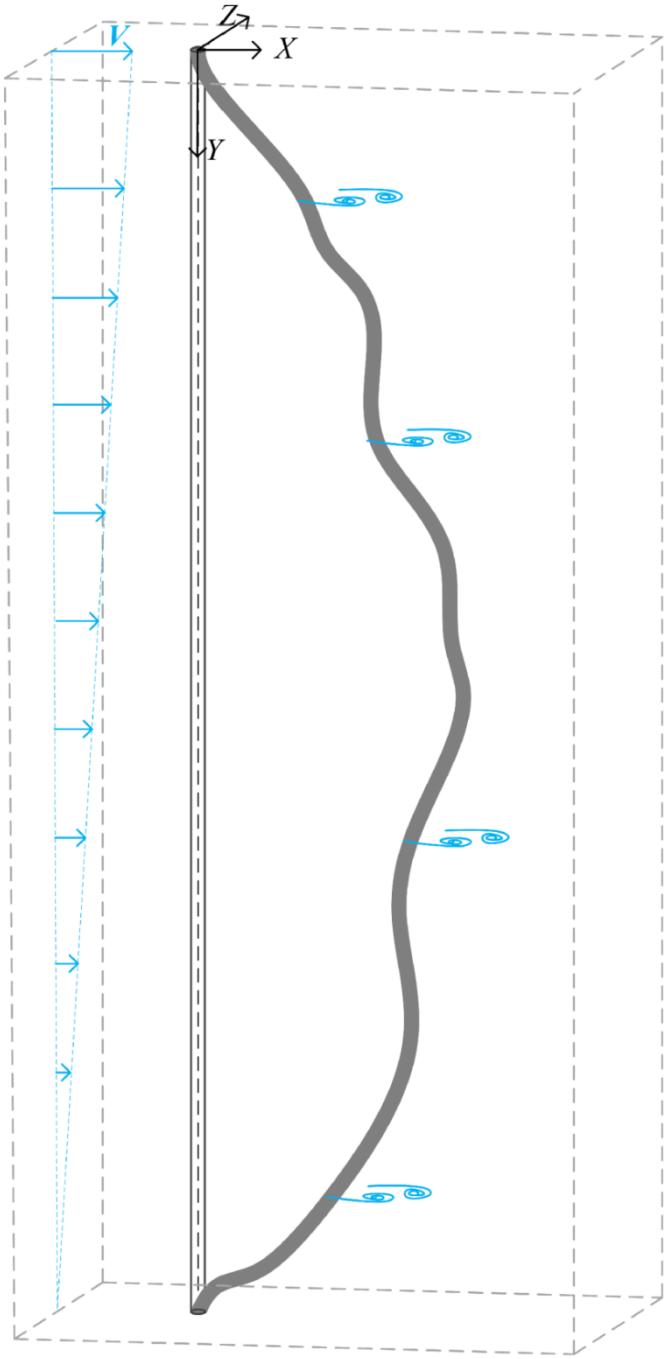

Figure 7.1: Schematic representation of a riser at rest (hollow cylinder) and during VIV (filled grey cylinder) subjected to a linearly sheared flow.

7.1 Model Predictions and Discussion

The numerical predictions of the semi-empirical model presented in Chapter 6 are discussed in this section. To this end, the model riser of the experimental study by [83] is used for computing the numerical results. The properties and given

parameters of this experimental riser model are presented in Table 7.1. The table shows that the riser model has a high aspect ratio of 3000 which makes oscillations at high vibrating modes possible. Moreover, it has a moderate mass ratio, m^*=3.13, which is below the value of m^*=6 suggested by [9] and infers that for such a structure, the IL oscillations will be considerable. To study and capture different aspects of VIV of flexible marine structures under linearly sheared flows, the numerical results presented in this section are obtained at low (V=0.3 and 0.4 m/s) and high (V=0.8 and 1 m/s) flow velocities. It is worth mentioning that these velocities refer to the maximum flow velocity at the top of the riser model, while the flow velocity along the span of the riser, and from bottom to the top of the riser, linearly increases from zero to V.

Table 7.1: Parameters of the riser models used for validation of the semi-empirical model.

Parameters	Experiment by [83]
Length, m	90
Inner diameter, m	0.026
Outer diameter, m	0.03
Mass ratio	3.13
Bending stiffness, N.m^2	3.64×10^3
Axial stiffness, N	3.69×10^7
Pretension, N	3700

7.1.1 Space-time variations of structural oscillations

The spatio-temporal plots of the lateral (CF/IL) and axial structural responses of the riser model of Table 7.1, at different flow velocities, are plotted in Figures 7.2. These results can be discussed in two levels of (i) collective overall trends and (ii) behaviours in each direction separately. These results illustrate that, at all velocities, travelling waves dominate the responses and propagate towards the bottom of the riser model where the flow velocity is lower. However, in some portions of the riser, standing waves can be distinguished as well. For instance, while above the section A-A of Figure 7.2 (b) a travelling wave dominates the response, below this section, the

structure shows a standing-wave-like behaviour. Such behaviour can be distinguished in other figures as well. Moreover, towards the direction of wave propagation, the oscillation amplitudes first increase and then decrease, e.g. compare the oscillation amplitudes at sections A-A, B-B and C-C of Figure 7.2 (d). This can be due to the fact that, as the wave travels along the span of this high aspect ratio riser mode, it loses its energy and since the flow velocity at the bottom parts is lower, this dissipation is not compensated. The figures also suggest that the higher the flow velocity is, the more dominating the travelling waves and the higher the oscillation frequencies are. Looking at just the CF oscillations, the responses show comparably similar maximum oscillation amplitudes. This behaviour is different from what it was observed in Section 6.2.1 for a riser model subjected to uniform flow. It, also, has been observed in the experimental investigations of [83] performed with a well-defined sheared flow and no reason were given for that. However, further analyses which will be performed in following sections will provide some explanations for this behaviour.

The amplitudes of IL oscillations gradually increase as the flow velocity increases. Moreover, looking at IL responses it is inferred that these oscillations occur at frequencies and vibrating modes twice those of CF oscillations. Furthermore, as the flow velocity increases, in addition to aforementioned high-frequency/high-mode vibrations, the structure undergoes low-frequency/low-mode oscillations as well. For example, the boxes in Figure 7.2 (g) specify one cycle of these oscillations which also can be found in the numerical results of [113]. Such behaviour, also, can be recognised in the axial oscillations, except that the low-mode axial oscillations occur at a frequency almost twice that of CF oscillations (which is much higher than the frequency of low-mode IL oscillations). The low-mode axial oscillation means that, at each moment of time, e.g. sections A-A and B-B of Figure 7.2 (i), the whole span of the riser is under tensile or compressive motion, respectively. At the same time that the structure undergoes low-mode axial motions, the longitudinal displacement along the span of the riser varies at a high-mode-manner. For example, at section A-A of Figure 7.2 (i) where the whole span of the cylinder has positive axial displacement, its magnitude varies along the span of the riser. Moreover, similar to IL responses, the amplitude of axial oscillations increases

with the increase of flow velocity. These amplitude amplifications along with high-frequency/high-mode oscillations infer that the IL and longitudinal oscillations become more significant at higher flow velocities

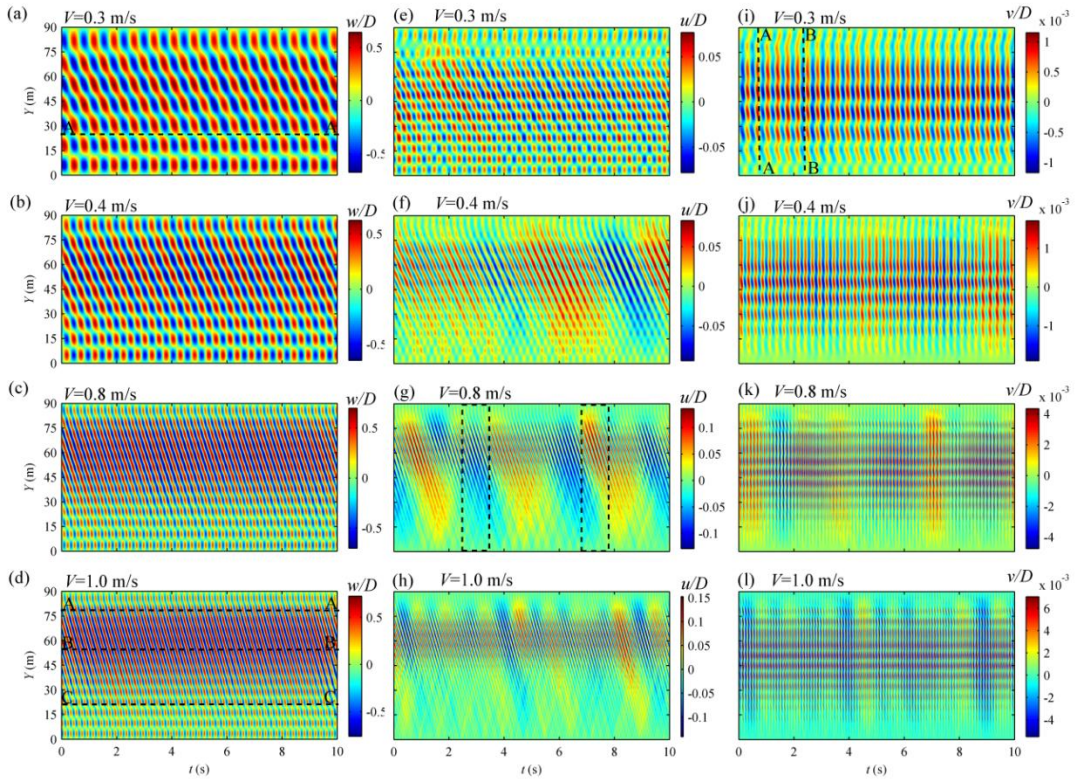

Figure 7.2: Spatio-temporal plot of: (a-d) CF oscillations; (e-h) IL oscillations; (i-l) axial oscillations.

7.1.2 Frequency domain analysis and higher harmonics

The results presented in Figures 7.2 showed the structural responses in the space-time domain. Figure 7.3 shows the space-frequency domain counterparts of these results. In this figure, the colours represent the power spectrum densities (PSD) normalised by maximum PSD at the corresponding *V* and riser section. These results illustrate that as the flow velocity increases the dominating oscillation frequency increases as well. Such increase was observed in Section 6.2.2 and it was shown that, following the Strouhal law, the oscillation frequency increases linearly. In the upcoming sections, it will be investigated if such trend occurs in here. The frequency domain analysis of the uniform flow results, also, showed that 3rd, 4th and 6th harmonic components appeared in the structural responses. However, for sheared

flow results presented in Figure 2, except for axial oscillations at high flow velocity V=1 m/s where 4th higher harmonics appear, the responses have no higher harmonic components. This might be due to the fact that the amplitudes of structural oscillations of a riser, when it is subjected to a sheared flow, are smaller than amplitudes caused by uniform flows. Therefore, the contribution of nonlinearities (particularly quadratic nonlinear fluid forces) in the structural responses becomes less important. In other words, as the flow velocity increases to V=1 m/s and the amplitude of axial oscillations amplifies enough, 4th harmonic components appear in the axial responses; while in the CF (IL) responses where the amplitude does not change (the increase of oscillation amplitudes occurs gradually) there are no higher harmonics.

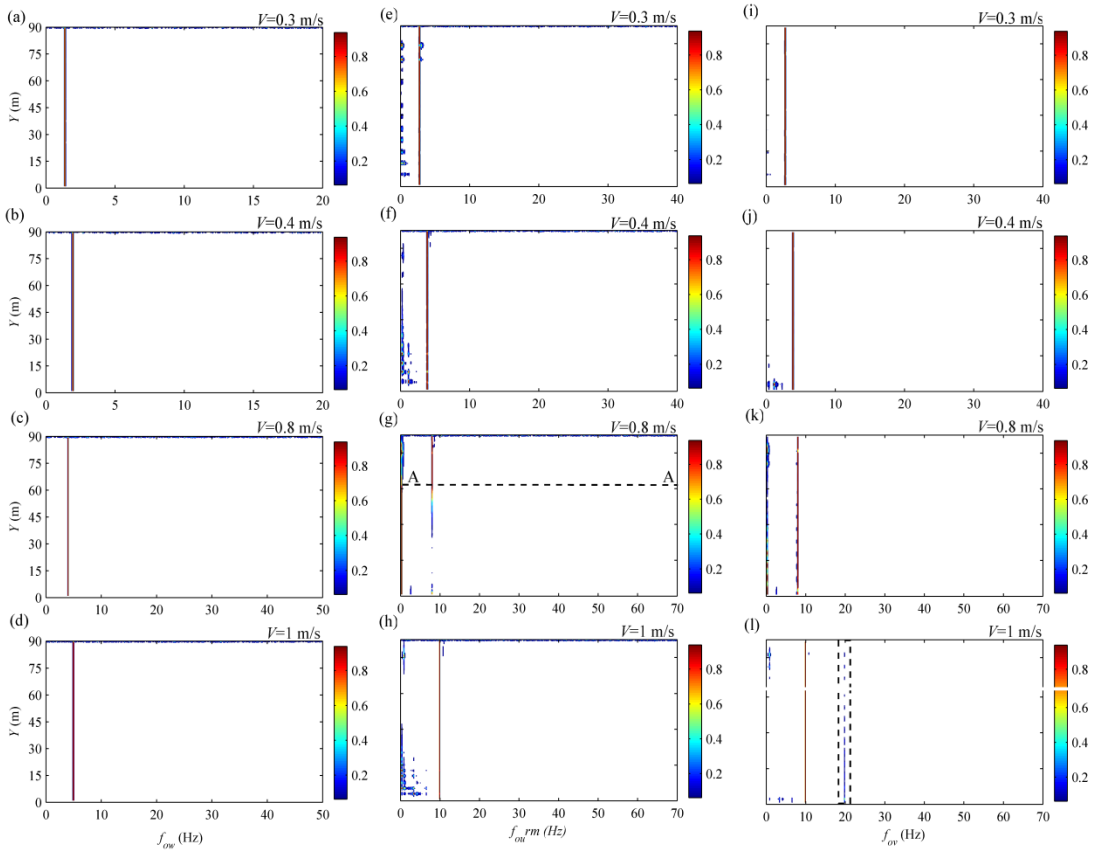

Figure 7.3: Frequency domain analysis of the numerical predictions of the structural oscillations in (a-d) CF direction; (e-h) IL direction and (i-l) axial direction.

The results depicted in Figures 7.3, also, illustrate that the dominant frequency of IL and axial oscillations is twice that of CF oscillations. This 2:1 frequency ratio

was inferred from the time histories depicted in Figure 7.2 as well. Moreover, those time histories suggested low-frequency/low-mode IL and axial oscillations. The frequency domain results of Figure 7.3 clearly reflect low-frequency components of the IL and axial responses. For instance, at V=0.8 m/s, while the riser parts above the section A-A of Figure 7.3 (g) are experiencing IL oscillations at a 2:1 frequency ratio, the riser parts below this section has a low dominant frequency. As it was explained in Section 6.2.2, the appearance of higher harmonics in the structural responses and 2:1 oscillation frequency ratios are interconnected with Fo8 trajectories of CF/IL oscillations. Analysis of these trajectories will provide more explanations about the behaviour of the VIV system of Figure 7.1. Variations of Fo8 trajectories along the span of the riser, along with the variation of mean IL displacement of the riser at different V, are studied in the following section.

7.1.3 Fo8 orbits and mean drag amplification

The Fo8 trajectories depicted in Figures 7.4 show that the shape of these trajectories along the span of the riser varies. However, when these variations are compared with those presented in the previous chapter, the trajectories shown in Figure 7.4 show less variety. As it was explained in Chapters 2 and 6, the shape of these trajectories controls the existence of higher harmonic frequencies. Since the trajectories shown in Figure 7.4 are not similar to those which facilitate occurrence of higher harmonics, hence this observation is consistent with the results discussed in Figure 7.3. The Trajectories also illustrate that, apart from Figure 7.4 (a) in which repetitive Fo8 orbits occur, in other cases, the trajectories are not repetitive. Moreover, in some cases such as the one highlighted with red colour in Figure 7.4 (c), it seems that the structure undergoes orbital motion with approximately 1:1 frequency ratio. Referring to the corresponding frequency domain analyses of these cases in Figure 7.3 shows that these are the cases with dominating low-frequency components. However, as it was illustrated in Figure 7.3 (g) as well, in the sections where the higher frequency dominates the IL response the structure oscillates under Fo8-like orbitals, e.g. see the trajectory highlighted with blue colour in Figure 7.4 (c).

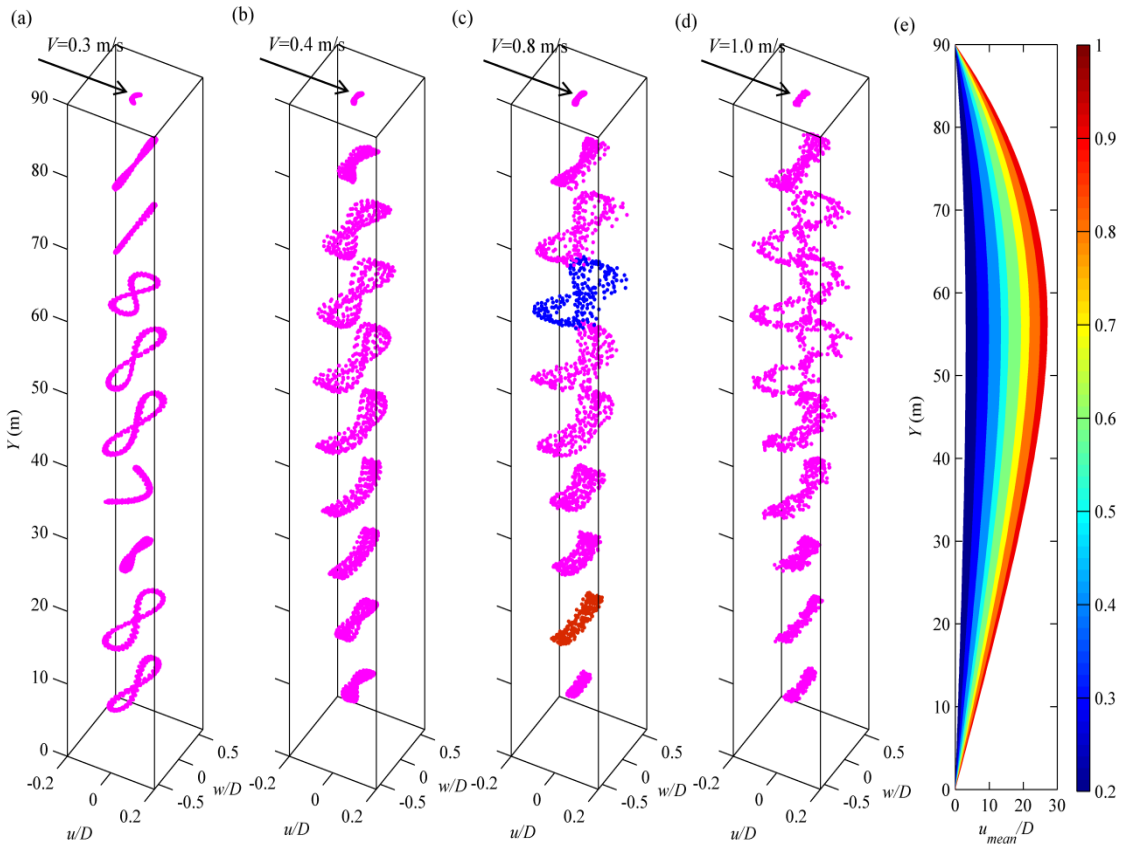

Figure 7.4: (a-d), Variation of Fo8 trajectories along the span of the riser; (e), mean IL displacement at different flow velocities.

Since just at V=0.3 m/s the trajectories are highly repetitive, the results depicted in Figure 7.4 also suggest that it might be just at this velocity that the structure oscillates under lock-in and dual resonance circumstances and at other flow velocities it is experiencing non-lock-in VIV. Though, further investigations through modal analysis are required to study lock-in and ono-lock-in VIV conditions. The modal analysis of the results presented in Figures 7.2-4 is performed in the next section. Before that, Figure 7.4 also depicts the mean IL displacements of the riser at different flow velocity. In Section 6.2.3, it was explained that the capabilities of the model for capturing this mean displacement is due to nonlinear fluid forcing terms which are responsible for the prediction of higher harmonics and Fo8 trajectories as well. This figure illustrates that, as the flow velocity increases, the riser has higher mean displacements and this displacement is bigger at top sections of the riser where the flow velocity is higher.

7.1.4 Modal decomposition: multi-mode vibrations and mode switching

The theoretical background and formulations for modal analysis of an elastic cylinder subjected to fluid flow were explained in Section 6.2.4. Now, a modal decomposition of the results presented in previous sections is performed. Figure 7.5 shows the first five vibrating modes which dominate the structural responses of the riser model of Figure 7.1. As these figures show, at all velocities and in all directions the structure undergoes multi-mode oscillations. This is due to the fact that, in all of these cases, the travelling waves dominate the structural responses. For instance, in here at V=0.3 m/s the CF oscillations are multi-modal, while in Section 6.2.4, for a riser model subjected to the same V, the CF response was standing-wave-dominated and single modal.

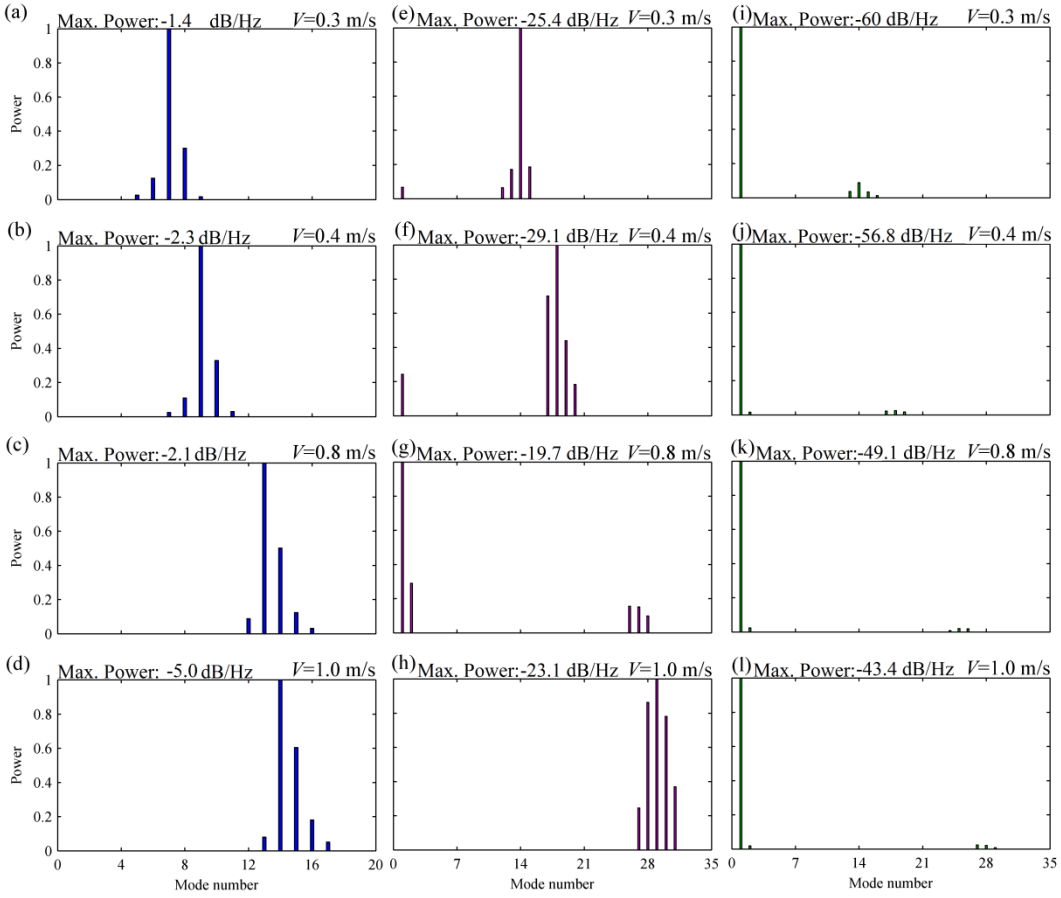

Figure 7.5: Modal decomposition of structural responses in (a-d) CF direction; (e-h) IL direction; (i-l) axial direction.

Figure 7.5 illustrates that as the flow velocity increases, there is less difference between the power of the first and the second dominating CF vibrating modes. In other words, apart from CF responses at V=0.3 m/s, in other velocities there are no absolute dominance of the first dominating mode. This observation infers non-lock-in conditions. Similar observations can be made for the IL oscillations as well. Hence, this modal analysis clarifies the reason for repetitive Fo8 trajectories at V=0.3 m/s and non-repetitive orbits at other flow velocities. Based on this analysis, at low flow velocity the dominating modes in both CF and IL oscillations are much stronger than other modes and provide circumstances suitable for lock-in conditions which lead to dual resonance. However, at other flow velocities such circumstances are not met.

The results depicted in Figures 7.5 (e-g), confirm the contribution of low vibrating modes in the IL responses. They also, illustrate how these modes get stronger with the increase of V and can dominate IL responses. It worth mentioning that for having lock-in condition, the mode possessing natural frequency close to the vortex-shedding frequency should be dominating the response. Hence, although in Figure 7.5 (g) the first mode clearly dominates the IL motion, since its corresponding natural frequency is far from f_v, it does not provide the system with lock-in condition and dual resonance. Similarly, the axial responses, in all flow velocities (Figures 7.5 (i-l)), are dominated by the first vibrating mode. However, as it was explained in sections 7.1.1 and 7.1.2, in spite of the IL responses in which low modes oscillate at low frequencies, the axial low-modes oscillate at frequencies twice that of CF dominating frequency.

To draw a clearer picture of the contributions of low and high modes in the structural responses, time histories of the modal weights of the first five dominating modes of CF, IL and axial vibrations reported in Figures 7.5, are depicted in Figures 7.6. This figure illustrates that the dominant CF and IL vibration modes momentarily switches from one mode to the other. In other words, while most of the times one mode dominates the CF and IL responses, there are some moments when another mode takes the lead. For instance, the colourful dashed lines in Figures 7.6 (a) and (e) represent the moments when the mode with the corresponding colour is

dominating. On the other hand, the axial motions are dominated by one single mode. Moreover, to clearly see the aforementioned low-frequency/low-modes of IL oscillations, in Figure 7.6 (g) the modal weights are plotted for a longer time. As it can be seen in this figure, two dominant modes oscillate at low frequencies and there are momentary interchanges between these modes (the colourful dashed lines represent these moments). Furthermore, Figure 7.6 (g) shows that, although in most of the times the two low-frequency modes dominate the response, there are switching to the high-frequency modes as well. For instance, the red dashed line shows one of these moments.

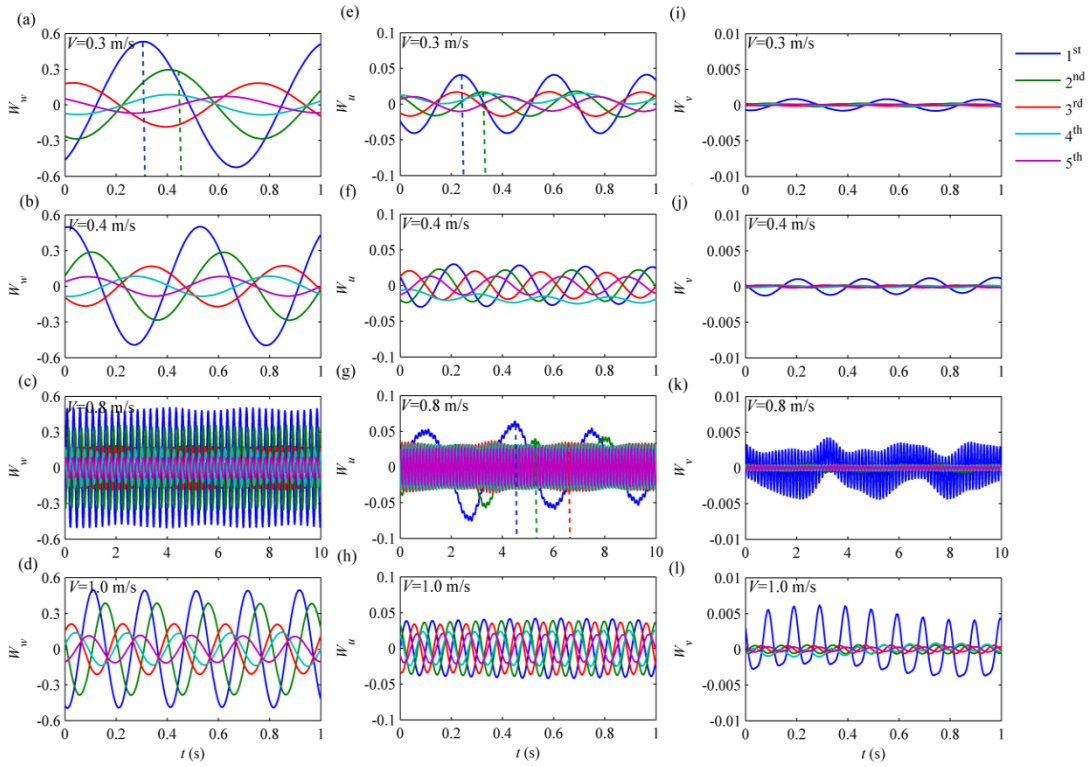

Figure 7.6: Modal weights of the first four dominant modes involved in the responses of: (a-d) CF oscillations; (e-h) IL oscillations; (i-l) axial oscillations.

7.1.5 Stress analysis: bending, axial stresses and dynamic tension

Doing stress analyses on the results discussed in the previous sections, along with more clarification of the riser behaviours, will provide more evidences of the importance of IL and axial oscillations. The theoretical formulations for such analysis were explained in Section 6.2.5. Using those formulas, Figure 7.7 shows the

axial and CF/IL bending stresses. These results illustrate that the stresses increase as the flow velocity increases. They also show that the magnitude of axial stresses can exceed IL stresses. Recalling the experimental results reporting the importance of considering IL oscillations [12, 84, 87], these results suggest that the axial oscillations can be as important as IL oscillations. And, since these oscillations compared to CF oscillations occur at higher frequency, their fatigue damages can be as significant as CF motions. Furthermore, the fluctuations of IL and axial stresses occur around a mean value stress which is due to mean IL displacement caused by mean drag. A comparison between the results depicted in Figures 7.7 (a-h) with their counterparts for a riser subjected to uniform flow, shows that in here the space-time distribution of CF/IL bending stresses resemble their corresponding responses, while for uniform flow cases with standing-wave-dominated responses there were not such resemblance and new trends were observed.

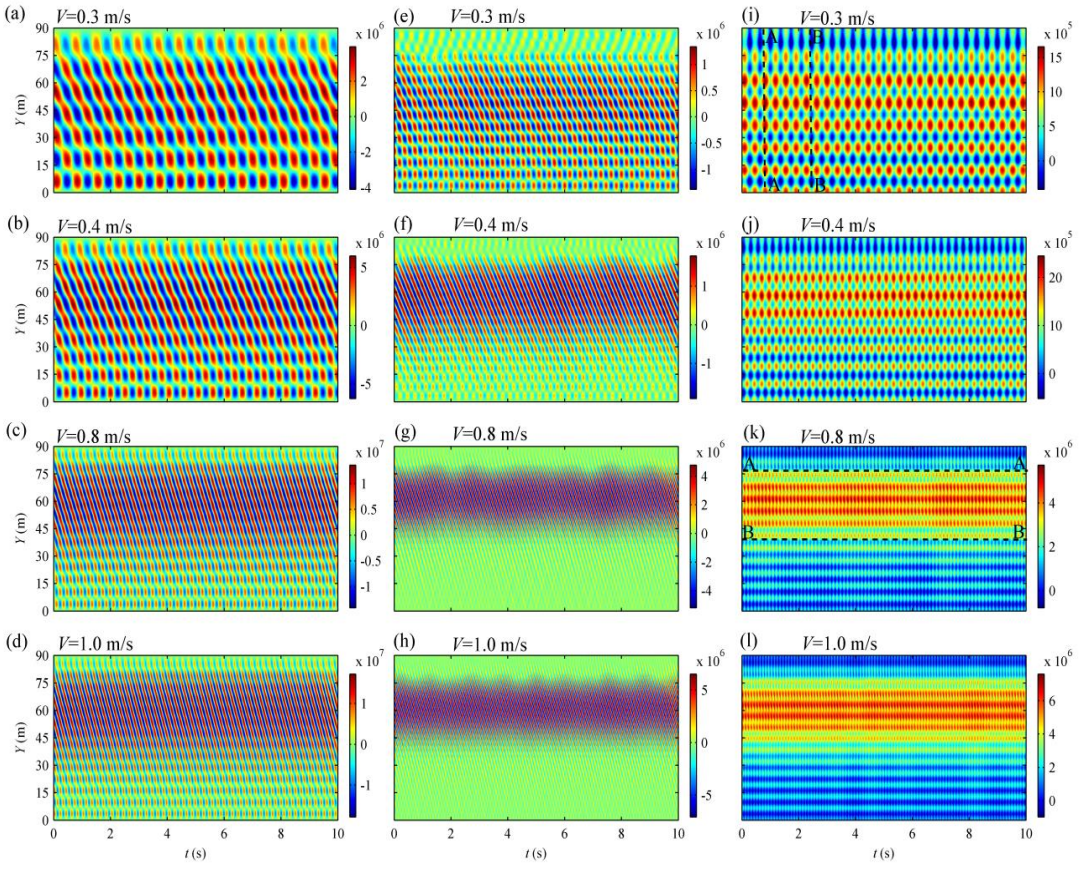

Figure 7.7: Spatio-temporal plots of (a-d) CF bending stress; (e-h) IL bending stress; (i-l) axial stress.

Regarding the axial stresses, it can be seen that at low flow velocities, V=0.3 and 0.4 m/s, the whole span of the riser periodically experiences tensile and compressive stresses, e.g. see the sections A-A and B-B of Figure 7.7 (i). At high flow velocities, V=0.8 and 1 m/s, the mid-sections of the riser, e.g. the riser sections between Sections A-A and B-B of Figure 7.7 (k), are constantly under tensile stresses, while other sections periodically experience compressive and tensile axial stresses. The maxima of these compressive stresses occur near top and bottom boundaries of the riser. These axial stresses also can be utilised for investigating variations of dynamic tension along the span of the riser. The spatio-temporal plots of dynamic tensions corresponding to the results discussed in previous sections are depicted in Figures 7.8. These results illustrate that the mean tension of the riser increases as the flow velocity increases. Moreover, the amplitude of tension fluctuations along the span of the riser increases with the increase of V. However, under the present circumstances, no section of the riser mode experiences negative tension. Therefore, no buckling or snapping occurs for these cases, however if lower pretensions are applied to the riser model such phenomenon become more probable.

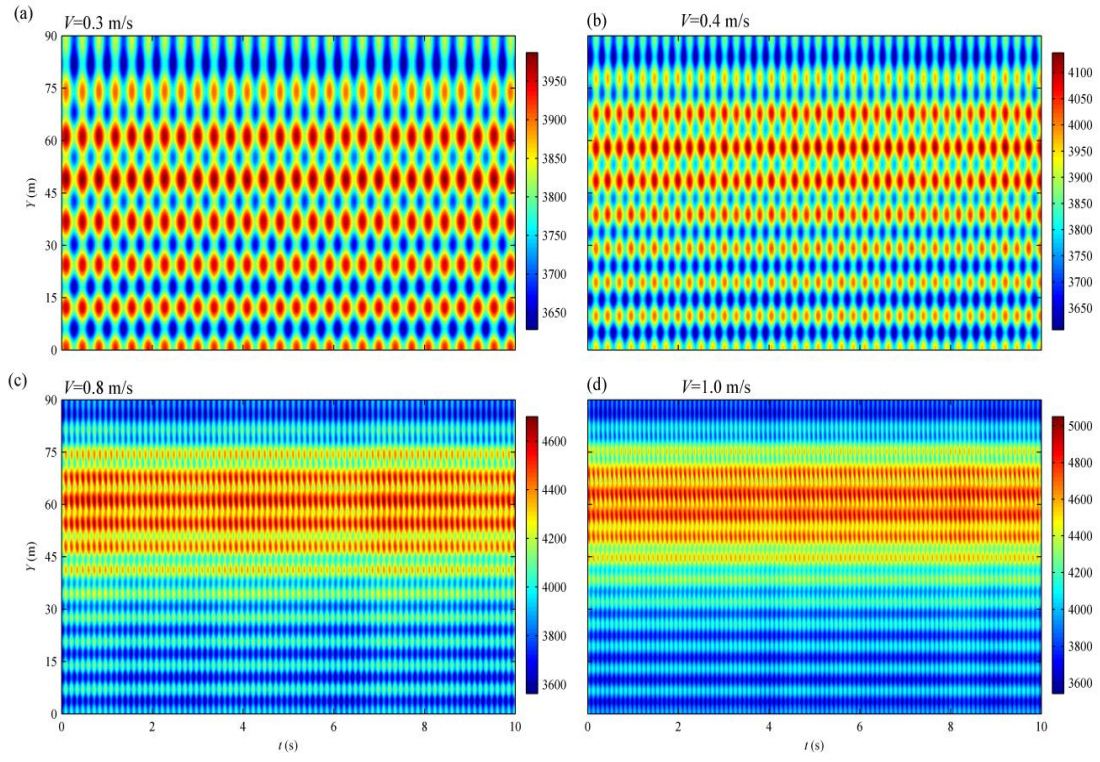

Figure 7.8: Spatio-temporal plots of the total tension, T_t=T_0+T_d.

7.2 Validation of the Proposed Model

In the previous sections, the numerical predictions of VIV behaviours and responses of a flexible circular cylinder subjected to linearly sheared flow were investigated and qualitatively compared with available results in the literature. In this section, these results are validated through quantitative comparisons with their corresponding experimental results.

7.2.1 Amplitude responses

Figure 7.9 shows the experimental and numerical results of average CF/IL RMS amplitudes at different flow velocities. The experimental results show that increasing flow velocity does not affect the average CF amplitudes. Such a trend is observed in the numerical predictions as well. This constant CF amplitude can be due to the fact that the lock-in condition does not occur and hence the "sawtooth" behaviour explained in Section 6.4.1 does not occur in here. Moreover, the numerical results quantitatively resemble the experimental CF amplitudes. The IL amplitudes, Figure 7.9 (b), show similar trends as well, and its quantitative agreement improves as the flow velocity increases. It is worth mentioning, both experimental and numerical CF/IL amplitudes presented in this section are much lower than the results presented in Section 6.4.1 or the results reported in other experimental results. The corresponding experimental study of [83] does not provide any reasons or explanations for this. However, the analyses performed in this Chapter suggest that low CF/IL oscillation amplitude can be due to non-lock-in conditions which prohibit high amplitude oscillations.

7.2.2 Frequency responses and dominant vibrating modes

The corresponding dominant frequency and vibrating mods of the results shown in Figure 7.9 are depicted in Figures 7.10 (a) and (b), respectively. The results illustrate that both experimental and numerical dominant frequencies linearly increase as the flow velocity increases. Moreover, this linear increase follows the Strouhal law. This comparison, also illustrate the quantitative agreement between numerical predictions and their corresponding experimental results. Such a quantitative resemblance can be observed in Figure 7.10 (b) between numerical and

experimental dominant vibrating modes. As it was discussed in previous sections, since in some velocities (V=0.6 and 0.8 m/s in this case) low/frequency/low-mode vibration trends appear in the IL responses, in these velocities the semi-empirical model predicts 1st mode to be dominating. However, the higher mode which (following the trend of the graph) is expected to be dominating is excited but overshadowed by the 1st mode. For instance, at V=0.8 m/s, the first mode is dominating while it is expected that the 26th or 27th mode be dominating. The modal decomposition of the IL responses at this flow velocity (Figure 7.5 (g)) shows that these modes are excited as well.

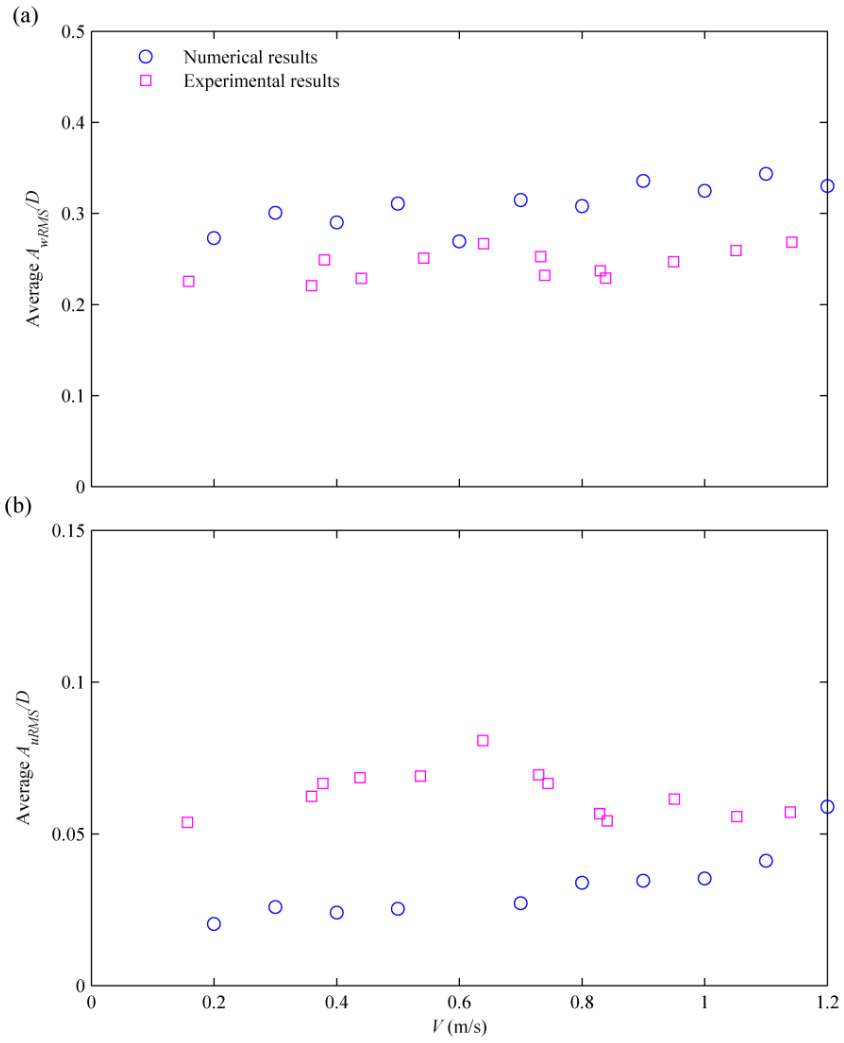

Figure 7.9: Comparison of numerical amplitude responses with their corresponding experimental results; (a) CF maximum amplitude responses; (b) IL maximum amplitude responses; (c) CF root mean square amplitude response; (d) IL root mean square amplitude response.

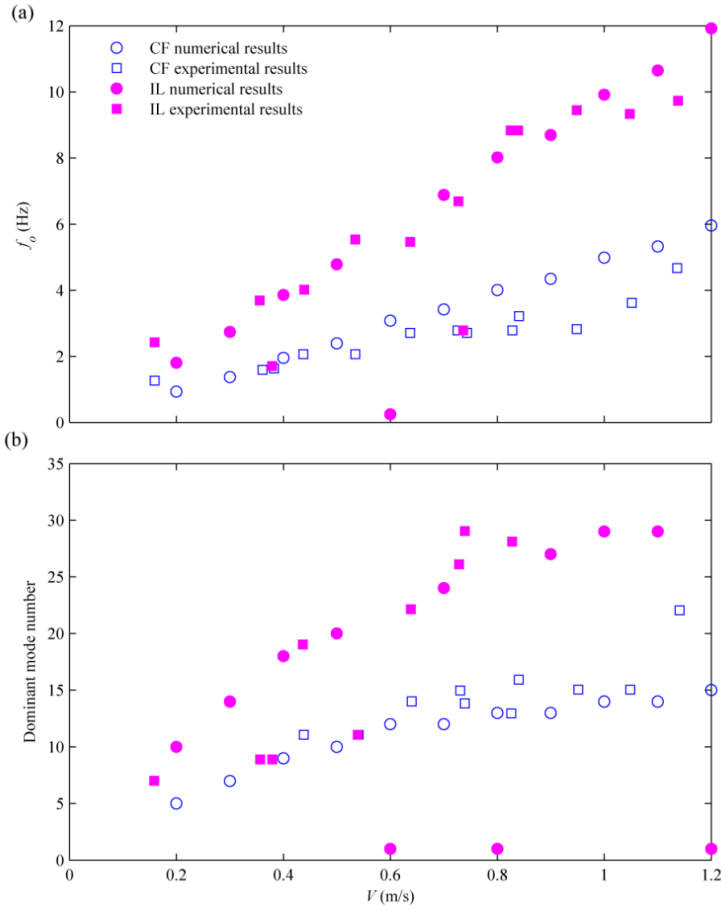

Figure 7.10: Comparison between numerical predictions of (a) CF/IL dominant oscillation frequencies; (b) CF/IL dominant vibration modes and their corresponding experimental results.

7.3 Conclusions

Vortex-induced oscillations of a flexible circular cylinder subjected to a linearly sheared flow were studied via the model proposed in the previous Chapter. The model was solved via a finite difference numerical scheme and the numerical results of different flow velocities were post-processed through time/frequency domain, modal and stress analyses. Through these analyses, the importance of considering IL and axial oscillations was confirmed and both lock-in and non-lock-in VIV conditions were captured which the former provided explanations for experimentally-observed low-amplitude oscillations. The numerical predictions of the model, also, were compared with their experimental counterparts. These comparisons showed qualitative and quantitative agreements between numerical and experimental results.

Chapter 8

Conclusions and Future Work

Novel fully-nonlinear phenomenological models for two/three-dimensional vortex-induced oscillations of rigid/flexible circular cylinders have been developed and different aspects of VIV phenomena have been tackled. In these models, the structural oscillations were modelled with nonlinear equations of motions which, through nonlinear hydrodynamic forces, were coupled to van der Pol-type wake oscillators representing time-dependent lift and drag forces. These models were then solved via analytical and numerical schemes and compared with in-house and published experimental studies.

8.1 Conclusions

The main outcomes of the present study are summarised as follows:

8.1.1 Combined CF/IL VIV of an elastically mounted rigid cylinder

- A model accounting for structural and geometric coupling nonlinearities has been developed. Owing to these cubic nonlinear terms, the model was capable of capturing jump and hysteresis phenomena observed in experimental results. Moreover, the hydrodynamic nonlinearities were taken into account. Through these quadratic nonlinearities, the model could capture some qualitative aspects of 2DOF VIV such as dual resonance, 2:1 oscillation frequency ratio, VIV-induced mean drag amplification and repetitive Fo8 trajectories. The parametric studies performed showed that neglecting quadratic hydrodynamic nonlinearities and considering classical linear hydrodynamic forcing terms would lead to a model failure in predicting the aforesaid phenomena.
- Empirical coefficients of the new model were defined as a function of physical parameters such as mass, damping and frequency ratio. Moreover, the sensitivity analysis was carried out to study the effects of these empirical coefficients on model predictions which could provide insights for further calibration of the model.
- The model was utilised for predicting and explaining the influence of important physical parameters such as mass ratio, damping ratio, mass damping parameter, frequency ratio and reduced velocity on the cylinder response. These results were then compared with available experimental results. These comparisons revealed that the new model can predict the high-amplitude super-upper branch amplitude responses, critical mass ratio and unbounded lock-in ranges at low mass ratios, the individual effect of mass and damping ratios on the determination of maximum attainable amplitudes of 2DOF VIV.

- Due to lack of experimental results studying on the effect of frequency ratio for cylinders with equal mass ratios in CF and IL directions, new in-house experiments were carried out. The outcomes of these experiments were then compared with the new prediction model and other available experimental results. These comparisons showed that, while the frequency ratio does not affect the maximum CF/IL amplitudes, it can influence the VIV mechanism by varying the relative phase difference between CF and IL oscillations. Such influence of the natural frequency ratio could be predicted by the numerical model.
- Analytical closed-form solutions for key hydrodynamic coefficients were derived. Comparing these solutions with experimental results illustrated some qualitative as well as quantitative agreements. Through these new formulations, practical graphs of hydrodynamic coefficients (with regard to important physical parameters) were provided. Furthermore, analytical closed-form solutions for evaluation of maximum attainable CF/IL amplitudes and hydrodynamic coefficients as functions of mass and damping parameters were developed. Using these solutions, the importance of structural geometric nonlinearities and variable empirical coefficients were highlighted.

8.1.2 Three-dimensional VIV of a flexible cylinder

- Experiences gained from the VIV study of rigid cylinders helped us develop a fully-nonlinear predictive VIV model for a straight flexible cylinder. In addition to CF and IL motions of the cylinder, its longitudinal oscillations were taken into account with the new model. In this model the CF/IL oscillations were excited through nonlinear hydrodynamic forcing terms while the lateral vibrations of the cylinder excited axial oscillations through geometrical nonlinear coupling terms.
- VIV responses of a flexible cylinder subjected to uniform and linearly sheared flows at moderate and high current velocities were obtained and analysed. At moderate uniform flow velocities, lower vibration modes were excited and the responses were dominated by standing waves. In uniform

flow cases, increasing flow velocity excited higher vibrating modes, caused a transition to travelling waves and led to the dominance of travelling waves at high flow velocities. These travelling waves propagated in arbitrary directions. When the flow was linearly sheared, at all velocities the travelling waves dominated responses.

- When standing waves dominated the structural response, in CF direction the structure undertake single-mode VIV whereas in IL and axial directions multi-mode vibrations occurred. When the responses were dominated by travelling waves, multi-mode VIV occurred in all directions. In the case of multi-mode oscillations, the model predictions showed that the dominating mode can vary momentarily.
- With uniform flows, the structural responses contained higher-harmonic frequency components. The contributions of these 3^{rd} (CF), 4^{th} (IL/axial) and 6^{th} (axial) higher harmonics to the CF, IL and axial responses fortified with increasing flow velocity. With sheared and high-velocity flow, higher harmonics appeared in axial responses.
- Model predictions showed that axial oscillations can cause fatigue damages comparable to CF and IL oscillations and their importance increases with increasing flow velocity. Moreover, the parametric studies highlighted the importance of considering geometrical and hydrodynamic nonlinearities. Through these nonlinearities, the model could predict axial oscillations and the aforementioned (and experimentally-observed) behaviours.
- The model could capture both lock-in and non-lock-in VIV conditions and showed that non-lock-in circumstances, caused by the sheared flow, result in lower amplitude responses compared to lock-in VIV conditions. The model can also predict dual resonance (and non-dual resonance) situations which were accompanied by repetitive (non-repetitive) Fo8 trajectories. It also showed that the shape of these trajectories changes along the span of the cylinder due to variable x-y phase differences.
- Comparisons between numerical predictions and experimental results showed how numerical results qualitatively resembled experimental results. These showed that the dominant frequencies (and vibrating modes) of structural

oscillations linearly (gradually) increase with increasing flow velocity. The comparisons also illustrated that when the cylinder undergoes lock-in VIV, its maximum oscillation amplitudes gradually increase with increasing flow velocity while at non-lock-in VIV conditions the maximum amplitudes do not vary.

8.2 Suggestions for Future Research

The proposed predictive models provided encouraging results; however, to the author's knowledge, they are the first of their kind to consider fully nonlinear two and multi-DOF VIV. There are number of research topics which can be performed and are suggested as follows:

i. Experimental results reporting the hydrodynamic coefficients of a circular cylinder undergoing combined CF/IL VIV is lacking in the literature. Hence, it is suggested to perform sets of well-designed forced and free 2DOF experiments to study the effect of frequency ratio on hydrodynamic coefficients and compare with the practical graphs provided in this thesis. Such a study, also, will be beneficial for further calibration and validation of the proposed model.

ii. A few Direct Numerical Simulations studies investigating 2DOF VIV assume structural oscillations to be linear. To check the significance of geometrical nonlinearities, it is recommended to carry out CFD simulations of simultaneous transverse/streamwise VIV by accounting for structural nonlinearities and make comparisons with linear model simulations.

iii. In the present study, vortex-induced oscillations of a flexible cylinder due to uniform and linearly sheared flows were investigated. Other current velocity profiles such as random flow can also be studied and be compared with the results presented.

iv. Numerical results presented in this thesis highlighted the significance of IL and longitudinal oscillations of a top tensioned marine riser. Some of the experimental results have also highlighted the importance of IL oscillations; however the axial oscillations have not been measured yet. Experimental studies measuring axial VIV of flexible cylinders and investigating the

importance of these oscillations with regards to CF and IL oscillations are suggested

v. The results presented in this thesis highlighted the significance of IL and longitudinal oscillations of a top tensioned marine riser. Such a model can be developed and applied to a steel catenary riser. Using this model, in addition to the analyses performed for the straight lay-out, the influence of changing flow direction and its effect on in-plane and out-of-plane oscillations of the riser should be investigated.

vi. The proposed model of this thesis provides reliable and accurate predictions of VIV of rigid and elastic circular cylinders subjected to uniform and linearly sheared flows. The offshore structures are usually subjected to ocean waves as well. Hence, further modification of the model can be achieved via accounting for wave forces and implementing wave effects into the proposed model. This modification will result in more realistic replication of environmental conditions and has a great practical importance.

References

[1] A. Khalak, C.H.K. Williamson, Dynamics of a hydroelastic cylinder with very low mass and damping, Journal of Fluids and Structures, 10 (1996) 455-472.

[2] T. Nishihara, S. Kaneko, T. Watanabe, Characteristics of fluid dynamic forces acting on a circular cylinder oscillated in the streamwise direction and its wake patterns, Journal of Fluids and Structures, 20 (2005) 505-518.

[3] E. Huse, G. Kleiven, F.G. Nielsen, VIV-Induced Axial Vibrations in Deep Sea Risers, in, Offshore Technology Conference.

[4] R.D. Gabbai, H. Benaroya, An overview of modeling and experiments of vortex-induced vibration of circular cylinders, Journal of Sound and Vibration, 282 (2005) 575-616.*

[5] P.W. Bearman, Circular cylinder wakes and vortex-induced vibrations, Journal of Fluids and Structures, 27 (2011) 648-658.

[6] C.H.K. Williamson, R. Govardhan, A brief review of recent results in vortex-induced vibrations, Journal of Wind Engineering and Industrial Aerodynamics, 96 (2008) 713-735.

[7] R.D. Blevins, Flow-Induced Vibrations, Van Nostrand Reinhold, New York, 1990.*

[8] T. Nakamura, S. Kaneko, Flow Induced Vibrations: Classifications and Lessons from Practical Experiences, Elsevier, 2008.

[9] N. Jauvtis, C.H.K. Williamson, The effect of two degrees of freedom on vortex-induced vibration at low mass and damping, Journal of Fluid Mechanics, 509 (2004) 23-62.*

[10] J.M. Dahl, Vortex-induced vibration of a circular cylinder with combined in-line and cross-flow motion, in: Department of Mechanical Engineering, Massachusetts Institute of Technology, 2008.*

[11] J.M. Dahl, F.S. Hover, M.S. Triantafyllou, Two-degree-of-freedom vortex-induced vibrations using a force assisted apparatus, Journal of Fluids and Structures, 22 (2006) 807-818.

[12] M.A. Tognarelli, S.T. Slocum, W.R. Frank, R.B. Campbell, VIV Response of a Long Flexible Cylinder in Uniform and Linearly Sheared Currents, in: Offshore Technology Conference, OTC16338, 2004.

[13] F.J. Huera-Huarte, Z.A. Bangash, L.M. González, Towing tank experiments on the vortex-induced vibrations of low mass ratio long flexible cylinders, Journal of Fluids and Structures, 48 (2014) 81-92.

[14] W.-H. Xu, X.-H. Zeng, Y.-X. Wu, High aspect ratio (L/D) riser VIV prediction using wake oscillator model, Ocean Engineering, 35 (2008) 1769-1774.

[15] H. Drescher, Messung der auf querongestromte Zylinder ausgeubten seitlich veranderten Drucke, zeitschrift für flugwissenschaften, 4 (1956) 17-21.

[16] B.M. Sumer, J. Fredsoe, Hydrodynamics around cylindrical structures, World Scientific, 2006.

[17] C. Norberg, Fluctuating lift on a circular cylinder: review and new measurements, Journal of Fluids and Structures, 17 (2003) 57-96.

[18] S.K. Chakrabarti, The Theory and Practice of Hydrodynamics and Vibration, World Scientific, 2002.

[19] M.M. Zdravkovich, Flow Around Circular Cylinders Volume I: Fundamentals, 1 ed., Oxford Science Press, 1997.

[20] T.-Y. Chung, Vortex-induced vibration of flexible cylinders in sheared flows, in: Department of Ocean Engineering., Massachusetts Institute of Technology, 1988.

[21] K. Vikestad, J.K. Vandiver, C.M. Larsen, Added mass and oscillation frequency for a circular cylinder subjected to vortex-induced vibrations and external disturbance, Journal of Fluids and Structures, 14 (2000) 1071-1088.

[22] R. King, Vortex Excited Oscillations of Yawed Circular Cylinders, Journal of Fluids Engineering, 99 (1977) 495-501.

[23] C.H.K. Williamson, R. Govardhan, Vortex-induced vibrations, Annual Review of Fluid Mechanics, 36 (2004) 413-455.

[24] O.M. Griffin, Vortex-excited cross-flow vibrations of a single cylindrical tube, ASME Journal of Pressure Vessel Technology, 102 (1980) 158-166.

[25] R. King, A review of vortex shedding research and its application, Ocean Engineering, 4 (1977) 141-171.

[26] A. Khalak, C.H.K. Williamson, Motions, forces and mode transitions in vortex-induced vibrations at low mass-damping, Journal of Fluids and Structures, 13 (1999) 813-851.

[27] R. Govardhan, C.H.K. Williamson, Resonance forever: existence of a critical mass and an infinite regime of resonance in vortex-induced vibration, Journal of Fluid Mechanics, 473 (2002) 147-166.

[28] R. Govardhan, C.H.K. Williamson, Critical mass in vortex-induced vibration of a cylinder, European Journal of Mechanics - B/Fluids, 23 (2004) 17-27.

[29] J.T. Klamo, A. Leonard, A. Roshko, The effects of damping on the amplitude and frequency response of a freely vibrating cylinder in cross-flow, Journal of Fluids and Structures, 22 (2006) 845-856.

[30] R.D. Blevins, C.S. Coughran, Experimental investigation of vortex-induced vibration in one and two dimensions with variable mass, damping, and Reynolds number, Journal of Fluids Engineering, 131 (2009) 101202-101207.*

[31] T. Sarpkaya, Fluid forces on oscillating cylinders, ASCE Journal of The Waterway, Port, Coastal and Ocean Division, 104 (1978) 275-290.

[32] B.J. Vickery, R.D. Watkins, Flow-induced vibrations of cylindrical structures, in: 1st Australian Conference on Hydraulics and Fluid Mechanics, Pergamon, New York, 1964, pp. 213–241.

[33] T. Sarpkaya, A critical review of the intrinsic nature of vortex-induced vibrations, Journal of Fluids and Structures, 19 (2004) 389-447.

[34] R.A. Skop, O.M. Griffin, A model for the vortex-excited resonant response of bluff cylinders, Journal of Sound and Vibration, 27 (1973) 225-233.

[35] J.T. Klamo, A. Leonard, A. Roshko, On the maximum amplitude for a freely vibrating cylinder in cross-flow, Journal of Fluids and Structures, 21 (2005) 429-434.

[36] R.N. Govardhan, C.H.K. Williamson, Defining the ‘modified Griffin plot’ in vortex-induced vibration: revealing the effect of Reynolds number using controlled damping, Journal of Fluid Mechanics, 561 (2006) 147-180.

[37] T.L. Morse, C.H.K. Williamson, Steady, unsteady and transient vortex-induced vibration predicted using controlled motion data, Journal of Fluid Mechanics, 649 (2010) 429-451.

[38] M.M. Zdravkovich, Modification of Vortex Shedding in the Synchronization Range, Journal of Fluids Engineering, 104 (1982) 513-517.

[39] C.C. Feng, The measurement of vortexinduced effects in flow past stationary and oscillating circular and d-section cylinders, in: Department of Mechanical Engineering, The University of British Columbia, Canada, 1968.

[40] Z.J. Ding, S. Balasubramanian, R.T. Lokken, T.W. Yung, Lift and damping characteristics of bare and straked cylinders at riser scale Reynolds numbers, in, Offshore Technology Conference.

[41] K. Raghavan, M.M. Bernitsas, Experimental investigation of Reynolds number effect on vortex induced vibration of rigid circular cylinder on elastic supports, Ocean Engineering, 38 (2011) 719-731.

[42] A. Protos, V.W. Goldschmidt, G.H. Toebes, Hydroelastic Forces on Bluff Cylinders, Journal of Fluids Engineering, 90 (1968) 378-386.

[43] G.H. Toebes, The Unsteady Flow and Wake Near an Oscillating Cylinder, Journal of Fluids Engineering, 91 (1969) 493-502.

[44] T. Staubli, Calculation of the Vibration of an Elastically Mounted Cylinder Using Experimental Data From Forced Oscillation, Journal of Fluids Engineering, 105 (1983) 225-229.

[45] C.H.K. Williamson, A. Roshko, Vortex formation in the wake of an oscillating cylinder, Journal of Fluids and Structures, 2 (1988) 355-381.

[46] R. Gopalkrishnan, Vortex-induced forces on oscillating bluff cylinders, in, MIT, USA, 1993.

[47] A. Leonard, A. Roshko, Aspects of flow-induced vibration, Journal of Fluids and Structures, 15 (2001) 415-425.

[48] J. Carberry, J. Sheridan, D. Rockwell, Forces and wake modes of an oscillating cylinder, Journal of Fluids and Structures, 15 (2001) 523-532.

[49] J. Carberry, R. Govardhan, J. Sheridan, D. Rockwell, C.H.K. Williamson, Wake states and response branches of forced and freely oscillating cylinders, European Journal of Mechanics - B/Fluids, 23 (2004) 89-97.

[50] T.L. Morse, C.H.K. Williamson, Prediction of vortex-induced vibration response by employing controlled motion, Journal of Fluid Mechanics, 634 (2009) 5-39.

[51] W.W. Martin, E. Naudascher, I.G. Currie, Streamwise Oscillations of Cylinders, Journal of the Engineering Mechanics Division, 107 (1981) 589-607.

[52] I.G. Currie, D.H. Turnbull, Streamwise oscillations of cylinders near the critical Reynolds number, Journal of Fluids and Structures, 1 (1987) 185-196.

[53] O.M. Griffin, S.E. Ramberg, Vortex shedding from a cylinder vibrating in line with an incident uniform flow, Journal of Fluid Mechanics, 75 (1976) 257-271.

[54] A. Ongoren, D. Rockwell, Flow structure from an oscillating cylinder Part 1. Mechanisms of phase shift and recovery in the near wake, Journal of Fluid Mechanics, 191 (1988) 197-223.

[55] H.T. Low, Y.T. Chew, K.T. Tan, Fluid forces on a cylinder oscillating in line with a uniform flow, Ocean Engineering, 16 (1989) 307-318.

[56] G. Parkinson, Phenomena and modeling of flow-induced vibrations of bluff bodies, Progress in Aerospace Sciences, 26 (1989) 169–224.

[57] G. Birkhoff, E.H. Zarantonello, Jets, Wakes and Cavities, New York : Academic Press, 1957.

[58] R.E.D. Bishop, A.Y. Hassan, The lift and drag forces on a circular cylinder oscillating in a flowing fluid, in: Proceedings of the Royal Society of London, 1964, pp. 51-75.

[59] R.T. Hartlen, I.G. Currie, Lift-oscillator model of vortex induced vibration, Journal of the Engineering Mechanics, 96 (1970) 577–591.

[60] W.D. Iwan, R.D. Blevins, A Model for Vortex Induced Oscillation of Structures, Journal of Applied Mechanics, 41 (1974) 581-586.

[61] E.H. Dowell, Non-linear oscillator models in bluff body aero-elasticity, Journal of Sound and Vibration, 75 (1981) 251-264.

[62] A.B. Poore, E.J. Doedel, J.E. Cermak, Dynamics of the Iwan-Blevins wake oscillator model, International Journal of Non-Linear Mechanics, 21 (1986) 291-302.

[63] R.A. Skop, S. Balasubramanian, A new twist on an old model for vortex-excited vibrations, Journal of Fluids and Structures, 11 (1997) 395-412.

[64] S. Krenk, S.R.K. Nielsen, Energy balanced double oscillator model for vortex-induced vibrations, Journal of Engineering Mechanics, 125 (1999) 263-271.

[65] A. Farshidianfar, H. Zanganeh, A modified wake oscillator model for vortex-induced vibration of circular cylinders for a wide range of mass-damping ratio, Journal of Fluids and Structures, 26 (2010) 430-441.

[66] M.L. Facchinetti, E. de Langre, F. Biolley, Coupling of structure and wake oscillators in vortex-induced vibrations, Journal of Fluids and Structures, 19 (2004) 123-140.*

[67] R.H.M. Ogink, A.V. Metrikine, A wake oscillator with frequency dependent coupling for the modeling of vortex-induced vibration, Journal of Sound and Vibration, 329 (2010) 5452-5473.

[68] W.H. Xu, Y.X. Wu, X.H. Zeng, X.F. Zhong, J.X. Yu, A new wake oscillator model for predicting vortex induced vibration of a circular cylinder, Journal of Hydrodynamics, Ser. B, 22 (2010) 381-386.

[69] J.K. Vandiver, J.Y. Jong, The relationship between in-line and cross-flow vortex-induced vibration of cylinders, Journal of Fluids and Structures, 1 (1987) 381-399.

[70] G. Moe, Z.J. Wu, The lift force on a cylinder vibrating in a current, Journal of Offshore Mechanics and Arctic Engineering, 112 (1990) 297-303.

[71] T. Sarpkaya, Hydrodynamic damping, flow-induced oscillations, and biharmonic response, Journal of Offshore Mechanics and Arctic Engineering, 117 (1995) 232-238.

[72] M.S. Triantafyllou, A.H. Techet, F.S. Hover, D.K.P. Yue, VIV of slender structures in shear flow, in: IUTAM Symposium on Flow-Structure Interactions, Rutgers State University, USA, 2003.

[73] D. Jeon, M. Gharib, On circular cylinders undergoing two-degree-of-freedom forced motions, Journal of Fluids and Structures, 15 (2001) 533-541.

[74] N. Jauvtis, C.H.K. Williamson, Vortex-induced vibration of a cylinder with two degrees of freedom, Journal of Fluids and Structures, 17 (2003) 1035-1042.

[75] C.H.K. Williamson, N. Jauvtis, A high-amplitude 2T mode of vortex-induced vibration for a light body in XY motion, European Journal of Mechanics - B/Fluids, 23 (2004) 107-114.*

[76] B. Stappenbelt, F. Lalji, G. Tan, Low mass ratio vortex-induced motion, in: The 16th Australasian Fluid Mechanics Conference, Gold Coast, Australia,, 2007, pp. 1491-1497.*

[77] J.M. Dahl, F.S. Hover, M.S. Triantafyllou, O.H. Oakley, Dual resonance in vortex-induced vibrations at subcritical and supercritical Reynolds numbers, in: Journal of Fluid Mechanics, 2010, pp. 395-424.

[78] Y. Bao, C. Huang, D. Zhou, J. Tu, Z. Han, Two-degree-of-freedom flow-induced vibrations on isolated and tandem cylinders with varying natural frequency ratios, Journal of Fluids and Structures, (2012).

[79] X. Wu, F. Ge, Y. Hong, A review of recent studies on vortex-induced vibrations of long slender cylinders, Journal of Fluids and Structures, 28 (2012) 292-308.

[80] F.J. Huera-Huarte, P.W. Bearman, Wake structures and vortex-induced vibrations of a long flexible cylinder—Part 2: Drag coefficients and vortex modes, Journal of Fluids and Structures, 25 (2009) 991-1006.

[81] J.K. Vandiver, V. Jaiswal, V. Jhingran, Insights on vortex-induced, traveling waves on long risers, Journal of Fluids and Structures, 25 (2009) 641-653.

[82] D. Brika, A. Laneville, Vortex-induced vibrations of a long flexible circular cylinder, Journal of Fluid Mechanics, 250 (1993) 481-508.

[83] H. Lie, K.E. Kaasen, Modal analysis of measurements from a large-scale VIV model test of a riser in linearly sheared flow, Journal of Fluids and Structures, 22 (2006) 557-575.

[84] J.R. Chaplin, P.W. Bearman, F.J. Huera Huarte, R.J. Pattenden, Laboratory measurements of vortex-induced vibrations of a vertical tension riser in a stepped current, Journal of Fluids and Structures, 21 (2005) 3-24.

[85] J.K. Vandiver, D. Allen, L. Li, The occurrence of lock-in under highly sheared conditions, Journal of Fluids and Structures, 10 (1996) 555-561.

[86] L. Lee, D. Allen, Vibration frequency and lock-in bandwidth of tensioned, flexible cylinders experiencing vortex shedding, Journal of Fluids and Structures, 26 (2010) 602-610.

[87] W.R. Frank, M.A. Tognarelli, S.T. Slocum, R.B. Campbell, S. Balasubramanian, Flow-induced vibration of a long, flexible, straked cylinder

in uniform and linearly sheared currents, in: Offshore Technology Conference, OTC16340, 2004.

[88] C.K. Morooka, R.I. Tsukada, Experiments with a steel catenary riser model in a towing tank, Applied Ocean Research, 43 (2013) 244-255.

[89] S.T. Santillan, L.N. Virgin, Numerical and experimental analysis of the static behavior of highly deformed risers, Ocean Engineering, 38 (2011) 1397-1402.

[90] A.D. Trim, H. Braaten, H. Lie, M.A. Tognarelli, Experimental investigation of vortex-induced vibration of long marine risers, Journal of Fluids and Structures, 21 (2005) 335-361.*

[91] H. Marcollo, J.B. Hinwood, On shear flow single mode lock-in with both cross-flow and in-line lock-in mechanisms, Journal of Fluids and Structures, 22 (2006) 197-211.

[92] V. Jaiswal, J.K. Vandiver, VIV response prediction for long risers with variable damping, in: 26th International Conference on Offshore Mechanics and Arctic Engineering, American Society of Mechanical Engineers, San Diego, California, USA, 2007, pp. 901-909.

[93] F.J. Huera-Huarte, P.W. Bearman, Wake structures and vortex-induced vibrations of a long flexible cylinder—Part 1: Dynamic response, Journal of Fluids and Structures, 25 (2009) 969-990.

[94] J.N. Song, L. Lu, B. Teng, H.I. Park, G.Q. Tang, H. Wu, Laboratory tests of vortex-induced vibrations of a long flexible riser pipe subjected to uniform flow, Ocean Engineering, 38 (2011) 1308-1322.

[95] B. Sanaati, N. Kato, A study on the effects of axial stiffness and pre-tension on VIV dynamics of a flexible cylinder in uniform cross-flow, Applied Ocean Research, 37 (2012) 198-210.

[96] H. Al-Jamal, C. Dalton, Vortex induced vibrations using Large Eddy Simulation at a moderate Reynolds number, Journal of Fluids and Structures, 19 (2004) 73-92.

[97] H. Al Jamal, C. Dalton, The contrast in phase angles between forced and self-excited oscillations of a circular cylinder, Journal of Fluids and Structures, 20 (2005) 467-482.

[98] C.T. Yamamoto, J.R. Meneghini, F. Saltara, R.A. Fregonesi, J.A. Ferrari Jr, Numerical simulations of vortex-induced vibration on flexible cylinders, Journal of Fluids and Structures, 19 (2004) 467-489.

[99] J.P. Pontaza, H.-C. Chen, Three-Dimensional Numerical Simulations of Circular Cylinders Undergoing Two Degree-of-Freedom Vortex-Induced Vibrations, Journal of Offshore Mechanics and Arctic Engineering, 129 (2006) 158-164.

[100] J.P. Pontaza, R.G. Menon, H.-C. Chen, Three-Dimensional Numerical Simulations of Flows Past Smooth and Rough/Bare and Helically Straked Circular Cylinders Allowed to Undergo Two Degree-of-Freedom Motions, Journal of Offshore Mechanics and Arctic Engineering, 131 (2009) 021301-021301.

[101] D. Lucor, M.S. Triantafyllou, Parametric study of a two degree-of-freedom cylinder subject to vortex-induced vibrations, Journal of Fluids and Structures, 24 (2008) 1284-1293.

[102] R. Bourguet, G.E. Karniadakis, M.S. Triantafyllou, Lock-in of the vortex-induced vibrations of a long tensioned beam in shear flow, Journal of Fluids and Structures, 27 (2011) 838-847.

[103] R. Bourguet, g.e. Karniadakis, M.s. Triantafyllou, Vortex-induced vibrations of a long flexible cylinder in shear flow, Journal of Fluid Mechanics, 677 (2011) 342-382.

[104] R. Bourguet, D. Lucor, M.S. Triantafyllou, Mono- and multi-frequency vortex-induced vibrations of a long tensioned beam in shear flow, Journal of Fluids and Structures, 32 (2012) 52-64.

[105] M.L. Facchinetti, E. de Langre, F. Biolley, Vortex-induced travelling waves along a cable, European Journal of Mechanics - B/Fluids, 23 (2004) 199-208.*

[106] D.J. Newman, G.E. Karniadakis, A direct numerical simulation study of flow past a freely vibrating cable, Journal of Fluid Mechanics, 344 (1997) 95-136.

[107] L. Mathelin, E. de Langre, Vortex-induced vibrations and waves under shear flow with a wake oscillator model, European Journal of Mechanics - B/Fluids, 24 (2005) 478-490.

[108] R. Violette, E. de Langre, J. Szydlowski, Computation of vortex-induced vibrations of long structures using a wake oscillator model: Comparison with DNS and experiments, Computers and Structures, 85 (2007) 1134-1141.

[109] R. Violette, E. de Langre, J. Szydlowski, A linear stability approach to vortex-induced vibrations and waves, Journal of Fluids and Structures, 26 (2010) 442-466.

[110] N. Srinil, Analysis and prediction of vortex-induced vibrations of variable-tension vertical risers in linearly sheared currents, Applied Ocean Research, 33 (2011) 41-53.*

[111] N. Srinil, Multi-mode interactions in vortex-induced vibrations of flexible curved/straight structures with geometric nonlinearities, Journal of Fluids and Structures, 26 (2010) 1098-1122.*

[112] F. Ge, X. Long, L. Wang, Y. Hong, Flow-induced vibrations of long circular cylinders modeled by coupled nonlinear oscillators, Science in China Series G: Physics Mechanics and Astronomy, 52 (2009) 1086-1093.

[113] F. Ge, W. Lu, L. Wang, Y.-S. Hong, Shear flow induced vibrations of long slender cylinders with a wake oscillator model, Acta Mech Sin, 27 (2011) 330-338.

[114] X.Q. Wang, R.M.C. So, K.T. Chan, A non-linear fluid force model for vortex-induced vibration of an elastic cylinder, Journal of Sound and Vibration, 260 (2003) 287-305.

[115] S.N. Kuchnicki, H. Benaroya, Coupled transverse and axial motion of a compliant structure in response to vortex-shedding loads, Journal of Sound and Vibration, 257 (2002) 903-929.

[116] C.M. Leong, T. Wei, Two-degree-of-freedom vortex-induced vibration of a pivoted cylinder below critical mass ratio, Proceedings of the Royal Society A: Mathematical, Physical and Engineering Science, 464 (2008) 2907-2927.

[117] R. Govardhan, C.H.K. Williamson, Modes of vortex formation and frequency response of a freely vibrating cylinder, Journal of Fluid Mechanics, 420 (2000) 85-130.

[118] R. Bellman, Perturbation techniques in mathematics, physics, and engineering, Dover publications 1972.

[119] A.H. Nayfeh, Introduction to perturbation techniques, Wiley, New York, 1993.

[120] S.P. Raj, S. Rajasekar, Migration control in two coupled Duffing oscillators, Physical Review E, 55 (1997) 6237-6240.

[121] J.-S. Fang, Z. Fang, X.-J. Liu, M.-S. Rong, Chaos synchronization in two coupled Duffing oscillators, Chinese Physics Letter, 18 (2001) 1438-1441.

[122] B.R. Noack, F. Ohle, H. Eckelmann, On cell formation in vortex streets, Journal of Fluid Mechanics, 227 (1991) 293-308.

[123] T.L. Morse, C.H.K. Williamson, Fluid forcing, wake modes, and transitions for a cylinder undergoing controlled oscillations, Journal of Fluids and Structures, 25 (2009) 697-712.

[124] S. Kheirkhah, S. Yarusevych, S. Narasimhan, Orbiting response in vortex-induced vibrations of a two-degree-of-freedom pivoted circular cylinder, Journal of Fluids and Structures, 28 (2012) 343-358.

[125] G.R.S. Assi, N. Srinil, C.M. Freire, I. Korkischko, Experimental investigation of the flow-induced vibration of a curved cylinder in convex and concave configurations, Journal of Fluids and Structures, 44 (2014) 52-66.

[126] T.L. Morse, R.N. Govardhan, C.H.K. Williamson, The effect of end conditions on the vortex-induced vibration of cylinders, Journal of Fluids and Structures, 24 (2008) 1227-1239.

[127] A. Sanchis, G. Sælevik, J. Grue, Two-degree-of-freedom vortex-induced vibrations of a spring-mounted rigid cylinder with low mass ratio, Journal of Fluids and Structures, 24 (2008) 907-919.

[128] W.W. Seto, Schaum's outline of theory and problems of mechanical vibrations, Schaum's Outline Series, 1964.

[129] J. Klamo, The application of controlled variable magnetic eddy current damping to the study of vortex-induced vibrations, Experiments in Fluids, 47 (2009) 357-367.

[130] I.G. Hughes, T.P.A. Hase, Measurements and their Uncertainties: A Practical Guide to Modern Error Analysis, Oxford, 2010.

[131] J.R. Taylor, An Introduction to Error Analysis: The Study of Uncertainties in Physical Measurements, University Science Books, 1997.

[132] G.R.S. Assi, P.W. Bearman, N. Kitney, Low drag solutions for suppressing vortex-induced vibration of circular cylinders, Journal of Fluids and Structures, 25 (2009) 666-675.

[133] F. Flemming, C.H.K. Williamson, Vortex-induced vibrations of a pivoted cylinder, Journal of Fluid Mechanics, 522 (2005) 215-252.

[134] J.M. Dahl, F.S. Hover, M.S. Triantafyllou, S. Dong, G.E. Karniadakis, Resonant Vibrations of Bluff Bodies Cause Multivortex Shedding and High Frequency Forces, Physical Review Letters, 99 (2007) 144503.

[135] R.D. Blevins, Models for vortex-induced vibration of cylinders based on measured forces, ASME Journal of Fluids Engineering, 131 (2009) 101203-101201-101209.

[136] L. Kaiktsis, G.S. Triantafyllou, M. Özbas, Excitation, inertia, and drag forces on a cylinder vibrating transversely to a steady flow, Journal of Fluids and Structures, 23 (2007) 1-21.

[137] G.R. Franzini, R.T. Goncalves, J.R. Meneghini, A.L.C. Fujarra, Comparison between force measurements of one and two degrees-of-freedom VIV on cylinder with small and large mass ratio, in: The 10th Int. Conf. on Flow-Induced Vibration & Flow-Induced Noise, Dublin, 2012, pp. 561-568.

[138] N. Srinil, M. Wiercigroch, P. O'Brien, Reduced-order modelling of vortex-induced vibration of catenary riser, Ocean Engineering, 36 (2009) 1404-1414.

[139] P. Soni, Hydrodynamic Coefficients for Vortex-Induced Vibrations of Flexible Beams, in, Norwegian University of Science and Technology, 2008.

[140] H. Wu, D.P. Sun, L. Lu, B. Teng, G.Q. Tang, J.N. Song, Experimental investigation on the suppression of vortex-induced vibration of long flexible riser by multiple control rods, Journal of Fluids and Structures, 30 (2012) 115-132.

[141] J.K. Vandiver, Dimensionless Parameters Important to the Prediction of Vortex-Induced Vibration of Long, Flexible Cylinders in Ocean Currents, Journal of Fluids and Structures, 7 (1993) 423-455.

[142] H. Mukundan, Y. Modarres-Sadeghi, J.M. Dahl, F.S. Hover, M.S. Triantafyllou, Monitoring VIV fatigue damage on marine risers, Journal of Fluids and Structures, 25 (2009) 617-628.

[143] F.J.H. Huarte, Multi-mode vortex-induced vibrations of a flexible circular cylinder, in, Imperial College London, 2006.*

[144] D. Wagg, S. Neild, Nonlinear Vibration with Control, A Springer-SBM - Canopus Academic Publishing Ltd co-publication, 2010.

[145] N. Srinil, G. Rega, S. Chucheepsakul, Two-to-one resonant multi-modal dynamics of horizontal/inclined cables. Part I: Theoretical formulation and model validation, Nonlinear Dynamics, 48 (2007) 231-252.

***Suggested references for further study.**